https://ntrs.nasa.gov/search.jsp?R=20050214696 2019-08-29T20:50:31+00:00Z

NASA/TM-2005-213783

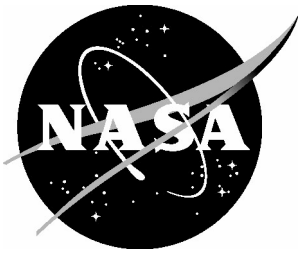

Experiment to Characterize Aircraft Volatile Aerosol and Trace-Species Emissions (EXCAVATE)

B. E. Anderson, H.-S. Branham, C. H. Hudgins, and J. V. Plant
Langley Research Center, Hampton, Virginia

J. O. Ballenthin, T. M. Miller, and A. A. Viggiano
Air Force Research Laboratory, Hanscom AFB, Massachusetts

D. R. Blake, University of California at Irvine, Irvine, California

H. Boudries, M. Canagaratna, R. C. Miake-Lye, T. Onasch, J. Wormhoudt, and D. Worsnop
Aerodyne Research, Inc., Billerica, Massachusetts

K. E. Brunke, Christopher Newport University, Newport News, Virginia

S. Culler, P. Penko, and T. Sanders, Glenn Research Center, Cleveland, Ohio

H.-S. Han, P. Lee, and D. Y. H. Pui, Univeristy of Minnesota, Minneapolis, Minnesota

K. L. Thornhill, Science Applications International Corporation, Hampton, Virginia

E. L. Winstead, GATS Inc., Hampton, Virginia

August 2005

The NASA STI Program Office . . . in Profile

Since its founding, NASA has been dedicated to the advancement of aeronautics and space science. The NASA Scientific and Technical Information (STI) Program Office plays a key part in helping NASA maintain this important role.

The NASA STI Program Office is operated by Langley Research Center, the lead center for NASA's scientific and technical information. The NASA STI Program Office provides access to the NASA STI Database, the largest collection of aeronautical and space science STI in the world. The Program Office is also NASA's institutional mechanism for disseminating the results of its research and development activities. These results are published by NASA in the NASA STI Report Series, which includes the following report types:

- TECHNICAL PUBLICATION. Reports of completed research or a major significant phase of research that present the results of NASA programs and include extensive data or theoretical analysis. Includes compilations of significant scientific and technical data and information deemed to be of continuing reference value. NASA counterpart of peer-reviewed formal professional papers, but having less stringent limitations on manuscript length and extent of graphic presentations.

- TECHNICAL MEMORANDUM. Scientific and technical findings that are preliminary or of specialized interest, e.g., quick release reports, working papers, and bibliographies that contain minimal annotation. Does not contain extensive analysis.

- CONTRACTOR REPORT. Scientific and technical findings by NASA-sponsored contractors and grantees.

- CONFERENCE PUBLICATION. Collected papers from scientific and technical conferences, symposia, seminars, or other meetings sponsored or co-sponsored by NASA.

- SPECIAL PUBLICATION. Scientific, technical, or historical information from NASA programs, projects, and missions, often concerned with subjects having substantial public interest.

- TECHNICAL TRANSLATION. English-language translations of foreign scientific and technical material pertinent to NASA's mission.

Specialized services that complement the STI Program Office's diverse offerings include creating custom thesauri, building customized databases, organizing and publishing research results ... even providing videos.

For more information about the NASA STI Program Office, see the following:

- Access the NASA STI Program Home Page at ***http://www.sti.nasa.gov***

- E-mail your question via the Internet to help@sti.nasa.gov

- Fax your question to the NASA STI Help Desk at (301) 621-0134

- Phone the NASA STI Help Desk at (301) 621-0390

- Write to:
  NASA STI Help Desk
  NASA Center for AeroSpace Information
  7121 Standard Drive
  Hanover, MD 21076-1320

NASA/TM-2005-213783

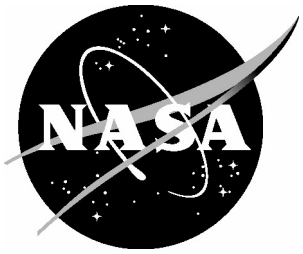

Experiment to Characterize Aircraft Volatile Aerosol and Trace-Species Emissions (EXCAVATE)

B. E. Anderson, H.-S. Branham, C. H. Hudgins, and J. V. Plant
Langley Research Center, Hampton, Virginia

J. O. Ballenthin, T. M. Miller, and A. A. Viggiano
Air Force Research Laboratory, Hanscom AFB, Massachusetts

D. R. Blake, University of California at Irvine, Irvine, California

H. Boudries, M. Canagaratna, R. C. Miake-Lye, T. Onasch, J. Wormhoudt, and D. Worsnop
Aerodyne Research, Inc., Billerica, Massachusetts

K. E. Brunke, Christopher Newport University, Newport News, Virginia

S. Culler, P. Penko, and T. Sanders, Glenn Research Center, Cleveland, Ohio

H.-S. Han, P. Lee, and D. Y. H. Pui, Univeristy of Minnesota, Minneapolis, Minnesota

K. L. Thornhill, Science Applications International Corporation, Hampton, Virginia

E. L. Winstead, GATS Inc., Hampton, Virginia

National Aeronautics and
Space Administration

Langley Research Center
Hampton, Virginia 23681-2199

August 2005

The use of trademarks or names of manufacturers in the report is for accurate reporting and does not constitute an official endorsement, either expressed or implied, of such products or manufacturers by the National Aeronautics and Space Administration.

Available from:

NASA Center for AeroSpace Information (CASI)
7121 Standard Drive
Hanover, MD 21076-1320
(301) 621-0390

National Technical Information Service (NTIS)
5285 Port Royal Road
Springfield, VA 22161-2171
(703) 605-6000

Contents

1.0. Project Summary

The Experiment to Characterize Aircraft Volatile and Trace Species Emissions (EXCAVATE) was conducted at Langley Research Center (LaRC) in January 2002 and focused upon assaying the production of aerosols and aerosol precursors by a modern commercial aircraft, the Langley B757, during ground-based operation. Remaining uncertainty in the post-combustion fate of jet fuel sulfur contaminants, the need for data to test new theories of particle formation and growth within engine exhaust plumes, and the need for observations to develop air quality models for predicting pollution levels in airport terminal areas were the primary factors motivating the experiment. NASA's Atmospheric Effects of Aviation Project (AEAP) and the Ultra Effect Engine Technology (UEET) Program sponsored the experiment which had the specific objectives of determining ion densities; the fraction of fuel S converted from S(IV) to S(VI); the concentration and speciation of volatile aerosols and black carbon; and gas-phase concentrations of long-chain hydrocarbon and PAH species, all as functions of engine power, fuel composition, and plume age.

Participants in EXCAVATE were solicited from among groups funded by AEAP and UEET to characterize engine emissions and near-field interactions and included: the tunable diode laser (TDL) and aerosol mass spectrometers (AMS) teams from Aerodyne Research, Inc.; the Particle and Gaseous Emissions Measurement System (PAGEMS) from NASA Glenn Research Center (GRC); the electron impact (EIMS) and chemical ionization mass spectrometer (CIMS) group from the Air Force Research Laboratory (AFRL); the nano-aerosol size analyzer (nASA) team from the University of Minnesota (UM); the whole air sampling group from the University of California at Irvine (UCI); and the in situ measurements group from NASA LaRC. Parameters and species that were measured included exhaust gas velocity, temperature, and CO_2 concentration; engine pressure ratios/power settings, fan speeds, combustor temperatures, and fuel-flow rates; sample stream CO_2, SO_2, SO_3, H_2SO_4, HONO, HNO_3, nonmethane hydro-carbons, and halocarbons; aerosol number densities and size distributions as a function of sample temperature; and aerosol mass and composition. Using well-characterized gas and aerosol probes and measurement systems, the participants collected data behind both the Langley T-38A (J85-GE engine) and B-757 (RB211) aircraft at sampling distances ranging from 1 to 35 m. For the B-757, fuels containing 810, 1050, and 1820 ppm S were burned in the tests to evaluate the impact of fuel S upon particle densities in the exhaust plume, and data were collected over a range of power settings from idle to near takeoff thrust. In the case of the T-38, a single fuel was burned (810 ppm), but data were collected over a variety of aerosol dilutions to evaluate the role of sampling techniques upon aerosol number densities and size distributions.

The following text, tables, and graphs provide detailed information regarding the aircraft operating parameters and engine emission characteristics. Important conclusions that one can draw from EXCAVATE observations include:

- Chem-ion densities were very high in the exhaust of both aircraft and are consistent with values that are presently being used in microphysical models of aerosol formation in exhaust plumes.
- Both aircraft emit high concentrations of organic aerosols at low power settings.

- At idle, the aircraft emit much higher levels of organic aerosols than black carbon particles.
- Black carbon emission indices increase significantly in going from idle to cruise power.
- Observed aerosol size distributions were highly dependent upon the sample dilution ratio.
- Higher than expected levels of HONO were observed in the B757 exhaust.
- Total particle emission indices were typically a factor of 10 higher at 25 to 35 m than at 1 m downstream of the exhaust plane, indicating that significant numbers of new particles form within the exhaust plume as it cools and dilutes.
- The concentration of sulfate aerosol increased considerably as sampling took place progressively further downstream of the exhaust plane, suggesting that sulfate particles form and undergo rapid growth within aircraft exhaust plumes.
- Emission indices for sulfate aerosols were directly dependent on the fuel sulfur concentration and typically represented ≈0.5 percent of the total sulfur budget.
- Aerosol concentrations and characteristics take several minutes to reach equilibrium values after changes in engine power. This was particularly notable when one reduced the engines from high to low power, a situation found during the aircraft landing cycle. In this case, the engines produced high concentrations of large organic aerosol particles for several minutes after power was reduced from a cruise setting to idle.

2.0. Introduction

Because of concern that aviation-related emissions may detrimentally impact the atmospheric environment, NASA initiated a major research effort-AEAP-aimed at characterizing the impact of current and future fleets of commercial aircraft on atmospheric chemical and radiative processes. To pursue this goal, the AEAP funded investigators to explore a wide range of topics, from determining what pollutants are formed within specific combustors to examining how the integrated emissions from the aircraft fleet influence ozone chemistry and cloud coverage.

In order to manage and assimilate information from these diverse topic areas, the AEAP was organized into six interacting subelements, each charged with specific goals and tasks. For example, the "Emission Scenarios" element gathers statistics on current and projected flight routes, the aircraft fleet, and the geographically distributed fuel use and pollutant production by aircraft (i.e., Baughcum et al., 1998). In turn, investigators funded under the "Global Modeling" element assimilate the emission scenario information into two-dimensional (2-D) and three dimensional (3-D) models to assess the impact of the emissions upon global trace chemical budgets and climate. The two subelements of AEAP addressed by EXCAVATE were "Engine Emission Characterization" and "Near-Field Interactions," which focus upon characterizing and quantifying the direct particulate and gas-phase emissions of aircraft and determining how these exhaust emissions are influenced by interaction with the atmosphere and the aircraft's trailing wingtip vortices. This paper describes a coordinated field experiment sponsored by these two subgroups to

characterize the speciation of sulfur and evolution of volatile aerosol particles in the exhaust from the turbine engine of a typical commercial airliner.

The task of characterizing aircraft exhaust emissions was initially scoped at obtaining in-flight verification of the test stand trace-gas emission index (EI) measurements and more quantitative data on the level and properties of particulate matter produced by the engines. The primary species of concern were reactive nitrogen compounds due to their role in regulating atmospheric O_3 and soot due to its ability to absorb solar radiation and its possible role in altering cloud microphysical properties.

A large base of turbine engine emission data was already available from the manufacturers because test stand measurements are required of all engines entering the commercial fleet. These tests consist of quantifying the amount of NO_x, CO, and unburned hydrocarbons emitted relative to fuel burned as a function of thrust. They also include a determination of "smoke number," a parameter roughly equivalent to the amount of soot an engine generates. Computational models were available to extrapolate the test stand EI data to cruise altitude conditions (Baughcum et al., 1996). Early in-flight observations indicated that values for NO_x derived in this manner were accurate at least to within experimental uncertainty and that wake or plume processing did not appreciably alter the expected EIs over time (Zheng et al., 1994; Fahey et al., 1995). It was thus assumed reasonable to adopt the test stand EI data along with fleet and fuel burn statistics and proceed with using 3-D models to evaluate the impact of aircraft NO_x on the global ozone budget (Friedl, 1997).

Characterizing the aerosol emissions from aircraft has proven to be a difficult task. Particulates directly emitted by jet aircraft are mostly soot with traces of metals and heavy unburned hydrocarbons. The smoke number data provided by manufacturers are only a qualitative estimate of soot emission, dependent on sampling conditions and soot characteristics and morphology, and of little value for estimating atmospheric impacts. Thus, new and more detailed studies were required. Subsequent exhaust exit-plane measurements on engines mounted in test cells and aircraft in runup facilities indicated that jet turbines produce on the order of 10^{15} soot particles with a mean mass diameter of 40 to 60 nm per kg of fuel burned. Hydration tests on the particles suggested they contain an appreciable amount of soluble material (Hagen et al., 1992). This result was not surprising because aviation fuel contains, as an impurity, varying amounts of sulfur (up to 3000 ppm), a fraction of which is oxidized during combustion to form H_2SO_4, which can, in turn, be adsorbed onto the soot particles to improve their hydration properties (Wyslouzil et al., 1994).

The AEAP sponsored in-flight measurements verified that aircraft are prodigious sources of soot particles but yielded the surprising observation that they also produce an enormous number of ultrafine volatile particles (Fahey, 1995). Assuming the particles were composed of sulfur species, the results suggested that a significant fraction of the sulfur contaminants in jet fuel is converted to S(VI) species either within the engine or very early in the exhaust plume evolution. High S(IV) to S(VI) conversion efficiencies in aircraft engines and rapid formation of sulfuric acid particles in aircraft plumes could have serious climatic implications as such particles play a significant role in heterogeneous chemical processes (i.e., ozone destruction) as well as in regulating cloud formation, duration, and radiative characteristics. The inferred amount of sulfate observed in the experiment was inconsistent with the sulfate being produced by hydroxyl radical (OH) oxidation alone and challenged the contemporary understanding of turbine engine chemical kinetics.

The observations of volatile particles in aircraft plumes and the recognition of their potential impact on atmospheric processes spurred a number of investigations to determine the fate of jet fuel sulfur contaminants. Because it is exceedingly difficult to capture sufficient particulate samples for quantitative analysis, these experiments took the approach of varying fuel S concentrations and observing the corresponding impact upon bulk aerosol production and characteristics. In the first of these tests, Busen and Schumman (1995) observed no visible difference in the contrails from an aircraft with one engine burning 2 ppm S fuel and the other aircraft burning 250 ppm S fuel. Subsequently, Schumman et al., (1996) found only a 25 percent difference in ultrafine (>7 nm in diameter) particle concentrations in the near-field exhaust of engines burning 170 and 5500 ppm S fuel. Later Miake-Lye et al. (1998) showed a direct correlation between fuel sulfur content and aircraft production of volatile particles and estimated an S(IV) to S(VI) conversion efficiency of 6 to 30% for a modern B757 airliner. In contrast, Schumman et al. (2002) more recently estimated a conversion efficiency of <1 percent for an ATTAS aircraft from observations of particulate and gas-phase H_2SO_4.

The lack of consensus in the experimental results coupled with the scarcity of data available to validate and stimulate the development of engine and exhaust plume models clearly established a need for more detailed and systematic studies of fuel S oxidation and aerosol production by aircraft engines. Thus, in 1997 the AEAP "Emission Characterization" and "Near-Field Interactions" groups developed collaborative experiments to sample the aerosol and aerosol precursor emissions of a specific turbine engine, both under carefully controlled test conditions and at cruise altitudes in varying environmental conditions. The engine tested was a Pratt & Whitney Model F100 series 200E of the type used on U.S. Air Force F-16 and F-15 fighter jet aircraft. The experiments included a ground-based measurement program conducted at the NASA Lewis Research Center Propulsion System Laboratory (Wey et al., 1998) and an airborne campaign based at NASA Wallops Flight Facility to sample the near-field emissions from U.S. Air National Guard F-16 aircraft (Anderson et al., 1999). Both venues included extensive characterization of the engine emissions-including measurements of aerosol size and volatility as well as gas-phase sulfur speciation-as functions of fuel sulfur, engine power, and ambient altitude. Results of the airborne study suggest that for the F100 engine, volatile aerosol production is highly dependent on fuel S concentration with observations being consistent with a maximum of ≈3 percent of the Fuel S being converted from S(IV) to S(VI) in the near-field wake. The ground-based tests gained insight into soot production and trace gas emissions as a function of engine temperature and operating pressure, but line losses in the necessarily long sampling tubes thwarted simultaneous attempts to measure SO_3 and H_2SO_4-the primary forms of S(VI) in the exhaust plume-to determine fuel S conversion efficiency.

Although the F100 engine tests and other experiments conducted by Europeans (Schumann et al., 2002) added to a body of information suggesting that fuel S conversion factors were more typically a few rather than tens of a percent, detailed information on precursor concentrations as well as the formation, evolution, and composition of volatile aerosol particles in the exhaust of commercial aircraft engines were still lacking. Thus, the AEAP in conjunction with the environmental effects component of NASA's UEET program sponsored EXCAVATE. A ground-based study conducted in an open-air facility, EXCAVATE had the objective of determining the concentration of chemi-ions; volatile aerosols and aerosol precursors; black carbon; and selected gas-phase species within the exhaust plume of a modern commercial turbofan engine as a function of engine power, fuel composition, and plume age. The experiment took advantage of recent advances in instrumentation and paid particular attention to

determining time-dependent aerosol composition as well as chemi-ion speciation. Significant efforts were made to minimize sample line lengths, characterize probe penetration efficiencies and transmission losses, and evaluate the impact of sampling strategies upon measured parameters. The paragraph below provides additional experimental details, summary results, and appendices reporting the specific observation from each participating group.

3.0. Experiment

3.1. Facilities and Aircraft Engines

EXCAVATE took place during January 2000 at NASA LaRC. Emissions from two aircraft were sampled during the mission: the NASA Langley Boeing 757 (B-757) and T-38A Talon. The B-757 is a dedicated research aircraft that was obtained by NASA from Eastern Airlines and has a relatively low number of hours on its engines and airframe. It is powered by a pair of Rolls Royce, RB-211-535E4 turbofan engines, as are ≈80 percent of all B-757s in service. These three-shaft, high bypass ratio engines produce 40100 lbs of thrust and have a single-stage wide-chord fan, six-stage IP compressor, six-stage HP compressor, single annular combustor, single-stage HP turbine, single-stage IP turbine, and a three-stage LP turbine. Langley's T-38A is powered by a pair of J85-GE-5A turbojet engines that produce 3850 lbs of thrust. Both aircraft nominally burn commercial Jet A or military JP-5 fuels.

The engine tests were conducted at NASA's "runup" facility that is located adjacent to a heavily wooded area on the west side of the Langley Air Force Base (see fig. 1).

Basically a large concrete pad, the facility includes a blast fence that deflects the engine exhaust upward to prevent damage to the neighboring vegetation. Water and electric power outlets located on either side of the pad were used for cooling instruments and providing power to experimenter equipment, respectively. Bolt holes and anchors are embedded at numerous places in the pad to provide restraining points for aircraft during high power engine runs and were used to secure the sampling probe sled and sample/electric lines to prevent them from being blown back by the exhaust blast.

During tests, the aircraft were parked on a line extending out from the center of the blast fence and chocked in place to keep them stationary during the high power engine runs. The sampling sled was positioned behind the engine so that the tips of the sampling probes were 1 m down steam and on the centerline of the turbine exhaust. For the B757, an additional aerosol-sampling probe was affixed to the blast fence 25 m downstream of the engine exhaust plane. To obtain aerosol samples at 10 and 35 m, the aircraft were rolled forward 9 m and rechocked. In the case of the T-38A, additional aerosol inlets were mounted on weighted stands positioned 10 and 25 m behind the engine exhaust plane; gas phase measurements were acquired only at 1-m separation distance.

3.2. Sample Probes and Systems

Figures 2 and 3 show a photograph and a diagram, respectively, of the gas and primary aerosol sampling probes that were designed by Robert Heirs from Arnold Engineering Development Center for use in EXCAVATE. The aerosol probe was designed to introduce a concentric flow of dilution gas as close behind the nozzle tip as possible to reduce particle

losses due to coagulation and thermophoresis. Tests conducted at UM indicate the probe is > 80 percent efficient for extracting particles >20 nm in diameter from hot gas flows (see appendix A). Constructed from standard 2-in. thick-walled stainless steel pipe, the gas inlet probe had a tear-drop shaped shield welded to the downstream side to reduce its coefficient of friction and provide protection to wires and tubes connected to sensors mounted to its tip. The probe was connected with a short length of thin-walled tubing to a manifold located in the sled that supplied sample air to the Air Force Lab chemical ionization and electron impact mass spectrometer and the Aerodyne tunable diode laser spectrometer. A small amount of flow was also extracted from the manifold and piped through 0.25-in. stainless tubing to the Langley trailer for CO_2 assay. The manifold terminated in a 2-in. pipe "T" clamped to the base of the sled that split the flow between pipes that exhausted out either side of the sled.

Welded to the back of the gas probe, the stainless steel aerosol inlet probe terminated just below the base mounting plate in two 0.5-in. Swagelok fittings that connected to lines to supply dilution gas and extract sample air (fig. 3). Boiloff from a liquid N_2 cylinder was used for dilution gas and the dilution ratio was set to approximately 8:1 by monitoring the ratio of CO_2 mixing ratio in the aerosol sample to that in the exhaust plume. Sample air was piped from the probe to the Langley equipment trailer through a combination of 0.5-in. stainless steel and carbon impregnated conductive tubing.

In addition to the aerosol probe, a Gerdien condenser was also welded to one side of the gas probe and a pitot tube and thermocouple were clapped to the other side (see fig. 2). Pressure transducers for the pitot tube, a thermocouple readout, and an electrometer to measure current on the Gerdien condenser were placed inside the sampling sled.

The gas sampling probe was bolted onto a 1-in. steel plate that was in turn bolted on top of the sampling sled (fig. 4). The sled was constructed of 4-in. steel tubing welded together and covered with a 0.25-in. steel plate. The sled was lined with 1-in. thick glass wool insulation to prevent engine heat from damaging the instrumentation it housed. When placed behind the B-757, the sled was pinned down to a hard point in the tarmac with a 1-in. diameter clevis pin. The combined weight of the sled and probes was estimated to be ≈3000 lbs.

Aerosol sampling inlets used to collect data at various distances downstream of the sampling sled were constructed from 0.25-in. Swagelok "T"s and stainless tubing. These inlets were raised to the height of the engine centerlines and connected with 0.5-in. stainless, copper, or conductive tubing to 0.5-in. stainless steel ball valves located in the Langley instrument trailer. The ball valves, in turn, were attached to a common sampling manifold to allow the operator to switch between sampling from one of the two or three inlets positioned behind the aircraft.

Additional instruments and data acquisition systems, along with operator stations, were located within the Langley and Aerodyne trailers and the NASA Glenn PAGEMS truck. These vehicles were parked along the edge of the runup area, typically 20 to 30 ft from the sampling sled, and were kept outside the conical region that extended out 45^o on either side behind the exhaust plane (fig. 5).

3.3. Measurements

Table 1 provides a list of the measurements acquired during the experiment. Langley was responsible for measuring the aircraft engine parameters, exhaust CO_2 mixing ratio, total CN

concentrations, black carbon, and submicron aerosol size distributions (see appendix B). Aerodyne Research, Inc., made measurements of aerosol composition, using their new aerosol mass spectrometer (appendix C), as well as operated the NASA GRC tunable diode laser system that determined mixing ratios of CO_2, SO_2, SO_3, and HONO (see appendix D). UM provided nucleation mode size distributions for heated and unheated samples using their rapid scanning, nASA (appendix E). AFRL provided a chemical ionization mass spectrometer, a Gerdien tube condenser, and an ion mass spectrometer to measure a variety of species including SO_2, H_2SO_4, HNO_3, total ion densities, and ion speciation (appendix F) and NASA GRC participated with their PAGEMS van to make comparative measurements of aerosols and trace gases to evaluate the status of their measurement systems and techniques with that of other participating groups.

Table 1. Measurements

Species/Parameter	Technique	Group
Engine parameters	Aircraft systems	LaRC
Fuel sulfur content	X-ray fluorescence	LaRC
Exhaust parameters (T, P, velocity)	Pitot tubes, thermocouples	LaRC
Sample and exhaust CO_2	IR spectrometer	LaRC
Aerosol size and volatility (3 to 100 nm)	Nano differential mobility analyzer (DMA)	UM
Aerosol size (10 to 1000 nm)	DMA, OPC	LaRC & GRC
Black carbon	Aethelometer	LaRC
Nonmethane hydrocarbons	Grab samples	LaRC/UCI
SO_2, CO_2, SO_3, H_2O, HONO	TDL	Aerodyne/GRC
Aerosol composition	Mass Spectrometer	Aerodyne
H_2SO_4, HONO, HNO_3, SO_2	Chemical ion mass spectrometer	AFRL
Ion density	Gerdien condenser	AFRL
Ion composition	Ion Mass Spectrometer	AFRL

LaRC: Langley Research Center, Bruce Anderson, PI

UCI: University of California, Don Blake, PI

UM: University of Minnesota, David Pui, PI

GRC: Glenn Research Center, Paul Penko and Clarence Change, PIs

Aerodyne MS group: Doug Worsnop, PI

Aerodyne TDL group: Joda Wormhoudt and Rick Miake-Lye, PIs

3.4. Fuels

EXCAVATE's primary objectives included determining the post-combustion fate of fuel S species and examining the formation and evolution of sulfur particles in the exhaust plume as a function of engine power and plume age. To meet these objectives required burning fuels of known and varying S concentrations. Although we had originally planned to obtain a low S Jet-A fuel (<5ppm) and produce a medium (i.e., 100 ppm) and high S (1000 ppm) fuels from it by adding tetrahydrothiophene, time and funding constraints forced us to purchase a JP-5 fuel from the local government contractor and to produce a single, higher S content fuel by mixing in tetrahydrothiophene sufficient to boost the S level by ≈1000 ppm. We thus ended with two fuels from a single hydrocarbon matrix containing 1050±100 and 1820±100 ppm S for use in the B-757 fuel S tests. A third JP-5 fuel obtained from the NASA Langley stock and containing 810±100 ppm S was used in the T-38A runs and in a B-757 experiment to test the sampling system and to fill the role of low S fuel when the supply of 1050 ppm S fuel was depleted. Fuel samples were sent to an independent testing laboratory where sulfur concentrations were determined using X-ray fluorescence techniques.

3.5. Experiment Matrices

As discussed above, exhaust plumes from both the Langley T-38A and B-757 were sampled during EXCAVATE, with the primary interest in sampling the T-38A being to test and perfect our measurement procedures, determine optimum dilution ratios, and to evaluate sampling losses as well as to obtain information on particle growth as the exhaust plume cools and disperses. Varying engine power, sample dilution ratio, and sampling distance satisfied these objectives.

Table 2 lists the dates, times, duration, and test variable settings for the T-38A runs. Figure 6 provides a plot of the T-38A test matrix as a function of time at each setting. Data were recorded on three different days (January 22, 24, and 29, 2002) at 10 percent power increments over |the range from idle (50 percent) to full military power (100 percent of maximum rpm). On January 29, data were collected from the 1-m probe using dilution ratios of approximately 8:1, 16:1, and 32:1 to test dilution effects and from additional probes located at 10 and 25 m to observe the formation and growth of volatile aerosols as the plume aged and dispersed.

Table 3 lists the dates, times, duration and test variable settings for the B-757 runs. Figure 7 provides a plot of the B-757 test matrix as a function of time at each particular setting. Our objectives in sampling this aircraft included determining the influence of fuel S on particle formation; thus, test variables included engine power, sampling distance, and three different levels of fuel S content. Based on results from the T-38A tests, dilution ratios were, where possible, maintained at >8:1. Tests conducted on January 25 were to check instrument functionality and to establish the range of engine power settings that the sampling rig could withstand, so the full set of measurements was not recorded during these runs. Based on these tests, we decided to collect data engine pressure ratios (EPRs) of 1.03 (idle), 1.15, 1.3, 1.4, and 1.5 when the probe was positioned at 1-m and to a maximum of 1.4 EPR when the probe was positioned 10 m behind the engine. The 1.5 EPR is less than takeoff power (typically 1.6 to 1.7), but was the highest power consistently achieved without overstressing the sampling stand and instrument operators. On January 26, the primary inlet probes were positioned at 1 m and the secondary aerosol inlet 25 m downstream. After a set of tests on the morning of January 27 to evaluate the effect of sample dilution and cold engine starting on aerosol emission properties, the

aircraft was rolled forward 9 m and sets of data were acquired with a primary probe separation of 10 m and the secondary inlet at 35-m.

4.0. Summary of Results

4.1. Engine Operating Parameters and Exhaust Properties

Engine operating parameters and exhaust plume characteristics were recorded to facilitate interpretation of simultaneous trace species measurements. Table 4 presents such data for the J85-GE engine as observed during the T-38A test runs. The aircraft operator visually averaged from cockpit indicators fuel-flow rate, exhaust gas temperatures at the combustor exit, and nozzle openings and recorded the information in a logbook. A LiCor instrument measured CO_2 fractions from exhaust gas samples collected 1-m downstream and on the centerline of the engine exhaust plane. We derived exhaust gas temperatures and Mach numbers 1-m downstream of the engine exhaust from total temperature and pressure measurements recorded from a thermocouple and pitot-static sensor, respectively. Values for each parameter are given at six power settings, ranging from idle (50 percent) to takeoff (100 percent). Not many of the plume thermodynamic parameters exhibited 10 to 15 percent variability at any given power setting. Our measurements for this study and those of others suggest that the engine requires several minutes to come to thermal equilibrium after power changes. However, the thermocouple used during EXCAVATE was very noisy, which may have exacerbated the problem.

Figure 8 shows how the fuel flow rate varies across the engine power range. At idle (50 percent), the engine consumes ≈0.07 kg s^{-1}, whereas at takeoff or "full-military-power" (100 percent), it burns about four times that amount. Assuming near 100 percent combustion efficiency, the fuel:air ratio for the engine appears to reach a minimum at medium, or cruise, power settings (≈80percent; see fig. 9). Combustor exit temperature is also a minimum at cruise power (fig. 10) and is positively correlated with exhaust CO_2 fraction (fig. 9), which is reasonable since both the temperature and CO_2 mixing ratio are dependent on the amount of ambient bypass air drawn through the engine in excess of that required for stoichiometric combustion. Temperatures recorded 1 m downstream of the engine exit plane were typically 100 to 200 ^{o}C lower than at the combustor exit as a result of both mixing with bypass air and radiational cooling (fig. 10). The Mach number at the core of the exhaust plume 1-m downstream of the engine exit plane varied from ≈0.16 to >0.9 on going from idle to 100 percent power (fig. 11), which corresponds to velocities of ≈70 to over 410 m s^{-1} (fig. 12).

Table 5 shows the performance data for the RB-211-535E4 engine as observed during the B-757 test runs. As for the T-38A, the aircraft operator visually averaged fuel-flow rates, exhaust gas temperatures at the combustor exit, and fan speeds from cockpit indicators and recorded them in a logbook. We determined the percentage power by comparing the measured fuel-flow rates for each EPR with those listed for the various power settings tested and archived by the International Civil Aviation Organization (ICAO: <http://www.qinetiq.com/aircraft/aviation.html>). Again, we measured CO_2 fractions by a LiCor instrument from exhaust gas samples collected 1-m downstream and on the centerline of the engine exhaust plane and exhaust gas temperatures, and derived Mach numbers 1-m downstream of the engine exhaust from total temperature and pressure measurements recorded from a thermocouple and pitot-static sensor, respectively. Values for each parameter are given at

EPRs of 1.03 (idle), 1.15, 1.30, 1.40, and 1.50. EPR and engine power increase approximately linearly with fuel flow (figs. 13 and 14) and calculations based on a polynomial fit to the EPR versus fuel flow curve (fig. 13) suggest that 100 percent power (fuel flow of 1.82 kg s^{-1}) is ≈1.72 EPR. Note that the highest EPR tested in EXCAVATE (1.5) roughly corresponds to a high cruise setting and that the aircraft with a light payload is capable of taking off at EPR >1.55.

In contrast to the J85 engine that exhibited a maximum fuel:air ratio at cruise power settings, the RB-211 CO_2 emissions were a minimum at idle and increased monotonically with power, ranging from a low of 1.7 percent at 1.03 EPR to > 3.4 percent at 1.5 EPR (fig. 15). Exhaust gas temperatures also increased with power (Figure 16), consistent with the fact that the air:fuel ratio dropped as fuel flow increased. The plume mach number and hence, velocity, measured at 1 m downstream of the exhaust plane increased dramatically with EPR (figs. 17 and 18), ranging from 0.19 (velocity of 94 m s^{-1}) at idle to ≈0.7 (350 m s^{-1}) at 1.5 EPR. Polynomial fits to the experimental data indicate that the 1-m downstream Mach number and velocity would be ~0.81 and 407 m s^{-1}) at 100 percent power (1.72 EPR).

Measurements recorded 10 m downstream of the engine exit suggest that although the plume dilutes and cools fairly rapidly, it maintains a fairly high velocity for some distance behind the plane (table 5). For example, carbon dioxide mixing ratios at 1.03 EPR are a factor of eight fewer at 10-m than at 1-m (fig. 15), whereas the plume velocity only decreases ≈40% over this distance (figs. 17 and 18). One may speculate that the disparity in the dilution of these parameters is due to the mixing of bypass air with core flow from the combustor. The bypass flow is expelled from the engine at roughly the same velocity as the core flow, but because it is ducted around the compressor stages and combustor, it is relatively cool and does not contain combustion byproducts.

4.2. Tracers and Hydrocarbons

Hydrocarbon measurements were made by UCI, Donald Blake, PI. In practice, 11 whole air samples were collected in stainless steel canisters and shipped to UCI for analysis in their analytical laboratory. Appendix B contains results and a discussion of the measurements interpreted in terms of emission indices.

4.3. Gas-Phase HOHO and SO_x Species

Aerodyne Research, Inc., in collaboration with NASA GRC deployed a TDL instrument during EXCAVATE to determine exhaust plume nitrogen and sulfur species concentrations. The TDL was located in the base of the sampling stand and its optical absorption cell was coupled to the sampling manifold with a short piece of Teflon tubing, the goal being to maintain the sample temperature at very high values to preserve any SO_3 that may have formed in the combustor. Appendix C reports the results of these measurements.

4.4. Particulate Physical Properties

Two groups working in collaboration determined the optical and microphysical properties of engine aerosol emissions. NASA Langley deployed a condensation nuclei counter to measure total aerosol concentrations, a dual differential mobility analyzer and an optical particle counter

to determine size distributions, and a particle soot absorption photometer to measure soot concentrations. Appendix D reports the results of their study. UM used a nASA coupled with an inlet heater to determine the size distribution of volatile and nonvolatile aerosols in the 3-100 nm size range. Appendix E describes the results of their efforts.

4.5. Particle Composition

Aerodyne Research, Inc., operated an AMS during EXCAVATE. This instrument determines the composition of individual aerosols in the 30-1000 nm size range as a function of aerodynamic diameter. The instrument is particularly sensitive to organic, sulfate, and nitrate species. Appendix F reports the results of the AMS study.

4.6. Ion Density and Chemi-ion Speciation

The AFGL contributed several instruments to the effort to characterize the aircraft engine emissions: a chemical ionization mass spectrometer to assay gas-phase sulfur and nitrogen species; a Gerdien tube condenser to determine total chemi-ion concentrations; and an electron impact mass spectrometer to measure the chemi-ion mass spectrum. Appendix G reports the results of their measurements.

5.0. References

Anderson, B., et al., 1999: Air Force F-16 Aircraft Engine Aerosol Emissions Under Cruise Altitude Conditions, NASA/TM-1999-209192.

Baughcum, S. L., et al., 1996: *Scheduled Civil Aircraft Emission Inventories for 1992: Database Development and Analysis*, NASA CR-4700.

Busen, R. and U. Schumann, 1995: Visible Contrail Formation from Fuels With Different Sulfur Contents, *Geophys. Res. Lett., 22*, pp. 1357-1360.

Fahey, D., et al., 1995: Emission Measurements of the Concorde Supersonic Aircraft in the Lower Stratosphere, *Science, 270*, pp. 70-74.

Friedl, R. (ed.), 1997: Atmospheric Effects of Subsonic Aaircraft: Interim Assessment Report of the Advanced Subsonic Technology Program, NASA Ref. Publ. 1400.

Miake-Lye, R., et al., 1998: SO_x Oxidation and Volatile Aerosol in Aircraft Exhaust Plumes Depend on Fuel Sulfur Content, *Geophys. Res. Lett., 25*, pp. 1677-1680.

Schumann, U., et al., 1996: In Situ Observations of Particles in Jet Aircraft Exhausts and Contrails for Different Sulfur Containing Fuels, *J. Geophys. Res., 101*, pp. 6853-6869.

Schumann, U., et al., 2002: Influence of Fuel Sulfur on the Composition of Aircraft Exhaust Plumes: The Experiments SULFUR 1-7, *J. Geophys. Res.,* Art. No. 4247, August.

Wey, C. C., et al., 1998: Engine Gaseous, Aerosol Precursor, and Particulate at Simulated Flight Altitude Conditions, NASA TM-1998-208509, ARL-TR-1804.

Wyslouzil, B. E., et al., 1994: Observations of Hydration of Single Modified Carbon Aerosols, Geophys. Res. Lett., 21, pp. 2107-2110.

Zheng, J., et al., 1994: An Analysis of Aircraft Exhaust Plumes From Accidental Eencounters, Geophys. Res. Lett., 21, pp. 2579-2582.

Table 2 Sample Runs Behind Langley T-38A

Run number	Julian day	Percent power	Probe distance, m	GMT start	GMT end	Sample pressure	Sample CO_2, ppm	Gas probe CO_2, ppm	Static T, C	Velocity, m/s
1	23	50	1	20:11:00	20:18:20					
2	23	60	1	20:19:10	20:28:53					
3	23	70	1	20:29:40	20:39:10					
4	23	80	1	20:41:10	20:49:30					
5	23	90	1	20:53:20	20:59:50					
6	23	100	1	21:02:32	21:10:40					
7	23	70	1	21:13:10	21:15:43					
8	23	50	1	21:18:15	21:20:30					
9	23	50	1	21:30:00	21:39:20					
10	23	100	1	21:41:00	21:48:30					
11	23	70	1	21:51:30	21:52:57					
12	23	50	1	21:53:20	21:57:14					
13	24	50	1	14:46:00	14:50:15	724	3395	3323	452.1	
14	24	50	10	14:50:46	14:56:40	686	831	10383	452.8	
15	24	60	10	14:58:00	15:03:00	688	1395	11962	389.3	
16	24	60	1	15:06:20	15:12:50	726	2783	11189	375.7	87.2
17	24	70	1	15:13:20	15:18:15	733	3048	11206	326.3	138.6
18	24	70	10	15:18:40	15:28:30	687	1796	10741	324.8	141.2
19	24	80	10	15:30:30	15:35:10	703	2196	10847	306.9	216.0
20	24	80	1	15:36:30	15:43:45	788	2903	10809	306.6	214.3
21	24	90	1	15:46:20	15:48:50	865	4280	12456	306.7	334.8
22	24	90	10	15:50:55	15:59:00	727	1289	12468	304.9	334.8
23	24	100	10	15:59:40	16:05:30	728	1539	9706	345.6	450.1
24	24	100	1	16:07:10	16:14:35	890	4291	8904	336.5	443.7
25	24	70	1	16:16:12	16:19:30	763	2115	9531	310.6	136.0
26	24	70	10	16:20:40	16:29:30	726	1166	11018	313.3	131.2
27	24	50	10	16:30:40	16:34:00	716	2017	14144	453.9	19.1
28	24	50	1	16:35:50	16:39:20	732	3101	14262	450.9	10.5
29	29	50	1	14:43:20	14:48:15	718	4059	23583		56.7
30	29	50	1	14:49:30	14:52:40	750	2050	23740		
31	29	50	1	14:55:00	14:59:20	762	651	23741		
32	29	50	1	15:28:40	15:31:40	754	1704	23453	244.3	66.6
33	29	50	10	15:34:25	15:36:20	709	2630	24334	278.8	68.7

Table 2 Concluded

Run number	Julian day	Percent power	Probe distance, m	GMT start	GMT end	Sample pressure	Sample CO_2, ppm	Gas probe CO_2, ppm	Static T, C	Velocity, m/s
34	29	50	1	15:39:10	15:39:40	707	3144	24254	268.5	71.1
35	29	60	1	15:42:20	15:45:00	721	3896	20841	233.5	83.5
36	29	60	1	15:45:20	15:48:35	757	1820	20903	232.9	83.8
37	29	60	1	15:48:50	15:52:10	768	634	20893	227.9	83.0
38	29	60	10	15:53:02	15:56:00	705	2388	20852	229.8	82.2
39	29	60	25	15:56:32	15:58:00	738	76	20813	225.9	82.0
40	29	60	1	15:58:30	15:59:20	755	1849	20795	225.9	82.4
41	29	70	1	16:00:50	16:03:15	742	3620	18653	197.2	118.7
42	29	70	1	16:03:50	16:06:35	771	2016	18687	193.8	118.0
43	29	70	1	16:07:04	16:10:16	784	978	18661	182.1	116.1
44	29	70	10	16:10:40	16:14:10	710	2652	18725	183.7	116.5
45	29	70	25	16:14:40	16:18:40	739	1376	18768	184.3	116.7
46	29	70	1	16:18:55	16:20:45	712	2672	18618	174.4	152.2
47	29	80	1	16:22:10	16:24:40	786	4048	18312	180.5	189.1
48	29	80	1	16:26:00	16:28:50	817	2110	18335	165.3	185.9
49	29	80	1	16:29:50	16:32:20	833	818	18321	168.8	186.6
50	29	80	10	16:32:35	16:36:15	725	1832	18359	168.6	186.1
51	29	80	25	16:36:30	16:39:25	739	1386	18359	169.3	189.6
52	29	90	1	16:40:45	16:43:06	818	3786	20735	244.1	313.8
53	29	90	1	16:44:00	16:46:40	842	2104	20540	245.0	315.4
54	29	90	1	16:47:10	16:50:20	902	953	20554	204.3	302.6
55	29	90	10	16:51:10	16:54:25	725	1951	20426	295.5	329.8
56	29	90	25	16:54:45	16:57:40	739	1378	20389	216.8	305.1
57	29	90	1	16:58:44	16:59:21	837	3404	20092	229.2	321.2
58	29	100	1	17:00:00	17:02:25	873	3973	27007	203.9	396.4
59	29	100	1	17:03:20	17:06:30	973	1980	28526	190.9	389.2
60	29	100	1	17:06:40	17:10:40	999	1348	28481	185.1	386.5
61	29	100	10	17:12:10	17:15:05	731	1977	28355	196.1	390.8
62	29	100	25	17:15:30	17:18:50	740	1502	27891	189.7	386.0
63	29	70	1	17:19:50	17:23:35	711	2725	18060	189.3	125.1
64	29	60	25	17:24:20	17:28:20	738	477	20886	200.4	82.2
65	29	60	10	17:28:34	17:29:20	714	2270	21752	210.5	78.5
66	29	50	10	17:29:20	17:35:00	714	1802	25011	246.9	59.9

Table 3 Sample Runs Behind Langley B-757

Run number	Julian day	Pressure ratio	Probe distance, m	Fuel sulfur	GMT start	GMT end	Sample pressure	Sample CO_2, ppm	Gas probe CO_2, ppm	Static T, C	Velocity, m/s
1	25	1.1	1	810	16:25:28	16:25:49	699	5785		191.9	155.5
2	25	1.15	1	810	16:26:10	16:27:13	736	5530		172.4	161.9
3	25	1.2	1	810	16:27:40	16:28:15	749	6018		79.7	167.7
4	25	1.25	1	810	16:28:30	16:29:25	753	7080		155.1	178.1
5	25	1.03	1	810	16:29:42	16:30:46	715	3584		229.1	81.0
6	25	1.03	1	810	16:44:40	16:45:36	749	2644		179.5	90.7
7	25	1.25	1	810	16:46:10	16:46:44	769	7765		207.4	219.4
8	25	1.3	1	810	16:48:00	16:49:10	803	5912		262.6	255.7
9	25	1.35	1	810	16:49:25	16:50:13	807	6845		283.0	280.8
10	25	1.4	1	810	16:50:30	16:50:50	822	7690		322.6	311.2
11	25	1.45	1	810	16:51:49	16:52:35	866	5306		365.7	342.7
12	25	1.5	1	810	16:52:50	16:53:38	869	5991		384.7	350.1
13	25	1.03	1	810	16:55:55	16:58:30	763	1091			
14	25	1.03	10	810	19:00:00	19:01:04	718	740	2007		
15	25	1.1	10	810	19:01:20	19:02:16	721	1060	2705		
16	25	1.15	10	810	19:02:30	19:04:40	720	1261	3013		104.4
17	25	1.2	10	810	19:05:20	19:07:30	709	1937	3373		119.4
18	25	1.03	10	810	19:33:27	19:34:43	756	1636	7063	309.8	97.8
19	25	1.1	10	810	19:34:48	19:35:15	765	3764	16097	372.9	189.9
20	25	1.15	10	810	19:35:27	19:35:55	771	5214	16246	335.3	237.5
21	25	1.2	10	810	19:36:05	19:36:25	774	7087	16052	359.5	281.4
22	25	1.25	10	810	19:36:41	19:37:00	815	5668	16006	343.0	303.3
23	25	1.3	10	810	19:37:07	19:38:07	817	6244	23240	361.3	321.1
24	25	1.35	10	810	19:38:16	19:38:46	819	6902	24544	339.8	336.3
25	25	1.4	10	810	19:38:54	19:39:12	832	7633	25624	326.9	345.1
26	25	1.03	10	810	19:43:10	19:45:26	740	2502	17892	276.0	82.1
27	26	1.03	1	1050	14:37:49	14:40:39	736	3356	17395	300.7	99.9
28	26	1.03	1	1050	14:40:58	14:46:31	750	2704	17573	300.9	104.7
29	26	1.03	25	1050	14:47:03	14:52:46	746	775	17608	303.4	100.9
30	26	1.03	1	1050	14:53:15	14:54:51	748	2774	17592	313.6	114.0
31	26	1.15	1	1050	14:56:12	15:04:14	764	3767	21572	310.6	193.3
32	26	1.15	25	1050	15:04:25	15:10:20	745	811	21537	307.5	194.0
33	26	1.3	1	1050	15:11:10	15:18:30	823	3555	25827	314.9	266.4

Table 3 Continued

Run number	Julian day	Pressure ratio	Probe distance, m	Fuel sulfur	GMT start	GMT end	Sample pressure	Sample CO_2, ppm	Gas probe CO_2, ppm	Static T, C	Velocity, m/s
34	26	1.3	25	1050	15:18:41	15:24:15	682	1321	25714	311.9	265.6
35	26	1.3	1	1050	15:24:34	15:25:55	821	3606	25636	315.2	268.5
36	26	1.4	1	1050	15:26:30	15:34:28	831	3830	28274	313.7	304.8
37	26	1.4	25	1050	15:34:40	15:40:15	684	1522	28338	304.7	302.5
38	26	1.4	1	1050	15:40:34	15:41:30	837	3788	28304	308.2	308.3
39	26	1.5	1	1050	15:41:53	15:45:05	846	3734	30390	303.0	339.3
40	26	1.5	25	1050	15:45:15	15:46:50	706	1647	30954	301.1	333.6
41	26	1.03	25	1050	15:47:02	15:52:30	686	617	18773	329.4	97.3
42	26	1.03	1	1820	16:28:40	16:33:40	738	2894	18208	326.2	95.6
43	26	1.03	1	1820	16:34:05	16:39:50	677	4071	18370	314.0	94.1
44	26	1.03	25	1820	16:40:03	16:45:58	675	553	18433	322.0	94.1
45	26	1.03	1	1820	16:46:44	16:47:52	659	4160	18325	356.1	103.5
46	26	1.15	1	1820	16:48:55	16:56:01	786	2748	23239	321.1	188.9
47	26	1.15	25	1820	16:56:13	17:01:50	684	961	23602	326.2	190.2
48	26	1.15	1	1820	17:02:20	17:03:28	791	2692	23605	327.4	196.5
49	26	1.3	1	1820	17:04:03	17:11:50	821	3786	27500	325.3	269.2
50	26	1.3	25	1820	17:12:08	17:15:56	691	1236	27627	324.3	269.4
51	26	1.3	1	1820	17:16:11	17:18:50	822	3756	27661	328.1	271.4
52	26	1.4	1	1820	17:19:30	17:26:00	830	4143	30499	332.4	309.1
53	26	1.4	25	1820	17:26:05	17:33:00	691	1416	30521	337.7	310.2
54	26	1.4	1	1820	17:33:05	17:34:10	844	3031	30574	343.1	313.3
55	26	1.5	1	1820	17:34:15	17:37:10	840	3893	32282	346.6	350.0
56	26	1.5	25	1820	17:37:17	17:39:25	697	1564	32745	346.1	344.6
57	26	1.03	25	1820	17:40:00	17:43:15	698	469	18935	334.2	94.4
58	26	1.03	1	1820	17:43:56	17:44:51	728	2612	15578	277.4	81.0
59	26	1.03	1	1820	19:52:23	19:53:03	726	2592	16075	295.8	90.0
60	26	1.03	1	1820	19:53:23	20:03:50	661	4315	18549	320.6	91.5
61	26	1.03	25	1820	20:04:05	20:09:49	682	631	19004	329.3	91.2
62	26	1.03	1	1820	20:10:24	20:11:31	673	3898	19092	336.7	97.7
63	26	1.15	1	1820	20:12:48	20:19:55	785	2743	23709	330.7	190.8
64	26	1.15	25	1820	20:20:08	20:23:57	684	929	23544	330.0	190.3
65	26	1.15	1	1820	20:24:20	20:27:02	790	2609	23528	334.5	193.6
66	26	1.3	1	1820	20:27:32	20:36:06	822	3613	29183	352.2	275.0

Table 3 Continued

Run number	Julian day	Pressure ratio	Probe distance, m	Fuel sulfur	GMT start	GMT end	Sample pressure	Sample CO_2, ppm	Gas probe CO_2, ppm	Static T, C	Velocity, m/s
67	26	1.3	25	1820	20:36:16	20:41:00	692	1284	29081	352.8	275.0
68	26	1.3	1	1820	20:41:05	20:42:27	817	3740	29089	353.2	278.3
69	26	1.4	1	1820	20:42:52	20:49:57	837	3252	32244	369.3	317.2
70	26	1.4	25	1820	20:50:01	20:55:36	694	1482	32668	371.5	318.0
71	26	1.4	1	1820	20:56:20	20:57:51	838	3237	32604	373.7	321.0
72	26	1.5	1	1820	20:58:01	21:01:04	837	3913	35176	381.1	360.6
73	26	1.5	25	1820	21:01:14	21:03:14	693	1620	36179	378.4	346.2
74	26	1.03	25	1820	21:03:31	21:05:17	694	504	24720	388.3	95.9
75	26	1.03	1	1050	21:05:50	21:12:31	735	2876	17591	375.0	92.5
76	26	1.03	1	1050	21:13:13	21:15:15	737	2898	17260	351.7	90.5
77	26	1.03	1	1050	21:23:20	21:25:55	706	3121	17130	340.7	90.0
78	26	1.15	1	1050	21:27:05	21:32:15	783	2751	23571	340.4	191.0
79	26	1.15	25	1050	21:32:23	21:37:16	683	946	23407	340.0	191.1
80	26	1.15	1	1050	21:37:40	21:38:22	785	2792	23387	346.9	203.1
81	26	1.3	1	1050	21:38:33	21:43:58	822	3699	28113	361.8	276.8
82	26	1.3	25	1050	21:44:10	21:49:08	693	1264	29016	357.6	275.5
83	26	1.3	1	1050	21:49:23	21:50:50	824	3644	28941	357.6	277.3
84	26	1.4	1	1050	21:51:13	21:57:09	831	3958	32465	372.2	320.1
85	26	1.4	25	1050	21:57:19	22:01:51	691	1505	32710	370.9	319.4
86	26	1.4	1	1050	22:02:05	22:02:35	836	3910	32602	369.7	319.3
87	26	1.5	1	1050	22:03:39	22:06:04	838	3980	35122	374.8	356.7
88	26	1.5	25	1050	22:06:13	22:08:37	692	1673	35587	375.3	358.0
89	26	1.03	1	1050	22:13:20	22:17:55	636	4789	15963	316.7	88.3
90	26	1.03	25	1050	22:19:00	22:20:30	738	1315	16323	318.8	87.9
91	26	1.03	1	1050	22:25:26	22:26:04	610	5226	16096	278.6	78.3
92	27	1.03	1	810	13:44:15	13:46:25	710	4525	18115	289.5	93.3
93	27	1.03	1	810	13:47:07	13:47:44	579	6774	18989	313.7	100.1
94	27	1.03	1	810	13:48:54	13:54:10	665	4033	17488	290.5	94.6
95	27	1.03	1	810	13:55:20	14:01:28	755	1488	17665	292.4	95.7
96	27	1.03	1	810	14:02:17	14:05:45	767	428	17691	294.3	91.1
97	27	1.03	1	810	14:07:07	14:12:25	679	3923	17752	296.8	94.6
98	27	1.3	1	810	14:14:55	14:20:52	822	4027	25945	325.9	268.5
99	27	1.3	1	810	14:22:40	14:26:14	841	2005	26051	318.3	266.5

Table 3 continued

Run number	Julian day	Pressure ratio	Probe distance, m	Fuel sulfur	GMT start	GMT end	Sample pressure	Sample CO_2, ppm	Gas probe CO_2, ppm	Static T, C	Velocity, m/s
100	27	1.3	1	810	14:28:05	14:32:00	863	1017	26156	314.7	266.3
101	27	1.03	1	810	14:35:40	14:38:53	619	5101	17482	322.7	91.2
102	27	1.03	10	1050	15:22:03	14:41:20	630	1181	2153	47.8	62.7
103	27	1.03	35	1050	15:43:14	15:45:50	637	349	2107	47.5	55.5
104	27	1.03	10	1050	15:46:20	15:49:35	702	1331	3191	65.2	123.6
105	27	1.15	10	1050	15:48:33	15:53:04	682	1468	3216	63.2	128.1
106	27	1.15	35	1050	15:53:18	15:57:13	698	724	3249	64.7	128.6
107	27	1.15	10	1050	15:57:40	15:59:33	683	1456	3191	63.9	129.9
108	27	1.3	10	1050	16:01:30	16:05:04	794	1420	4841	83.5	180.9
109	27	1.3	35	1050	16:05:17	16:05:17	706	899	4871	84.4	181.0
110	27	1.3	10	1050	16:11:23	16:12:20	793	1498	4865	87.4	184.3
111	27	1.4	10	1050	16:13:05	16:15:05	822	1524	6358	98.9	211.5
112	27	1.4	35	1050	16:15:26	16:18:30	707	1124	6374	99.5	208.8
113	27	1.03	35	1050	16:19:16	16:20:56	701	319	2276	55.9	57.7
114	27	1.03	10	1050	16:21:45	16:23:54	613	1193	2101	50.4	56.2
115	27	1.03	10	1820	17:57:10	18:04:35	683	917	2228	54.5	57.7
116	27	1.03	35	1820	18:04:56	18:12:17	692	353	2110	66.2	61.5
117	27	1.03	10	1820	18:13:20	18:15:10	663	1048	2180	71.8	60.5
118	27	1.15	10	1820	18:16:20	18:20:50	757	904	3175	68.7	128.5
119	27	1.15	35	1820	18:22:56	18:25:18	745	450	3163	70.0	128.0
120	27	1.15	10	1820	18:25:40	18:28:33	760	880	3206	69.3	129.9
121	27	1.3	10	1820	18:28:55	18:34:30	782	1069	4910	89.5	179.5
122	27	1.3	35	1820	18:34:50	18:39:22	699	905	4917	90.5	182.1
123	27	1.3	10	1820	18:39:46	18:40:57	817	912	4997	91.2	181.1
124	27	1.4	10	1820	18:41:13	18:43:58	826	1107	6415	104.2	212.1
125	27	1.4	35	1820	18:44:20	18:47:20	697	1127	6620	105.3	213.6
126	27	1.03	10	1820	18:48:25	18:50:00	611	1227	2165	67.6	58.7
127	27	1.03	10	810	18:54:40	18:57:36	667	967	2108	52.9	57.5
128	27	1.03	35	810	18:57:50	19:04:34	694	394	2095	54.0	56.9
129	27	1.03	10	810	19:05:07	19:06:31	655	1065	2394	59.6	58.3
130	27	1.15	10	810	19:09:25	19:13:55	687	1366	3184	77.9	127.5
131	27	1.15	35	810	19:14:19	19:15:59	695	716	3233	110.4	134.0
132	27	1.15	10	810	19:16:17	19:18:58	746	1045	3193	69.8	127.9

Table 3 Concluded

Run number	Julian day	Pressure ratio	Probe distance, m	Fuel sulfur	GMT start	GMT end	Sample pressure	Sample CO_2, ppm	Gas probe CO_2, ppm	Static T, C	Velocity, m/s
133	27	1.3	10	810	19:19:24	19:25:26	757	1393	4887	92.6	185.4
134	27	1.3	35	810	19:27:00	19:30:48	697	920	4968	91.5	183.9
135	27	1.3	10	810	19:31:12	19:31:54	808	1243	5048	94.1	190.0
136	27	1.4	10	810	19:32:06	19:34:42	821	1316	6350	106.2	214.3
137	27	1.4	35	810	19:35:04	19:38:07	702	1099	6405	106.3	209.9
138	27	1.03	10	1820	19:39:05	19:50:36	626	1112	2113	77.8	62.8
139	27	1.03	35	1820	19:50:58	19:55:12	697	357	2212	71.9	61.3
140	27	1.03	10	1820	19:55:33	19:57:14	688	703	2097	72.5	63.8
141	27	1.15	10	1820	19:59:36	20:05:08	720	1220	3140	70.0	128.8
142	27	1.15	35	1820	20:05:30	20:08:52	698	707	3101	72.5	128.6
143	27	1.15	10	1820	20:09:20	20:09:48	729	1172	3044	85.5	144.3
144	27	1.3	10	1820	20:10:20	20:14:56	789	1630	4937	92.7	184.8
145	27	1.3	35	1820	20:15:39	20:20:12	697	959	4968	94.3	185.4
146	27	1.3	10	1820	20:20:42	20:22:05	782	1668	4962	95.2	188.6
147	27	1.4	10	1820	20:22:45	20:25:03	819	1552	6378	107.0	212.3
148	27	1.4	35	1820	20:25:26	20:28:24	709	1099	6442	107.2	208.3
149	27	1.03	10	1820	20:29:24	20:33:40	594	1244	2074	78.2	60.4

Table 4 List of J85-GE-5 Performance Characteristics Averaged Over All Runs

	Engine power setting											
	50		60		70		80		90		100	
Measured parameter	Avg	Std dev	Avg	Std dev	Avg	Std dev	Avg	Std dev	Avg	Std dev	Avg	Std dev
Fuel flow, kg/sec	0.066	-	0.077	-	0.090	-	0.122	-	0.172	-	0.268	-
Exhaust gas temp, deg C	500	-	430	-	405	-	430	-	500	-	640	-
Nozzle opening, percent	85	-	83	-	68	-	43	-	24	-	15	-
Exhaust CO_2, percent	2.41	0.09	2.12	0.08	1.86	0.05	1.83	0.00	2.05	0.02	2.81	0.06
Exhaust Temp @ 1 m, deg C	403	53	363	36	300	35	302	48	341	34	409	36
Exhaust Mach number at 1 m	0.16	0.02	0.19	0.02	0.29	0.03	0.45	0.01	0.70	0.01	0.91	0.01
Exhaust velocity @ 1 m, m/s	70	15	86	10	132	13	197	13	321	12	413	28

Table 5 List of RB211-535E4 Performance Parameters Averaged Over All Data Runs

	Engine pressure ratio									
	1.03		1.15		1.30		1.40		1.50	
Measured parameter	Avg	Std dev	Avg	Std dev	Avg	Std dev	Avg	Std dev	Avg	Std dev
Percent power	4.0	0.8	26.3	1.1	47.6	1.8	60.7	0.6	73.9	-
Low pressure fan speed, percent	23.5	0.2	53.3	1.2	72.1	0.6	80.4	0.7	86.1	-
Medium pressure fan speed, percent	34.2	0.4	63.8	0.4	76.3	1.5	80.6	0.5	84.0	-
High pressure fan speed, percent	53.8	0.7	75.4	0.9	82.8	0.8	85.6	0.5	88.0	-
Exhaust gas temp, deg C	355.6	29.2	456.2	11.7	547.5	15.0	599.6	8.7	638.0	-
Fuel flow, kg/s	0.14	0.01	0.46	0.02	0.81	0.03	1.04	0.01	1.29	-
Exhaust temperature @ 1 m, deg C	318.3	26.8	328.7	12.2	334.3	19.0	347.3	27.4	350.8	33.0
Exhaust CO_2 @ 1 m, percent	1.76	0.10	2.32	0.08	2.74	0.14	3.10	0.18	3.36	0.22
Exhaust velocity @ 1 m, m/s	94.3	6.9	193.0	4.0	271.3	4.6	313.6	6.5	348.6	9.5
Exhaust Mach number @ 1 m	0.194	0.014	0.393	0.008	0.550	0.002	0.629	0.003	0.697	0.010
Exhaust temperature at 10 m, deg C	61.9	10.9	73.8	13.1	90.6	3.8	104.3	3.3	-	-
Exhaust CO_2 @ 10 m, percent	0.22	0.01	0.32	0.01	0.49	0.01	0.64	0.01	-	-
Exhaust velocity @ 10 m, m/s	59.4	2.6	130.3	4.7	183.9	3.2	211.4	2.2	-	-
Exhaust Mach number @ 10 m	0.162	0.008	0.349	0.014	0.481	0.010	0.543	0.007		

Figure 1. Photograph of the NASA Langley engine runup area showing blast fence in rear of pad with B-757 parked in front. Power and water connections are available on either side of pad.

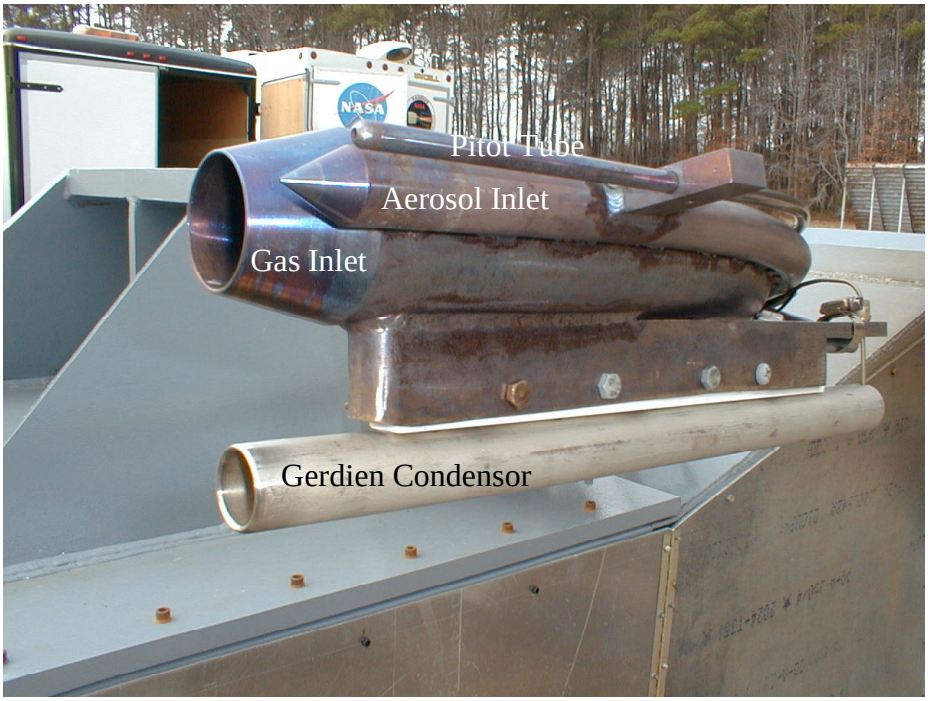

Figure 2. Photograph of inlet probe system mounted upon the sampling sled in position to sample emissions from T-38A, J85-GE-5 engines.

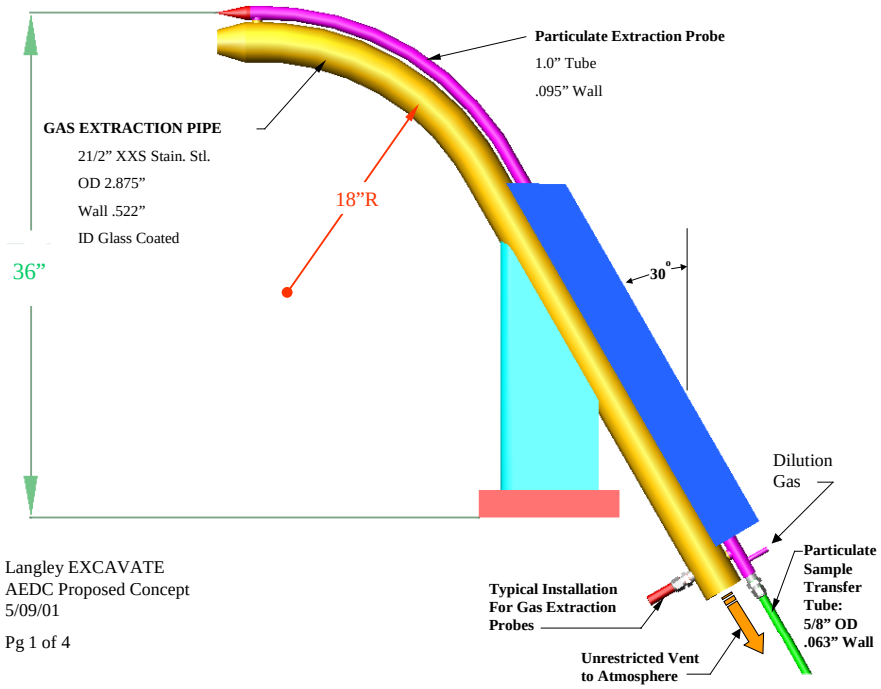

Figure 3. Diagram of gas and aerosol probes used in EXCAVATE. The gas probe was fabricated from standard 2-in. pipe, whereas particulate probe was constructed from two concentric tubes, which allowed dilution gas to be introduced near probe tip to reduce effects of condensation and coagulation on sampled aerosol populations.

Figure 4. Photograph of sampling sled and instrument container positioned behind the right engine of B-757.

Figure 5. Photograph of experimental setup showing B-757 with the sampling stand positioned behind right engine and equipment trailers parked off right wing.

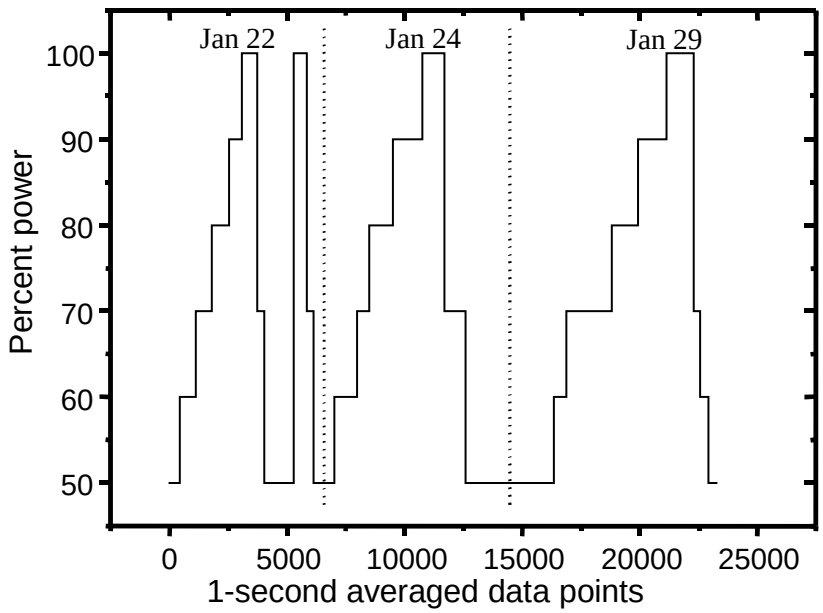

Figure 6. Plot of T-38A test sequence for 3 days on which its right engine was sampled.

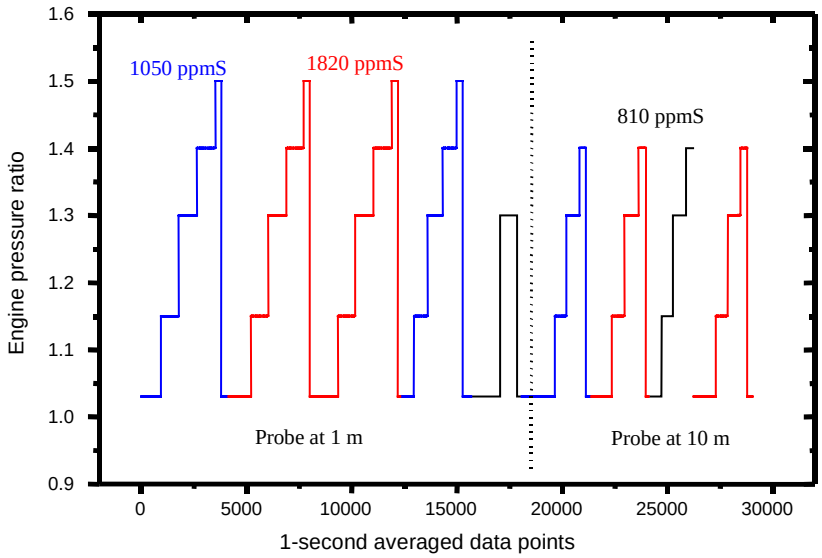

Figure 7. Plot of B-757 test matrix showing power sequence and utilization of different fuels.

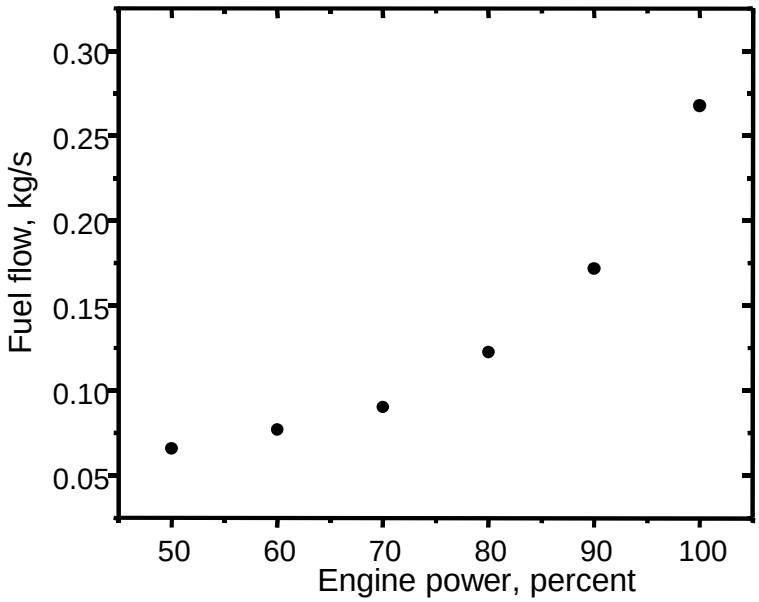

Figure 8. Plot of fuel-flow rate versus power for J85-GE-5 engines on NASA T-38A aircraft.

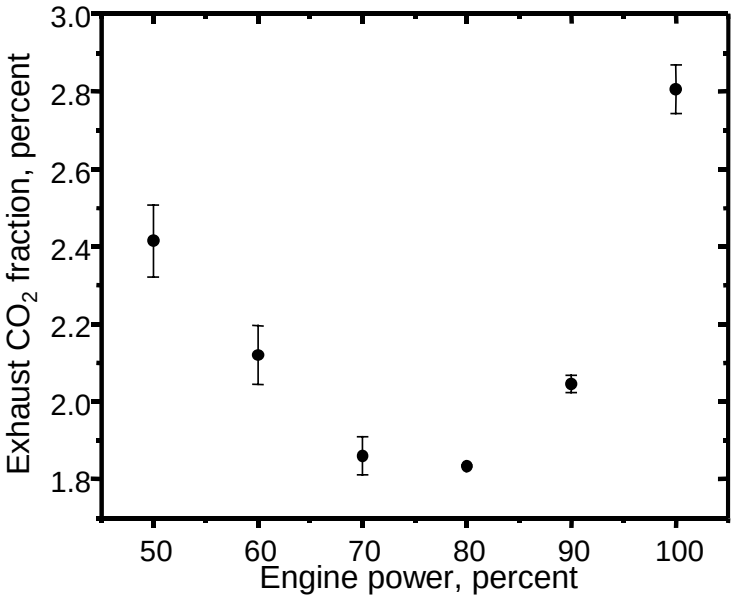

Figure 9. Plot of CO_2 concentration versus power as measured on engine centerline, 1-m downstream of J85-GE-5 exit plane.

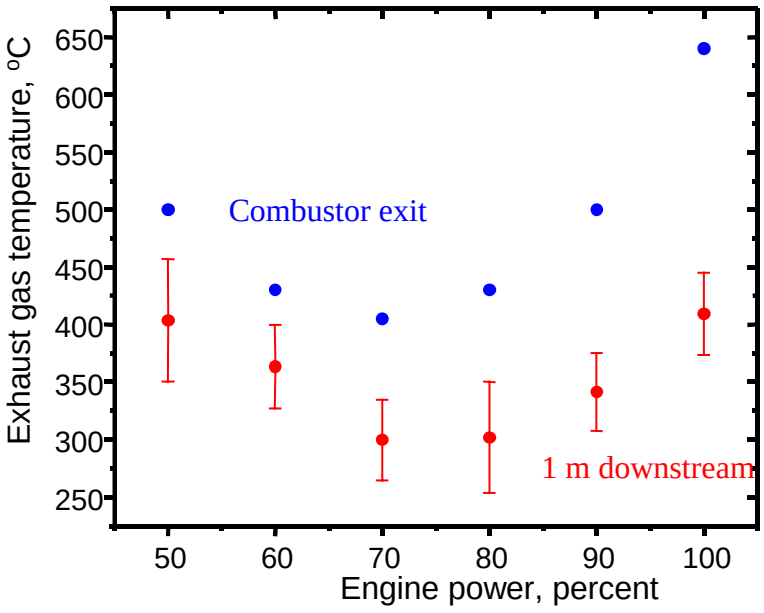

Figure 10. Plot of exhaust gas temperatures for J85-GE-5 as measured at combustor exit and 1 m downstream of exit plane.

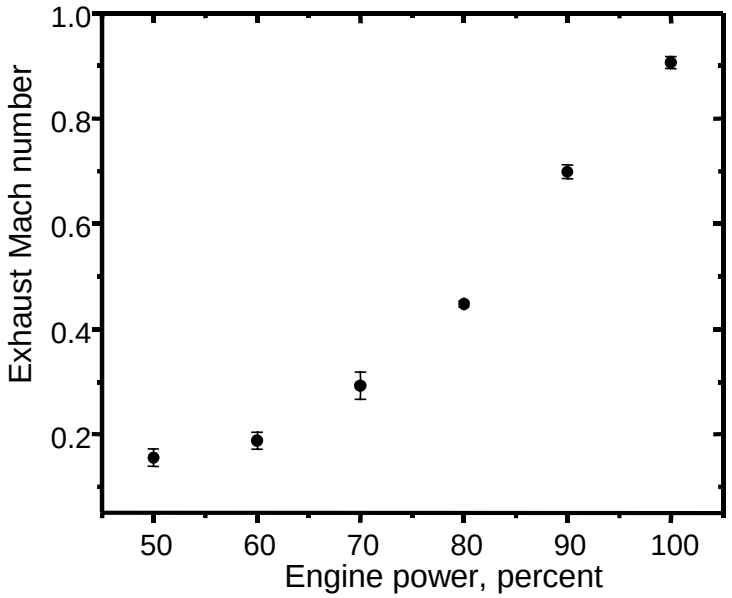

Figure 11. Exhaust gas Mach number versus power for J85-GE-5 engine as measured on engine center line 1-m downstream of exit plane.

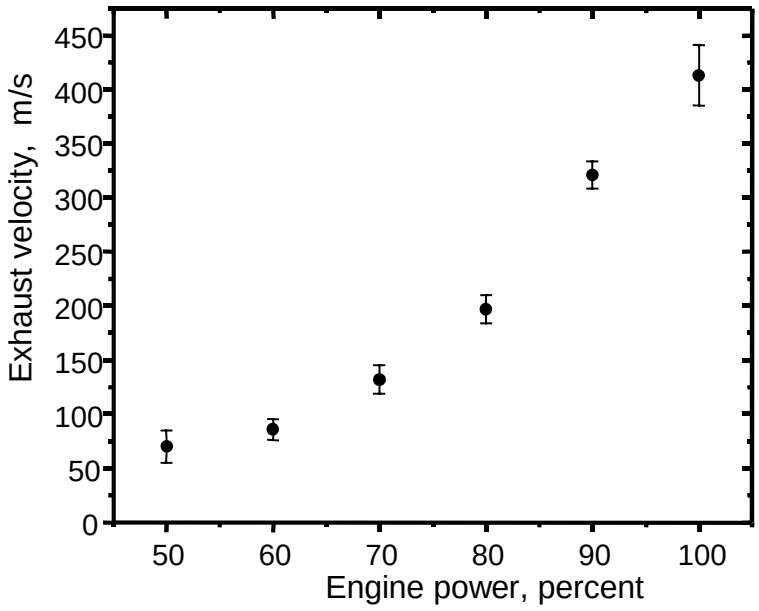

Figure 12. Exhaust gas velocity versus power for J85-GE-5 engine as measured on engine centerline 1-m downstream of exit plane.

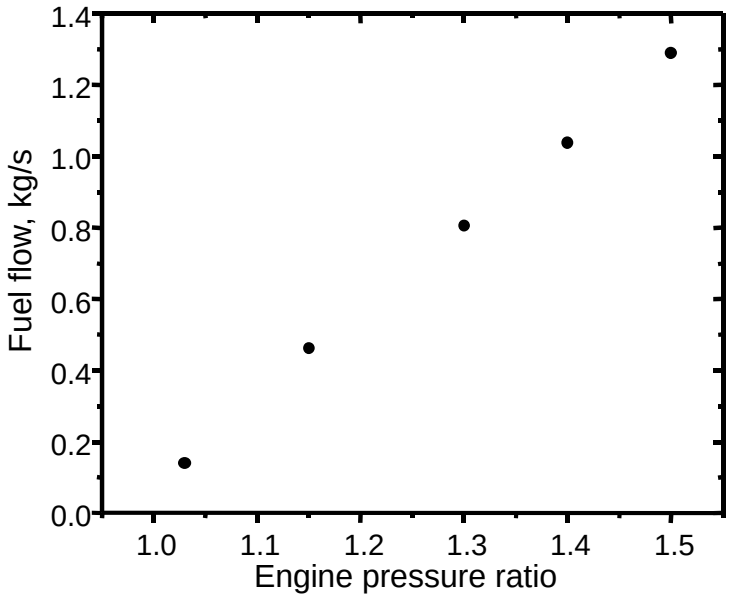

Figure 13. Fuel-flow rate versus EPR for RB-211-E4 engines of B757.

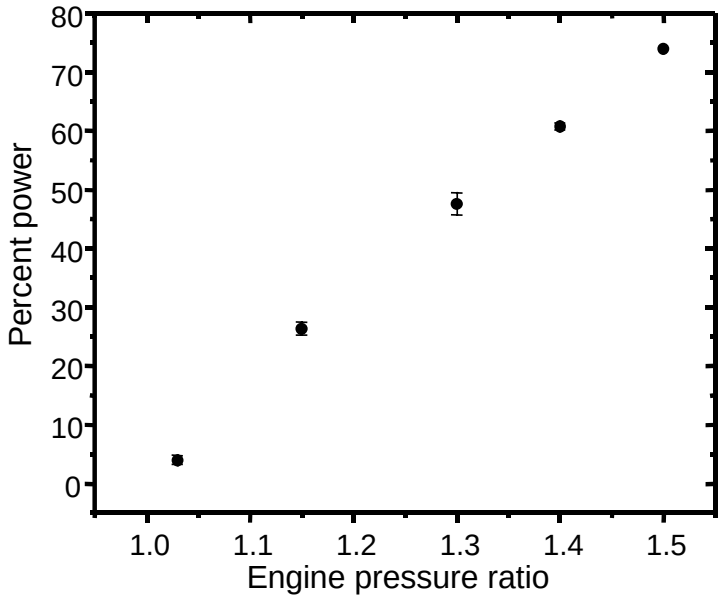

Figure 14. Plot of percent power versus EPR for RB-211-E4 engine, where relationship between the two variables was established by fitting a third order polynomial to fuel flow/power data provided on most current ICAO engine qualification sheet (http://www.qinetiq.com/aircraft/aviation.html).

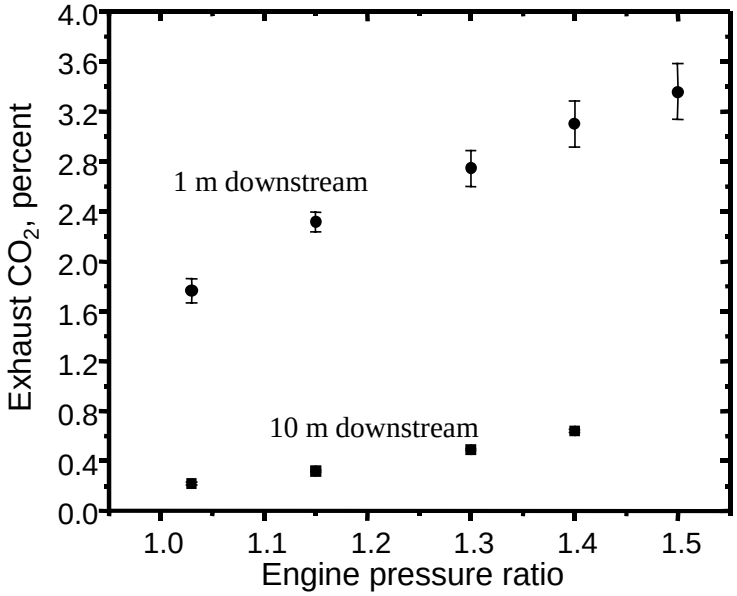

Figure 15. Carbon dioxide concentrations versus power as measured on engine center at 1 and 10-m downstream of RB-211-E4 exit plane.

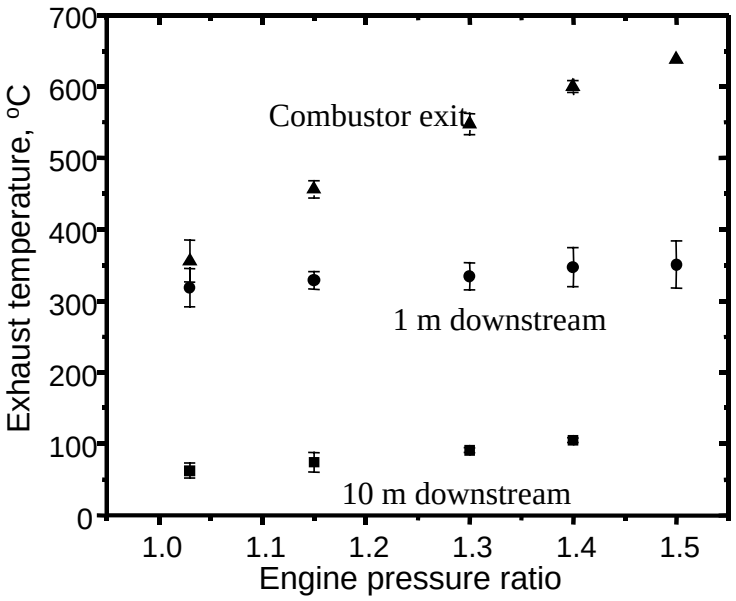

Figure 16. Plot of exhaust gas temperatures as function of power for RB-211-E4 engine as measured at combustor exit and on engine centerline at 1 and 10-m downstream of the exit plane.

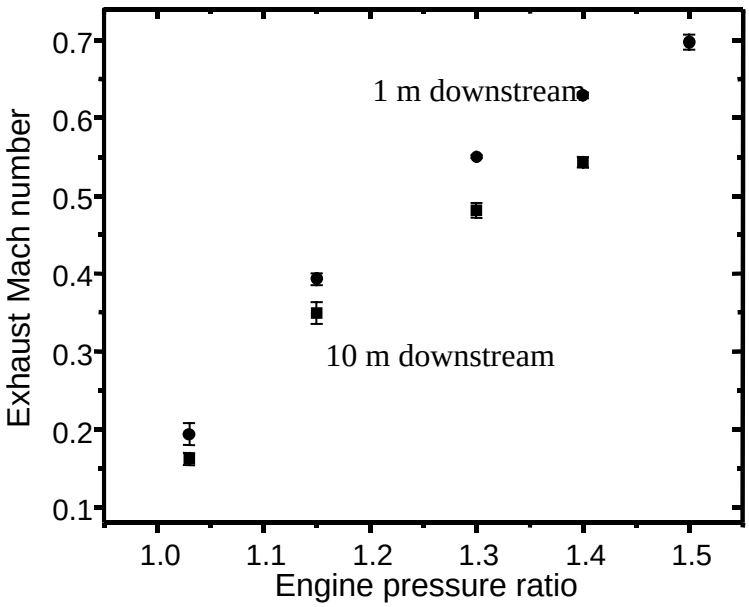

Figure 17. Plot of exhaust plume Mach number as function of power for RB-211-E4 engine measured on engine centerline at 1 and 10-m downstream of exit plane.

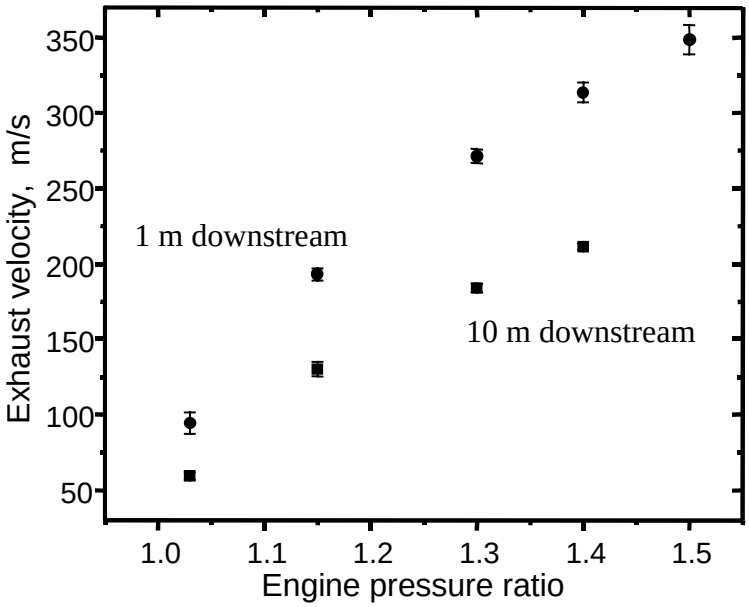

Figure 18. Plot of exhaust plume velocity as function of power for RB-211-E4 engine as measured on engine centerline at 1 and 10-m downstream of exit plane.

APPENDIX A: Performance Evaluation of Particle Sampling Probes for Emission Measurements of Aircraft Jet Engines

Poshin Lee and David Y. H. Pui
Particle Technology Laboratory,
Mechanical Engineering Department,
University of Minnesota, Minneapolis, USA

Abstract

Considerable attention has been recently received on the impact of aircraft-produced aerosols upon global climate. Sampling particles directly from jet engines has been performed by different research groups in US and Europe. However, a large variation has been observed among published data on the conversion efficiency and emission indexes of jet engines. The variation results surely from the differences in test engine types, engine operation conditions, and environmental conditions. The other factor that could result in the observed variation is the performance of used sampling probes. Unfortunately, it is often neglected in the jet engine community. Particle losses during the sampling, transport and dilution processes are often not discussed/considered in literatures. To address this issue, we evaluated the performance of two sampling probes by challenging them with monodisperse particles. A significant performance difference was observed under different operation conditions. Thermophoretic effect, non-isokinetic sampling and turbulence loss contribute to the particle loss in the sampling probe.

Keywords: aircraft exhaust, particle emission, sampling probe, jet engine

Introduction

It is known that atmospheric aerosols play a key role in the earth's radiation balance, and thereby strongly influence global climate. Due to the heavy air travel nowadays, aircraft engines directly emit a great amount of both soot and sulfuric acid particles to the upper troposphere and lower stratosphere. These particles may have negative impact on climate through the processes of inducing the formation of new ice clouds (contrails), modifying physical properties of existing cirrus clouds, and providing additional surface area for heterogeneous chemical reactions such as ozone destruction.

In order to address this issue, researches have been performed to evaluate the emission of jet engines when aircrafts are either on ground or in air. To be able to understand the detail particle formation processes, sampling particles from jet engine exhaust or in the near field has been performed by NASA Subsonic aircraft Contrail and Cloud Effect Special Study (SUCCESS) and SULFUR series experiments by German agency, Deutsche Forschungsanstalt fur Luft- and Raumfahut (DLR). For sulfate particle measurement, the values of ξ, the efficiency of conversion of fuel sulfate to sulfate in the forms of SO_3 and H_2SO_4, by SUCCESS showed that ξ does not have a strong dependence with the fuel sulfur content (FSC) (1-3). In contrast, studies of DLR showed a decrease in ξ with an increase of FSC (4-5). These variations may result from the differences in engine types, engine operation conditions, environmental conditions, sampling and measuring methods (6). However, a significant difference is found by the comparison of non-volatile particle emission indices (EIs), the amount of pollutant generated per kilogram of fuel burned, measured in NASA B757 exhaust plumes (1, 2) during the SUCCESS project. Researchers began to suspect that the variation may result from the sampling probe design, sampling losses, and other uncertainties associated with particle size measurement. Unfortunately, the issue had not been addressed in all the related studies. The purpose of this study is focused on the experimental evaluation of the performance of sampling probe for the accurate measurement of jet engine particle emission.

Background

In this study, the performance of sampling probes is evaluated by the comparison of inlet and outlet concentrations. The dilution ratio is defined by the ratio of outlet flow rate, Q_{out}, and inlet flow rates, Q_{in}. And the particle penetration, P, is defined by

$$P = \frac{C_{out} \times Q_{out}}{C_{in} \times Q_{in}}$$

where C_{in} is the inlet concentration and C_{out} is the particle outlet concentration. Ideally, particle penetration should equal to 1 if there is no loss.

Experimental Setup

The setup of particle generation system is shown in Figure 1. The compressed air was first dry and cleaned by passing through a diffusion dryer and a HEPA filter before it is used in a collision type of atomizer. A flow rate of 2 lpm was controlled by the orifice installed in the atomizer. NaCl solutions were used in the atomizer. Two different solution concentrations, 1% and 0.1% (by weight), were used in order to provide the test particles in the sizes ranging from 20 to 200 nm. Polydisperse NaCl particle was produced by atomizing a NaCl solution and drying the airborne droplet stream by a diffusion dryer. For getting monodisperse particles, a nano-DMA with a high voltage power supply was used. By changing the DMA voltage and sheath flow rate, monodisperse particles of different particle sizes can be classified. In order to improve the control of excess and sheath flows of the classifer, a flow re-circulation loop between excess and sheath air ports was implemented as described in (7). The flow rate in the loop was set to be 5 and 15 lpm, so the maximum particle that can be classified is around 200 nm.

Figure 2 shows the experimental setup for evaluating the sampling probe. Lindberg/Blue M (Asheville, NC) Module HTF55322A tube furnace with a ceramic tubing (5/8"(1.59cm) OD, 26"(66.04 cm) in length) was used to simulate the high temperature situation of real operation condition. Another Lindgerg/blue M tube furnace was used to heat up the dilution air. In high temperature testing, both furnaces were kept at 300 or 600 °C depending on the testing conditions. The head of test probes was connected to ceramic tubing by Swage lock fitting and placed inside the furnace. The rest of the probe was insulated with a heating tape and insulation material. This arrangement allows the test probe temperature be maintained at 150 °C. It is also the air temperature inside the furnace. 2.5 feet of copper cooling coil and a ½" OD 10-feet copper tubing were connected after the probe to dissipating the heat before the concentration measurement by condensation particle counter. A clean dry air is used as dilution air and its maximum flow rate is 25 lpm. Two TSI 3025 condensation particle counters were used to measure the particle concentration upstream and downstream of the sampling probes. The actual dilution ratio at different particle sizes is then calculated from the upstream and downstream particle concentration readings.

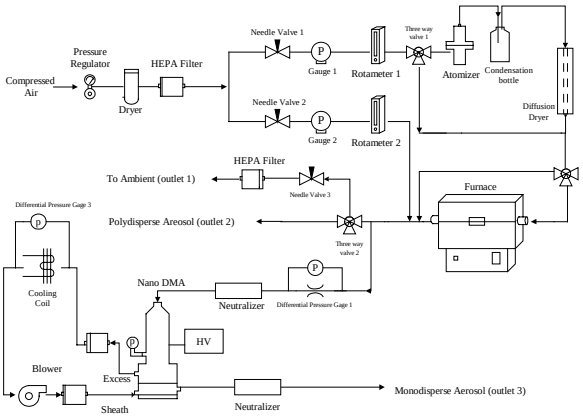

Figure 1. Schematic of Particle Generation System

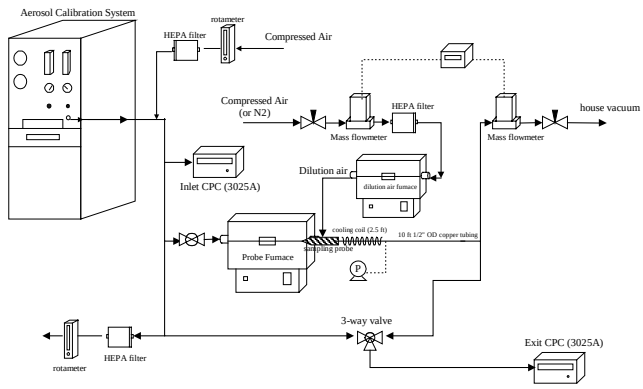

Figure 2. Experimental Setup

Results and Discussions

Three different operation temperatures, 27, 300 and 600^{o}C, were used in this study. The probe sampling flow rate was fixed at 5 lpm, and the dilution flow rate was changed to obtain a dilution ratio ranging from 1 to 7 depending on test conditions. Figure 3 shows the particle penetration through the sampling probe with different dilution ratios at room temperature. It is observed that the penetration at room temperature decreases as the increase of dilution ratios. Further, the loss is also increased as the particle size is reduced. This is normally the general trend of particle loss when turbulence mixing is occurred. Figure 4 and Figure 5 show the particle penetration with different dilution ratios at 300 and 600^{o}C, respectively. In both cases, particle penetrations are lower than 70% for particle smaller than 50nm; however, it reaches a relatively stable value when the particle sizes are getting larger. Overall, the particle penetration can be higher than 70% for particles within 30 to 200 nm when different dilution ratios and operation temperatures are used. If we compare the same dilution ratio with different operation temperatures, the particle penetration decreases with the increase of operation temperature. The results are shown in Figure 6 and Figure 7 when dilution ratios are 1 and 7, respectively. It is because of more particle deposition on the inner wall of probe due to the particle thermophoretic effect.

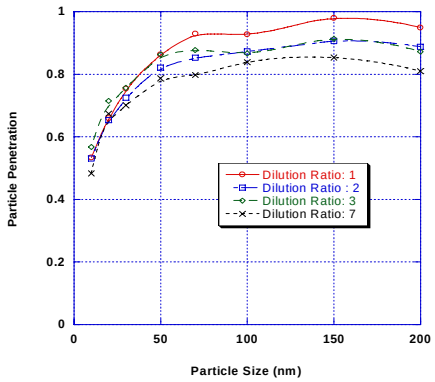

Figure 3 Particle penetrations with Different Dilution Ratios at Room Temperature

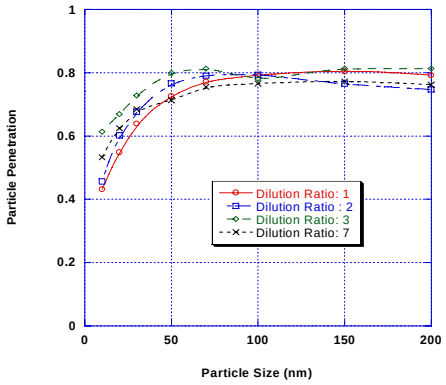

Figure 4 Particle penetrations with Different Dilution Ratios at 300 ^{0}C

Conclusion and future works

A significant performance differences were shown at different operation temperatures and dilution ratios. More works need to be done to further investigate the effect of thermophoresis on particle penetration through sampling probes. The particle loss increases with the increase of dilution ratios. From the observed trend of particle loss, it is evidenced that the turbulent mixing is happened inside the sampling probes. From the viewpoint of the mixing, the turbulent mixing is a need. On the other hand, the loss of particles, especially for nanometer particles, can be very significant under the turbulence flow condition. The balance between these two factors becomes a challenge for the future probe design. Our results show sampling probes do have a great influence on the accuracy of jet engine exhaust

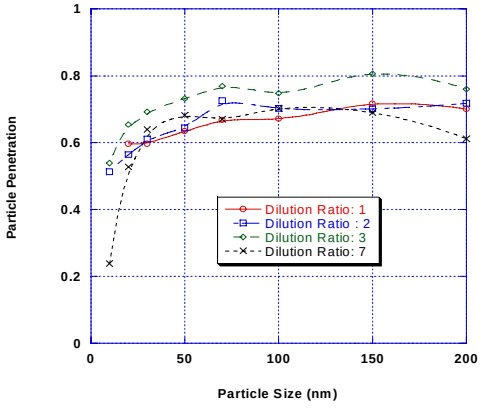

Figure 5 Particle penetrations with Different Dilution Ratios at 600 ^{0}C

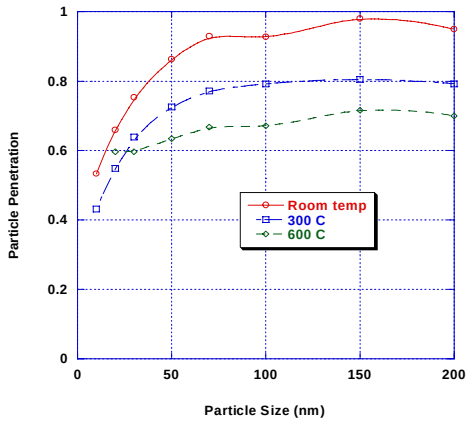

Figure 6 Particle Penetrations at Different Operation Temperature (Dilution ratio: 1)

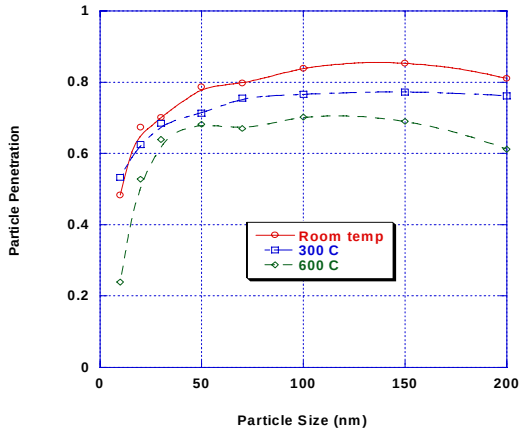

Figure 7 Particle Penetrations at Different Operation Temperature (Dilution ratio: 7)

Reference

1. Anderson, B.E., W.R. Cofer, D.R. Bagwell, *et al.*, "Airborne Observations of Aircraft Aerosol Emissions I: Total Nonvalatile Particle Emission Indices," Geophysical Research Letters, **25**(10): pp. 1689-1692(1998).
2. Hagen, D., P. Whitefield, J. Paladino, *et al.*, "Particulate Sizing and Emission Indices for A Jet Engine Exhaust Sampled at Cruise," Geophysical Research Letters, **25**(10): pp. 1681-1684(1998).
3. Miake-Lye, R.C., B.E. Anderson, W.R. Cofer, *et al.*, "SOx Oxiidation and Volatile Aerosol in Aircraft Exhaust Plumes Depend On Fuel Sulfur Content," Geophysical Research Letters, **25**(10): pp. 1677-1680(1998).
4. Schroder, F.P., B. Karcher, A. Petzold, *et al.*, "Ultrafine Aerosol Particles in Aircraft Plumes: In Situ Observations," Geophysical Research Letters, **25**(15): pp. 2789-2792(1998).
5. Karcher, B., F. Yu, F.P. Schroder, *et al.*, "Ultrafine Aerosol Particles in Aircraft Plumes: Analysis of Growth Mechanisms," Geophysical Research Letters, **25**(15): pp. 2793-2796(1998).
6. Kawa, S.R., J.G. Anderson, S.L. Baughcum, *et al.*, "Assessment of the Effects of High-Speed Aircraft in the Stratosphere: 1998," NASA Technical Paper, 1999-209237(1999).
7. Chen, D.-R., D.Y.H. Pui, D. Hummes, *et al.*, "Design and Evaluation of a Nanometer Aerosol Differential Mobility Analyzer (Nano-DMA)," J. Aerosol Sci., **29**(5/6): pp. 497-509(1998).

APPENDIX B: Hydrocarbon Emissions from a Modern Commercial Airliner

Bruce E. Anderson[1], Donald R. Blake[2], and Murray McEachern[2]

1-- NASA Langley Research Center
Hampton VA 23662

2-- University of California at Irvine
Irvine California

1.0. Background

Aircraft consume about 3 percent of the fossil fuels burned in the atmosphere each year, about 10 percent of this during landing and takeoff cycles (i.e., Friedl et al., 1997). Though the combustion of this fuel primarily produces carbon dioxide and water, a small fraction is emitted as non-methane hydrocarbons (NMHCs). These compounds are ozone precursors, can condense to form particles that impact visibility and inhibit respiratory function, and may be toxic or carcinogenic to exposed animal life. Though miniscule in comparison to the levels produced by automobiles and other surface-based transportation systems and judged to be relatively unimportant in ozone cycles at cruise altitudes (Friedl et al., 1997), aircraft NMHC emissions can potentially impact air quality and present a health hazard to workers, residents, and travelers within and around airport terminal areas.

To understand, better predict, and mitigate the impact of aircraft operations upon local air quality, detailed information on NMHC emissions by aircraft is required. At present, such data are exceedingly sparse. The International Civil Aviation Organization (ICAO) does require that all commercial aircraft engines be emission qualified, meaning that their levels of CO, NO_x, and total hydrocarbon (HC) emissions must be measured at idle, approach, climb out, and takeoff powers. However, HC measurements include contributions from methane and are not corrected for background ambient HC levels within intake air.

In response this measurement need, several recent studies have determined NMHC speciation within turbine engine exhaust plumes. Spicer and coworkers investigated the emissions from both military,GE F101 and F110, (Spicer et al., 1992) and commercial engines, CFM-56-3, (Spicer et al., 1994) and found they generated cracking products, unburned fuel, and products of incomplete combustion at idle, with ethene, propene, acetylene and formaldehyde comprising 30~40 percent of the total emissions. At higher powers, relative NMHC emissions dropped by a factor of 20~50 and unburned fuel components disappeared. Slemr et al. (2001) report similar findings for an older technology engine, Rolls M 45H Mk501, and a more modern commercial high bypass turbo-fan, CFM 56-2C1, and note that the emission indices for these engines are highly power dependent and dominated by alkenes and alkynes related to fuel cracking and

aromatic compounds arising from unburned fuel. Both Slemr et al. (1998; 2001) and Spicer et al. (1992; 1994) note that NMHC emissions are likely dependent upon engine type, use, and maintenance history as well as fuel composition.

Although the Spicer et al. (1994) and Slemr et al. (2001) studies provide significant insight into NMHC emissions from aircraft, their conclusions are drawn from limited sampling of just a few of the >300 types of commercial engines that are presently in use within the commercial aviation fleet and listed within the ICAO emissions database (www.qinetiq.com/aircraft/aviation.html). Clearly data from a broader range of engines are needed to provide a better statistical base for parameterizing aircraft NMHC emissions. For this reason, NMHC determinations were included as part of the measurement priorities for the NASA Experiment to Characterize Aircraft Volatile Aerosol and Trace Species Emissions (EXCAVATE).

EXCAVATE was conducted during January 2002 with the primary objectives of characterizing the aerosol and aerosol precursor emissions from a modern commercial turbofan engine. The NASA Langley Boeing 757 that has a pair of Rolls Royce RB-211-535-E4 engines was used as the emission source. These engines produce over 40,000 lbs thrust, were designed for low-NO_x and HC emissions and are used on ~80 percent of the B757 aircraft in service. Whole air samples were collected, both from the exhaust plume of one of these engines as it was operated at a variety of power settings, and from the background air being drawn into the engine intake. The samples were shipped to our laboratory at the University of California at Irvine where very sensitive gas chromatographic techniques were used to assay their halo- and hydrocarbon species content. We subsequently used these concentration data in concert with simultaneous engine CO_2 emission measurements to calculate emission indices for each of the measured species. The paragraphs below describe our sample collection and analysis procedures and present the RB-211 NMHC emission observations. Results are compared to previous data sets and the implication of the measurements for aircraft operations poorly ventilated regions is explored.

2.0. Experiment

Whole air samples were collected in evacuated stainless steel canisters from the aerosol-sampling manifold that, in turn was connected to a stainless steel sample inlet positioned 10 m downstream and on the centerline of the B-757 engine exit plane. A total of 11 samples were collected, eight of engine emissions and three of background air in the vicinity of the aerosol instrument trailer. The set of canisters was subsequently shipped to UCI for detailed analysis of trace gas species.

Details of the analytical procedures employed by the UCI laboratory are given by ***Sive* [1998]**, ***Colman et al.* [2001]**, and ***Blake et al.* [2003]**. Aliquots of air from each canister were preconcentrated in a liquid nitrogen-cooled loop. This sample was directed to five different gas chromatographic column/detector combinations. Electron capture detectors (ECD, sensitive to halocarbons and alkyl nitrates), flame ionization detectors (FID, sensitive to hydrocarbons), and quadrupole mass spectrometers (MSD,

for unambiguous compound identification and selected ion monitoring) were employed. The first column–detector combination (abbreviated as "DB5ms/MSD") was a DB5ms column (J&W; 60 m, 0.25 mm I.D., 0.5 µm film thickness) output to a MSD (HP-5973). The second combination ("DB1/FID") was a DB-1 column (J&W; 60 m, 0.32 mm I.D., 1 µm film thickness) output to a FID (HP-6890). The third combination ("PLOT-DB1/FID") was a PLOT column (J&W GS-Alumina; 30 m, 0.53 mm I.D.) connected in series to a DB-1 column (J&W; 5 m, 0.53 mm I.D., 1.5 µm film thickness) and output to an FID. The fourth combination ("Restek1701/ECD") was a RESTEK 1701 column (60 m, 0.25 mm I.D., 0.50 µm film thickness), which was output to an ECD. The fifth combination ("DB5-Restek1701/ECD") was a DB5 (J&W; 30 m, 0.25 mm I.D., 1 µm film thickness) column connected in series to a RESTEK 1701 column (5 m, 0.25 mm I.D., 0.5 µm film thickness) and output to an ECD. The DB5ms/MS, DB1/FID, PLOT-DB1/FID, Restek1701/ECD, and DB5-Restek1701/ECD combinations received 10.1 percent, 15.1 percent, 60.8 percent, 7.2 percent, and 6.8 percent of the sample flow, respectively. Our analytical accuracy ranges from 2 percent to 20 percent. The precision of the measurements varies by compound and by mixing ratio. For example, the measurement precision is 1 percent or 1.5 pptv (whichever is larger) for the alkanes and alkynes, and 3 percent or 3 pptv (whichever is larger) for the alkenes (***Sive*, 1998**). The precision for the alkyl nitrates was better than 2 percent at the levels observed during the Pacific Exploratory Mission-Tropical Phase (***Colman et al.*, 2001**). The precision for C_2Cl_4 at 5 pptv is ±0.05 pptv (***Colman et al.*, 2001**). The limit of detection (LOD) is 3 pptv for the NMHCs. The alkyl nitrate detection limit was 0.02 pptv (except 0.01 pptv for methyl nitrate) (***Colman et al.*, 2001**). C_2Cl_4 was present at mixing ratios well above its detection limit at all times. The canister air was also analyzed for CO using GC with FID, as described by ***Hurst* [1990]** and ***Lopez* [2002]** using a packed column GC separation of CO followed by reduction to methane on a nickel catalyst and detection by FID. The absolute accuracy of the CO measurements calibrated against NIST standards was ±7 percent, with a DL of 5 ppbv (***Lopez*, 2002**).

3.0. Results

Along with run specific information, Table 1 lists the dilution-corrected mixing ratios of 56 carbon species that were measured in each of the 11 samples collected during EXCAVATE. Note that eight of the samples were obtained from the engine exhaust plume as it ran at four different power settings (1.03, 1.15, 1.3 and 1.4 engine pressure ratios, where 1.03 is idle and 1.4 is cruise) and burned two fuels that were different in both hydrocarbon and sulfur content. Three samples are of background air, collected to determine the ambient concentrations of each of the measured species. The CO_2 values shown in the list were determined using two different nondispersive infrared instruments, one monitoring concentrations in the dry N_2-diluted sample air that was aspired into the whole-air canisters and the other measuring mixing ratios in undiluted air collected from the engine exhaust with a separate inlet probe. The ratio of the CO_2 concentrations yield the sample dilution ratios that were used for correcting the carbon species concentrations to those that would have been observed in undiluted exhaust flow 10 meters behind the engine exhaust plane. We estimate that the dilution factors derived in this manner are accurate to $\pm$20 percent.

Table 2 provides averages of the carbon species mixing ratios, comparing values obtained in the exhaust plume at idle (1.03 EPR) and higher powers (1.15 + 1.30 + 1.40) with the average of measurements from the first two samples collected in from background air. We chose to disregard the third background sample because it contained high levels of several reactive species (i.e., HCFC 22, n-Heptane, n-hexane, benzene, toluene), suggesting that the air mass from which it was extracted was recently exposed to some unknown pollution source.

Table 3 lists mass emission indices (EIs) in units of g kg^{-1} fuel burned for CO and CH_4 and μg kg^{-1} fuel burned for the remainder of the measured species. EIs were calculated using the following formula:

$$EI_x = EI_{CO2} \times \Delta(X)/\Delta(CO_2) \times (AMU_x)/(AMU_{CO2}) \qquad \text{Eq. 1}$$

where EI_{CO2} is calculated from the fuel carbon content assuming combustion to be 100 percent efficient, Δ(X) and Δ(CO_2) are the enhancements of compound X and CO_2 within the plume, respectively, and AMUx and AMU_{CO2} are the molecular weights of X and CO_2, respectively. A nominal value of 3160 g kg^{-1} fuel burned was used for EI_{CO2} in all the calculations. Δ(X) values were determined by subtracting average background mixing ratios of X from the dilution corrected values measured in the plume. Cases where X was consumed within the combustor yielded negative EI values.

Examining the tables we note that CO and CH_4 are by far the most abundant trace carbon species in engine exhaust, the former arising from incomplete combustion of jet fuel and the latter derived primarily from background air. At engine idle, CO comprises almost 2 percent of the exhaust emissions, but contributes <0.1 percent at high EPRs indicating that the engine runs much more efficiently at the higher temperatures and pressures associated with high power settings. Its emission indices, EI_{co}, was 12 and ~16 g kg^{-1} for the two samples taken at idle and between 0.6 and 0.8 g kg^{-1} in samples acquired at power settings more typical of cruise and climb out (1.3 – 1.4 EPR). These compare extremely well to the RB211-535E4 values archived in the International Civil Aviation Organization (ICAO) Engine Emissions Data Bank (**http://www.qinetiq.com/aircraft/aviation.html**) of 13 – 16 g kg^{-1} for idle; 1.1 – 2.7 g kg^{-1} for approach; 0.5 – 1.2 g kg^{-1} for climb out; and 0.7 to 1.0 g kg^{-1} for take off. Simultaneous aerosol measurements suggest that the engine's efficiency varies significantly just after engine start and when power is reduced from higher settings to idle so that any single grab sample taken at idle would not necessarily be representative of the average emissions at that power setting. The ICAO values are averaged over several minutes of engine operation, which may explain why one of our instantaneous idle readings was 50 percent above their range of published values.

Regarding CH_4, its concentrations were typically not more than 20 percent higher than ambient values at engine idle and tended to drop off with increasing engine powers, with some mixing ratios being lower than ambient values (Table 1) which suggests that under some conditions the engine actually burns methane out of the background air.

This observation is not surprising, since negative methane emission indices were observed for this same aircraft in flight during the SUCCESS mission (Vay et al., 1998) and Spicer et. al., (1992) note that most high efficiency engines tend to produce minor amounts of CH_4 at idle and consume it at higher engine powers. Correcting for background mixing ratios, EI_{CH4} varied from –0.09 to 0.3 g kg^{-1}. The ICAO database does not report EIs for this species, but we suspect that the positive values calculated for higher engine powers may be caused by either errors in the dilution ratio or variations in the background mixing ratio of CH_4. Note that the sample that yielded the greatest EI_{CH4} also exhibited significantly positive EIs for a number of halocarbon species suggesting the background air at the time was more polluted than average. Also, for the plume dilutions that we were dealing with, a 20 percent error in the calculated dilution ratio equates to a variation of 0.1 to 0.2 g kg-1 in EI_{CH4}. In any case, our results and those of others (Spicer et al., 1992; Spicer et al., 1994; Vay et al., 1998; and Slemr et al., 2001) suggest that turbine engines are not a significant source of CH_4.

In terms of other species, the fuels burned during EXCAVATE contained varying levels of sulfur contaminants, for the two cases sampled here, 810 and 1820 ppm by weight. Thus, sulfur compounds should be prevalent within the engine exhaust. Indeed, mixing ratios for OCS and CS_2 were two to five times higher in the exhaust plume than within ambient air and appeared to show a slight trend with fuel S content. However, their EIs were several orders of magnitude lower than SO_2, the primary sulfur species emitted by the aircraft (Wormhoudt et al., Appendix C of this report). DMS, like CH_4, was depleted in most samples collected at high engine powers suggesting that the engine consumes this species from background air at high combustor temperatures.

As for halocarbon emissions, of the 16 species assayed, 14 were either unchanged or depleted within the engine exhaust relative to ambient air (Tables 1 and 2). Only CH_3Cl and CH_3Br exhibited slight enhancements, but these were less than a factor of two above average background mixing ratios and may have been related to ambient variability rather than formation from fuel components. However, biomass burning is known to generate these species (Blake et al., 2003) so it is conceivable that they are produced within the combustor, either from fuel components or the oxidation of species from within the background air.

Hydrocarbon-nitrate species were slightly enhanced within the plume. Of the five species measured, methyl nitrate was most abundant, both within the plume and background air. Its average mixing ratio was three fold higher than ambient at high power (1.4 EPR), five times higher at idle (1.03), but tended to be somewhat depleted at medium powers (1.15 and 1.3). Nonmethane hydrocarbon concentrations decrease with engine power whereas NOx increases; the product of the two is at a minimum at the settings where we see lower RNO_2 values. As for EIs, the sum for all five species is < 0.0005 g kg^{-1} at idle and < 0.0001 g kg^{-1} at 1.4 EPR. Comparing this to the RB211-535-E4 ICAO values of 4 g kg^{-1} and ~18 g kg^{-1} NOx at idle and climbout power, respectively, we conclude that an insignificant amount of aircraft emissions are sequestered as RNOx species.

The remaining species listed in the tables are hydrocarbons and showed a great range of enhancement ratios within the engine exhaust plume relative to background air. Data are presented for 27 NMHC species with two to nine carbon atoms. Figure 1 shows that at idle, the engine primarily emits species containing two to four carbon atoms, but when engine power is increased to 1.4 EPR, light hydrocarbon emissions are greatly reduced and the peak in the carbon emission distribution shifts out to seven atoms (heptane +toluene). Spicer et al. (1994) notes that jet fuel is primarily composed of species with five or more carbons and, by weight, 70 percent of the compounds it contains has 11 to 14 carbons. Thus, the low molecular weight species found in the exhaust are derived from reactions occurring within the combustor rather than being residual, unburned fuel. Aromatics are present in the fuel but are also byproducts of incomplete hydrocarbon oxidation, thus the enhancements in benzene and toluene mixing ratios can be either "combustion" or "fuel" derived.

Table 4 provides a summary of the NMHC emissions from the RB211 engine for each of the exhaust samples, broken down into the functional groupings of alkanes (all single bonded hydrocarbons), alkenes (at least one double bond), alkynes (at least one triple bond), and aromatics (benzene ring compounds). Figure 2 shows a plot of the fraction of the NMHCs emitted in each functional group over the range of engine power settings. At idle (1.03 EPR) > 90 percent of the emissions are double or triple-bonded, straight chain hydrocarbons, whereas at high power, these compounds account for < 20 percent of the total. The fractional contribution of aromatics grows from < 10 percent to > 50 percent as power is increased from idle to climb-out settings, respectively. Alkanes are the least abundant species at low power but generally comprise 20 to 40 percent of the total NMHC mass emissions at high powers.

In terms of individual species, at idle, the most abundant were ethene, ethyne, and propene. Their mixing ratios were enhanced by factors of 200 to 1000 above those measured in ambient air, and, taken together, accounted for 88 percent of the measured NMHC emissions on a molar basis. Ethene alone accounted for 57 percent of the emissions that were quantified. Excluding contributions from oxygenated HC species that we did not measure, this is consistent with observations from military engines acquired by Spicer et al. (1992) and the CFM-56-2 engines of the NASA DC-8 by Slemr et al. (2001). At higher engine powers, the light hydrocarbon species all but disappear, and n-heptane and toluene become more dominant. As noted above, these could be either fuel or combustion derived.

As shown in Table 4 and illustrated in Figure 3, total NMHC emissions drop off precipitously as power is increased. At idle, the engine emits ~1 g kg^{-1} of 2 – 9 carbon HC compounds, whereas at 1.4 EPR, which is essentially climb-out power, it produces ~0.005 g kg-1, or about factor of 200 less. Similar reductions were apparent in the CO emissions (Table 3 and Figure 3). Variations in CO and NMHC EIs were highly correlated (Figure 4) which one might expect for incomplete combustion at low engine temperatures.

Comparing our total NMHC EIs with ICAO data, we find relatively good agreement at idle, but that EXCAVATE values tend to be somewhat lower at higher engine powers. The ICAO archive reports values of 0.4-1, 0.04, and 0.01 g kg^{-1} at idle, approach, and climb-out, respectively. These compare to our observations of 0.5—1, ~0.01, and ~0.005 g kg^{-1} for roughly the same power settings, respectively. ICAO engine emission qualification tests are performed with multi-gas analyzers that give an integrated signal proportional to the total hydrocarbons present in the sample. Thus, differences between the EXCAVATE and ICAO values can probably be attributed to contributions from species, such as oxygenated HC compounds, that we did not measure as well as the fact that ICAO data are not corrected for ambient NMHC contributions. We note that Spicer et al. (1994) resolved 182 chromatographic peaks in samples collected in the exhaust of a CFM-56 engine and found significant amounts of formaldehyde, acetaldehyde, and acetone that, at high power settings, accounted for > 50 percent of the total NMHC emissions.

Two separate batches of JP-5 fuel were burned in the tests, thus one might expect to see some systematic differences in the NMHC emissions based on the differences in the fuel hydrocarbon matrices. Examining Table 4, we see that total NMHC emissions were slightly higher for 1820 ppm S fuel than the 810 ppm S fuel. These differences are particularly notable at idle where the total NMHC EI for the high S fuel is ~two times (1.1 g kg^{-1} vs. 0.55 g kg^{-1}) that of the low sulfur fuel. Though these differences are significant, they may not reflect fuel-induced effects. Simultaneous aerosol measurements show that the engine emissions are highly variable at low powers, with mass emissions decreasing by more than an order of magnitude in the 10 minutes after engine start. The low S samples were collected after more than an hour of continuous runtime and may simply reflect the fact that the engine runs more efficiently after it has warmed up. Clearly more measurements are needed to discriminate fuel matrix from operational parameter impacts on NMHC emissions.

4.0. References

Blake, N. J., D. R. Blake, A. L. Swanson, E. Atlas, F. Flocke, and F. S. Rowland, 2003: Latitudinal, vertical, and seasonal variations of C_1–C_4 alkyl nitrates in the troposphere over the Pacific Ocean during PEM-Tropics A and B: Oceanic and continental sources. *J. Geophys. Res.*, doi:10.1029/2001JD001444.

Civil Aviation Authority, 2002-2004: ICAO aircraft engine emissions databank, Civil Aviation Authority Web Site. **http://www.qinetiq.com/aircraft/aviation.html**.

Colman, J. J., A. L. Swanson, S. Meinardi, B. C. Sive, D. R. Blake, and F. S. Rowland, 2001: Description of the analysis of a wide range of volatile organic compounds in whole air samples collected during PEM-Tropics A and B. *Anal. Chem., 73*, pp. 3723–3731.

Hurst, D. F., 1990: Seasonal variations in the latitudinal distribution of tropospheric carbon monoxide, 1986–1988. Dissertation, Univ. of Calif., Irvine.

Lopez, J. d. P., 2002: Seasonality and global growth trends of carbon monoxide during 1995–2001. Ph.D. thesis, Univ. of Calif., Irvine, Irvine.

Sive, B. C., 1998: Analytical methods and estimated hydroxyl radical concentrations. Ph.D. thesis, Univ. of Calif., Irvine, Irvine.

Slemr, F., et al., 1999: In-flight measurement of aircraft non-methane hydrocarbon emission indices. Geophys. Res. Lett., 26, pp.3053-3056.

Slemr, F., et al., 1998: In-flight measurement of aircraft non-methane hydrocarbon emission indices. Geophys. Res. Lett., 25(3), pp. 321-324.

Slemr, F., et al., 2001: In-flight measurements of aircraft CO and nonmethane hydrocarbon emission indices. J. Geophys. Res., 106, pp. 7485-7494.

Spicer, C.W., et. al., 1992: Chemical composition of exhaust from aircraft turbine engines. J. Eng. Gas Turbines Power, 114, pp. 111-115.

Spicer, C.W, et. al., 1994: Chemical composition and photochemical reactivity of exhaust from aircraft turbine engines. Ann. Geophys., 12, pp. 944-955.

Vay, S.A., et al., 1998: DC-8-based observations of aircraft CO, CH4, N2O, and H2O (g) emission indices during SUCCESS. Geophys. Res. Lett., 25, pp. 1717-1720.

Table 1. Carbon Species Measurements Corrected for Sample Dilution

Species	DE1149	DE1181	DE1166	DE1062	DE2358	DE1008	DE1302	DE1020	DE6602	DE7010	DE7146
Julian Date	27	27	27	27	27	27	27	27	27	27	27
UT time	18:19:30	18:32:00	18:43:00	19:13:00	19:26:00	19:34:00	19:39:00	20:30:00	18:00:00	19:00:00	20:00:00
CO2_samp	865	1088	1102	1404	1384	1305	1235	1222			
CO2_ex	3111	4900	6509	3206	5006	6346	2761	2058			
dilution ratio	3.60	4.50	5.91	2.28	3.62	4.86	2.24	1.68			
Engine Pressure Ratio	1.15	1.30	1.40	1.15	1.30	1.40	1.03	1.03	N/A	N/A	N/A
Fuel Sulfur (ppmv)	1820	1820	1820	810	810	810	810	1820	Bkg Air	Bkg Air	Bkg Air
Sample Distance (m)	10	10	10	10	10	10	10	10	N/A	N/A	N/A
CO (ppbv)	2153	2030	2683	1363	1756	2221	16686	23448	172	177	284
CH4 (ppmv)	2.32	1.40	1.39	2.60	1.80	2.41	1.95	2.15	1.707	1.854	1.769
OCS (pptv)	1454	518	721	985	503	1040	999	895	516	504	478
DMS (pptv)	0	9	59	5	0	0	67	52	59	37	31
CS2 (pptv)	212	14	71	46	25	39	92	52	13	6	13
F-12 (pptv)	702	464	467	782	561	481	914	598	571	549	609
F-11 (pptv)	313	194	189	369	243	199	432	286	276	269	281
F-113 (pptv)	104	68	71	119	94	83	172	94	89	83	98
F-114 (pptv)	18	9	12	21	14	10	25	15	15	15	16
H-1211 (pptv)	5	3	4	6	4	3	7	5	5.2	4.8	5.1
HFC 134a (pptv)	36	32	35	50	36	39	60	39	38	32	255
HCFC 22 (pptv)	263	149	154	260	224	180	320	240	207	224	1417
HCFC 142b (pptv)	22	14	12	25	22	19	29	20	19	22	22
HCFC 141b (pptv)	25	14	12	27	18	19	40	29	24	23	181
CHCl3 (pptv)	25	18	30	30	33	68	54	25	16	15	69
MeCCl3 (pptv)	47	32	30	48	33	29	58	37	40	38	43
CCl4 (pptv)	126	77	89	137	87	73	159	104	106	110	114
CH2Cl2 (pptv)	187	50	118	217	141	296	426	156	66	67	338
C2HCl3 (pptv)	7	5	11	8	8	11	27	4	7.8	3	5.6
C2Cl4 (pptv)	32	23	35	32	22	24	43	22	33	18	28
CH3Cl (pptv)	1001	1035	1761	980	594	826	1133	692	634	644	626
CH3Br (pptv)	20	18	30	20	10	25	19	14	10.3	9.9	12.4
CH3I (pptv)	1	1	1	1	1	2	2	1	0.75	0.55	0.69
1,2-DCE (pptv)	9	4	7	7	3	4	8	6	5.2	3.9	5.1
MeONO2 (pptv)	17	31	147	14	18	65	130	169	33.9	14.8	8.2
EtONO2 (pptv)	10	8	20	8	8	14	19	23	4.5	3.7	4.8
i-PrONO2 (pptv)	19	16	27	21	21	22	26	19	14.5	14	14.9
n-PrONO2 (pptv)	3	3	5	3	4	4	4	4	1.1	1	1.2

Table 1. Concluded

Species	DE1149	DE1181	DE1166	DE1062	DE2358	DE1008	DE1302	DE1020	DE6602	DE7010	DE7146
2-BuONO2 (pptv)	23	16	18	25	21	19	31	22	18.3	18.6	18.9
Ethane (pptv)	3416	1782	1803	3135	2241	1920	17248	23372	2451	2142	2474
Ethene (pptv)	1782	558	1111	885	489	758	368204	577431	409	297	591
Ethyne (pptv)	1253	635	597	1176	749	768	129067	198342	782	662	1058
Propane (pptv)	1584	914	957	1696	1180	1055	4968	2722	1477	1190	1532
Propene (pptv)	338	243	390	223	145	238	67959	109586	83	40	122
i-Butane (pptv)	421	270	254	321	362	272	746	287	288	204	1214
n-Butane (pptv)	907	594	556	923	815	719	2309	1771	815	605	1797
1-Butene (pptv)	90	50	89	50	65	68	13261	21623	25	11	48
i-Butene (pptv)	605	999	1537	1101	395	705	4809	7074	51	51	156
trans-2-Butene (pptv)	25	27	41	46	25	19	1337	2103	11	7	41
cis-2-Butene (pptv)	29	36	30	18	14	0	1062	1717	10	6	38
i-Pentane (pptv)	457	243	189	442	319	272	1147	480	309	222	920
n-Pentane (pptv)	176	86	100	153	130	102	354	344	130	98	664
1,3-Butadiene (pptv)	0	0	0	0	0	0	15176	23797	8		55
Isoprene (pptv)	270	0	0	41	0	0	2466	2755	14	7	17
2-Methylpentane (pptv)	90	59	59	84	65	58	78	146	85	54	158
3-Methylpentane (pptv)	94	0	0	64	40	0	141	101	68	58	131
n-Hexane (pptv)	112	36	230	100	36	97	215	239	62	32	299
n-Heptane (pptv)	983	1175	5047	613	1756	2051	1850	1263	469	749	28186
Benzene (pptv)	508	293	301	360	272	501	11330	17569	181	139	234
Toluene (pptv)	1271	792	1383	939	757	821	4063	5132	340	246	3569
Ethylbenzene (pptv)	259	189	142	128	69	102	647	709	78	42	124
m-Xylene (pptv)	540	410	378	221	163	301	827	949	117	46	222
p-Xylene (pptv)	392	356	313	185	141	214	620	647	79	38	163
o-Xylene (pptv)	670	522	479	292	232	326	1129	1210	83	46	166
1,3,5-Trimethylbenzene (pptv)	450	293	183	121	83	175	287	423	100	26	113
1,2,4-Trimethylbenzene (pptv)	1044	729	579	372	337	413	710	949	50	23	76

Table 2. Summary of Hydrocarbon Mixing Ratios in RB211 Exhaust at 10 m Sampling Distance

Parameter Number	Parameter Description	Background Air		RB211 Stable Power		RB211 IDLE	
		Average, N=3	Std Dev	Average, N=7	Std Dev	Average, N=2	Std Dev
1	CO Emission Index (g/kg)			0.88	0.23	17.40	7.50
2	CO2 (ppmv)	370	5	4846	1466	2410	497
3	CO (ppbv)	211	63	2034	447	20067	4781
4	CH4 (ppmv)	1.78	0.07	1.99	0.53	2.05	0.14
5	OCS (pptv)	499	19	870	365	947	73
6	DMS (pptv)	42.3	14.7	12.1	23.3	59.6	10.7
7	CS2 (pptv)	10.7	4.0	67.8	73.5	72.0	28.1
8	F-12 (pptv)	576.3	30.4	576.1	135.7	756.0	223.3
9	F-11 (pptv)	275.3	6.0	251.2	74.5	359.0	103.7
10	F-113 (pptv)	90.0	7.5	89.7	19.8	133.3	55.4
11	F-114 (pptv)	15.3	0.6	13.9	4.6	19.9	6.7
12	H-1211 (pptv)	5.0	0.2	4.1	1.1	6.2	1.4
13	HFC 134a (pptv)	108.3	127.1	38.0	6.4	49.6	15.4
14	HCFC 22 (pptv)	616.0	693.7	204.9	51.4	280.3	56.6
15	HCFC 142b (pptv)	21.0	1.7	18.9	5.2	24.6	6.3
16	HCFC 141b (pptv)	76.0	90.9	19.2	6.2	34.4	8.3
17	CHCl3 (pptv)	33.3	30.9	33.8	17.5	39.5	20.2
18	MeCCl3 (pptv)	40.3	2.5	36.2	8.7	47.6	15.0
19	CCl4 (pptv)	110.0	4.0	98.0	26.8	131.6	38.8
20	CH2Cl2 (pptv)	157	157	168	85	291	190
21	C2HCl3 (pptv)	5.5	2.4	8.1	2.3	15.1	16.4
22	C2Cl4 (pptv)	26.3	7.6	28.1	5.9	32.2	14.7
23	CH3Cl (pptv)	634.7	9.0	1032.9	392.4	912.8	312.0
24	CH3Br (pptv)	10.9	1.3	20.4	6.8	16.7	3.9
25	CH3I (pptv)	0.7	0.1	1.2	0.3	1.3	0.4
26	1,2-DCE (pptv)	4.7	0.7	5.5	2.2	6.8	1.8
27	MeONO2 (pptv)	19.0	13.3	48.5	51.7	149.3	27.1
28	EtONO2 (pptv)	4.3	0.6	11.4	4.9	20.9	2.7
29	i-PrONO2 (pptv)	14.5	0.5	21.0	3.6	22.4	5.3
30	n-PrONO2 (pptv)	1.1	0.1	3.5	1.0	4.1	0.1
31	2-BuONO2 (pptv)	18.6	0.3	20.3	3.3	26.7	6.6
32	Ethane (pptv)	2356	185	2383	716	20310	4330
33	Ethene (pptv)	432	148	930	474	472818	147946

Table 2. Concluded

Parameter Number	Parameter Description	Background Air		RB211 Stable Power		RB211 IDLE	
		Average, N=3	Std Dev	Average, N=3	Std Dev	Average, N=2	Std Dev
34	Ethyne (pptv)	834	203	863	281	163705	48985
35	Propane (pptv)	1400	184	1231	332	3845	1589
36	Propene (pptv)	81.7	41.0	263.0	87.6	88773	29435
37	i-Butane (pptv)	568.7	560.5	316.8	64.9	517	324
38	n-Butane (pptv)	1072.3	636.3	752.3	156.2	2040	381
39	1-Butene (pptv)	28.0	18.7	68.6	17.8	17442	5913
40	i-Butene (pptv)	86.0	60.6	890.2	408.8	5942	1602
41	trans-2-Butene (pptv)	19.7	18.6	30.7	10.3	1720	542
42	cis-2-Butene (pptv)	18.0	17.4	21.2	13.0	1389	463
43	i-Pentane (pptv)	483.7	380.4	320.4	108.8	814	471
44	n-Pentane (pptv)	297.3	317.9	124.6	35.0	349	7
45	1,3-Butadiene (pptv)	31.5	33.2	0.0	0.0	19487	6096
46	Isoprene (pptv)	12.7	5.1	51.8	108.1	2611	204
47	2-Methylpentane (pptv)	99.0	53.4	69.2	14.2	112	48
48	3-Methylpentane (pptv)	85.7	39.6	32.9	39.8	121	29
49	n-Hexane (pptv)	131.0	146.3	102.0	71.2	227	17
50	n-Heptane (pptv)	9801	15922	1937	1610	1557	415
51	Benzene (pptv)	185	48	372	106	14450	4412
52	Toluene (pptv)	1385	1892	994	268	4598	756
53	Ethylbenzene (pptv)	81.3	41.1	148.1	67.7	678.2	43.6
54	m-Xylene (pptv)	128.3	88.5	335.5	136.5	887.9	86.7
55	p-Xylene (pptv)	93.3	63.7	266.8	101.1	633.6	18.6
56	o-Xylene (pptv)	98.3	61.5	419.9	165.5	1169.3	57.0
57	1,3,5-Trimethylbenzene (pptv)	79.7	46.9	217.5	134.2	355.0	96.6
58	1,2,4-Trimethylbenzene (pptv)	49.7	26.5	578.9	271.3	829.6	169.1

Table 3. Mass Emission Indices; CO and CH4 in g/kg, All Else in ug/kg Fuel

Parameters or Species	SAMPLE CAN							
	DE1149	DE1181	DE1166	DE1062	DE2358	DE1008	DE1302	DE1020
Julian Date	27	27	27	27	27	27	27	27
UT time	18:19:30	18:32:00	18:43:00	19:13:00	19:26:00	19:34:00	19:39:00	20:30:00
Engine Pressure Ratio	1.15	1.30	1.40	1.15	1.30	1.40	1.03	1.03
Fuel Sulfur (ppmv)	1820	1820	1820	810	810	810	810	1820
Sample Distance (m)	10	10	10	10	10	10	10	10
CO (g/kg)	1.28	0.76	0.77	0.75	0.64	0.65	12.0	22.7
CH4 (g/kg)	0.20	-0.09	-0.07	0.29	0.00	0.11	0.07	0.21
OCS (ug/kg)	1308	7	139	638	-6	360	763	807
DMS (ug/kg)	-69	-35	8	-60	-43	-34	31	9
CS2 (ug/kg)	356	4	51	61	17	25	163	113
F-12 (ug/kg)	396	-171	-125	601	2	-108	1113	161
F-11 (ug/kg)	129	-159	-127	298	-59	-114	571	63
F-113 (ug/kg)	80	-51	-31	137	22	-7	422	53
F-114 (ug/kg)	12	-15	-6	21	-1	-10	43	1
H-1211 (ug/kg)	-1	-4	-3	4	-3	-3	9	1
HFC 134a (ug/kg)	2	-5	0	35	2	4	68	13
HCFC 22 (ug/kg)	94	-85	-59	86	11	-35	236	75
HCFC 142b (ug/kg)	4	-15	-14	15	3	-2	34	-2
HCFC 141b (ug/kg)	5	-17	-15	10	-9	-5	51	21
CHCl3 (ug/kg)	26	4	18	37	29	70	117	40
MeCCl3 (ug/kg)	24	-15	-14	27	-12	-15	67	-10
CCl4 (ug/kg)	64	-71	-33	99	-47	-61	204	-21
CH2Cl2 (ug/kg)	237	-21	48	286	91	221	794	266
C2HCl3 (ug/kg)	5	-2	8	6	6	8	73	-9
C2Cl4 (ug/kg)	26	-7	18	24	-9	-2	74	-21
CH3Cl (ug/kg)	422	293	624	386	-33	107	649	94
CH3Br (ug/kg)	21	10	21	21	0	16	23	13
CH3I (ug/kg)	2	1	1	1	0	2	4	2
1,2-DCE (ug/kg)	9	-1	2	5	-2	-1	9	3
MeONO2 (ug/kg)	-14	7	104	-18	-7	36	212	388
EtONO2 (ug/kg)	12	5	16	9	6	10	35	60
i-PrONO2 (ug/kg)	12	2	14	16	10	10	33	16
n-PrONO2 (ug/kg)	4	3	4	4	4	4	8	12
2-BuONO2 (ug/kg)	13	-4	-1	18	4	1	40	15
Ethane (ug/kg)	777	-227	-165	565	-24	-128	11695	22116
Ethene (ug/kg)	925	84	234	334	55	129	268394	564880
Ethyne (ug/kg)	319	-33	-36	265	10	14	86933	179582
Propane (ug/kg)	255	-271	-184	358	-97	-139	4169	2136
Propene (ug/kg)	269	112	152	153	50	84	74319	160834
i-Butane (ug/kg)	235	20	5	98	97	17	756	84
n-Butane (ug/kg)	264	-99	-100	278	87	6	2417	2151
1-Butene (ug/kg)	93	26	44	40	38	32	19325	42297
i-Butene (ug/kg)	717	779	918	1320	277	415	6944	13750
trans-2-Butene (ug/kg)	21	15	20	46	13	7	1938	4100
cis-2-Butene (ug/kg)	27	23	13	13	5	-5	1538	3346
i-Pentane (ug/kg)	319	-24	-61	286	55	5	1653	541
n-Pentane (ug/kg)	104	-30	-11	63	17	-10	450	580
1,3-Butadiene (ug/kg)	-10	-6	-5	-10	-6	-5	21341	44904

Table 3. Concluded

Parameters or Species	SAMPLE CAN							
	DE1149	DE1181	DE1166	DE1062	DE2358	DE1008	DE1302	DE1020
Isoprene (ug/kg)	408	-10	-8	47	-10	-8	4350	6523
2-Methylpentane (ug/kg)	41	-14	-10	29	-5	-11	20	231
3-Methylpentane (ug/kg)	61	-80	-60	2	-29	-61	175	114
n-Hexane (ug/kg)	129	-14	174	103	-13	49	377	576
n-Heptane (ug/kg)	865	830	4897	10	1648	1635	3235	2288
Benzene (ug/kg)	627	152	121	350	125	301	22692	47449
Toluene (ug/kg)	2079	674	1105	1334	613	551	9033	15554
Ethylbenzene (ug/kg)	488	201	96	161	13	51	1622	2404
m-Xylene (ug/kg)	1124	510	347	332	124	264	2058	3215
p-Xylene (ug/kg)	818	462	298	300	126	187	1552	2180
o-Xylene (ug/kg)	1483	712	484	541	255	314	2940	4243
1,3,5-Trimethylbenzene (ug/kg)	1074	404	159	156	35	152	699	1511
1,2,4-Trimethylbenzene (ug/kg)	2795	1220	718	902	518	512	2106	3828

Table 4. Summary of NMHC Mass Emission Indices

Parameters or Species	SAMPLE CAN							
	DE1020	DE1149	DE1181	DE1166	DE1302	DE1062	DE2358	DE1008
Julian Date	27	27	27	27	27	27	27	27
UT time	20:30:00	18:19:30	18:32:00	18:43:00	19:39:00	19:13:00	19:26:00	19:34:00
Engine Pressure Ratio	1.03	1.15	1.30	1.40	1.03	1.15	1.30	1.40
Fuel Sulfur (ppmv)	1820	1820	1820	1820	810	810	810	810
Sample Distance (m)	10	10	10	10	10	10	10	10
CO (g/kg)	23	1.28	0.76	0.77	12	0.75	0.64	0.65
Total NMHC EI (mg/kg)	1131.4	16.3	5.4	5.8	552.7	8.1	4.0	4.4
Alkanes (mg/kg)	30.8	3.05	0.09	1.19	24.9	1.79	1.74	1.36
Total Alkenes (mg/kg)	840.6	2.45	1.02	1.37	398.1	1.94	0.42	0.65
Total Alkynes (mg/kg)	179.6	0.32	-0.03	-0.04	86.9	0.27	0.01	0.01
Total Aromatics (mg/kg)	80.4	10.49	4.33	3.33	42.7	4.08	1.81	2.33
Alkane Fraction (%)	2.7	18.7	1.7	20.5	4.5	22.2	43.7	31.3
Alkene Fraction (%)	74.3	15.0	18.9	23.6	72.0	24.1	10.6	14.9
Alkyne Fraction (%)	15.9	2.0	-0.6	-0.6	15.7	3.3	0.3	0.3
Aromatic Fraction (%)	7.1	64.3	80.0	57.4	7.7	50.5	45.5	53.5

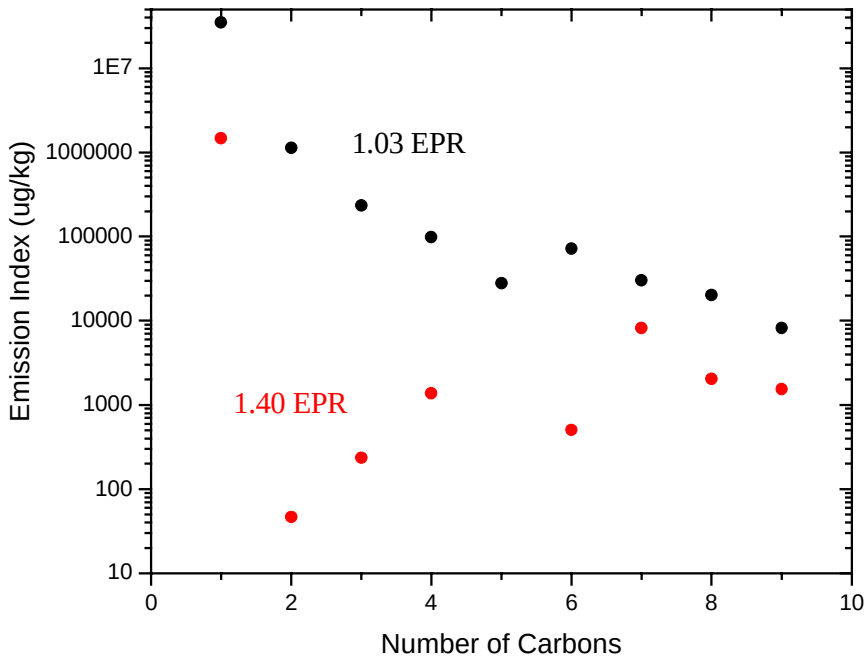

Figure 1. Carbon species emissions at idle and climb-out power plotted as a function of the number of carbons in each compound. CO and CH4 compose the single carbon group which accounts for the majority of mass emissions at both power settings.

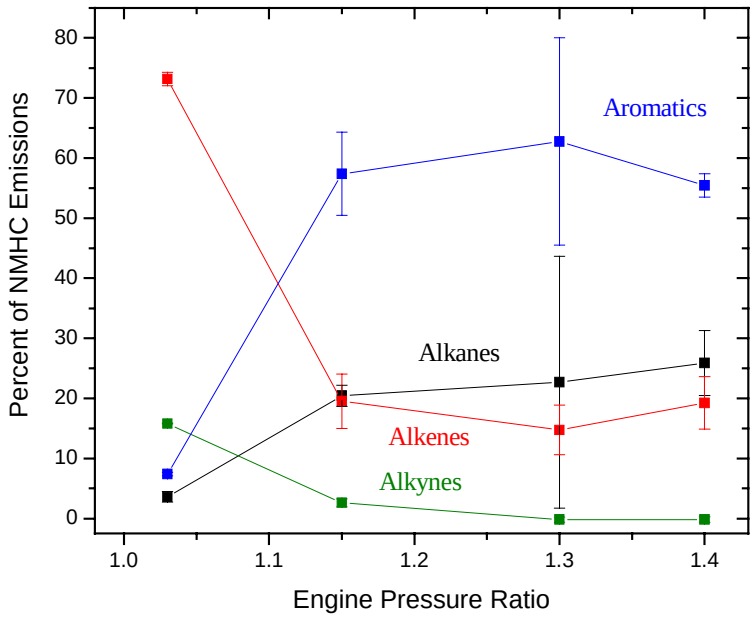

Figure 2. Hydrocarbon emissions from the RB211 engine at idle and climb-out power, broken down into the fractional contribution from different functional groups. Note that CH4 has been excluded from the alkane group.

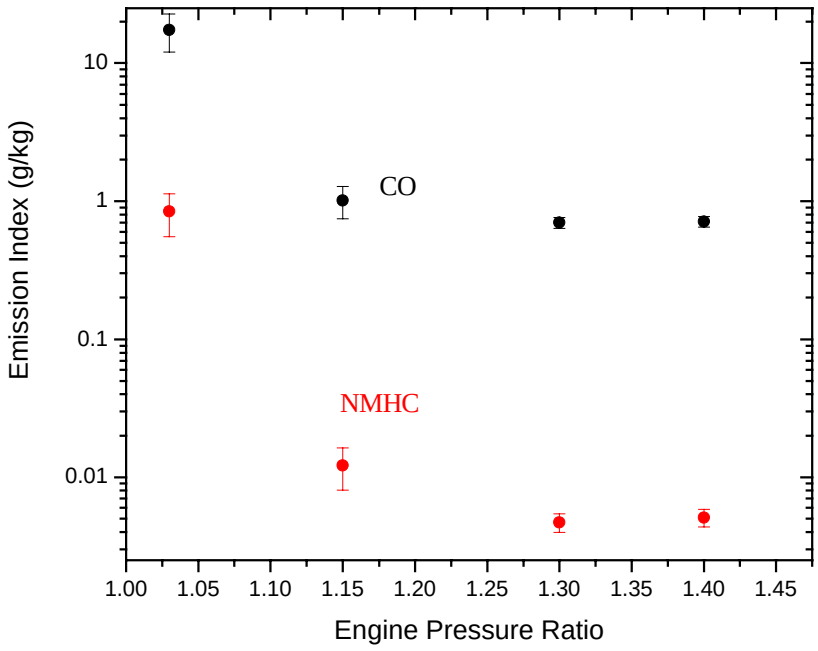

Figure 3. CO and total NMHC emission indices as a function of engine power where 1.03 EPR is idle and 1.4 is equivalent to climb-out.

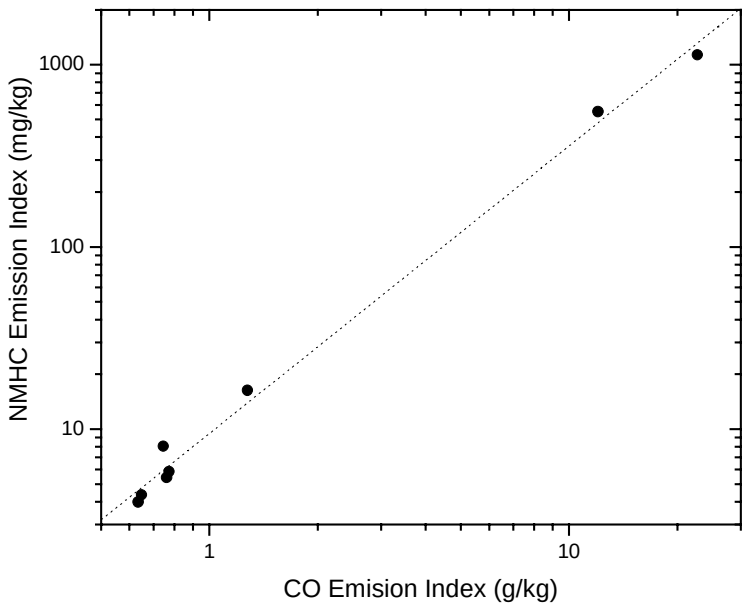

Figure 4. Total NMHC EI's plotted as a function of CO EI.

APPENDIX C:

ARI-RR-1362
ARI Contract # 10154
NASA Contract # C76653N

TECHNICAL SUPPORT OF MEASUREMENTS OF SO_2, SO_3, HONO, CO_2

Final Report for Task 2 of Contract C7665N

Prepared by

J. Wormhoudt and R. Miake-Lye
Aerodyne Research, Inc.
45 Manning Road
Billerica, MA 01821-3976

Prepared for

Dr. Chowen Wey
Aeropropulsion and Information Technology Branch
NASA Glenn Research Center
21000 Brookpark Road
Cleveland, OH 44135-3191

June 2003

Introduction

This is the final report for Task 2 of Contract C76653N with the NASA Glenn Research Center. It details the observations made using the NASA Glenn tunable diode laser (TDL) apparatus at NASA Langley Research Center during the Experiment to Characterize Aircraft Volatile Aerosol and Trace Species Emissions (EXCAVATE) in January of 2002. The program objectives for this apparatus were measurement of several of the gaseous constituents of aircraft exhausts. These included the reactive trace species HONO (nitrous acid) and SO_3 (sulfur trioxide) the major sulfur oxide species, SO_2 (sulfur dioxide), and the reference species water vapor by long-path infrared TDL absorption, and measurement of CO_2, also a reference species, by non-dispersive infrared absorption. Secondary objectives included assessments of the systematic and random error limits and detection sensitivity for trace species, and of the precision and accuracy of reference species (CO_2 and H_2O) measurements. Measurements of the T-38 exhaust were made on 1/22/02 and 1/29/02, while measurements of the B757 exhaust were made on 1/26/02 and 1/27/02. All T-38 measurements were of gas sampled at the engine exit plane, as were the 1/26 B757 measurements, while on 1/27 the B757 was sampled both at the exit plane and at a point 10m downstream.

Instrumentation

Figure 1 gives a schematic diagram of the instrument as it was used in the tests. The main gas flow in the gaseous species probe was sampled into the Glenn instrument through a smaller probe inserted through the wall of the large probe. This probe, and the characterization of it and the sampling system downstream of it, will be treated in detail below. The stainless steel probe was cut to a length of 12 cm from tip to a union fitting with a 36 cm length of 1.59 cm OD PFA tubing which carried the exhaust into the multipass cell. At its downstream end, this tubing was turned on a lathe to reduce its wall thickness, allowing it to flex enough to pass over the upstream multipass cell mirror.

The multipass cell, using Aerodyne's patented off-axis resonator design, had a total absorption path length of 100m. The mechanical pump indicated in Figure 1 was actually a manifold connecting three pumps, two 15 cfm Busch pumps and one 30 cfm Alcatel pump. With all three pumps in operation, the cell pressure varied from about 34 Torr when the B757 was at idle to 25 Torr at its highest power setting. A Baratron pressure transducer connected to the multipass cell allows the data acquisition and analysis computer to read the cell pressure and take the changing absorption linewidths into account.

The laser diodes and infrared detectors used in the TDL measurement are all contained in a single liquid nitrogen dewar. Two separately controlled diode stages and time-multiplexing software allow simultaneous operation of two diodes, but for maximum sensitivity we made measurements with one diode at a time. Two diodes were used in the test, a HONO diode and a SO_x diode. The HONO diode was operated in two spectral regions between 1666 and 1667 cm^{-1}, while the SO_x diode was operated in the region around 1400 cm^{-1} for SO_3 and in two regions in the range 1381 to 1383 cm^{-1} for SO_2. Data acquisition and analysis software on the TDL computer collects and averages absorption scans, and can least-squares fit them to model spectra to derive real-time outputs of multiple species concentrations. This was done occasionally, with most data saved as averaged spectra for post-test analysis. The cables between the lasers, the laser controller, the detectors, and the data acquisition computer must all be kept short, so the TDL instrument and its electronics rack were all in the protective housing behind the engine. A Cybex Longview KVM extender and a 200 foot cable were used to connect to a remote monitor, keyboard and mouse in a trailer. This system and the flat panel monitor were new for this test. For reasons not yet understood, the result was poor monitor reliability at high engine powers.

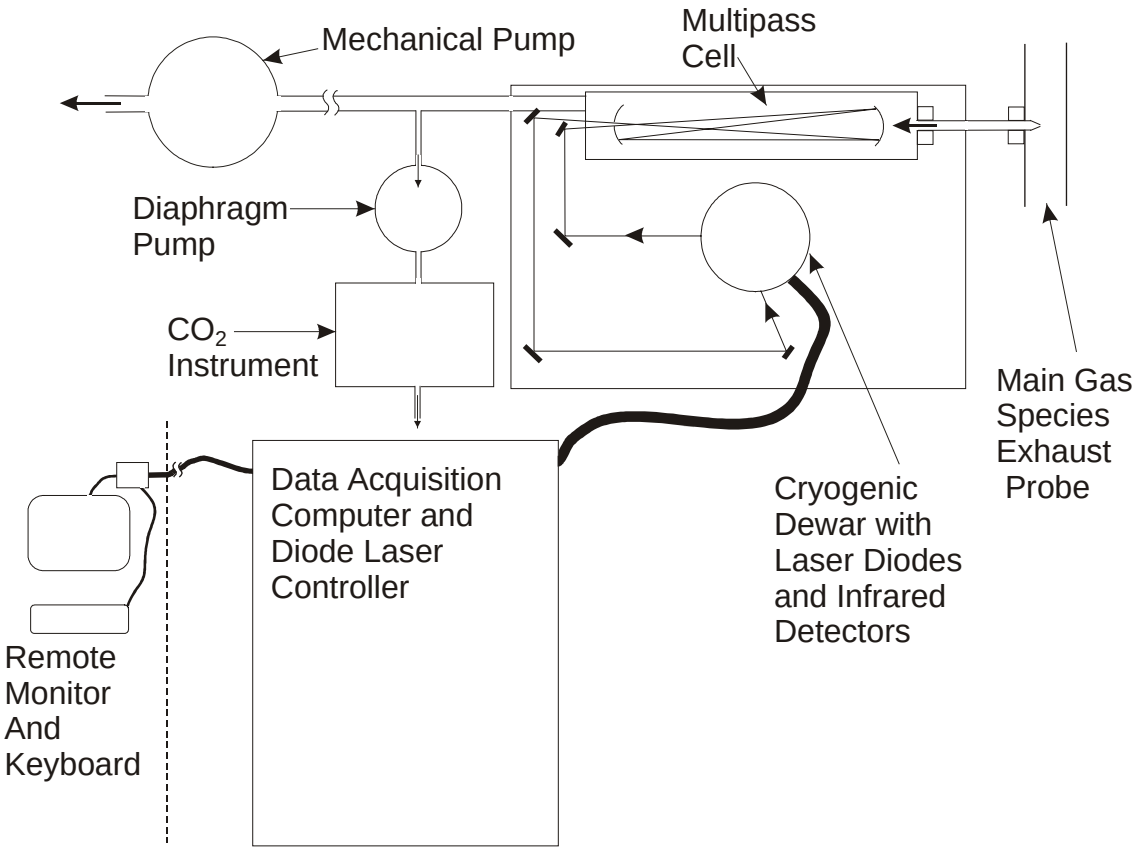

Figure 1. Schematic diagram of the NASA Glenn TDL apparatus used in EXCAVATE.

A KNF Neuberger Model N726 1 cfm diaphragm pump is used to extract part of the exhaust from the multipass cell and send it to the CO_2 sensor. This sensor was a Vaisala Model GMT 221 with maximum measurable concentration of 5% CO_2. Its output was monitored and stored using a Dataq DI-151RS data acquisition board and WINDAQ data acquisition and analysis software.

TDL Probe and Sampling System Characterization

As mentioned above, the atmospheric pressure flow in the 4.5 cm ID gaseous species probe was sampled into the TDL instrument using a second, smaller probe. This probe was fabricated by NASA Glenn Research Center from stainless steel tubing with 1.59 cm OD and 1.4 cm ID. A 4 cm long cone tip was welded onto one end of the tubing, which passed through a fitting in the wall of the large probe to project about 1.5 cm into the atmospheric pressure flow. As supplied by NASA Glenn, the cone of the TDL probe had a 0.127 cm diameter sampling orifice, but before the final tests at Aerodyne the orifice was enlarged to a diameter of 0.23 cm.

A laboratory simulation apparatus was constructed which connected the probe tip to a flow of dry air to which could be added varying amounts of SO_3 and water vapor. The main goal of the tests carried out using this apparatus was the understanding of sampling losses of SO_3. However, the observations during these tests also served to improve our model of the SO_3 high resolution infrared spectrum, necessary for detection and quantification of SO_3. Added to spectra obtained in earlier laboratory studies of SO_3 and a band strength from the literature, the spectra obtained during the sampling tests give us a

quantitative spectral model. Furthermore, this allows us to estimate the detection limits for SO_3 by this technique. In the NASA/QinetiQ engine sampling studies carried out in the UK in 2001, we estimated detection limits in the range of 15 to 50 ppbv of SO_3 in the multipass cell, where a cell concentration of 1 ppmv corresponded there to a fuel sulfur fraction of about 100 ppmm.

Initial experiments on SO_3 losses verified our observations in earlier laboratory tests of the sampling systems used in the NASA/QinetiQ tests: in the absence of water vapor, losses of SO_3 can in fact be negligible. All experiments were made with the stainless steel sections of the sampling train heated to 150 ^oC, in order to minimize adsorbed water on the walls. We then went on to the last, critical experiments, involving addition of varying concentrations of water vapor to the flow, measured using a water line in the SO_3 spectral region. We found a substantial decrease in SO_3 observed in the multipass cell with added water, with the final measured point being 0.03 of initial SO_3 at a water fraction of 0.008. Water fractions in engine exhaust would be several times this value, but because of the deleterious effects of sulfuric acid (reaction product of SO_3 and water) we used already damaged multipass cell mirrors, and the water fraction of 0.008 was our last measurable point.

Although we investigated fitting our SO_3 loss data set to a variety of model forms, we could not make a convincing case that we had a valid extrapolation formula. Key to our inability to extrapolate our data was the fact that we cannot make a clear-cut case for the detailed mechanism of SO_3 loss: wall loss was still a candidate, although our understanding of fluid dynamics in the multipass cell is not adequate for a quantitative model, and wall losses in the probe were estimated to be moderate; reaction on aerosol particles condensed in the sampling expansion is a possibility, although again a quantitative model would require additional work; finally, gas phase reactions known to us will not lead to observed losses, but our knowledge of the gas phase chemistry could also be incomplete.

Therefore, we entered the EXCAVATE tests with the expectation that SO_3 loss fractions in the sampling system could easily be two orders of magnitude, and more likely between three and four orders of magnitude. This uncertainty and the added uncertainty over the loss mechanism clearly would have made it difficult to interpret any results. However, for the first time we had a sampling system capable of carrying hot exhaust gas into the multipass cell (and this turned out to be a severe perturbation on the optics, greatly limiting the amount of data we could obtain). This encouraged us to think that at least some transient species might survive to be observed.

Results of SO_3 Observations

No clear observations of SO_3 were made. In the best spectra, any SO_3 present in the multipass cell must be at concentrations below 50 ppbv. Comparing to the multipass cell concentrations of the major sulfur oxide species, SO_2, we conclude that the fraction of total sulfur that existed in the multipass cell as SO_3 would have to be less than 0.005. Dividing this fraction by the range of loss factors quoted above, we see that this upper limit on detectable SO_3 is unlikely to provide any useful information about SO_3 levels in the unperturbed exhaust.

Results of CO_2 and H_2O Observations

The overall goal of the work reported here is the measurement of emission indices of trace species, where the emission index is the ratio of the mass of trace species emitted (in g) to the mass of fuel consumed (in kg) over the same time period. The TDL instrument does this by measuring a trace species concentration in the multipass cell, and the concentration of a reference species, one of the two major combustion product species CO_2 and H_2O whose emission rates are directly proportional to fuel consumption.

H_2O lines appear in each of the spectral regions described above for the various trace gases, and thus water vapor concentrations can be measured "for free" with every trace species measurement. However, each spectral region is selected so that the strengths and positions of the trace species lines will be optimal for sensitive and accurate detection, and the result is that the coincidental water lines are not optimal for accurate measurement. In the EXCAVATE data set we found the same situation as in earlier tests: the H_2O concentration data sets extracted from TDL spectra both had larger variances and larger systematic errors than the CO_2 data sets. In addition, use of H_2O as the reference species means that accurate values of inlet air humidity must be obtained and subtracted from the TDL observations to give the H_2O derived from the fuel. Although we had thought that humidity values would be available from the local weather observation station, we have so far been unable to retrieve these records for several of the test days. Therefore, we will not discuss the H_2O data set in detail here, but go on to the CO_2 data measured by the Vaisala instrument monitoring the NASA Glenn multipass cell exhaust, and compare it to CO_2 measurements made by NASA LaRC.

A representation of these data sets is given in the plots in Figures 2 through 4. Figure 2 presents a critical selection of the measurements made during the two T-38 test days observed by the NASA Glenn instrument. Figure 3 summarizes observations made at the B757 exit plane, while Figure 4 does the same for observations made 10m behind the B757 engine. In all cases, error bars represent the standard deviations in multiple measurements, and when there is no error bar, only one measurement is involved.

It can be seen that the NASA Glenn and NASA LaRC measurements often agree to within the error bars, though not always. In general, there are reasons to prefer the NASA Glenn values for the 1/22 test, and to prefer the NASA LaRC values for the other three days. (In the comparison plots, the good values from each instruments are used, so some comparisons are for the same conditions but between different days.) We have concluded, after detailed analysis, that the two data sets taken together allow us to deduce a reliable value of CO_2 concentration for every set of engine and sampling parameters.

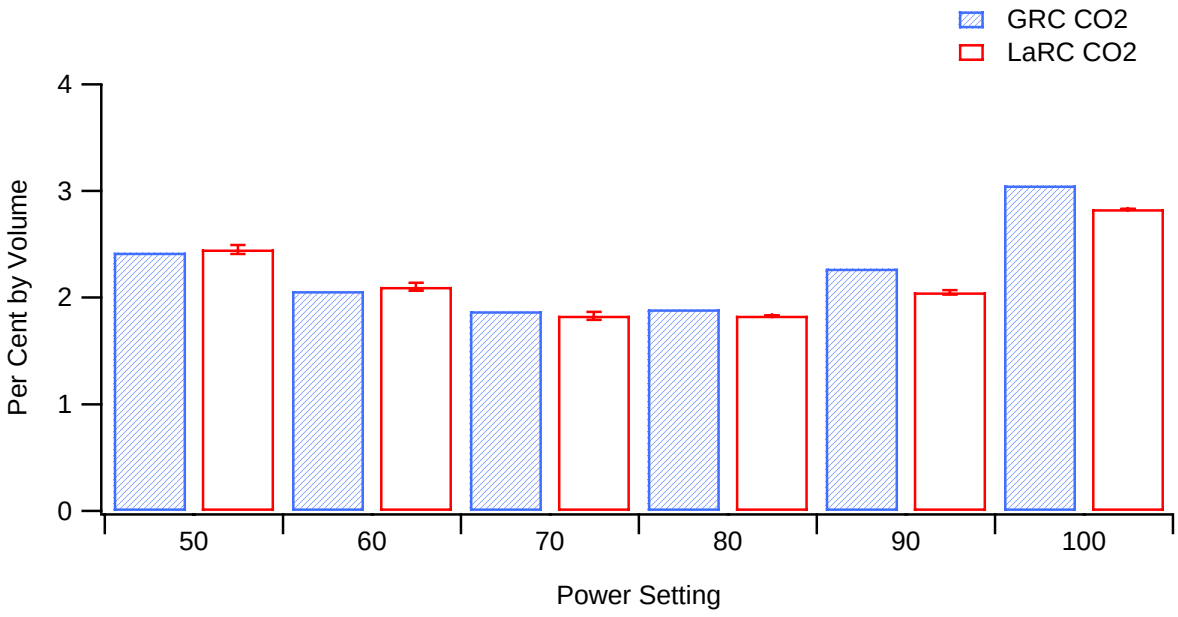

Figure 2. Best values for T-38 exhaust CO_2 concentrations from NASA Glenn and NASA LaRC.

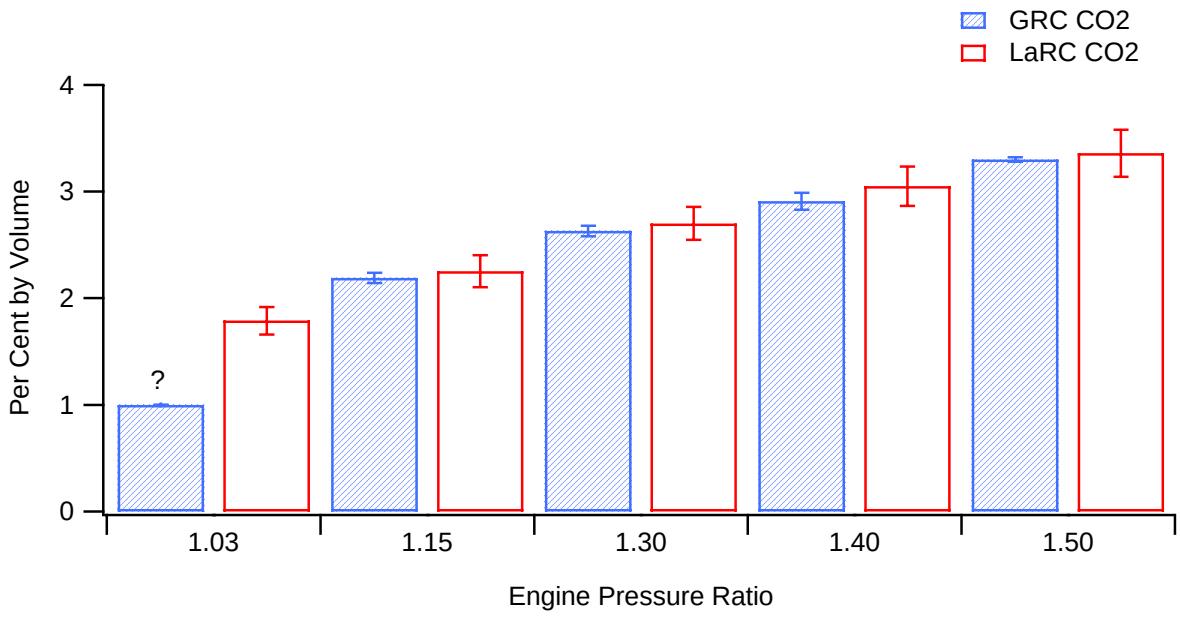

Figure 3. Comparison of NASA Glenn and NASA LaRC CO_2 observations for the B757 sampled at 1m.

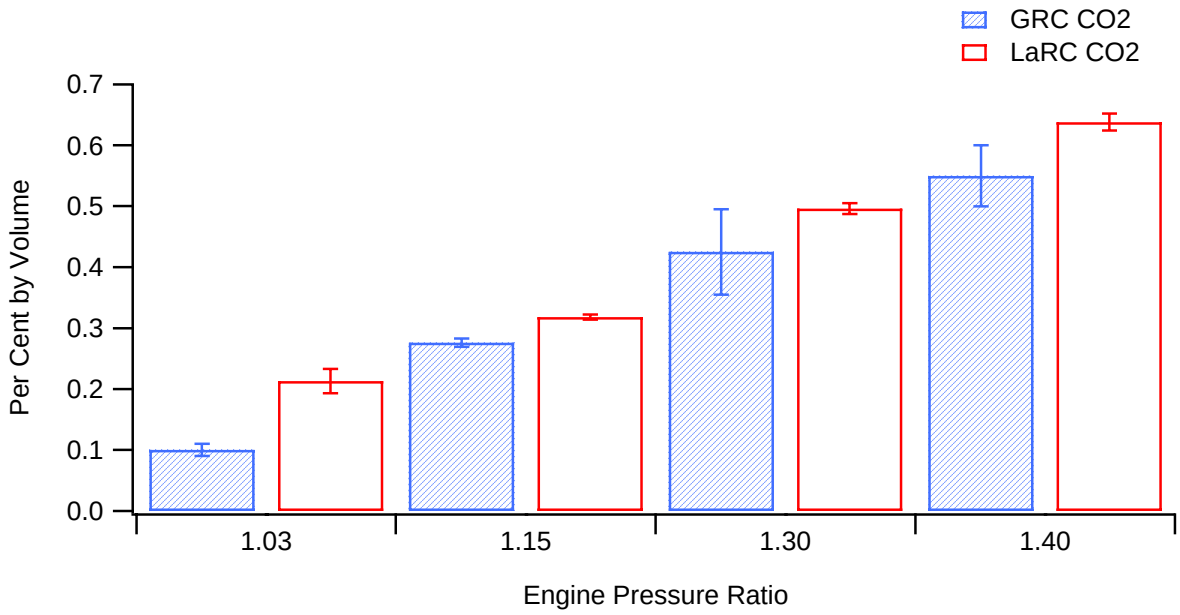

Figure 4. Comparison of NASA Glenn and NASA LaRC CO_2 observations for the B757 sampled at 10m.

Results of SO_2 Observations

Since SO_2 is the overwhelmingly predominant sulfur oxide species, and since its only source is the sulfur contained in the fuel, measurements of SO_2 emission indices are constrained in a way that those of NO_x, for example, are not. That is, the SO_2 emission index, or g SO_2 per kg of fuel, is directly related to the fuel sulfur fraction, or g S per g of fuel. In fact, in presenting our results, we will simply make that conversion and then, when fuel sulfur analyses are available, take the ratio and report SO_2 as a fraction of total fuel sulfur. A fraction of fuel sulfur in SO_2 that is significantly less than one could indicate that some other sulfur oxide species was present in the exhaust, but a fraction that is greater than one is simply an indication of systematic errors in measurements of SO_2 and/or CO_2 concentrations.

In the T-38 tests, measurements of SO_2 expressed as fuel sulfur fraction were obtained for the 50, 70 and 90 per cent power settings. For the first two settings the value obtained was 1665 ppmm, while for the 90 per cent power setting it was 1440 ppmm. When we take into account the roughly 20 per cent error bars we expect from the combination of systematic and random errors, these two values are not significantly different. At present we do not have a sulfur analysis for the T-38 fuel, so we cannot comment further on these results.

Figures 5 and 6 present results of SO_2 measurements of the B757 exhaust at the two measurement positions. SO_2 emission index fractional standard deviations in multiple measurements were typically less than 10 per cent. The analysis of systematic as well as random errors detailed in previous reports leads to total error estimates of 20 per cent or more. By this standard, all points in Figure 5 and all but one or two in Figure 6 show the TDL measured SO_2 to agree with the total fuel sulfur from the LaRC fuel analyses. The values in Figure 5 lie in the range of 0.75 to 1.0, while those in Figure 6 are distributed evenly above and below a ratio of 1. Table 1 lists the SO_2 emission index values used to prepare the figures.

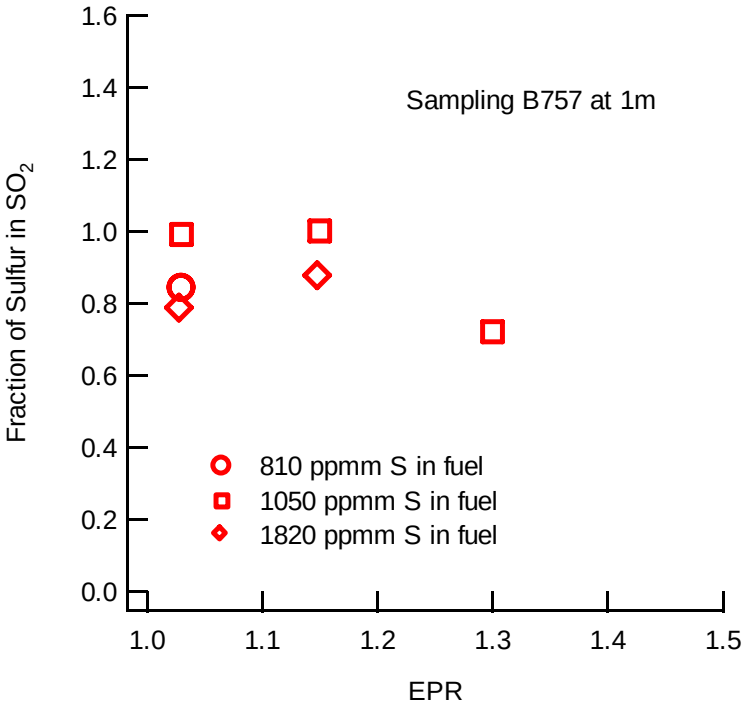

Figure 5. SO_2 measurements at 1m behind the B757, expressed as fraction of fuel sulfur.

The measurements in Figure 6 taken at 10m represent a less stressful environment but lower concentrations of SO_2, which could lead to a noisier data set. There is indeed a larger spread in the ratios in Figure 6. This makes it difficult to be sure that the apparent trend, of decreasing fraction in SO_2 with increasing power, is real. This trend is at least consistent with an additional data set, in which automatic fitting of the SO_2 spectra was used to write a real-time record of SO_2 and water concentrations, a so-called "streaming file". In a period of less than an hour, the B757 power was varied from 1.03 pressure ratio through the two intermediate settings all the way to 1.40, then returned to 1.03 (idle). Each increase in power showed a clear decrease in SO_2 fraction, outside of the range of variation, with the total change from 1.03 to 1.40 being about 30%, and the final return to 1.03 coincided with a return to the original high value of SO_2. At this point, we simply note this as a possible systematic problem in the 10m sampling, although we cannot suggest a mechanism for an actual change in plume chemistry.

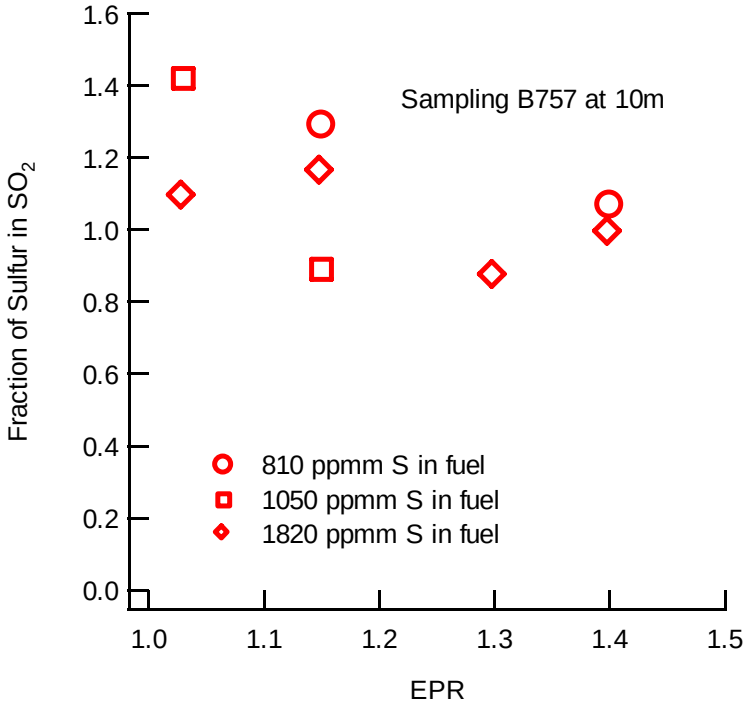

Figure 6. SO_2 measurements at 10m behind the B757, expressed as fraction of fuel sulfur.

Table 1. TDL measured SO_2 emission index values (as ppmv in fuel) for B757 exhaust sampling.

At 1m: EPR	Run	Fuel Sulfur, ppmv	EI(SO_2), ppmv
1.03	92	810	680
1.03	28,30	1050	1040
1.03	42,60	1820	1410
1.15	31	1050	1020
1.15	46,65	1820	1580
1.30	82	1050	680

At 10m: EPR	Run	Fuel Sulfur, ppmv	EI(SO_2), ppmv
1.03	102,103	1050	1490
1.03	115,138,149	1820	1980
1.15	132-132	810	1045
1.15	105-107	1050	940
1.15	141	1820	2110
1.30	121,144-146	1820	1575
1.40	136-137	810	870
1.40	147-148	1820	1810

Results of HONO Observations

The richest data set involved measurements of nitrous acid, HONO. In the previous NASA/QinetiQ tests[1], HONO had been measured, both at the combustor exit and, at higher levels, at the engine exit. However, due to substantial etalon fringes, the HONO concentrations measured in these tests had been near the detection limit. Also, because sampling was carried out in a single configuration, it was difficult to rule out the possibility that HONO was being formed from NO and H_2O in the sampling probe.

In the EXCAVATE measurements behind the B757, the detection limit was as low as 100 ppbv in the multipass cell. At high powers, over 2 ppmv of HONO was observed. When converted to emission indices, the B757 HONO results shown in Figure 7 show a clear power dependence, decreasing with decreasing power at the two lower settings but roughly constant at the highest three settings. When the sampling point was moved back to 10m behind the engine, the HONO concentration may have decreased somewhat, though when the total error estimates shown in the figure are taken into account, this decrease is not necessarily significant.

In contrast to the B757, which showed much more HONO than observed in the engine exhaust sampled in the 2001 NASA/QinetiQ tests, the T-38 HONO levels were not measurable, meaning they were at least well below 100 ppbv in the multipass cell. Thus, the EXCAVATE observations contain three points of comparison which suggest HONO formation in the probe is not a serious problem. In the move from sampling at 1m to sampling at 10m, the temperature and composition of the exhaust have changed substantially, but the HONO fraction of exhaust species has not. In both the case of B757 engine power variation and in the change from B757 to T-38 exhaust, the exhaust properties have changed less than the HONO concentration. This is especially true for the comparison between engines: the change in HONO is more than an order of magnitude, while changes in temperature, NO and H_2O are much less than that.

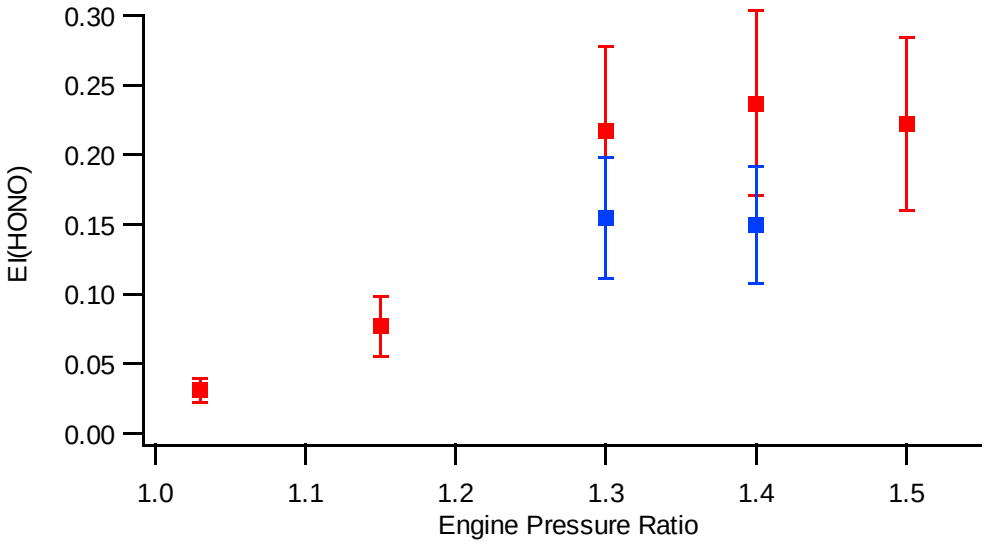

Figure 7. HONO emission indices measured at 1 and 10m behind the B757.

Summary

In summary, several points can be made about the data taken by the NASA Glenn TDL instrument at EXCAVATE. Analysis of the CO_2 data taken by the Vaisala instrument which sampled the TDL instrument's exhaust, and the CO_2 data taken by NASA LaRC should give a reliable value for each value of engine and sampling parameters.

The detection limit for SO_3 in the multipass cell less than 50 ppbv. However, SO_3 was not observed, with an upper limit for SO_3 as a fraction of total sulfur in cell being less than 0.005. Because we expected sampling losses of at least two orders of magnitude, and more likely between three and four orders of magnitude, this upper limit most likely does not provide any useful information about the level of SO_3 in the exhaust.

Multiple measurements of SO_2 showed good repeatability, with SO_2 emission index fractional standard deviations typically less than 10 per cent. For the B757 measured at 1m, the EI(SO_2) values derived from TDL measurements of SO_2 and NASA LaRC measurements of CO_2 were not significantly different from the total exhaust sulfur emission index derived from the NASA LaRC fuel analyses. For the B757 measured at 10m, where the EI(SO_2) values are more scattered, there may be a trend of decreasing fraction in SO_2 with increasing power, but the scatter in the data does not allow us to conclude that this is a real trend.

The TDL detection limit for HONO was as low as 100 ppbv. At high power, over 2 ppmv of HONO was detected in the B757 exhaust. These values correspond to EI(HONO) values of up to 0.25 (if nominal values apply to this exhaust, this is somewhat less than 5% of the NO). By contrast, HONO was not detected in the T-38 exhaust. HONO variation with a change in sampling position in the B757 exhaust from 1m to 10m was not significant. Changes with B757 power setting, on the other hand, were clearly seen, with the lower two power settings yielding significantly lower emission indices than the higher settings. All of these trends confirm earlier HONO observations, and argue against the possibility that significant HONO is formed in the sampling line.

References

1. "QinetiQ/NASA Collaborative Programme – Final Report," produced for UK Department of Trade and Industry Under Order/Contract reference F11X1DXX by QinetiQ Ltd, Cody Technology Park, Farnborough, Hampshire GU14 0LX, UK.

APPENDIX D: Concentrations and Physical Properties of Jet Engine Exhaust Aerosols Sampled during EXCAVATE

Bruce E. Anderson, Edward L. Winstead, Charles H. Hudgins, James V. Plant, H.-S. Branham, and K. Lee Thornhill

NASA Langley Research Center
Hampton VA 23662

1.0 Background

Aircraft are prolific sources of both primary and secondary aerosol particles (i.e., Friedl et al., 1997). Composed of soot and perhaps condensed organic carbon and sulfur species, these particles can potentially impact climate by influencing a number of important atmospheric processes including radiation transfer; cloud formation, duration, and albedo; and heterogeneous chemical reaction rates. In addition, release of such particles in airport terminal areas can have deleterious health effects upon exposed workers as well as reduce local air quality and visibility.

To quantify and better understand the generation of particulates and pollutants by aircraft, the National Aeronautics and Space Administration (NASA), through its Atmospheric Effects of Aviation Project, has sponsored several cooperative field investigations, the latest of which was the Experiment to Characterize Aircraft Volatile Aerosol and Trace Species Emissions or EXCAVATE. Conducted at NASA LaRC during January 2002, EXCAVATE was designed to address a number of particle-related objectives, including quantifying and characterizing turbine engine black carbon and nonvolatile particle emissions as well as investigating the formation and growth of volatile particles in the plume as a function of plume age, fuel S content, and engine power. The experiment included sampling exhaust emissions from the J85-GE and a RB-211 engines on the LaRC T-38A and B-757 aircraft, respectively, as they were operated in a ground-based run-up facility. The LaRC In Situ Measurements Group participated in EXCAVATE and played a key role in addressing project objectives by providing a suite of instruments to measure particle number density as a function of size diameter and aerosol absorption coefficients from which black carbon mass is inferred. The text below provides a description of the LaRC instrument package and sampling procedures and a summary of observations.

2.0 Experiment

Figure 1 shows a diagram of the LaRC aerosol characterization system. Important components include 1) a TSI 3022 condensation nuclei counter (CNC) to measure total aerosol number density; 2) a pair of TSI 3760 CNCs to determine the fraction of particles >12 nm that are volatile at temperatures below 300 ^{o}C; 3) a dual, differential mobility analyzer (dDMA) to provide 60-second resolution, particle size distributions over the 0.004 to 0.240 μm diameter range; 4) an optical particle counter to measure aerosol size

distributions in the 0.1 to 1 μm range; and 5) a particle soot absorption photometer (PSAP) for total aerosol absorption (i.e., carbon black) measurements. The specific parameters measured by these instruments along with their anticipated precisions and accuracies are listed in Table 1; brief descriptions are provided below.

Total aerosol concentrations were monitored with a TSI3022 CNC because, unlike the single particle counting units like the TSI3025 and 3760, it has a photometric, ensemble sampling mode that extends its dynamic range to $>10^7$ cm^{-3}. This is particularly important because the exhaust samples often contained $>10^{-6}$ cm^{-3} particles, even after a 10-fold dilution. This CNC has a 50 percent cut size of ~7 nm at sea level pressure and a response time of < 5 seconds.

Cofer et al., (1999) describes the identical CNCs (TSI3760 CNCs) that were used to determine the fractional volatility of aerosol samples and discusses their calibration and performance at subambient pressures. These instruments provided a means for distinguishing soot from condensed hydrocarbon and sulfate particles, but, unfortunately, their upper concentration range is ~2×10^4 cm^{-3}, so their signals were often saturated when sampling the highly concentrated exhaust plumes.

The dual differential mobility analyzer (dDMA) used to record nucleation and accumulation mode size distributions was composed of a TSI nano-DMA column (nDMA) and a TSI long-DMA column (lDMA), both connected to the same voltage sweep generator and input particle neutralizer. Output from the nDMA was routed to a TSI 3025 CNC, whereas the lDMA was connected to a TSI 3762. Both systems provided 25 channels of logarithmically spaced sizing data, the nDMA over the range for 3 to 85 nm and the lDMA from 9 to 240 nm. The particle transfer functions for the DMAs were determined for 500 Torr operation and were applied to the voltage sweeps to obtain size distributions appropriate for the pressure and temperature of operation. Size distributions were derived using the technique described by Wang and Flagan (1990) and the accuracy of the inversions were verified by comparing integrated number densities to those recorded by a CNC that continuously monitored number densities in the sample stream. Size scans recorded during times when concentrations changed by more than 50 percent were rejected as bad data. The two DMAs were operated in overlap mode (i.e., both sampled the same input stream) while sampling the B-757 to provide improved resolution and counting efficiency for nucleation mode particles; however, an inline heater was placed on the input of the lDMA on the last set of T-38 engine runs to allow us to distinguish the portion of the observed aerosol size distribution that could be attributed to soot from that related to condensed hydrocarbons and sulfates.

Aerosol size in the 0.1 to 1 um size range was determined using a Particle Measuring Systems (PMS), High Sensitivity Laser Aerosol Spectrometer (HSLAS). Based on Mie scattering principle, this instrument sizes particles by measuring the hemispheric side-scatter from particles passing through feedback cavity of a 683 nm helium-neon laser. The instrument provides 30 bins of size data that are updated continuously. It was calibrated for size sensitivity using latex spheres and for concentration by comparison to a CNC for measuring the number density of monodisperse particles output by a DMA.

Table 1. In Situ Aerosol Instrumentation

Measured Parameter	Instrument	Size Range (microns)	Response (seconds)	Precision
Total CN	TSI 3022	0.01 - 1.00	1	20 percent
Total and Nonvolatile Aerosols	TSI 3760	0.012 - 1.00	1	20 percent
Ultrafine/Fine Aerosol Size	Dual DMA	0.006 - 0.25	60	20 percent
Fine, Coarse Aerosol Size Distribution	HSLAS	0.1 - 1.0	1	20 percent
Aerosol Absorption	PSAP	< 1.0	5 sec	$10^{-7}m^{-1}$

Aerosol absorption coefficients were determined with a Radiance Research Particle Soot Absorption Spectrometer (PSAP). Composed of a light source, filter, and photodector, the instrument is based on the generally accepted integrating plate (IP) technique in which the change in optical transmission of a filter caused by particle deposition is related to the optical absorption coefficient using Beer's law and a calibration transfer coefficient. In practice, the instrument employs a vacuum pump to draw a metered amount of sample air though a translucent, quartz filter. Using a chopper, it alternately measures the attenuation of 565 nm light though a clean portion of the filter and the portion where the sample is being collected. The difference in measured light intensity along the two paths is due to the absorption by particles. A microprocessor within the instrument applies a factory-determined calibration equation to convert the measured changes in filter transmission into an absorption coefficient with units of inverse meters (m^{-1}). We applied additional corrections described by Bond et al. (1999) to account for reflectance of the filter, the change in response of the instrument as a function of filter transmission, and effects of scattering from non-absorbing particles. Absorption coefficients were converted into mass of black carbon using the mass absorption coefficient of 7 m^2g^{-1} that was observed in turbine engine exhaust plume studies conducted in Europe (Petzold and Dopelheuer, 1998).

The instruments shown in Figure 1 and described above were plumbed to a common sampling manifold. In order to provide immunity to the frequently changing inlet pressure and to add a 10-fold or so dilution, the entire system was operated at subambient pressure by drawing sample through a small diameter orifice, then adding a concentric flow of

filtered air via a pressure controlled valve. Sample flow rate was determined by subtracting the measured dilution flow from the total system flow and the dilution ratio was found by dividing the total flow by sample flow. Dilution ratios varied from ~9 to 15, depending on the pressure in the common sampling line leading in from the selected aerosol inlet.

The aerosol instruments and their associated control units and power supplies were mounted within a standard, double-bay aircraft instrument rack and placed inside the "aerosol sampling trailer" that was parked adjacent to the aircraft run-up area, about10 meters to the right side of the engine exhaust axis. Sample air from one of a selection of aerosol inlets placed in the exhaust was delivered to the system through a common sampling line that also had taps to supply samples to complementary aerosol characterization systems operated by Aerodyne, the University of Minnesota, and Glen Research Center. Pressure and CO_2 concentration within the sampling line were continuously recorded to provide a means for subsequently determining fuel burn normalized statistics of engine emission parameters.

2.1 Calculated Parameters

Data acquired from the LaRC instruments were corrected for sampling pressure, dilution, and known system losses, and used to calculate the secondary variables listed in Table 2 Values for aerosol mass were found by integrating volume-size distributions over a specific size range, then multiplying the resulting volumes by an appropriate aerosol mass density. Because the particles sampled during EXCAVATE were often a superposition of soot and condensed sulfates and hydrocarbons with a poorly defined morphologies, we assumed a mass density of 1 g cm^{-3}.

Aerosol size statistics were derived from the measured size distributions using formulas discussed by Hinds(1999) . The number "mode" corresponds to the peak in the size distribution when plotted as a function of dN/dLn(Dp) vs Dp. The geometric mean diameter is found using the following formula:

$$GMD = EXP\{\Sigma[(n_i/dLn(Dp_i)) * Ln(d_i))/\Sigma(n_i/dLn(Dp_i))\} \quad \text{Eq. 1}$$

where n_i, d_i, and dLn(Dpi) are the number density, mean diameter, and normalized width in/of i^{th} size channel. Similarly, the volume mean diameter is calculated using the formula

$$VMD = EXP\{\Sigma[(v_i/dLn(Dp_i)) * Ln(d_i))/\Sigma(v_i/dLn(Dp_i))\} \quad \text{Eq. 2}$$

where v_i is the total volume calculated for the i^{th} channel as given by $v_i = n_i * \pi * d_i^3 / 6$. Assuming the aerosols are log-normally distributed in a single mode, i.e., unimodal, the geometric standard deviation of the size distribution is given by

$$\sigma_g = EXP\{(\Sigma\, n_i\, (\ln(d_i) - \ln(GMD))^2)/(N-1)\}^{0.5} \quad \text{Eq. 3}$$

In conjunction with the GMD, the geometric standard deviation is useful for modeling aerosol emissions and represents the broadness or spread of the log normal function in that 95 percent of the particles within a log normal distribution fall within the size range defined by EXP(ln (GMD) $\pm$ 2 * ln(σ_g)).

Emission indices (EIs) are fundamental parameters used to describe the amount of pollutants emitted by a combustion source per unit of fuel consumed. Values were calculated for aerosol number density, mass and black carbon as follows:

$$EI(X)\ (kg^{-1}\ \text{fuel burned}) = (\Delta X/\Delta CO2) * EI(CO2) * M_{air}/(\rho * M_{co2}) \qquad \text{Eq. 4}$$

Where ΔX and $\Delta CO2$ are the enhancements above background concentration for parameter X and CO_2, M_{air} and M_{CO2} are the molar masses of air and CO2, respectively, and ρ is the density of air. For our calculations, we assumed the fuel contained ~86 percent carbon which yields a EI(CO_2) of ~3160 g (CO_2) kg^{-1} fuel burned.

Table 2 List of Parameters Derived From Experimental Measurements

Parameter	Symbol	Units	Temporal resolution	Estimated precision
Aerosol Volume	V	$\mu m^3\ cm^{-3}$	60 s	25 percent
Aerosol Mass	M	$mg\ m^{-3}$	60 s	50 percent
Geometric Mean Diameter	GMD or d_g	nm	60 s	< 5 nm
Volume Mean Diameter	VMD	nm	60 s	< 5 nm
Geometric Standard Deviation	σ_g	-		
Number Emission Index	EI(N)	particles kg^{-1}	1 s	20 percent
Mass Emission Index	EI(M)	$mg\ kg^{-1}$	60 s	50 percent
Black Carbon Emission Index	EI(BC)	$mg\ kg^{-1}$	60 s	20 percent

3.0. Results

3.1. J85-GE Engine Emissions

EXCAVATE was conducted over a two-week period in mid-to-late January 2002 and included sampling behind the T-38A on January 22, 24, and 29. The primary objective in sampling the J85-GE engines on this aircraft was to test our instrument performance and sampling procedures in preparation for making what were considered the more important characterizations of the RB-211 emissions. The test matrix for the T-38A included sampling at six different power settings ranging from idle to 100 percent of maximum RPM and at sampling probe-exit plane separations of 1-m on January 22 and 24, and at 1, 10, and 25-m on the January 29. A single fuel mixture (JP-5 containing 820 ppmvS) was used in all tests. Aerosol characterization measurements were made at a total of 66 different power setting/probe separation combinations. The runs varied from ~1 to 20

minutes in duration, but typically lasted ≈4 minutes, which allowed us to record four dDMA size scans to examine the variability size/volume parameters.

Results from each run are presented in Table 3 and are not corrected for sampling losses that occurred in the sampling probes and transmission lines. Values reported for Number EI are derived from continuous, TSI3022 CN data and, thus, are representative of the total particles > 10 nm in diameter. Black carbon values were calculated from the integrated change in filter attenuation across the run and are not available for runs 1–12, conducted on the first day of operation because samples delivered to the PSAP were insufficiently diluted and the instrument became saturated within minutes after beginning the first run. Mass EI and the size distribution parameters (mode, GMD, and VMD) were calculated from the long DMA observations (i.e. over the range from ~10 to 240 nm) and assuming a mass density of 1 g cm-3 for the measured aerosol that was constant across the size spectrum.

An examination of Table 3 values suggests that the T-38 emissions are quite variable across the J85-GE operational and sampling envelope. Number EIs varied from 0.8 to 23 x 10^{-15} kg^{-1} and averaged 6 x 10^{-15} kg^{-1} for the entire data set. Assuming an aerosol mass density of 1 g cm^{-3}, mass EI values ranged from ~8 to 465 mg kg-1, and averaged 111 mg kg^{-1}; black carbon varied from 17 to 400 mg kg^{-1} and averaged 111 mg kg-1; the mode of the number-size distribution varied from 15 to 61 nm, averaged 23 nm--almost identical to the statistics exhibited by the GMD. VMD values ranged from 31 to 91 nm, and averaged 52 nm.

The power and plume age dependencies of the aerosol parameters are more easily observed in the summary data shown in Table 4 and Figures 2-6. At 1 m sampling distance where the aerosol should be composed primarily of soot and other nonvolatile species (i.e., metals, PAHs), number EI values peaked at idle (50 percent power), then dropped by >60 percent and became relatively constant at turbine speeds above 70 percent of maximum (Figure 2). Conversely, mass EIs were relatively constant at or below 70 percent power, then increased by a factor of two upon reaching 100 percent power (Figure 3). This inverse relationship between number and mass EI suggests that the particle size increases with engine power, which is borne out by the calculated values for GMD and VMD (Figures 4 and 5); these parameters increased from 23 to 30 nm and 48 to 66 nm, respectively, in going from idle to full military power. Black carbon EI increased from ~85 mg kg-1 at idle to 272 mg kg at 100 percent power (Figure 6). Note also that the ratio of BC to mass EI changed from 0.44 to 0.67 across this power range, indicating that, perhaps, a higher fraction of the aerosol emissions was composed of nonvolatile organics at the lower combustor temperatures characteristic of low power conditions.

Ten meters downstream from the engine exhaust plane, the plume had diluted by more than tenfold and its temperature dropped to < 70 ^{o}C. Here, at low to medium turbine speeds, aerosol number EIs (Figure 2) were typically higher and VMD's lower (Figures 5) than at 1 m, suggesting that low volatility species had condensed to form new particles as the plume cooled. Because of their small sizes, these aerosols did not significantly

add to the mass loading (Figure 3), except at the idle condition (50 percent) where the mass EI is twice the value observed at 1 m. This might be related to the longer growth period experienced by the aerosols in the low velocity plume, the propensity of the engine to emit more condensable hydrocarbons at low powers, or it might simply be caused by poor sampling statistics. Samples collected from the 25 m inlet exhibited even higher number EIs (Figure 2) but the trend in mass EIs could not be delineated because, at that sampling distance, concentrations were too variable across the 60 second scan time of the DMA to yield reliable size distributions.

Black carbon EIs tended to increase with sampling distance (Figure 6), which may be caused by a number of factors. First, the freshly formed sulfate and organic aerosols could have deposited on the PSAP filter and caused enhanced scattering that is, from the instruments perspective, indistinguishable from the absorption due to soot. Ideally, simultaneous measurements of aerosol scattering coefficient (σ_s) at 565 nm would have been recorded and used to correct the measured absorption coefficient via the method developed by Bond et al., (1999). Lacking these measurements, we may in the future use the measured size distributions and Mie theory to calculate σ_s to evaluate the extent to which scattering effects the measurement. We note, however, that most of the newly formed sulfate particles are <<100 nm in diameter and should not exhibit appreciable scattering. On the other hand, organic molecules condensing upon existing soot particles could have increased their scattering cross-sections, but the size distribution scans, at least at 10 m, do not suggest that any great changes occur in the population of aerosols in the 50 to 250 nm size range. Another entirely different explanation is that aerosol losses were greater in the 1 m inlet than the 10-m inlet probe. It is easy to visualize enhanced losses at the 1 m sampling distance because the environment there is very hot (>300 ^{o}C) and highly turbulent (mean velocities of 50 to 400 m s^{-1}) and aerosol concentrations are extremely high (~10^{8} cm^{-3}) which might lead to rapid losses though thermophoretic effects, Brownian diffusion, turbulent deposition, and coagulation. However, this does not account for why the 25 m values are in most cases higher than those observed at 10 m. Perhaps the primary factor is that, as the plume ages, the small soot particles grow through agglomeration, coagulation, or accretion of gas phase material to sizes that are less susceptible to loss in the inlet/sample transport systems. We note that even with the low transmission efficiency of the sampling probes for nucleation mode aerosols (<20 percent for diameters < 10 nm), size scans recorded by U. Minnesota at the 1-m sampling distance showed there were large numbers of nonvolatile aerosol in the 3 to 10 nm size range, which supports the notion that a significant fraction of the absorbing aerosols may have escaped detection at the closest sampling distance.

Indeed, because jet engine exhaust plumes contain a great deal of nanometer-sized particles and condensable material (i.e., water, sulfuric acid, organics), we have observed that aerosol characteristics are highly dependent upon the details of sample collection and dilution. For example, experiments conducted at Langley in the summer of 1999 indicated that the T-38A number EI at any given power could be manipulated by a factor of eight by turning on and off the cooling water supplied to the sample collection probe that was positioned 1-m downstream of the exhaust plane (Cofer et al., 2001). To

examine the effects of sample dilution during EXCAVATE, we recorded data from 1-m samples that had been diluted by factors of ~8, 16, and 24 (Figure 7).

Values were always higher in the more dilute samples (factor of 2 at idle), but the differences became less distinct at higher engine speeds. We speculate that higher relative nanometer-sized aerosol densities and slower sample flow rates combined to produce a higher coagulation rate at low engine speeds.

3.1. RB-211 Engine Emissions

The exhaust plume from the right-side RB-211 engine on the NASA Langley B-757 was sampled on January 25-27, 2002. Primary objectives for these tests were to establish the physical and chemical characteristics of particulate emissions from a commercial-type aircraft and to observe how these emissions vary as a function of engine power, plume age, and fuel sulfur concentration. To meet these objectives, the test matrix included sampling at 5 different power settings (as indicated by engine pressure ratios, EPR) ranging from 1.03 (idle) to 1.5 EPR (slightly lower than takeoff power); at sampling probe-exit plane separations of 1 m and 25 m on January 25 and 26 and at 10 and 35 m on January 27; and burning JP-5 fuels containing 810, 1050, and 1820 ppmvS. Note that the high S fuel was obtained by adding tetrahydrothiophene to the 1050 ppmS fuel, thus these two fuels had identical hydrocarbon matrices. Aerosol characterization measurements were made for a total of 149 different power setting/probe separation/fuel S combinations. The runs varied from ~30 sec to 21 minutes in duration, but typically lasted >2 minutes, which allowed us to record 2 or more dDMA size scans to examine the variability size/volume parameters.

Results from RB-211 sample runs are presented in Table 5 and, as was the case for the T-38 data, are not corrected for sampling losses that occurred in the sampling probes and transmission lines. Again, number EI are derived from continuous, TSI3022 CN data, Black carbon values were calculated from the integrated change in filter attenuation across the run, and the size distribution parameters (mass, mode, GMD, and VMD) were calculated from the long DMA observations (i.e. over the range from 9 to 240 nm), assuming an aerosol mass density of 1 g cm-3.

Close examination of Table 5 values suggests that the RB-211 aerosol emissions are even more variable than those from the T-38. For example, number EIs ranged 0.01 to 85 x 10^{15} kg-1, and averaged ~9 x 10^{-15} kg^{-1} for the entire data set. Mass EI values ranged from ~1 to >9000 mg kg-1 and averaged ~500 mg kg^{-1}; black carbon varied from 0.6 to 218 mg kg^{-1} and averaged 59 mg kg^{-1}; and the mode of the number-size distribution varied from 10 to 101 nm, and averaged 27 nm--almost identical to that of the GMD. VMD values ranged from 31 to 91 nm and averaged 52 nm.

To investigate how aerosol characteristics varied as a function of the test variables, we calculated statistics for each sampling distance, power setting, and fuel sulfur content. Results are shown in Tables 6-9. Note that the data matrices in theses tables are more complete for the 1050 and 1820 ppmS cases. This is because the 810 ppmS fuel was

used primarily during the sampling apparatus shakedown tests (runs 1–26 of Table 5), to evaluate the impact of cold engine starts and sample dilution on aerosol properties (runs 92 –101 of Table 5), and as an alternate low S fuel when the supply of 1050 ppmS fuel was depleted. Because of these "holes" in 810 ppmS data base, our subsequent discussions will focus primarily upon aerosol characteristics observed when the aircraft was burning the two higher S content fuels.

As noted above, number EIs varied by over three orders of magnitude between individual sampling runs. Upon examining Table 6, we see that, although fuel S content plays a role, engine power and sampling distance are the primary factors that govern this variation. For example, for 1820 ppm S fuel and 1 m sampling case, number EI drops from ~8 x 10^{15} to 0.37 x 10^{15} kg^{-1}, or more than a factor of 20, upon increasing power from idle (1.03 EPR) up to 1.5 EPR (Figure 8). Similarly, for 1820 ppm S and a power setting of 1.5 EPR, number EI increases from ~0.4 x 10^{15} to 14.3 x 10^{15} kg-1, or a factor of 38, between 1 and 35 meters downstream of the engine exit plane. Results from the 1050 ppmS fuel runs exhibited similar trends (Table 6). Measurements carried out by Aerodyne during EXCAVATE suggest a large fraction of the particles present at low engine powers are composed of organic material, thus, it is likely that the decrease in particle number emissions with increasing EPR is caused by more efficient combustion of low volatility fuel components as the engine exhaust gas temperature (EGT) increases from ~355^{o}C at idle to ~630^{o}C at 1.5 EPR. The increasing number concentrations with plume age are also consistent with Aerodyne observations of increasing amounts of organic and sulfate aerosols within the plume as sampling takes place further downstream from the engine.

It is interesting to note that the 810 ppm S fuel cases show much less pronounced age and power dependencies than the other fuels and larger concentrations of aerosols at high engine powers. This possibly suggests that the production soot within the engine and condensation of organic particles in the plume are highly dependent upon the fuel hydrocarbon matrix.

As for mass emissions, except for the idle condition where, as we'll discuss later, the engine emitted variable and sometimes significant amounts of organic aerosols, depending on the temperature history of the combustor, EI values tended to increase with power (Table 7). For example, for 1820 ppm S and 1-m sampling distance, mass EI increased from 64 to 98 mg kg-1 in going from 1.15 to 1.5 EPR (Figure 9). At 25-m sampling distance, this fuel case exhibited a factor-of-two increase in mass EI over the same power range. Indeed, within samples collected at 10, 25, and 35 m under steady-state engine operating conditions, the overall trend was for aerosol mass emissions to increase by a factor of two to three in going from 1.15 EPR to the highest available power setting. This positive correlation between Mass EI and EPR appears to be driven by the tendency of the engine to produce greater amounts of black carbon (BC) aerosols at higher temperatures/engine powers (Table 8; Figure 10). For example, for the1820 ppmS fuel runs, the average BC EI increases from 21 to 98 and 29 to 151 mg kg-1 for power increases from 1.15 to 1.5 in samples collected at 1 and 25 m, respectively. As discussed within the T-38 results section, the higher BC EI's measured in the aged

plumes may be related to lower aerosol losses in the secondary sampling probes or light-scattering from condensed organic or sulfate particles. In any case, from examining the 1 m data in Tables 7 and 8, we deduce that BC accounts for < 10 percent of total aerosol emissions at idle but almost 100 percent for the higher power settings.

Examining the data in Table 7 and Figure 9, we also see that mass EIs increased with plume age, presumably due to condensation of low volatility material as the emissions cooled. For example, for 1820 ppmS fuel and an EPR of 1.4, mMass EI increased from 95 to 247 mg kg^{-1} between samples collected at 1 and 35 m. The 1050 ppmS fuel exhibited the same, factor of two-to-three trend, but age-related enhancements in the 810 ppmS cases were more modest and harder to discriminate because of poor sampling statistics and the fact that much of the low to medium power data was acquired during non-steady state conditions.

The observed anti-correlation between the Number and Mass EIs suggests that particle size increased with engine power; this is supported by the GMD and VMD data shown in Table 8. For example, for 1820 ppmS and 1 m sampling, GMD increased from 20 to 38 nm and the VMD from 45 to 103 nm in going from 1.15 to 1.5 EPR (Figures 11 and 12). Similar trends are seen in the 1050 ppmS data, but again, the 810 ppmS size statistics appear somewhat random which is probably due to the data set for this fuel being heavily biased toward non-steady state sampling conditions.

The GMD data also support the notion that new particles form within the plume as it cools and ages. Note that for 1820 ppmS fuel and 1.5 EPR, GMD decreases from 38 to 27 nm in going from 1 to 25 m downstream of the engine exhaust plane (Figure 11). The age-related changes in mean size were even more dramatic in measurements recorded by the University of Minnesota nanometer aerosol analyzer (nASA), which is sensitive to sizes down to 3 nm (the effective cutoff of the long DMA used to acquire Table 6-8 data was >8 nm); GMD values calculated from its size scans drop to < 12 nm for many of the 35 m samples (see Appendix C of this Report). Individual size distributions of the aged emissions are bimodal in nature and show that the decrease in GMD is caused by the nucleation and growth of aerosols at diameters less than 30 nm (Figure 13). Mass spectrometer measurements suggest these particles are composed of either sulfuric acid or neutralized sulfate. Their large concentrations tend to dominate number EI values; however, they contribute only a few percent to the overall mass loading and produce essentially little change in calculated VMDs (Figure 12). The fact that mass emissions increase by factors of two or more between the 1 and 35 m samples can be partially attributed to low volatility hydrocarbons condensing upon existing black carbon aerosols (Appendix D of the EXCAVATE Report).

A primary EXCAVATE objective was to examine the role that fuel S played in the formation of secondary aerosols within the aircraft exhaust plume. Disregarding data acquired at low power settings (1.03 and 1.15 EPR) where transient emissions of unburned organic compounds biased the statistics, the data shown in Tables 7 and 8 indicate that downstream particle loadings were significantly greater for the 1820 ppmS than 1050 ppmS cases. For example, at 1.3 EPR and a 10 m sampling distance, number

and mass EI values were a factor 3 and ~14 percent greater, respectively, for 1820 ppmS fuel in comparison to the 1050 ppmS fuel. Size distributions recorded at 25 and 35 m indicate the primary difference between the two fuel cases is the relative amplitude of the nucleation mode peak that forms at diameters < 30 nm—it is clearly much larger in the higher fuel S samples. At 25 m sampling distance the greater contribution from nucleation mode aerosols to the number-based size distribution causes the GMD to be shifted to slightly smaller diameters for the 1820 ppmS relative to the 1050 ppmS emissions (Table 8). In contrast, at 35 m GMDs are actually smaller for the lower fuel S cases. Note that between 25 and 35 m and for engine powers of 1.3 and 1.4 EPR, Number EIs increased by factors 3 to 4 in the low S plume, but by < 2 for the high S emissions (Table 7). Also the differences in number EIs between the two fuels are much less at 35 m than at 25 m (20 to 40 percent as opposed to factors of 2 to 3). Thus, it appears that particle formation and growth processes, though highly active in both cases, occur at slower rates in the lower S fuel cases because of the lower saturation ratio of sulfuric acid within the exhaust plume.

Using BC and aerosol mass EI values for the various sampling distance/fuel S combinations, it is possible to estimate the relative contributions of organic and sulfate aerosols to overall aerosol mass loadings. For a power setting of 1.3 EPR, the residual Mass EI (i.e., the difference between total aerosol and BC EI) varies from -20 to 94 mg, and -11 to 138 mg kg-1, for the 1050 and 1820 ppmv, respectively, between the 1 and 35 m sampling distance (Figure 14). Assuming that organic aerosol loadings are identical in the two fuel cases, we calculate that the extra 770 ppmS in the high S fuel enhanced the overall aerosol Mass EI ~44 mg kg^{-1} in the 35 m samples. Using an average sulfate aerosol molecular weight of 150 g $mole^{-1}$ to make allowances for hydration and partial neutralization of sulfuric acid by ambient ammonia or sea salt, the 44 mg kg-1 EI corresponds to a fuel S conversion factor, ε, of ~1.2 percent which is consistent with many previous observations (Schumann et al., 2002). A similar analysis of data recorded at 1.4 EPR yields ε ~0.5 percent at the 35 m sampling distance; this lower value is probably related to the shorter growth period experienced by aerosols in the higher velocity 1.4 EPR plume. Amazingly, if we use the inferred sulfate conversion efficiencies shown in Figure 14 to back-calculate organic aerosol Eis, we obtain exactly the same values at all sampling distances for the two fuels, although the values are negative for the 1 and 10 m cases which indicates that either the aerosols mass density is > 1 g cm^{-3} or that the absorption cross-section for soot is >7 m^2 g^{-1}. If we subtract the 1 m organic aerosol EI from the 35 m value, we find that ~70 mg kg^{-1} of secondary organic particulate matter formed as the 1.3 EPR plume cooled and expanded. This observation is consistent with the simultaneous composition measurements that showed the engine emitted significantly greater quantities of condensed hydrocarbons than of sulfate under steady state conditions (see Aerodyne AMS report).

Plots of inferred sulfate and organic aerosol EI vs distance (Figure 14) also provide information on the relative rates that the two volatile species condense. Note that sulfate aerosol mass increases rapidly between 1 and 10 meters then begins to level off whereas organic aerosol EI continues to increase as the plume ages, which indicates that sulfuric acid is less volatile than many of the organic species that are condensing within the

plume. The steep slope of the curve between 25 and 35 m suggests that significant additional organic aerosol would be formed as the plume undergoes further aging.

As noted above, data acquired at idle and 1.15 EPR were highly variable and depended more on how long the engine had been running, the time since power change, and the details of sample collection than upon the selected test variables of fuel S or plume age. For example, Figure 15 shows a 1-second resolution time-series plot of the RB-211 number EI for 1820 ppmS fuel and samples extracted at 1 and 25 m downstream of the engine exhaust plane. The engine had cooled for ~1 hr prior to the beginning of the record. Note that 1 m values are ~10^{16} kg^{-1} at startup then drift downward by a factor of 5 over the 20 minute run at 1.03 EPR. When power is increased to 1.15 EPR, number EI jumps back up to 10^{-16} kg^{-1}, then begins to drift downward as the engine re-equilibrates to the new fuel flow rates and combustor temperatures, reaching ~10^{15} kg^{-1} just before the power is increased to 1.3 EPR Similar jumps in number EI occurred after each power change, although the subsequent drift was less at the higher EPR settings.

Note that number EI values also took a few minutes to settle down after flow was switched from the 25 m to the 1 m inlet probe (Figure 15). When sample air was drawn from the downstream probe, flow was completely stopped in the 1 m inlet lines trapping a significant volume of air that would, because of diffusion and deposition losses, within a few minutes become essentially particle-free. Thus, we speculate that the initial drop in aerosol number density observed when sampling from the 1 m inlet resumed was caused by dilution with aerosol-depleted air. Changes in temperature may also contribute by causing differential thermophoretic losses as the probe reheated to reach thermal equilibrium with the impinging sample flow.

Transients in the RB-211 aerosol number density emissions were accompanied by equally dramatic changes in mass emissions. Figure 16 displays a 1-minute resolution time-series of mass EI corresponding to the number EI data shown in Figure 15. At engine start, mass EI peaked at ~3000 mg kg-1, then decreased to < 100 mg kg-1 some 10 minutes later. Although a reduction contributed to this change, it was primarily driven by a shift in the number modal diameter from ~100 nm to < 25 nm during this time period (Figure 17 and 18). The power increase from 1.03 to 1.15 EPR produced similar enhancements in mass emissions (and GMD) that required 3 to 4 minutes to settle back down to a steady state value(s). Order-of-magnitude transients also occurred when power was reduced from 1.5 EPR to idle. These observations are consistent with aerosol measurements made by other groups during EXCAVATE [see Appendices B, C, and D] and were found to occur for all fuel types and sampling conditions. To our knowledge, there are no published reports of transient aerosol or gas phase emissions from jet turbines, but it is a well-know phenomena in diesel engines (refs). In terms of an explanation, simultaneous aerosol mass spectral data indicate the transient aerosols were composed of organic species that possessed mass signatures similar to those of engine oil. After cold starts and power changes, it takes a few minutes for the compressor stages to reach thermal equilibrium and establish the very tight component tolerances necessary for optimum engine performance. We speculate that during this thermal adjustment period, a minor amount of engine oil leaks around the seals and produces the observed organic

aerosol enhancements. It is significant to note that the enhancements were present in samples collected at 1 m where the exhaust gas temperature was quite high; this supports the idea that they were composed of relatively nonvolatile species such as those present in thermally stable turbine engine lubricating fluid. It is also possible that a fraction of these particles were derived from unburned fuel, as whole air samples, collected within the plume shortly after engine start, contained significant enhancements in relatively low-molecular weight hydrocarbon species (see Appendix E). Unburned fuel is certainly present within the exhaust just before combustor ignition and may take a few minutes to volatilize and be cleared from the downstream sections of the engine.

4.0. Conclusions

Extensive characterization measurements were made of aerosols collected at various points downstream from the engine exhaust planes of the Langley T-38A and B-757 aircraft. Results indicate these aircraft emit significant quantities of black carbon and that volatile species condense and grow very rapidly within their exhaust plumes as the emissions cool and age.

For the J85-GE engine, aerosol properties in samples collected at 1 m depended upon dilution ratio, particularly for low power settings where high levels of volatile organic species were present. Maintaining constant dilution ratios of 8:1 to minimize coagulation effects, number EIs measured at 1 m sampling distance peaked at idle, decreased monotonically with increasing engine power, and averaged ~3 x 10^{15} kg^{-1} at typical cruise power settings (70-80 percent of maximum RPM) which is comparable to nonvolatile aerosol EI values observed behind the aircraft in flight (Anderson et al., 1999). Mean particle volume diameters increased with combustor temperature ranging from ~48 nm at idle to 66 at takeoff power (100 percent). This produced mass EIs that varied from ~190 to 380 mg kg-1 at the extremes of the power range and averaged ~200 mg kg at cruise settings. Black carbon apparently comprised the greatest fraction of the emissions, contributing ~50 percent at idle and 67 percent at takeoff power. Samples collected 10 and 25 m behind the engine exhibited significantly greater number EIs and slightly increased black carbon EIs. The enhancement in relative aerosol number concentrations is attributed to condensation of sulfate and low volatility organic species. Interestingly, the added material caused the VMD of size distributions observed at 10 m to shift to smaller diameters but produced no noticeable change in GMD, suggesting that the aerosols were simply being added to an already existing, dominant mode. Size distributions recorded 25 m downstream were too variable to provide data to further elucidate this problem. As for the age-dependence in black carbon EI, several factors may have contributed including the uncorrected effects of sulfate aerosol scattering, more efficient sample collection by the downstream probes, and growth of the soot particles to sizes less susceptible to diffusional losses.

The RB211 engine shared the J85-GE's tendency to produce fewer particles of larger size and greater black carbon content with increasing power, but it also displayed a propensity to emit huge quantities of organic aerosols after cold starts or following power changes, particularly within its low power operating range. For steady-state operating conditions

and 1 m sampling, the engine nominally produced between 0.5 and 5 x 10^{15} kg^{-1} across the power range from 1.03 to 1.5 EPR (note that 1.7 EPR is takeoff power) with values of ~10^{15} kg^{-1} typical for cruise power settings of 1.3 to 1.4 EPR. Excluding transient data, GMD and VMD values varied from 20 to 35 and 45 to 100 nm, respectively, between the power extremes and were typically 25 and 85 nm, respectively, for cruise. Stable mass EIs were difficult to delineate for idle conditions because of transient effects, but median values varied from ~50 to 100 mg kg-1 between 1.15 and 1.5 EPR and were typically in the range of 60 to 80 mg kg-1 for cruise power settings. For the 1 m sampling and assuming an aerosol mass density of 1 g cm-3, black carbon accounted for essentially 100 percent of the observed aerosol emissions over the medium to high power operating range.

Levels of volatile particulates within the exhaust plume increased dramatically as it aged. Number EIs depended upon fuel S content and were, for the higher engine powers, factors of 10 to 40 greater at 25 to 35 m downstream in comparison to the 1 m measurements. Corresponding Mass EI enhancements were more moderate but still quite evident. Based partly on simultaneous composition measurements acquired by Aerodyne, we speculate that the increase in aerosol number EI was driven primarily by formation of new sulfate aerosols in the size range below 30 nm, and that increased mass concentrations were caused not only by the condensation of the sulfates but accretion of low volatility organic compounds onto existing soot particles. Contrasting the data acquired using fuels of different sulfur content at a single power settting, we calculated that the 770 ppm higher S content in the 1820 ppmS fuel was responsible for producing >40 mg kg^{-1} of the aerosol mass sampled at 35 m; this corresponds to a fuel S conversion efficiency of 1.2 percent which is comparable to previous observations. Our calculations also showed that organic aerosols contributed at least 70 mg kg^{-1} to the overall mass EI in samples collected at 35 m and that, given the steep increase in organic aerosol loading between the 25 and 35 m sampling distances, volatile organics would most likely continue to condense within the plume as it underwent additional cooling and aging.

Aerosol mass emissions from the RB-211 after cold starts and power changes were significantly greater than observed when the engine was operating at thermal equilibrium. Indeed mass EIs approaching 10 g kg^{-1} were common as the engine idled just after combustor ignition and values exceeding 1 g kg-1 were frequently observed after power was increased from 1.03 to 1.15 EPR or when the engine was rapidly brought back to idle from medium to high power settings. These findings are likely to have significant implications for aircraft operations in terminal areas as every aircraft flown must at some point, undergo a cold start and experience a sometimes large number of brief power surges during taxi to and from passenger loading gates. Current emission models that employ steady-state emission factors are thus likely to severely underestimate actual aerosol concentrations within the aircraft operating areas.

Data and analyses presented within this report will do little to resolve the debate over what aerosol parameters should be measured and what sampling distances should be employed to replace/augment the smoke number standards currently required for

emission qualification for jet turbine engines. The SAE-31 committee has suggested DMA-determined number EIs, GMDs and geometric standard deviations (GSD) of the size distributions as measured in samples extracted from 1 m downstream of the engine exit plane as possible candidates. This study has shown that, even at the close sampling range, number EIs and GMDs are highly variable depending upon fuel composition, power setting, sample dilution, power-change history. We elected not to discuss GSD values because measured size distributions were often multimodal and seldom exhibited simple log-normal characteristics. In addition, samples collected at 1 m fail to provide any information about the more volatile aerosols that condense slightly further downstream and are likely to have equally significant impacts upon local air quality.

5.0. References

Anderson, B. E., et al., 1998: Airborne observations of aircraft aerosol emissions I: Total nonvolatile particle emission indices, Geophys. Res. Let., 25, pp. 1689-1692.

Bond, T. et al., 1999: Calibration and intercomparisons of filter-based measurements of visible light absorption by aerosols, Aero. Sci. Tech., 30, pp. 582-600.

Cofer, W. R., et al., 1997: Calibration and demonstration of a condensation nuclei counting system for airborne measurements of aircraft exhausted particles, Atmospheric Environment, 32, pp. 169-176.

Cofer, R., et al., 2001: Results of the August 1999 Aerosol Measurement Intercomparison Workshop, T-38 aircraft sampling phase, NASA/TM-2001-211226.

Petzold, A., and A. Dopelheuer, 1998: Re-examination of black carbon mass emissions indices of a jet engine, Aero. Sci. Tech., 29, pp. 355-356.

Shumann, U., et al., 2002: Influence of fuel sulfur on the composition of aircraft exhaust plumes: The experiments SULFUR 1-7, J. Geophys. Res., 107, 10.1029/2001JD000813.

Wang, S. and R. Flagan, 1990: Scanning Electrical Mobility Spectrometer, Aero. Sci. Tech., 13, pp. 230-240.

Table 3. Sample Runs Behind Langley T-38A; Particle Statistics Calculated For the Duration of Each Run

Test run	Julian date	Start UT secs	End UT secs	Engine power (EPR)	Distance (m)	Number EI (#/kg)		Black carbon (mg/kg)		Mass EI (mg/kg)		Mode (nm)	GMD (nm)	VMD (nm)
						Avg	Std dev	Avg	Std dev	Avg	Std			
1	22	72660	73100	50	1	3.26E+15	2.91E+14			193	23	24	23	48
2	22	73150	73733	60	1	2.93E+15	1.80E+14			176	6	21	23	51
3	22	73780	74350	70	1	2.79E+15	1.53E+14			194	22	22	24	55
4	22	74470	74970	80	1	2.21E+15	1.15E+14			214	48	24	26	59
5	22	75200	75590	90	1	1.69E+15	4.86E+13			227	153	26	27	61
6	22	75752	76240	100	1	1.78E+15	2.63E+13			386	151	29	32	66
7	22	76390	76543	70	1	2.11E+15	6.40E+13			110	4	21	23	52
8	22	76695	76830	50	1	2.74E+15	5.95E+13			158	7	22	24	51
9	22	77400	77960	50	1	2.87E+15	1.71E+14			181	233	24	24	50
10	22	78060	78510	100	1	1.79E+15	2.90E+13			387	153	30	33	67
11	22	78690	78777	70	1	2.41E+15	9.76E+13			143	19	26	27	59
12	22	78800	79034	50	1	3.08E+15	1.47E+14			178	43	23	24	52
13	24	53160	53415	50	1	5.73E+15	7.35E+14	91	12	172	47	27	25	47
14	24	53446	53800	50	10	1.09E+16	3.12E+15	83	42	376	173	22	23	46
15	24	53880	54180	60	10	1.51E+16	3.34E+15	94	42	224	75	22	23	46
16	24	54380	54770	60	1	3.92E+15	1.16E+14	70	2	105	6	19	21	49
17	24	54800	55095	70	1	3.84E+15	1.36E+14	86	3	116	7	20	22	52
18	24	55120	55710	70	10	1.41E+16	4.40E+15	97	39	191	51	21	21	43
19	24	55830	56110	80	10	6.80E+15	3.32E+15	60	21	169	76	21	22	46
20	24	56190	56625	80	1	2.86E+15	8.02E+13	67	4	102	73	21	23	55
21	24	56780	56930	90	1	3.12E+15	7.51E+13	118	2	203	167	24	27	59
22	24	57055	57540	90	10	4.53E+15	5.60E+14	72	8	152	20	27	26	52
23	24	57580	57930	100	10	4.21E+15	6.88E+14	130	8	244	98	29	29	58
24	24	58030	58475	100	1	4.09E+15	3.08E+14	198	4	246	109	26	27	60
25	24	58572	58770	70	1	2.44E+15	7.88E+13	55	7	60	43	19	22	64
26	24	58840	59370	70	10	4.20E+15	7.66E+14	51	23	106	102	18	21	58
27	24	59440	59640	50	10	2.08E+15	7.22E+14	36	17	46	30	25	25	50
28	24	59750	59960	50	1	1.85E+15	1.60E+13	31	3	40	51	20	21	54
29	29	53000	53295	50	1	1.05E+16	6.66E+14			294	35	27	26	41
30	29	53370	53560	50	1	1.73E+16	2.26E+15	76	37	466	341	27	26	39
31	29	53700	53960	50	1	2.31E+16	7.11E+15	75	6	213	100	18	19	35
32	29	55720	55900	50	1	4.29E+15	1.27E+14	123	19	75	28	61	58	92
33	29	56065	56180	50	10	1.06E+16	1.36E+15	123	17					

Table 3. Concluded

Test run	Julian date	Start UT secs	End UT secs	Engine power (EPR)	Distance (m)	Number EI (#/kg)		Black carbon (mg/kg)		Mass EI (mg/kg)		Mode (nm)	GMD (nm)	VMD (nm)
						Avg	Std dev	Avg	Std dev	Avg	Std			
34	29	56350	56380	50	1	8.97E+15	5.22E+14	114	10					
35	29	56540	56700	60	1	4.48E+15	1.34E+14	89	2	100	16	19	23	49
36	29	56720	56915	60	1	5.83E+15	3.10E+14	65	5	110	14	18	21	48
37	29	56930	57130	60	1	5.73E+15	4.69E+14	19	10	141	117	18	21	48
38	29	57182	57360	60	10	1.05E+16	2.07E+15	143	34	120		18	21	45
39	29	57392	57480	60	25	8.34E+14	1.51E+15	77	31					
40	29	57510	57560	60	1	3.33E+15	7.84E+13	19	7	8		15	19	93
41	29	57650	57795	70	1	3.49E+15	5.86E+13	90	3	78	2	21	23	51
42	29	57830	57995	70	1	3.90E+15	7.15E+13	64	6	98	60	19	23	51
43	29	58024	58216	70	1	4.35E+15	1.32E+14	38	16	95		18	22	51
44	29	58240	58450	70	10	9.12E+15	8.82E+14	159	53	89	4	18	20	47
45	29	58480	58720	70	25	1.13E+16	1.10E+15	118	20	148		23	22	43
46	29	58735	58845	70	1	8.80E+15	4.15E+14	94	6	81		21	21	41
47	29	58930	59080	80	1	2.53E+15	7.74E+13	75	4	70		21	24	52
48	29	59160	59330	80	1	3.04E+15	7.71E+13	53	8	58		21	22	49
49	29	59390	59540	80	1	2.88E+15	6.69E+13	17	8	58	13	21	23	51
50	29	59555	59775	80	10	8.66E+15	1.00E+15	168	76	58		16	21	48
51	29	59790	59965	80	25	1.10E+16	6.86E+14	140	33	126		18	21	43
52	29	60045	60186	90	1	2.93E+15	7.23E+13	104	17	177		24	27	56
53	29	60240	60400	90	1	3.54E+15	1.95E+14	99	9	99		21	24	51
54	29	60430	60620	90	1	3.93E+15	1.57E+14	76	19	105		21	23	50
55	29	60670	60865	90	10	5.19E+15	4.34E+14	174	57	92		18	23	51
56	29	60885	61060	90	25	9.52E+15	4.24E+14	173	50	135		18	22	47
57	29	61124	61161	90	1	2.47E+15	3.53E+13	90	7					
58	29	61200	61345	100	1	3.78E+15	4.99E+13	307	7	228		29	29	59
59	29	61400	61590	100	1			275	9	280	45	29	28	59
60	29	61600	61840	100	1			270	16	223	11	25	28	59
61	29	61930	62105	100	10	6.57E+15	7.28E+14	400	53	253		25	26	57
62	29	62130	62330	100	25	6.03E+15	2.15E+14	371	37	294	367	25	28	60
63	29	62390	62615	70	1	6.77E+15	4.87E+14	82	8	100	62	21	23	52
64	29	62660	62900	60	25	5.57E+15	3.29E+15	81	54	75	44	18	20	48
65	29	62914	62960	60	10	6.97E+15	1.26E+15	64	18	26		21	20	32
66	29	62960	63300	50	10	6.59E+15	1.60E+15	76	35	69	26	18	21	51

Table 4. Aerosol Statistics From T-38A Runs

Probe distance (m)	Engine power %	Number scans	Number EI (#/kg)			Mass EI (mg/kg)			GMD (nm)			VMD (nm)			BC EI (mg/kg)		
			Avg	Med	Sigma	Avg	Med	Sigma	Avg	Med	Sigma	Avg	Med	Sigma	Avg	Med	Sigma
1	50	4	7.3E+15	4.0E+15	6.4E+15	193	178	55	23	24	2	48	48	5	85	84	33
	60	6	4.2E+15	4.1E+15	1.1E+15	176	141	137	21	23	2	51	51	6	52	65	32
	70	10	3.9E+15	3.6E+15	2.0E+15	194	156	125	22	23	2	55	55	35	73	82	21
	80	4	2.6E+15	2.7E+15	2.7E+14	214	107	55	24	22	2	59	59	5	53	60	26
	90	5	2.8E+15	3.0E+15	7.1E+14	227	120	78	25	21	3	61	61	19	98	99	15
	100	6	2.4E+15	2.0E+15	1.5E+15	386	145	145	30	23	5	66	66	9	262	272	46
10	50	4	7.1E+15	8.2E+15	3.9E+15	376	163	52	23	23	3	46	46	7	79	79	36
	60	3	1.0E+16	1.0E+16	3.8E+15	224	105	108	23	23	4	46	46	9	100	94	40
	70	3	8.6E+15	8.7E+15	4.7E+15	191	92	28	21	21	2	43	43	5	102	97	54
	80	2	7.3E+15	7.3E+15	1.2E+15	169	96	55	22	22	1	46	46	1	114	114	77
	90	1	4.6E+15	4.6E+15	4.7E+14	152	58	0	26	26	0	52	52	0	123	123	73
	100	2	5.1E+15	5.1E+15	1.6E+15	244	143	120	29	29	6	58	58	8	265	265	191
25	60	2	7.1E+15	7.1E+15	4.8E+15	161	161	130	23	23	4	54	54	4	79	79	3
	70	1	1.4E+16	1.4E+16		294	294	0	28	28	0	60	60	0	118	118	
	80	1	1.3E+16	1.3E+16		100	100	0	23	23	0	52	52	0	140	140	
	90	1	1.1E+16	1.1E+16		75	75	0	20	20	0	48	48	0	173	173	
	100	1	7.0E+15	7.0E+15		26	26	0	20	20	0	32	32	0	371	371	

Table 5. Sample Runs Behind Langley B-757; Particle Statistics Calculated For the Last 60 Seconds of Each Run

Test run	Julian date	Start UT secs	End UT secs	Engine power (EPR)	Distance (m)	Fuel S (ppm)	Number EI (#/kg)		Black carbon (mg/kg)		Mass EI (mg/kg)		Mode (nm)	GMD (nm)	VMD (nm)
							Avg	Std dev	Avg	Std dev	Avg	Std			
1	25	59128	59149	1.1	1	810	9.9E+15	6.5E+14	16	1					
2	25	59170	59233	1.15	1	810	8.9E+15	4.0E+14	23	2	634	0	44	41	53
3	25	59260	59295	1.2	1	810	7.0E+15	5.0E+14	35	1	627	0	44	39	55
4	25	59310	59365	1.25	1	810	4.7E+15	4.0E+14	50	2	174	43	28	30	45
5	25	59382	59446	1.03	1	810	1.4E+16	2.7E+15	12	3	290	0	28	26	40
6	25	60280	60336	1.03	1	810	1.1E+16	1.4E+15	53						
7	25	60370	60404	1.25	1	810	5.2E+15	2.2E+14							
8	25	60480	60550	1.3	1	810	5.8E+15	1.9E+14	3		201	31	24	27	49
9	25	60565	60613	1.35	1	810	5.0E+15	9.8E+13			119	0	24	25	49
10	25	60630	60650	1.4	1	810	4.4E+15	5.1E+13							
11	25	60709	60755	1.45	1	810	4.6E+15	2.9E+14			180	34	20	23	71
12	25	60770	60818	1.5	1	810	3.8E+15	4.3E+14	6	5	137	166	20	22	68
13	25	60955	61110	1.03	1	810	3.5E+16	1.4E+15	6	4	931	0	31	29	36
14	25	68400	68464	1.03	10	810	8.8E+15	1.0E+15	9	6	30	11	28	38	91
15	25	68480	68536	1.1	10	810	8.0E+15	6.0E+14	23	3	473	115	45	40	52
16	25	68550	68680	1.15	10	810	4.1E+15	1.0E+15	22	4	1029	1196	53	44	59
17	25	68720	68850	1.2	10	810	4.1E+14	9.0E+13	13	4	35	0	21	22	53
18	25	70407	70483	1.03	10	810	3.2E+16	2.2E+15	111	80	217	126	101	76	103
19	25	70488	70515	1.1	10	810	1.9E+16	1.1E+15	218	18					
20	25	70527	70555	1.15	10	810	1.4E+16	7.9E+14	47	2	1171	0	53	53	66
21	25	70565	70585	1.2	10	810	9.9E+15	3.3E+14	81	0					
22	25	70601	70620	1.25	10	810	1.2E+16	2.6E+14	95	1					
23	25	70627	70687	1.3	10	810	9.7E+15	6.2E+14	109	3	3706	0	62	63	95
24	25	70696	70726	1.35	10	810	7.6E+15	1.3E+14	114	1	846	163	53	47	62
25	25	70734	70752	1.4	10	810	6.6E+15	1.2E+14	123	1					
26	25	70990	71126	1.03	10	810	1.1E+16	3.4E+14	22	7	1211	841	54	63	101
27	26	52669	52839	1.03	1	1050	1.1E+15	3.6E+14	8	5	27	8	22	22	40
28	26	52858	53191	1.03	1	1050	1.7E+15	5.1E+13	5	1	76	54	28	27	36
29	26	53223	53566	1.03	25	1050	4.4E+15	6.9E+14	3	2	81	10	24	22	33
30	26	53595	53691	1.03	1	1050	1.7E+15	1.1E+14	5	1	27	21	24	22	37
31	26	53772	54254	1.15	1	1050	1.9E+15	1.3E+14	25	2	35	13	16	17	42
32	26	54265	54620	1.15	25	1050	6.4E+15	3.4E+14	19	3	79	24	19	19	47
33	26	54670	55110	1.3	1	1050	1.2E+15	1.1E+14	63	2	62	15	13	16	71

Table 5. Continued

Test run	Julian date	Start UT secs	End UT secs	Engine power (EPR)	Distance (m)	Fuel S (ppm)	Number EI (#/kg)		Black carbon (mg/kg)		Mass EI (mg/kg)		Mode (nm)	GMD (nm)	VMD (nm)
							Avg	Std dev	Avg	Std dev	Avg	Std			
34	26	55121	55455	1.3	25	1050	3.8E+15	1.6E+14	108	4	159	35	13	17	91
35	26	55474	55555	1.3	1	1050	7.9E+14	8.0E+13	63	1	37	7	13	18	92
36	26	55590	56068	1.4	1	1050	1.1E+15	1.9E+14	84	1	82	24	11	17	86
37	26	56080	56415	1.4	25	1050	2.6E+15	5.8E+14	141	6	192	54	13	20	100
38	26	56434	56490	1.4	1	1050	4.2E+14	1.0E+14	85	1	46	12	13	20	100
39	26	56513	56705	1.5	1	1050	6.7E+14	1.3E+14	87	1	84	3	38	31	92
40	26	56715	56810	1.5	25	1050	2.6E+15	2.7E+14	146	3	267	204	38	31	94
41	26	56822	57150	1.03	25	1050	6.0E+16	3.2E+16	73	29	5783	5218	45	42	55
42	26	59320	59620	1.03	1	1820	4.0E+15	5.3E+14	73	29	1984	1494	57	57	73
43	26	59645	59990	1.03	1	1820	4.9E+15	1.8E+15	2	1	70	18	24	23	31
44	26	60003	60358	1.03	25	1820	1.7E+16	8.0E+14	1	0	212	86	21	19	28
45	26	60404	60472	1.03	1	1820	2.4E+15	2.4E+14	10	2	17	19	21	18	28
46	26	60535	60961	1.15	1	1820	2.7E+15	3.8E+14	14	3	69	13	19	19	34
47	26	60973	61310	1.15	25	1820	1.1E+16	2.3E+14	26	6	154	27	18	19	39
48	26	61340	61408	1.15	1	1820	8.6E+14	2.2E+14	11	1	37	15	18	19	39
49	26	61443	61910	1.3	1	1820	1.3E+15	5.8E+13	56	1	61	13	13	17	73
50	26	61928	62156	1.3	25	1820	6.6E+15	4.7E+14	98	8	205	39	18	19	76
51	26	62171	62330	1.3	1	1820	3.2E+14	1.8E+13	56	2	49	12	27	25	81
52	26	62370	62760	1.4	1	1820	7.5E+14	1.6E+14	81	1	83	26	10	21	90
53	26	62765	63120	1.4	25	1820	9.2E+15	2.8E+14	139	5	230	101	15	18	86
54	26	63185	63250	1.4	1	1820	4.7E+14	5.4E+13	60	3	128	38	18	21	74
55	26	63255	63430	1.5	1	1820	7.3E+14	5.8E+13	89	1	95	28	42	36	101
56	26	63437	63565	1.5	25	1820	8.9E+15	8.9E+14	147	5	325	200	27	25	96
57	26	63600	63795	1.03	25	1820	5.3E+16	3.1E+16	96	32	4306	504	42	39	54
58	26	63836	63891	1.03	1	1820	1.3E+16	4.3E+14	88	24	1229	486	53	44	59
59	26	71543	71583	1.03	1	1820	1.4E+16	1.5E+15	11	5	186	209	46	45	66
60	26	71603	72230	1.03	1	1820	7.0E+15	1.9E+14	5	1	214	196	32	30	38
61	26	72245	72589	1.03	25	1820	2.7E+16	5.0E+15	8	7	217	42	21	20	30
62	26	72624	72691	1.03	1	1820	4.9E+15	3.1E+14	11	2	41	49	21	20	30
63	26	72768	73195	1.15	1	1820	4.2E+15	3.9E+14	33	7	117	23	21	21	41
64	26	73208	73437	1.15	25	1820	2.0E+16	1.8E+15	32	3	183	61	19	19	43
65	26	73460	73622	1.15	1	1820	1.5E+15	5.0E+13	28	2	33	10	14	21	67
66	26	73652	74166	1.3	1	1820	7.1E+14	3.9E+13	91	2	88	27	22	25	87

Table 5. Continued

Test run	Julian date	Start UT secs	End UT secs	Engine power (EPR)	Distance (m)	Fuel S (ppm)	Number EI (#/kg)		Black carbon (mg/kg)		Mass EI (mg/kg)		Mode (nm)	GMD (nm)	VMD (nm)
							Avg	Std dev	Avg	Std dev	Avg	Std			
67	26	74176	74460	1.3	25	1820	9.2E+15	1.8E+14	111	3	206	36	18	19	80
68	26	74447	74547	1.3	1	1820	4.8E+14	1.7E+13	86	3	53	8	18	19	79
69	26	74572	74997	1.4	1	1820	4.2E+14	2.2E+13	100	2	98	11	39	36	95
70	26	75001	75336	1.4	25	1820	7.3E+15	1.7E+14	144	3	224	53	15	18	93
71	26	75380	75471	1.4	1	1820	1.0E+14	3.1E+12	99	2	72	19	15	19	92
72	26	75481	75664	1.5	1	1820	1.3E+14	9.1E+13	106	1	101	16	46	40	105
73	26	75674	75794	1.5	25	1820	7.2E+15	2.2E+14	154	6	291	109	31	28	105
74	26	75811	75917	1.03	25	1820	5.3E+16	2.4E+16	53	45	695	292	15	18	103
75	26	75950	76351	1.03	1	1050	7.8E+15	3.0E+14	20	12	1622	822	50	50	74
76	26	76393	76515	1.03	1	1050	5.6E+15	1.1E+14	1	0	433	367	36	35	53
77	26	77000	77155	1.03	1	1050	1.5E+15	5.0E+13			10	13	15	20	49
78	26	77225	77535	1.15	1	1050	5.8E+15	7.1E+14	33	7	220	84	25	24	40
79	26	77543	77836	1.15	25	1050	1.0E+16	6.2E+14	26	4	89	0	15	16	60
80	26	77860	77902	1.15	1	1050	8.4E+14	5.6E+13	27	2	24	13	15	16	65
81	26	77913	78238	1.3	1	1050	5.3E+14	2.5E+13	100	1	100	41	22	24	89
82	26	78250	78548	1.3	25	1050	3.3E+15	4.5E+14	105	3	171	50	13	20	102
83	26	78563	78650	1.3	1	1050	1.1E+14	7.9E+12	98	1	46	10	13	21	104
84	26	78673	79029	1.4	1	1050	1.4E+14	9.6E+13	102	1	101	31	39	39	98
85	26	79039	79311	1.4	25	1050	2.7E+15	4.5E+14	139	3	206	0	13	22	108
86	26	79325	79355	1.4	1	1050	1.1E+14	7.2E+12	91	3	58	20	13	23	108
87	26	79419	79564	1.5	1	1050	2.8E+14	1.2E+14	100	1	85	20	46	40	96
88	26	79573	79717	1.5	25	1050	2.8E+15	8.1E+13	151	5	266	195	29	32	109
89	26	80000	80275	1.03	1	1050	1.1E+16	2.2E+15	33	21	3722	3265	77	70	91
90	26	80340	80430	1.03	25	1050	1.8E+16	3.2E+15			4172	444	52	47	62
91	26	80726	80764	1.03	1	1050	1.1E+15	2.5E+14	22	6					
92	27	49455	49585	1.03	1	810	1.9E+15	5.8E+14	11	6	57	2	27	27	42
93	27	49627	49664	1.03	1	810	2.9E+15	8.2E+14	10	0	13	5	21	23	40
94	27	49734	50050	1.03	1	810	1.1E+16	2.5E+14	11	1	122	152	24	22	30
95	27	50120	50488	1.03	1	810	1.0E+16	3.5E+14	3	2	27	26	14	14	26
96	27	50537	50745	1.03	1	810	1.8E+15	3.8E+14			7	2	18	20	48
97	27	50827	51145	1.03	1	810	6.6E+15	2.5E+14	9	1	56	78	20	20	27
98	27	51295	51652	1.3	1	810	1.8E+15	2.7E+14	73	2	76	13	14	17	69
99	27	51760	51974	1.3	1	810	4.4E+14	1.2E+13	66	2	67	10	30	32	76

Table 5. Continued

Test run	Julian date	Start UT secs	End UT secs	Engine power (EPR)	Distance (m)	Fuel S (ppm)	Number EI (#/kg)		Black carbon (mg/kg)		Mass EI (mg/kg)		Mode (nm)	GMD (nm)	VMD (nm)
							Avg	Std dev	Avg	Std dev	Avg	Std			
100	27	52085	52320	1.3	1	810	4.4E+14	1.1E+13	62	3	66	25	33	32	76
101	27	52540	52733	1.03	1	810	1.4E+16	2.1E+15	30	11	9027	26228	80	74	98
102	27	55323	56580	1.03	10	1050	6.9E+15	4.5E+14	17	13	49	9	18	18	28
103	27	56594	56750	1.03	35	1050	3.6E+16	1.1E+16	19	4	130	156	17	17	29
104	27	56780	56975	1.03	10	1050	1.2E+16	3.0E+15	35	18	445	601	27	25	34
105	27	56913	57184	1.15	10	1050	6.4E+14	7.0E+13	33	2	53	16	12	17	63
106	27	57198	57433	1.15	35	1050	2.2E+16	1.1E+15	31	5	149	47	17	17	41
107	27	57460	57573	1.15	10	1050	4.0E+14	7.9E+12	24	3	51	7	15	20	63
108	27	57690	57904	1.3	10	1050	6.7E+14	1.4E+13	114	3	126	8	39	33	86
109	27	57917	58260	1.3	35	1050	1.2E+16	6.5E+14	104	5	199	31	15	16	78
110	27	58283	58340	1.3	10	1050	6.2E+14	3.3E+13	97	2					
111	27	58385	58505	1.4	10	1050	5.5E+14	1.5E+13	137	4	130	3	36	35	86
112	27	58526	58710	1.4	35	1050	1.1E+16	2.5E+14	146	5	237	146	15	17	85
113	27	58756	58856	1.03	35	1050	8.5E+16	7.2E+15	42	6	758	394	15	17	91
114	27	58905	59034	1.03	10	1050	3.3E+16	2.0E+15	35	5	4466	5772	54	48	63
115	27	64630	65075	1.03	10	1820	1.9E+16	8.2E+14	10	6	258	63	26	24	30
116	27	65096	65537	1.03	35	1820	3.6E+16	3.3E+15	9	5	261	45	21	19	29
117	27	65600	65710	1.03	10	1820	1.1E+16	2.9E+14	9	1	52	71	19	18	29
118	27	65780	66050	1.15	10	1820	9.2E+14	1.8E+14	20	13	83	35	16	16	49
119	27	66176	66318	1.15	35	1820	1.3E+16	4.0E+14	27	4	224	70	19	19	38
120	27	66340	66513	1.15	10	1820	4.4E+14	1.8E+13	8	5	53	22	25	24	58
121	27	66535	66870	1.3	10	1820	6.0E+14	1.4E+13	99	6	124	23	33	34	89
122	27	66890	67162	1.3	35	1820	1.7E+16	4.6E+14	100	6	237	56	18	18	63
123	27	67186	67257	1.3	10	1820	5.9E+14	4.1E+13	50	12	174	32	18	19	63
124	27	67273	67438	1.4	10	1820	5.0E+14	9.4E+12	122	5	118	19	36	35	93
125	27	67460	67640	1.4	35	1820	1.4E+16	4.1E+14	140	7	238	79	18	18	68
126	27	67705	67800	1.03	10	1820	7.0E+16	2.0E+16	144	13	122	55	29	26	45
127	27	68080	68256	1.03	10	810	2.0E+16	2.0E+15	144	13	1172	1177	36	33	43
128	27	68270	68674	1.03	35	810	2.5E+16	1.8E+15	4	4	114	17	18	17	33
129	27	68707	68791	1.03	10	810	3.4E+15	2.2E+14			35	12	15	16	34
130	27	68965	69235	1.15	10	810	3.4E+14	1.1E+13	25	7	37	2	27	29	81
131	27	69259	69359	1.15	35	810	1.1E+16	2.9E+14	45	8	73	17	29	30	84
132	27	69377	69538	1.15	10	810	3.5E+15	4.3E+14	18	7	49	19	17	16	72

Table 5. Concluded

Test run	Julian date	Start UT secs	End UT secs	Engine power (EPR)	Distance (m)	Fuel S (ppm)	Number EI (#/kg)		Black carbon (mg/kg)		Mass EI (mg/kg)		Mode (nm)	GMD (nm)	VMD (nm)
							Avg	Std dev	Avg	Std dev	Avg	Std			
133	27	69564	69926	1.3	10	810	5.6E+14	1.3E+13	93	31	115	18	34	35	91
134	27	70020	70248	1.3	35	810	4.5E+15	1.1E+14	38	34	165	22	13	18	99
135	27	70272	70314	1.3	10	810	5.6E+14	1.1E+13			0	0			
136	27	70326	70482	1.4	10	810	4.9E+14	1.1E+13	38	34	127	6	43	37	95
137	27	70504	70687	1.4	35	810	4.2E+15	9.8E+13	14	10	187	166	13	19	105
138	27	70745	71436	1.03	10	1820	1.4E+16	9.6E+14	13	15	508	89	31	29	38
139	27	71458	71712	1.03	35	1820	3.6E+16	3.0E+15	5	4	228	26	21	19	30
140	27	71733	71834	1.03	10	1820	1.8E+16	9.0E+14	5	2	120	189	21	19	31
141	27	71976	72308	1.15	10	1820	5.2E+14	4.2E+13	29	5	41	15	29	28	80
142	27	72330	72532	1.15	35	1820	2.3E+16	5.5E+14	31	6	167	41	20	20	45
143	27	72560	72588	1.15	10	1820	4.6E+14	4.5E+13							
144	27	72620	72896	1.3	10	1820	2.4E+15	1.1E+14	104	2	139	14	25	25	86
145	27	72939	73212	1.3	35	1820	1.5E+16	2.9E+14	96	5	235	48	18	19	66
146	27	73242	73325	1.3	10	1820	9.7E+14	4.7E+13	88	3	106	13	20	23	82
147	27	73365	73503	1.4	10	1820	1.2E+15	8.7E+13	119	3	144	6	36	32	87
148	27	73526	73704	1.4	35	1820	1.4E+16	2.9E+14	133	6	255	167	20	21	76
149	27	73764	74020	1.03	10	1820	3.9E+16	1.5E+16	74	22	5433	0	66	59	76

Table 6. Summary of B-757 Particle Number Emission Indices

Sample probe distance (m)	Engine pressure ratio (EPR)	810 ppm fuel sulfur number EI x 1e15				1050 ppm fuel sulfur number EI x 1e15				1820 ppm fuel sulfur number EI x 1e15			
		N	Average	Median	Sigma	N	Average	Median	Sigma	N	Average	Median	Sigma
1	1.03	10	11.16	10.44	9.67	8	4.14	1.78	3.89	7	8.01	7.89	4.58
	1.15	1	8.83	8.83		3	5.85	4.12	6.07	4	3.80	3.88	3.07
	1.3	4	3.03	2.89	2.99	4	1.05	0.95	0.87	4	1.81	1.78	1.55
	1.4	1	4.40	4.40		4	0.60	0.27	0.78	4	0.49	0.48	0.33
	1.5	1	3.79	3.79		2	0.51	0.51	0.33	2	0.37	0.37	0.35
10	1.03	5	15.55	11.60	11.11	3	21.21	18.60	14.46	6	27.53	26.25	14.95
	1.15	4	5.98	4.61	5.86	2	1.52	1.52	1.56	4	2.91	1.04	4.17
	1.3	3	3.65	0.66	5.26	2	0.71	0.71	0.13	4	1.08	0.79	0.72
	1.4	2	3.54	3.54	4.31	1	0.55	0.55		2	0.89	0.89	0.56
25	1.03					3	26.06	21.00	24.60	4	39.03	38.40	19.74
	1.15					2	8.41	8.41	4.09	2	16.30	16.30	5.80
	1.3					2	3.92	3.92	0.13	2	8.69	8.69	1.39
	1.4					2	2.90	2.90	0.02	2	8.52	8.52	1.51
	1.5					2	2.94	2.94	0.08	2	8.15	8.15	1.43
35	1.03	1	26.3	26.3		2	57.70	57.70	30.97	2	37.90	37.90	1.13
	1.15	1	11.20	11.20		1	22.80	22.80		2	18.30	18.30	6.51
	1.3	1	4.65	4.65		1	12.80	12.80		2	16.25	16.25	1.34
	1.4	1	4.24	4.24		1	10.70	10.70		2	14.30	14.30	

Table 7. B-757 Aerosol Emission Indices Derived From DMA Scans Using Aerosol Mass Density of 1 g/cm3

Sample probe distance (m)	Engine pressure ratio (EPR)	810 ppm fuel sulfur aerosol EI (mg/kg)				1050 ppm fuel sulfur aerosol EI (mg/kg)				1820 ppm fuel sulfur aerosol EI (mg/kg)			
		N	Average	Median	Sigma	N	Average	Median	Sigma	N	Average	Median	Sigma
1	1.03	9	1170	57	2961	7	845	76	1395	7	534	186	768
	1.15	1	634	634	0	3	93	35	110	4	64	53	39
	1.3	4	102	71	66	4	61	54	28	4	63	57	18
	1.4	1	137	137	0	4	72	70	25	4	95	90	24
	1.5					2	84	84	1	2	98	98	4
10	1.03	5	533	217	606	3	1653	445	2444	6	1082	190	2138
	1.15	4	572	539	613	2	52	52	1	4	44	47	34
	1.3	2	1911	1911	2539	1	126	126	0	4	136	131	29
	1.4	1	127	127	0	1	130	130	0	2	131	131	18
25	1.03					3	3345	4172	2939	4	1358	456	1979
	1.15					2	84	84	8	2	168	168	21
	1.3					2	165	165	9	2	206	206	1
	1.4					2	199	199	10	2	227	227	5
	1.5					2	266	266	1	2	308	308	25
35	1.03	1	114	114	0	2	444	444	444	2	245	245	23
	1.15	1	73	73	0	1	149	149	0	2	195	195	40
	1.3	1	165	165	0	1	199	199	0	2	236	236	2
	1.4	1	187	187	0	1	237	237	0	2	247	247	12

Table 8. B-757 Black Carbon Emission Indices Derived From Particle Soot Absorption Spectrometer Data Using Absorption Efficiency of 7 m2/g

Sample probe distance (m)	Engine pressure ratio (EPR)	810 ppm fuel sulfur Black carbon EI (mg/kg)				1050 ppm fuel sulfur Black carbon EI (mg/kg)				1820 ppm fuel sulfur Black carbon EI (mg/kg)			
		N	Average	Median	Sigma	N	Average	Median	Sigma	N	Average	Median	Sigma
1	1.03	9	16	11	16	7	13	8	12	7	29	11	36
	1.15					3	28	27	4	4	21	21	11
	1.3	4	51	64	32	4	81	81	21	4	72	71	19
	1.4					4	91	88	8	4	85	90	19
	1.5					2	93	93	9	2	98	98	11
10	1.03	4	72	67	66	3	29	35	11	6	42	12	56
	1.15	4	28	24	13	2	29	29	7	3	19	20	10
	1.3	2	101	101	17	2	106	106	12	4	85	93	24
	1.4	2	80	80	60	1	137	137	4	2	120	120	4
25	1.03					2	38	38	49	4	40	30	44
	1.15					2	22	22	5	2	29	29	5
	1.3					2	106	106	4	2	105	105	9
	1.4					2	140	140	5	2	142	142	4
	1.5					2	148	148	4	2	151	151	5
35	1.03	1	4	4	4	2	30	30	16	2	7	7	4
	1.15	1	45	45	8	1	31	31	5	2	29	29	5
	1.3	1	38	38	33	1	104	104	5	2	98	98	6
	1.4					1	146	146	5	2	137	137	7

Table 9. Summary of B-757 Geometric Mean and Volume Mean Diameters Derived From DMA Over 9 to 240 nm Size Range

Sample probe distance (m)	Engine pressure ratio (EPR)	810 ppm fuel sulfur nanometers					1050 ppm fuel sulfur nanometers					1820 ppm fuel sulfur nanometers				
		N	GMD	Sigma	VMD	Sigma	N	GMD	Sigma	VMD	Sigma	N	GMD	Sigma	VMD	Sigma
1	1.03	9	28	18	43	22	7	35	19	54	21	7	34	15	46	19
	1.15	1	41	0	53	0	3	19	5	49	14	4	20	1	45	15
	1.3	4	27	7	68	13	4	20	3	89	14	4	21	4	80	6
	1.4						4	25	10	98	9	4	24	8	88	9
	1.5	1	22	0	68	0	2	35	6	94	3	2	38	3	103	3
10	1.03	5	45	24	74	33	3	30	16			6	29	15	42	18
	1.15	4	36	16	69	9	2	19	2			3	23	6	63	16
	1.3	2	49	20	93	3	1	33	0			4	25	7	80	12
	1.4	1	37	0	95	0	1	35	0			2	34	2	90	4
25	1.03						3	37	13	50	15	4	24	10	53	35
	1.15						2	17	2	54	10	2	19	0	41	3
	1.3						2	19	2	97	8	2	19	0	78	3
	1.4						2	21	1	104	6	2	18	0	89	5
	1.5						2	32	1	101	10	2	27	2	101	6
35	1.03	1	17	0	33	0	2	17	0	60	44	2	19	0	30	1
	1.15	1	30	0	84	0	1	17	0	41	0	2	20	1	42	5
	1.3	1	18	0	99	0	1	16	0	78	0	2	19	0	64	2
	1.4	1	19	0	105	0	1	17	0	85	0	2	20	2	72	5

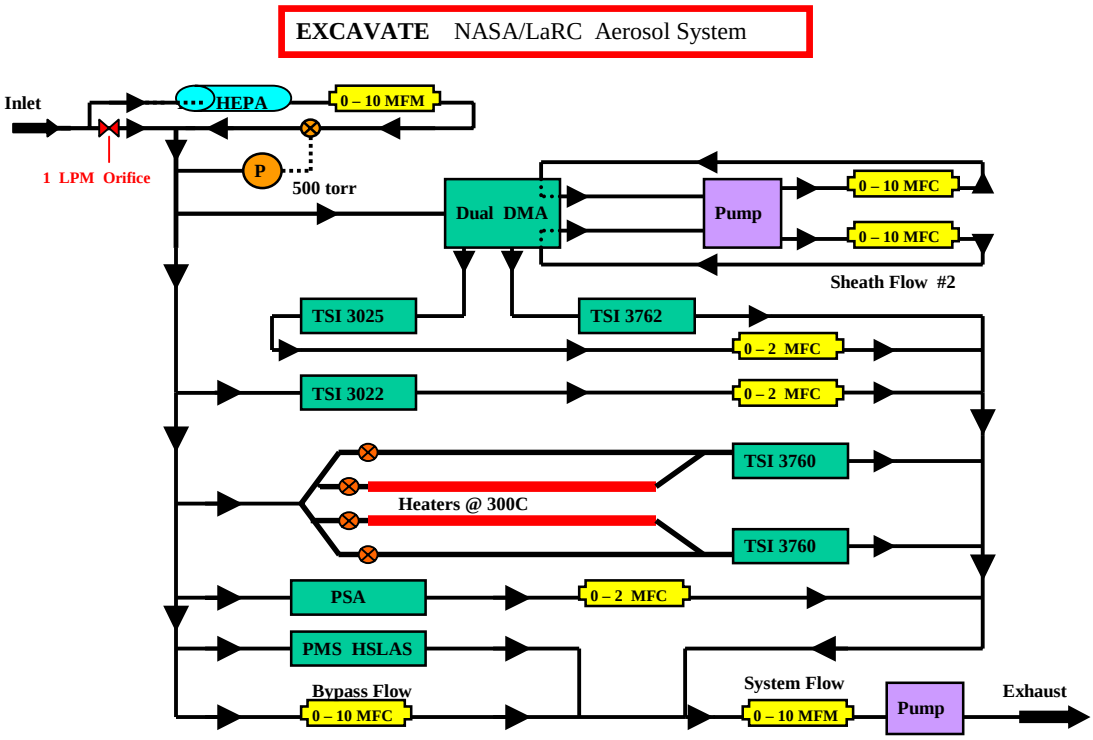

Figure 1. Diagram of LaRC aerosol sampling system as deployed during EXCAVATE. All interconnecting tubing was composed of either stainless steel or conductive flexible tubing. The system was operated at 500 Torr pressure and filtered air flow was typically 10 times greater than sample flow producing a ~10:1 sample dilution ratio.

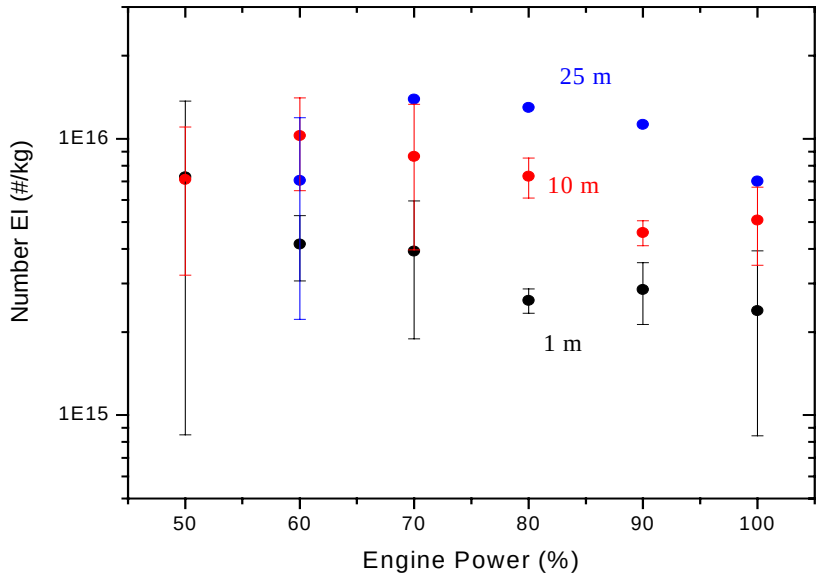

Figure 2. Number EI values measured at 1, 10 and 25 m behind J85-GE engine on LaRC T-38A aircraft. Values are derived from data recorded during last 60-seconds of each sample run.

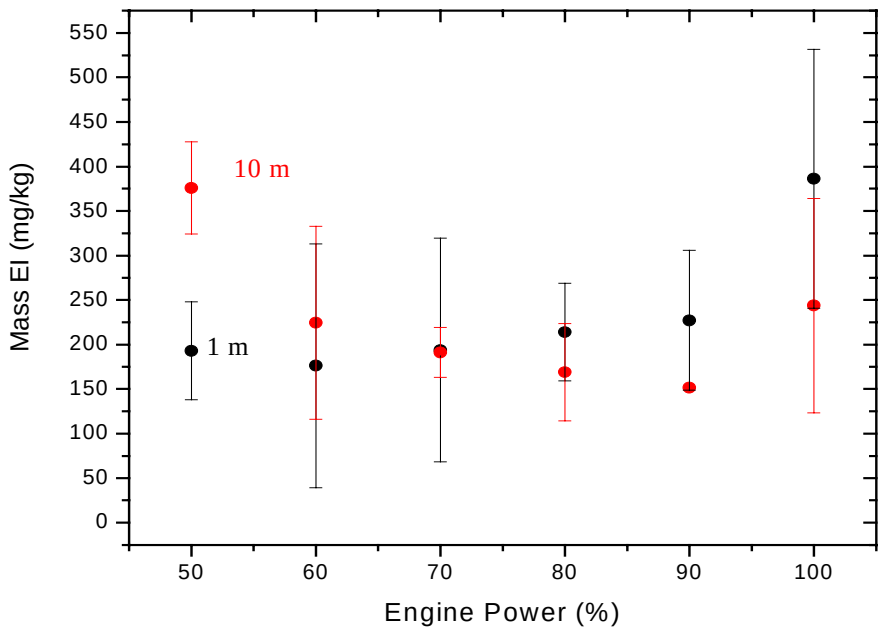

Figure 3. Aerosol mass EI values derived from DMA size distribution scans performed on samples collected at 1 and 10 m behind T-38A exhaust plane.

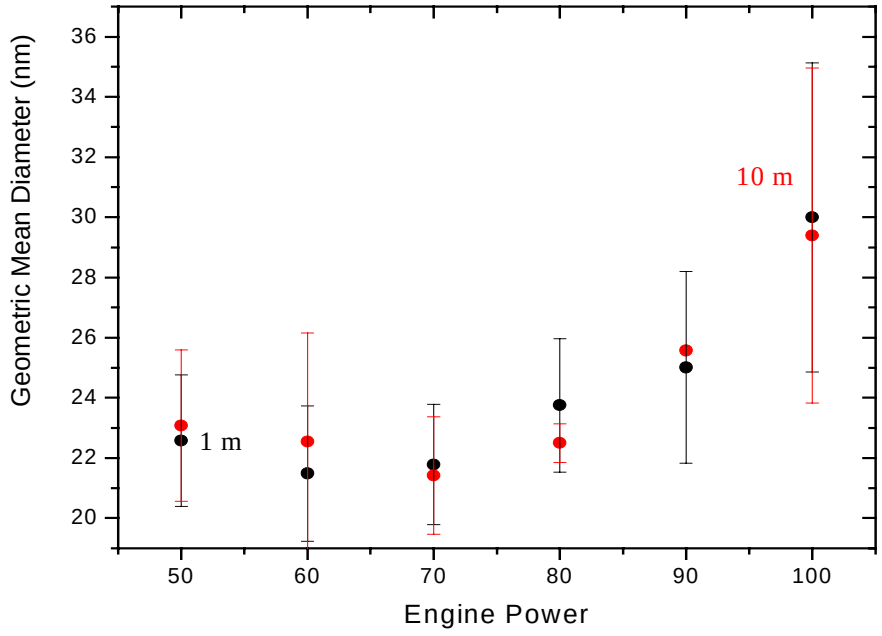

Figure 4. Geometric mean diameters derived from DMA size distribution scans performed on samples collected at 1 and 10 m behind T-38A exhaust plane.

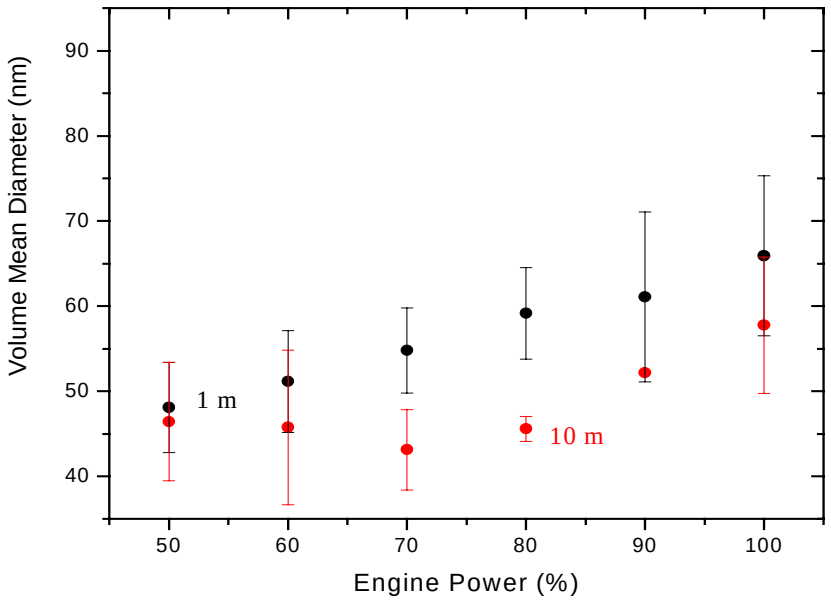

Figure 5. Geometric mean diameters derived from DMA size distribution scans performed on samples collected at 1 and 10 m behind T-38A exhaust plane.

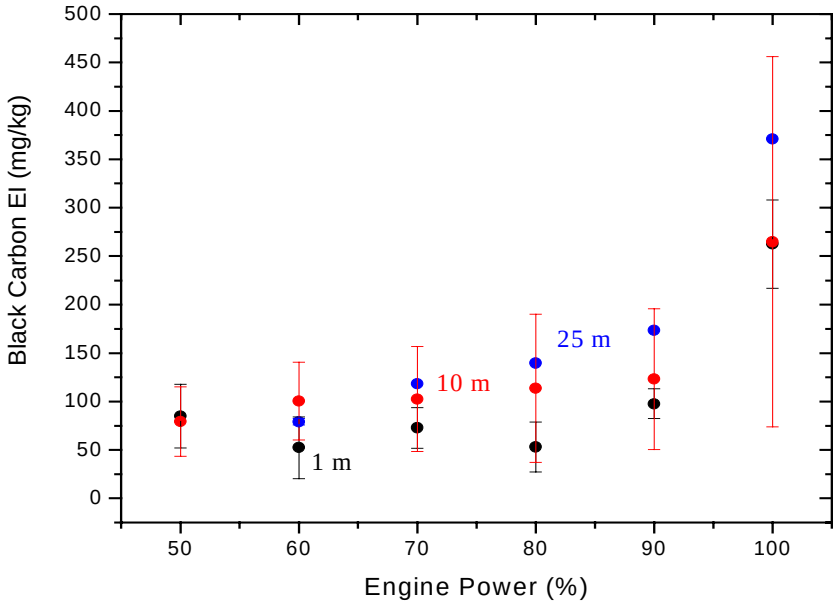

Figure 6. Black carbon EI as determined by PSAP measurements performed on samples collected at 1, 10, and 25 m behind T-38 engine exhaust plane. Values were calculated assuming mass absorption coefficient of 7 m^2g^{-1}.

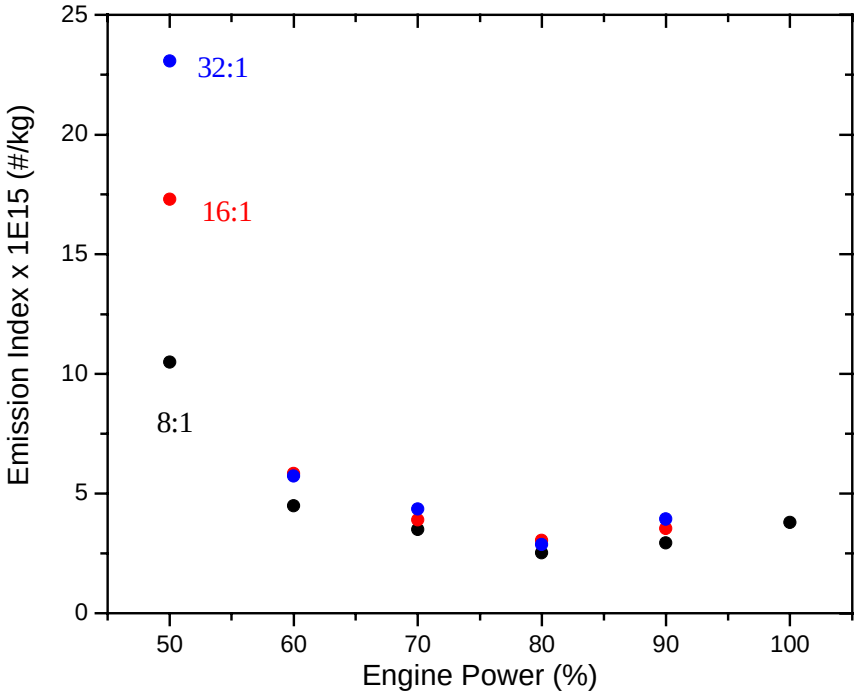

Figure 7. Aerosol number EI values for samples collected 1 m behind T-38 using dilution ratios of 8:1, 16:1 and 32:1, as determined from CO_2 mixing ratio measurements.

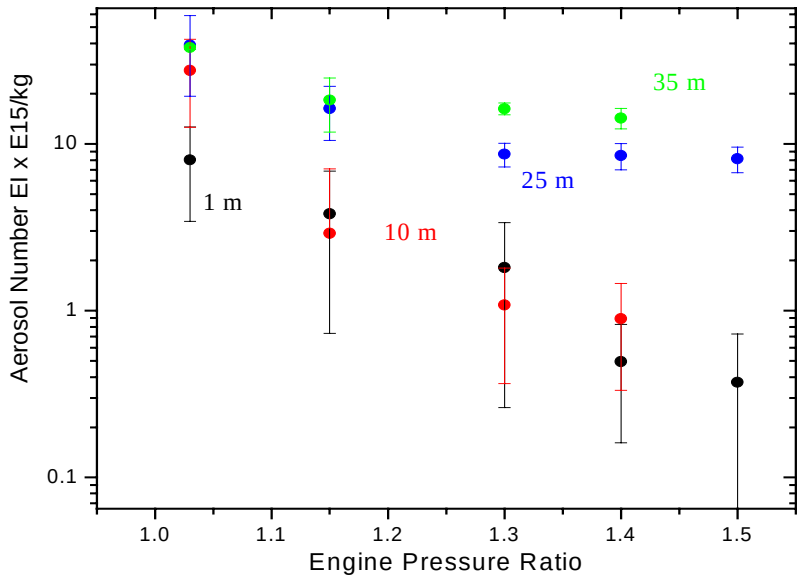

Figure 8. Number EI values for various engine power settings as determined at 1, 10, 25 and 35 m sampling distances for cases when aircraft was burning 1820 ppmS fuel.

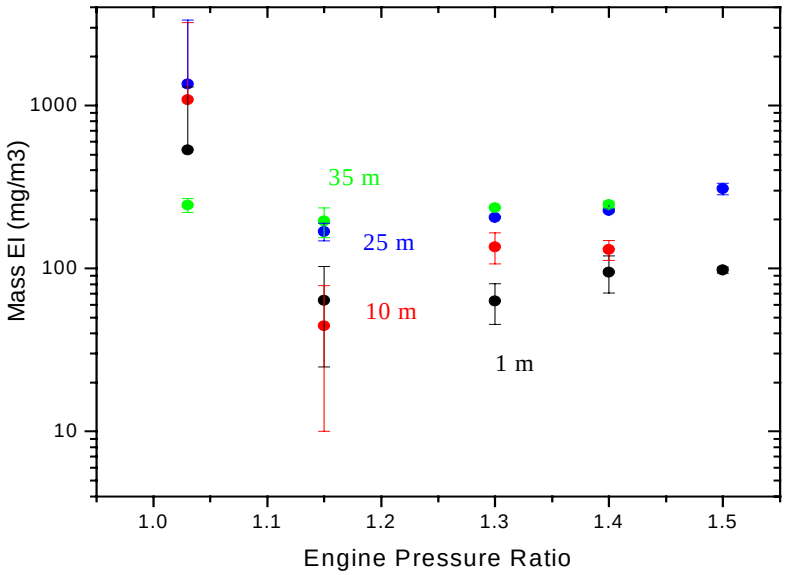

Figure 9. Aerosol mass EI for various engine power settings as determined at 1, 10, 25 and 35 m sampling distances for cases when aircraft was burning 1820 ppmS fuel. Values are derived from integrated DMA volumes over 9 to 240 nm diameter range and using aerosol mass density of 1 g cm^{-3}.

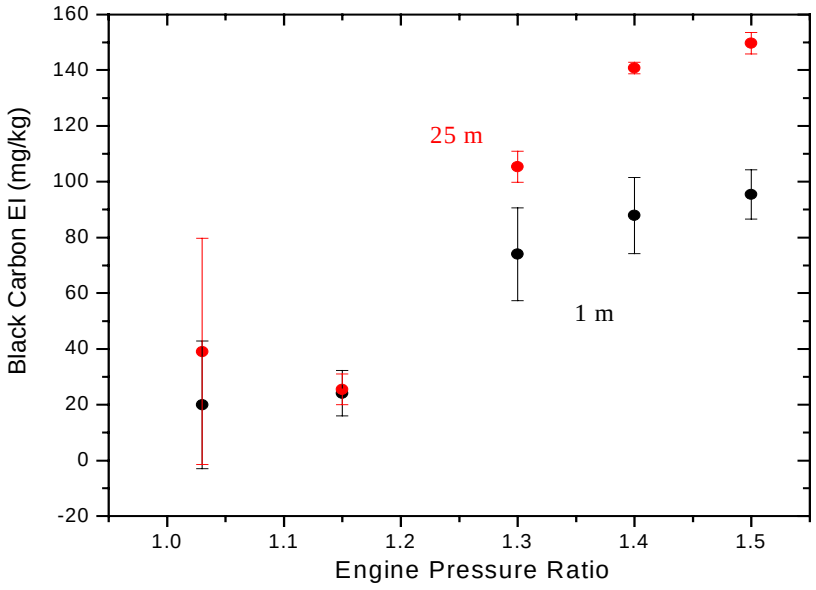

Figure 10. Black carbon EI as determined by PSAP measurements performed on samples collected at 1 and 25 m behind exhaust plane of the B-757 as the engine burned fuel containing 1820 ppmS. Values were calculated assuming mass absorption coefficient of 7 m^2 g^{-1}.

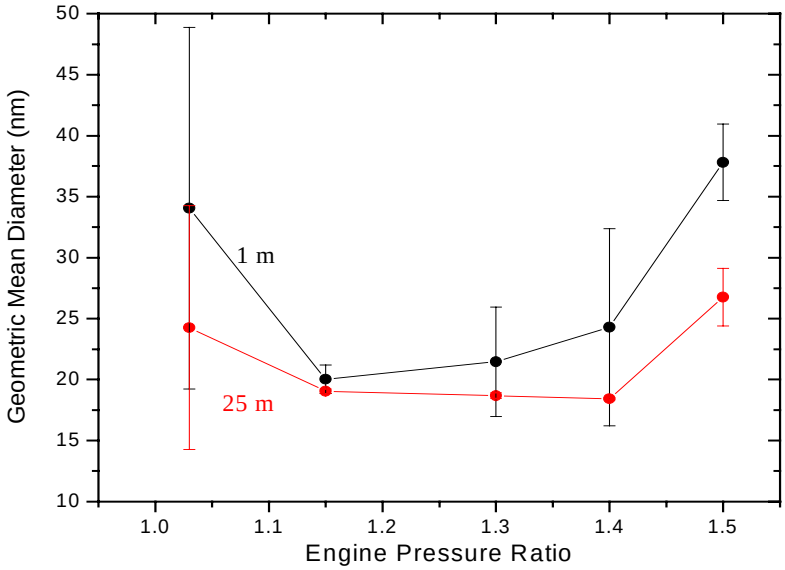

Figure 11. Geometric mean diameters derived from DMA size distribution scans performed on samples collected at 1 and 25 m behind B-757 exhaust plane as engine burned fuel containing 1820 ppmS.

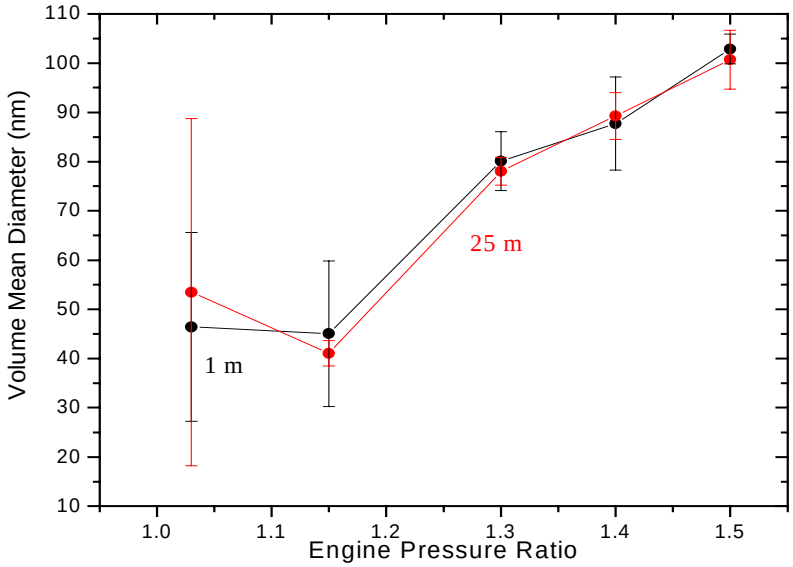

Figure 12. Volume mean diameters derived from DMA size distribution scans performed on samples collected at 1 and 25 m behind B-757 exhaust plane as engine burned fuel containing 1820 ppmS.

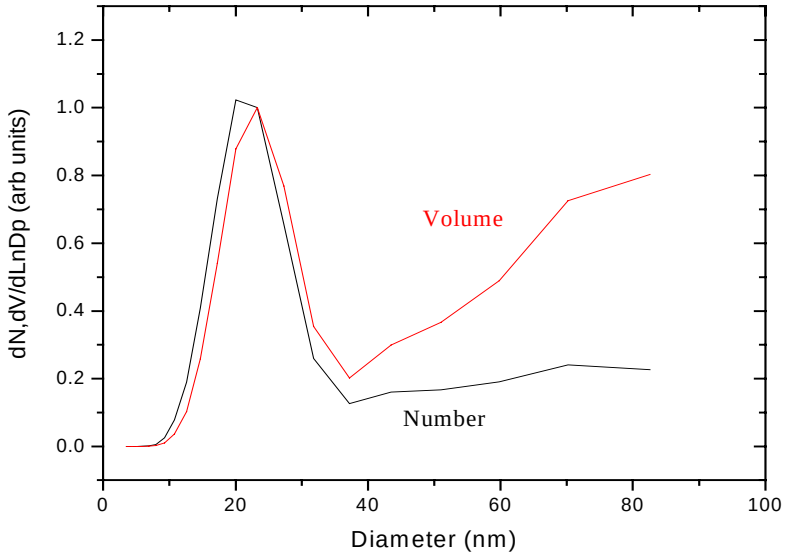

Figure 13. Number and volume-based size distributions derived from nDMA scans of samples collected at 35 m behind the B-757 as engine burned 1820 ppmS fuel. Two distributions have been normalized to illustrate that while nucleation mode contributes significantly to total number concentrations, it only moderately impacts total aerosol mass emissions.

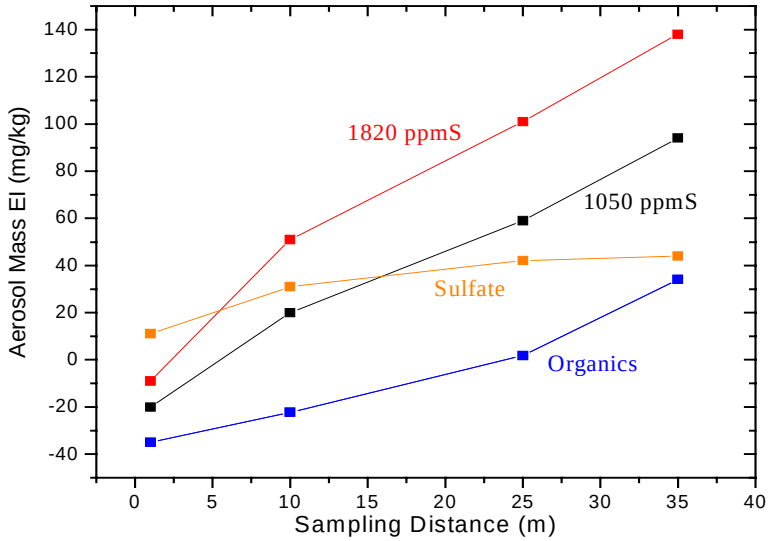

Figure 14. Aerosol mass EI in excess of black carbon EI determined at various sampling distances behind B-757 as engine was burning 1050 (black curve) and 1820 ppmS fuel (red) at 1.3 EPR. The orange curve was obtained by subtracting the 1050 from the 1820 ppmS curve and is inferred to represent mass of sulfate aerosol formed from 770 ppm of excess S present in 1820 ppmS fuel. The blue curves (two are superimposed) represent amount of organic aerosol formed in plume as it aged and were obtained by subtracting calculated mass fractions of sulfate for 1050 and 1820 ppmS fuel at each data point from black and red curves, respectively.

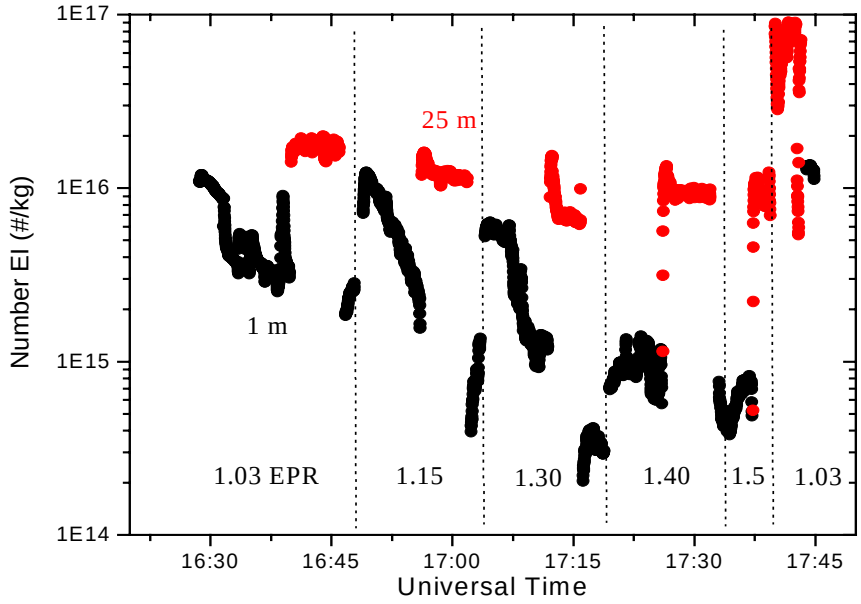

Figure 15. Time series of number EI as determined for samples extracted from exhaust plume at 1 and 25 m behind the B-757 as engine burned 1820 ppmS fuel. Vertical dashed lines indicate when power changes were implemented.

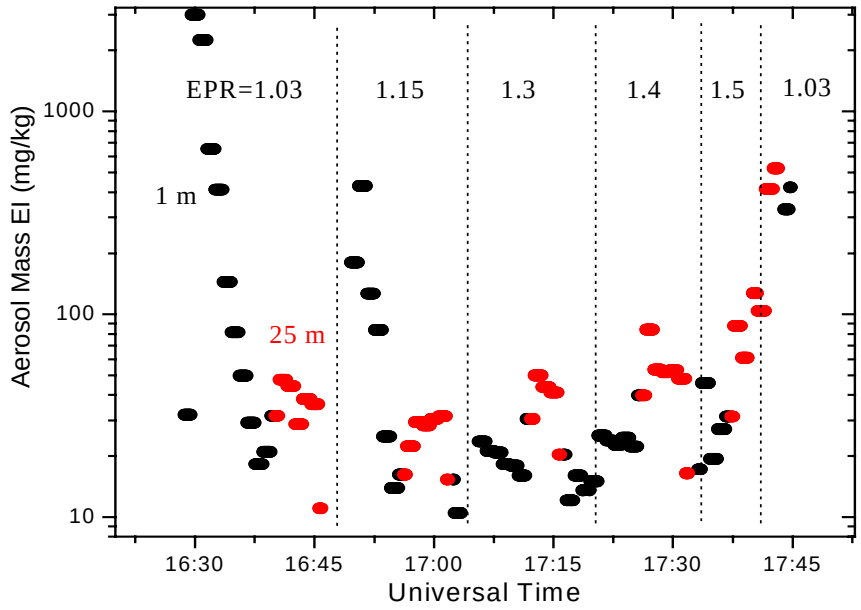

Figure 16. Time series of mass EI as determined from DMA scans of samples extracted from exhaust plume at 1 and 25 m behind B-757 as the engine burned 1820 ppmS fuel. Corresponding number EIs are shown in Figure 17. The vertical dashed lines indicate when power changes were implemented.

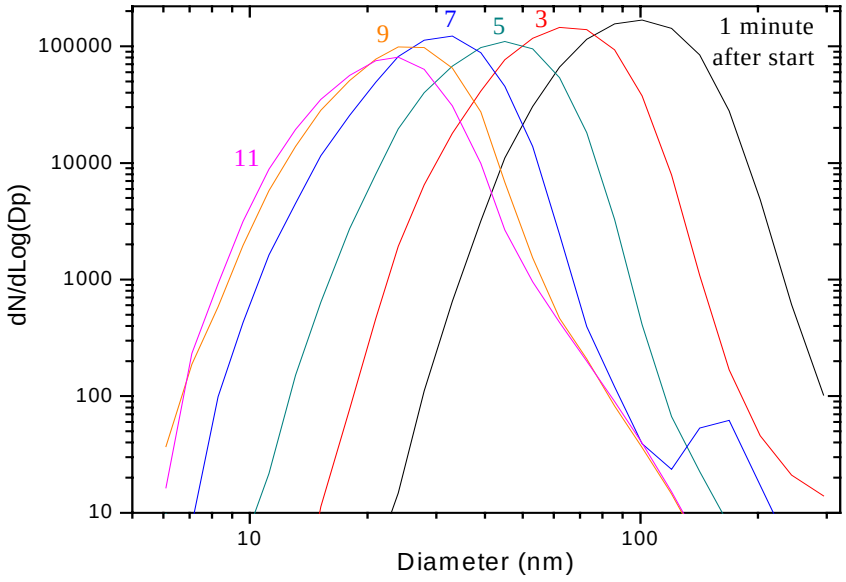

Figure 17. Series of size distributions recorded during first 11 minutes that B-757 RB-211 engine operated after undergoing cold start. Corresponding number and mass EI values are shown in Figures 15 and 16, respectively. Samples were extracted from 1 m downstream of the exhaust plane as engine was burning 1820 ppmS fuel.

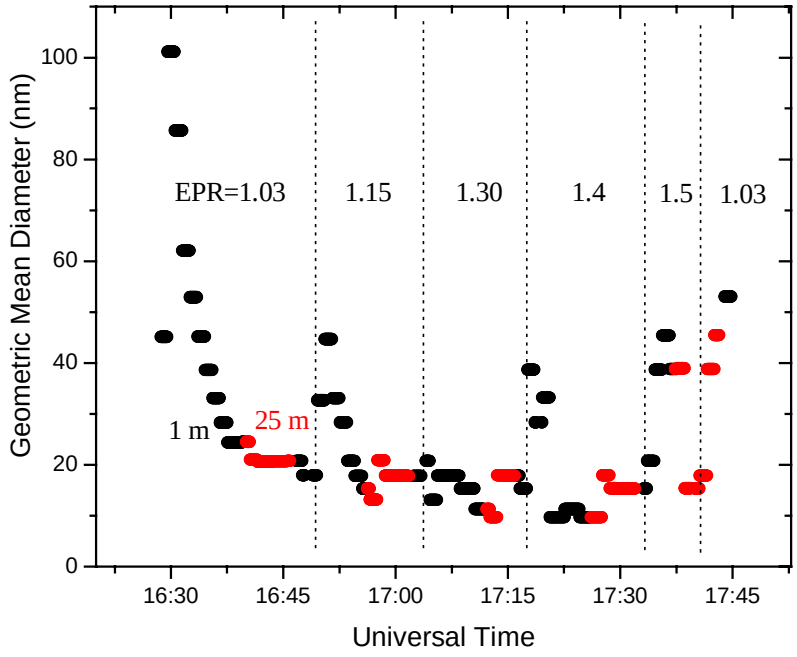

Figure 18. Time series of GMD as determined from DMA scans of samples extracted from exhaust plume at 1 and 25 m behind B-757 as the engine burned 1820 ppmS fuel. Corresponding number and mass EI data are shown in Figures 15 and 16, respectively. Vertical dashed lines indicate when power changes were implemented.

APPENDIX E: Improved Nanometer Aerosol Size Analyzer

H.-S Han and D. Y. H. Pui
Particle Technology Laboratory
Mechanical Engineering Department
University of Minnesota, Minneapolis, MN

7.1 Introduction

In this chapter, an improved version of Nanometer Aerosol Size Analyzer (nASA) is described. The hardware of this nASA is redesigned so that it is much smaller and robust than the previous one. Base on the previous extensive simulation study for the data inversion algorithms, MICRON is proved to provide the most accurate particle size distribution function with reasonable speed and stability. Therefore, MICRON is incorporated into the inversion software of this nASA. Figure 7.1 shows the picture of the modified nASA. The system was calibrated carefully for its delay time, and evaluated extensively using sodium chloride and silver particles. Finally, the system was used in the EXperiment to Characterize Aircraft Volatile Aerosol and Trace species Emissions (EXCAVATE) workshop. The purpose of this workshop, which was organized by NASA Langley Research Center in Hampton, VA, is to evaluate the particles emitted from T-38 and Boeing 757 aircraft engines. The workshop was conducted in Hampton, VA from January 15th to 29th, 2002. Experimental setup and results from this field trip are presented in the following sections.

Figure 7.1 Improved Nanometer Aerosol Size Analyzer

7.2 Experimental Setup

The experimental setup for this field study is shown in Figure 7.2. Aircraft-generated particles were drawn into a sampling probe which is developed by NASA Langley Research Center. After entering the sampling probe, the aerosols were diluted and quenched by dilution air, which in this field study is dry Nitrogen. In order to observe the aerosol growing characteristics and the effects of the ambient dilution, different dilution ratios were implemented. Different dilution ratio of the sample can be archived by adjusting the flow rate of Nitrogen. Depending on the engine power and the probe distance, the temperature of the aerosol sample exited the sampling probe was in the range of 30 to 80 ˚C. After the dilution, the aerosol samples were then distributed to aerosol instruments by 40 ft of stainless tubing. The losses in the tubing were carefully evaluated in the laboratory using the NaCl particles. Some of the aerosol samples were also heated to 300 ˚C before they were drawn into the nASA. Doing this will vaporize the volatile particles and the only remaining particles are non-volatile particles. The flow rate used by the nASA was 1.5 lpm and controlled by a vacuum pump and a valve.

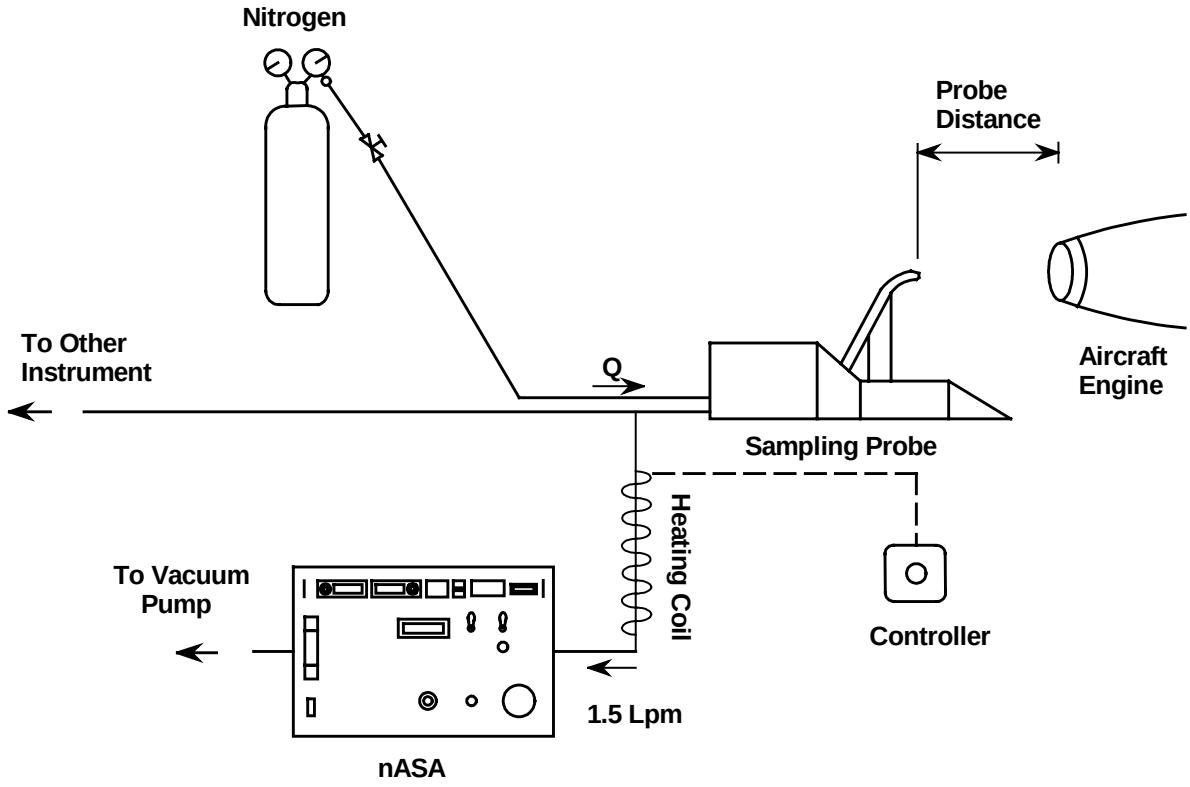

Figure 7.2 Experimental setup for EXCAVATE.

As mentioned before, the sample probe system is designed and manufactured by NASA Langley Research Center. It is capable of sampling aerosols, gases and ions, and its schematic diagram is shown in Figure 7.3. The basic stand has a 42" L x 42" W x 20" D compartment at the base that provides space to house some of the gas sensors, the electronics for thermocouples, pitot tubes and the ion concentration instrument Gerdien Tube Condenser. The base of the stand and caboose are framed from 3" x 3" x 1/4" stainless steel tubing and the surfaces subjected to engine blast are covered with ¼" stainless steel plate. The top of the stand that supports the sampling probe is constructed from 1" stainless steel plate welded onto a 48" x 48" x 1" plate that is bolted to the 24"

high base of the stand. The sampling probe system weight about 2000 lbs. To further prevent it moving while the engine is running, the stand has a trailer hitch on the front which can be bolted to a hard point in the tarmac. Figure 7.4 shows the close look of the sampling probe. The biggest stainless steel tubing is used for gas sampling. The dynamic pressure is measured by a pitot tube which is the smallest tubing shown in the photo. Between the gas sampling tube and pitot tube is the aerosol sampling tube. At the tip of this aerosol sampling tube, there is a critical orifice and its performance is evaluated in Particle Technology Laboratory, University of Minnesota, MN using NaCl. The calibration curve is presented in next section. Underneath the three tubings is the Gerdien Condenser. Thermocouples were also mounted to the support (not shown in the photo). Some of the gas instruments are located in the caboose, as shown in Figure 7.5. After the dilution, the samples were distributed to aerosol, gas and ion measurement systems which were located in several trailers, as shown in Figure 7.6.

Emissions of sulfur oxides (SO_x) are primary determined by the sulfur content of the jet fuel. These sulfur oxides are mainly in the form of SO_2, which will oxidize and condense on the background aerosols, at the combustor exit. In order to verify how efficiency the fuel sulfur content (FSC) is converted to sulfate particles, in the form of SO_3 and H_2SO_4, in the engine and near and far field, a parameter ξ is defined. The value of ξ is believed to be determined largely by the sulfur oxidation mechanisms within the combustor, turbine and exhaust nozzle. Observations taken from NASA SUbsonic aircraft Contrail and Cloud Effects Special Study (SUCCESS) show that ξ doesn't have strong dependence with FSC (Miake-Lye et al., 1998). In another study, SULFUR which

conducted by German agency the Deutsches Zentrum für Luft- und Raumfahrt (DLR), indicates that ξ decreases with the increase of FSC (Schröder et al., 1998). In order to investigate whether FSC will influence the amount of sulfate particles generated, fuels with 810, 1050 and 1820 ppm of sulfur content were used in the experiment.

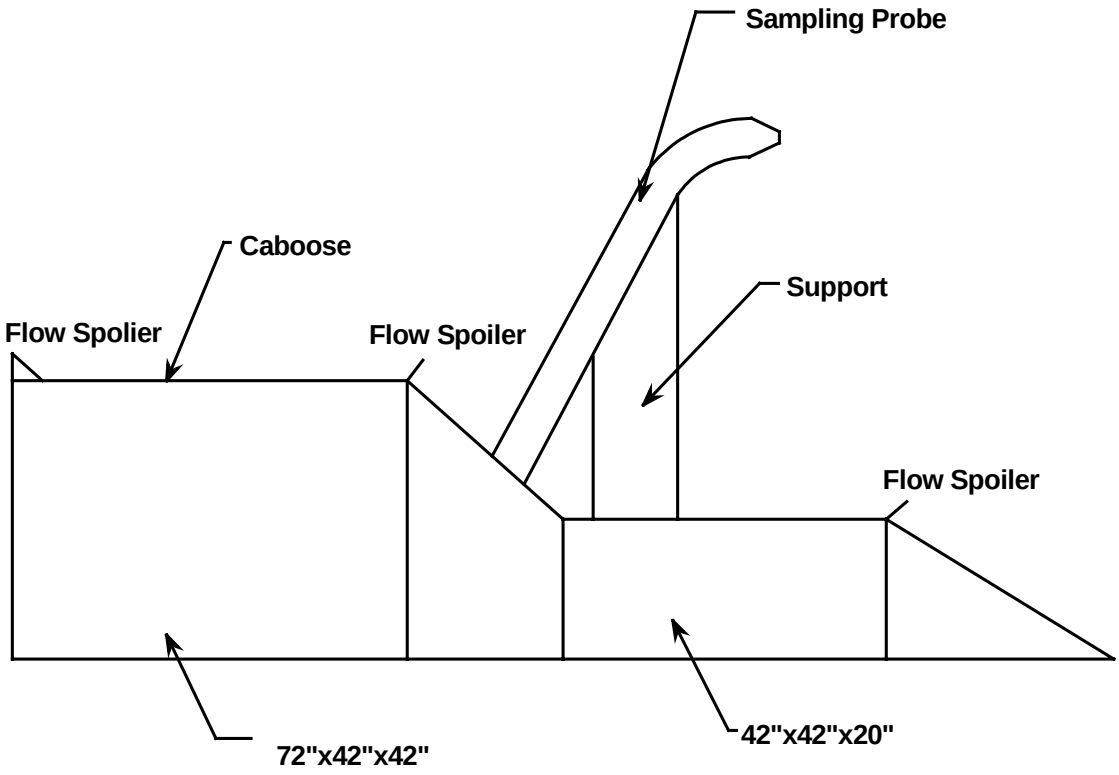

Figure 7.3 Sampling probe system.

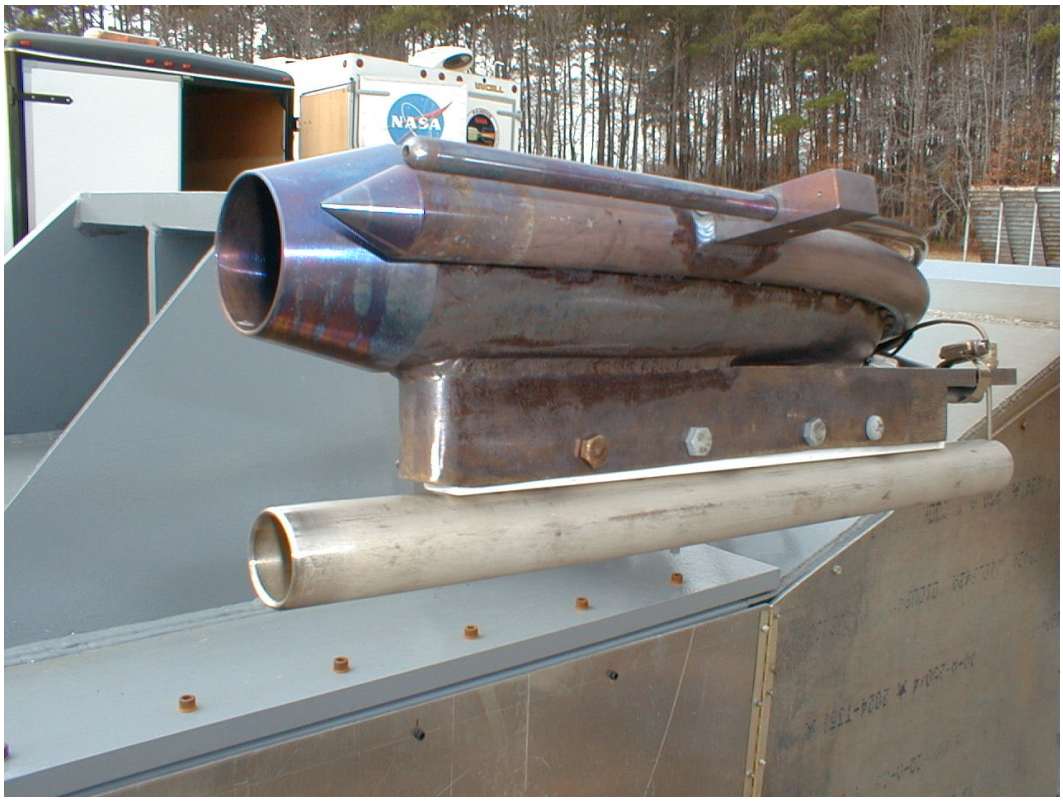

Figure 7.4 Close look of the sampling probe.

Figure 7.5 Some gas instruments located in the caboose.

Figure 7.6 Trailers that stationed aerosol, gas and ion measurement systems.

7.3 Results and Discussion

In this study, probe distances of 1, 10, 25 and 35m were used. Most of the engine used by modern passenger and military aircraft are powered by gas turbine engine, and the simplest type of it is turbojet engine. In order to represent the thrust of a turbojet engine, the term Engine Pressure Ratio (EPR) is commonly used. EPR is defined as the total pressure ratio across the engine, or in more detail is the ratio of nozzle total pressure to compressor face total pressure. It is also equivalent to the product of the pressure ratio of the compressor pressure ratio, burner pressure ratio, turbine pressure ratio and nozzle

pressure ratio. In this experiment, the EPR of the Boeing 757 engine was adjusted from 1.03 (idle) to 1.5.

Figure 7.7 shows the aerosol size distribution when the FSC of the fuel is 1050 ppm, probe distance is 1m and the EPR is 1.3. The heated curve represents the aerosol sample that is heated to 300˚C, and represents the size distribution of the non-volatile particles in the sample. Most of them are believed to be soot. Other particles include zinc, aluminum, and titanium which are from the abrasion of engine components or the trace metal impurities in the fuel. Figure 7.8 shows the corresponding aerosol size distribution inverted by MICRON. The unheated sample, which is the combination of volatile and non-volatile particles, obviously is bimodal distribution. The NMDs of the first and second mode are around 7nm and 20 nm. The aerosol size distribution of the heated sample is almost overlapping with the second mode of the unheated sample. This may indicate that the composition of the second mode of the unheated sample is mainly non-volatile particles. The observation is probably the first finding in aircraft emission measurement. Previous studies didn't observe this phenomenon is probably due to the lack of high resolution and low detection limit instruments, like the nASA used in this experiment. When increasing the engine power to 1.4 EPR, the first mode disappears, as shown in Figure 7.9. This interesting observation is possible due to the high temperature introduced by the high engine power. High temperature vaporized most of the volatile particles. The remaining particles after the vaporization are mainly non-volatile particles because its distribution closely matches to the heated sample, which is made up by non-volatile particles. If this theory is correct, then if we measure the aerosol size distribution

further away from the engine, the volatile part should reappear because of the cooler temperature at this location. Figure 7.10 confirms this is really the case. The volatile mode reappears and its concentration is so high that the non-volatile mode becomes less obvious. This indicates that coagulation and condensation are happening here.

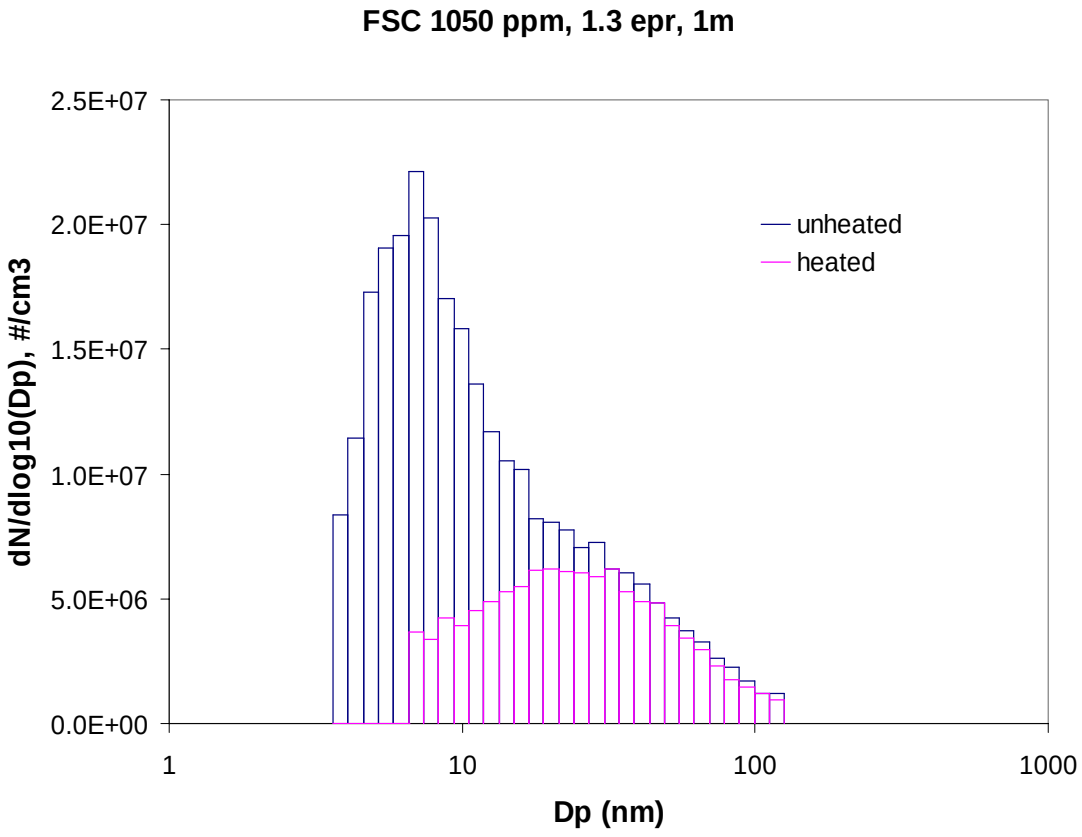

Figure 7.7 Aerosol size distribution from B757 engine. The FSC is 1050 ppm, the EPR is 1.3 and the distance between the sampling probe and engine exhaust is 1 m.

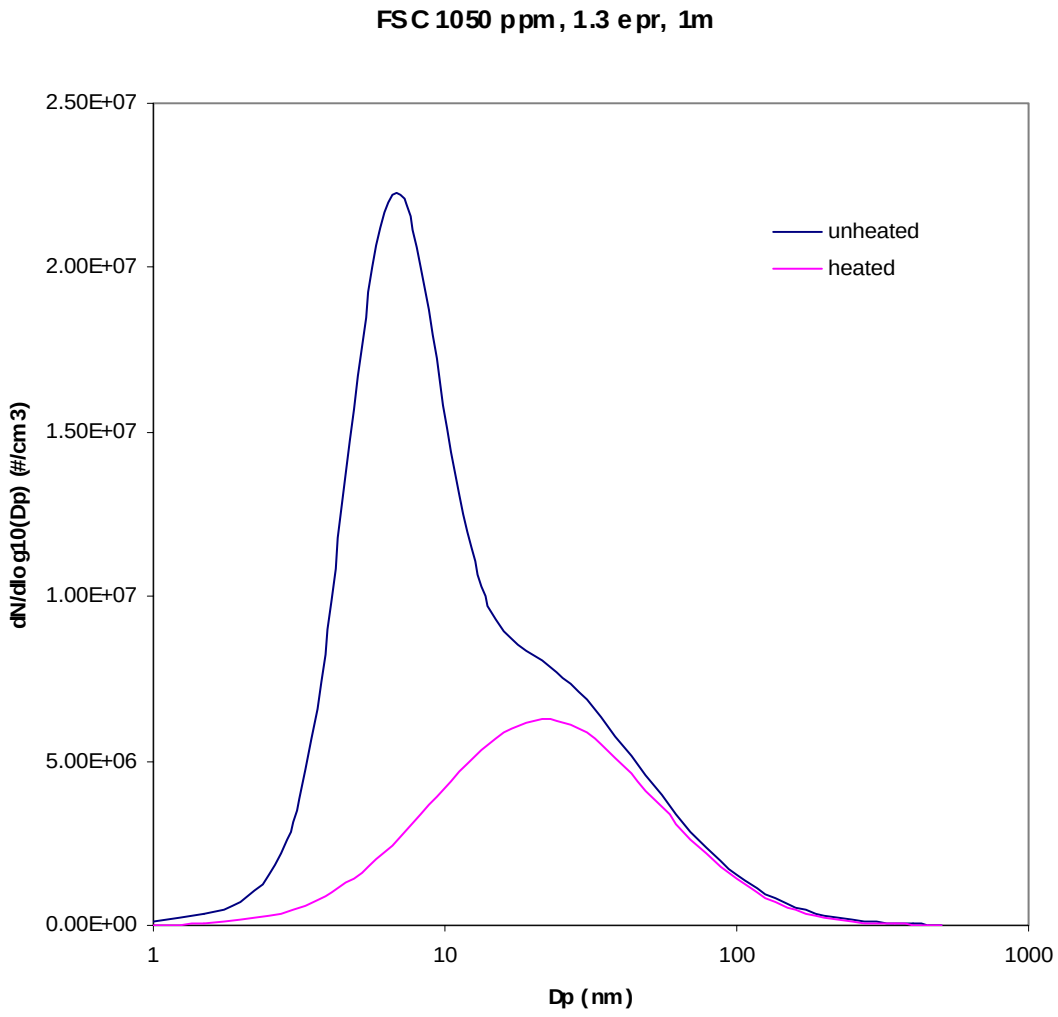

Figure 7.8 Aerosol size distribution inverted by MICRON.

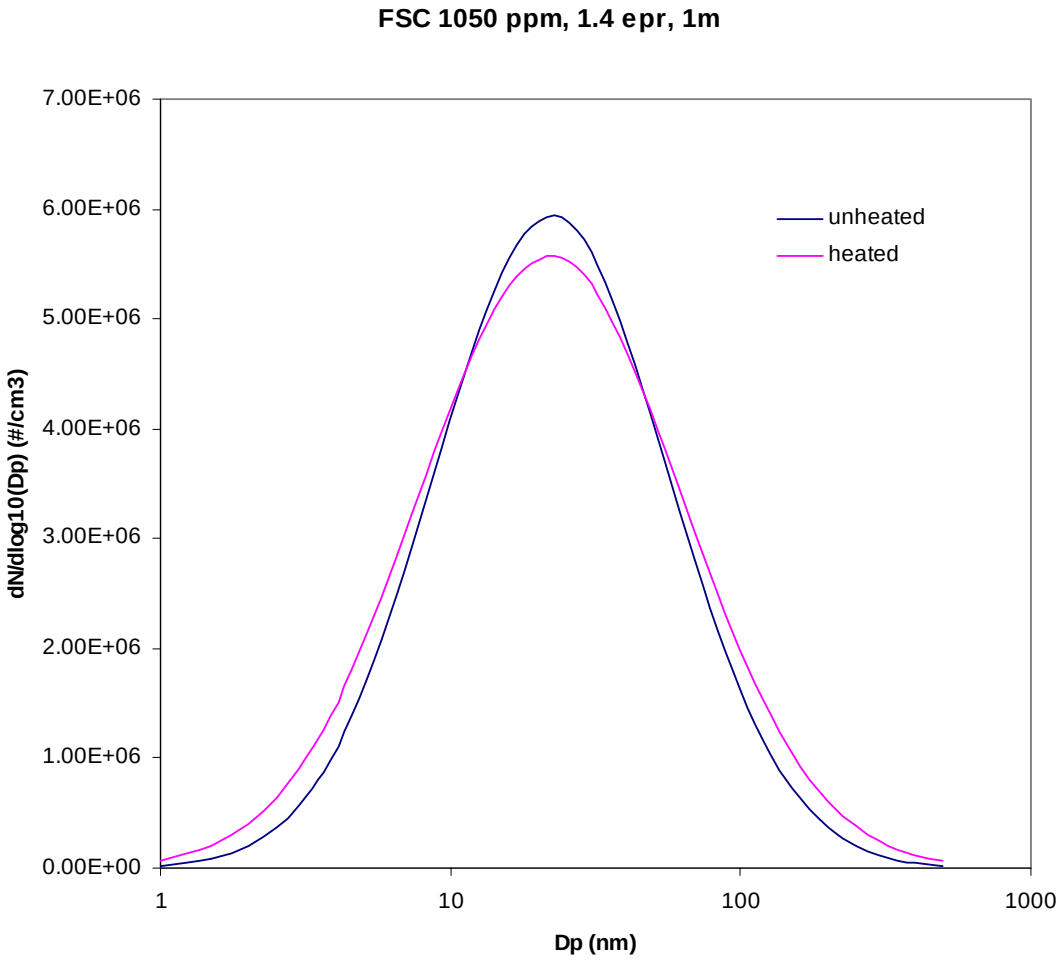

Figure 7.9 Aerosol size distribution when FSC is 1050 ppm, EPR is 1.4 and probe distance is 1 m.

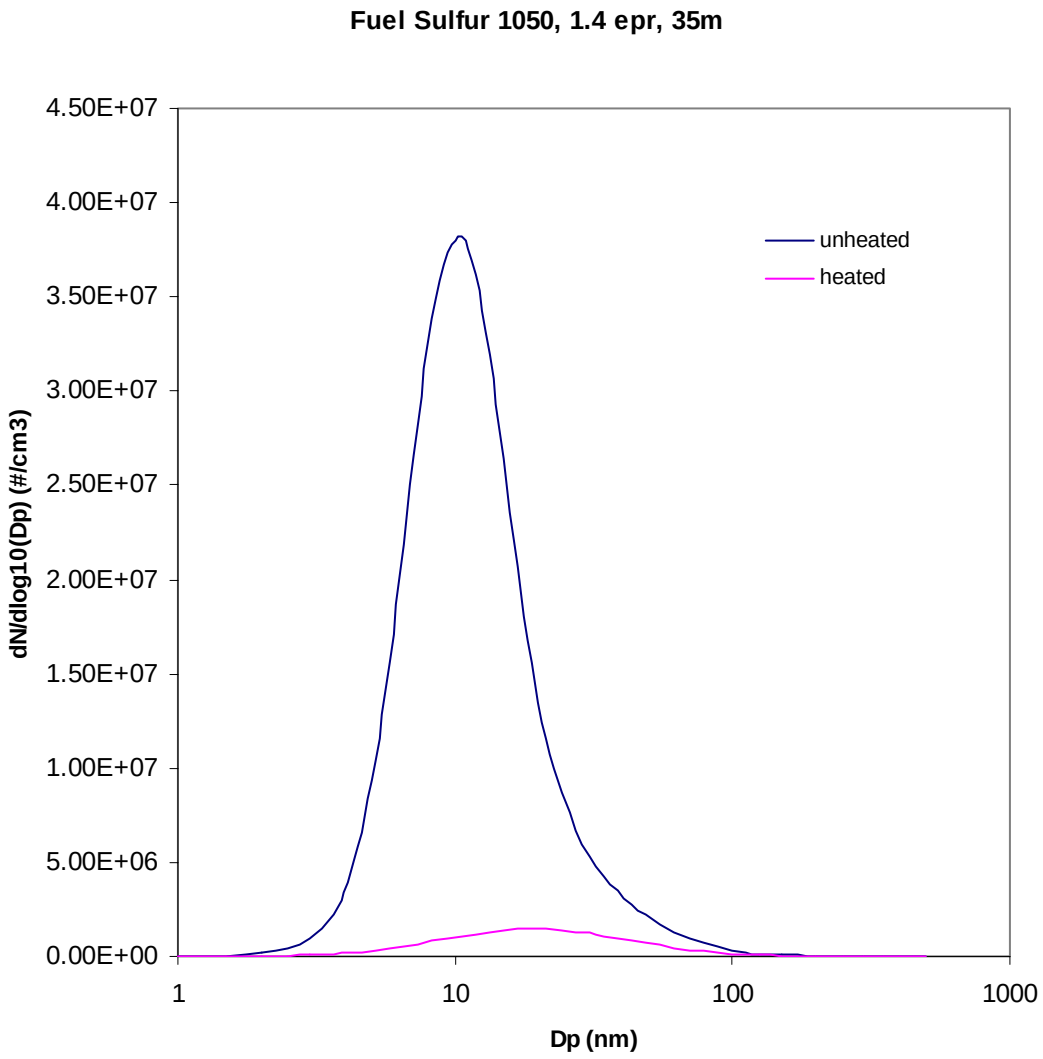

Figure 7.10 Aerosol size distribution when FSC is 1050 ppm, EPR is 1.4 and probe distance is 35 m.

The results for high FSC 1820 ppm fuel are shown in Figure 7.11 and 7.12. For 1.3 EPR, the non-volatile mode is not obvious and this is due to the high concentration of the volatile mode. When the engine power increases to 1.4 EPR, because of the high temperature surrounding the sampling probe and the engine, most of the volatile particles are vaporized and the non-volatile mode is appeared. However, due to the high

concentration of these volatile particles, they start condense and coagulate once the temperature is cool down, as shown in the left hand side of the unheated curve in Figure 7.12. Figure 7.13 and 7.14 show the aerosol size distributions for FSC 810 ppm. The results are similar to the previous two cases.

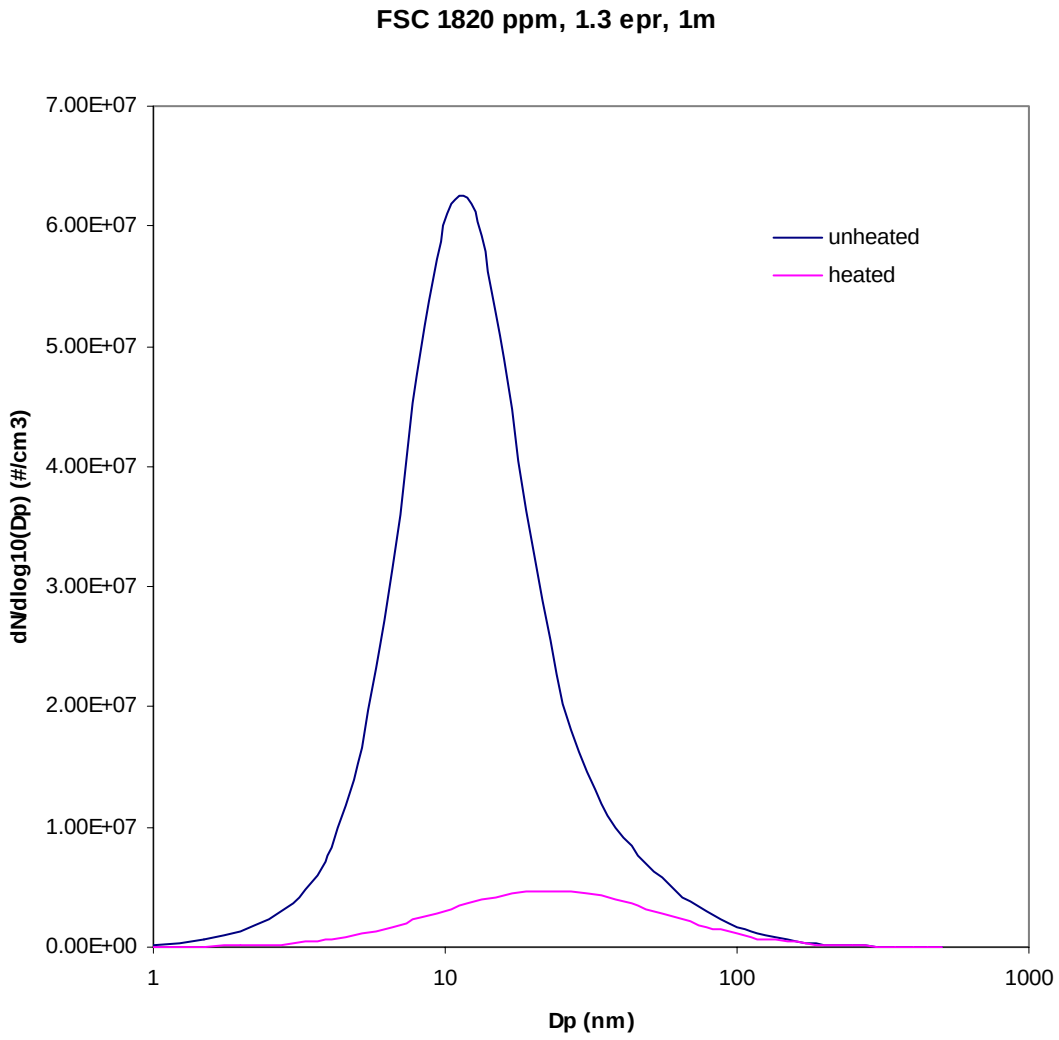

Figure 7.11 Aerosol size distribution when FSC is 1820 ppm, EPR is 1.3 and probe distance is 1 m.

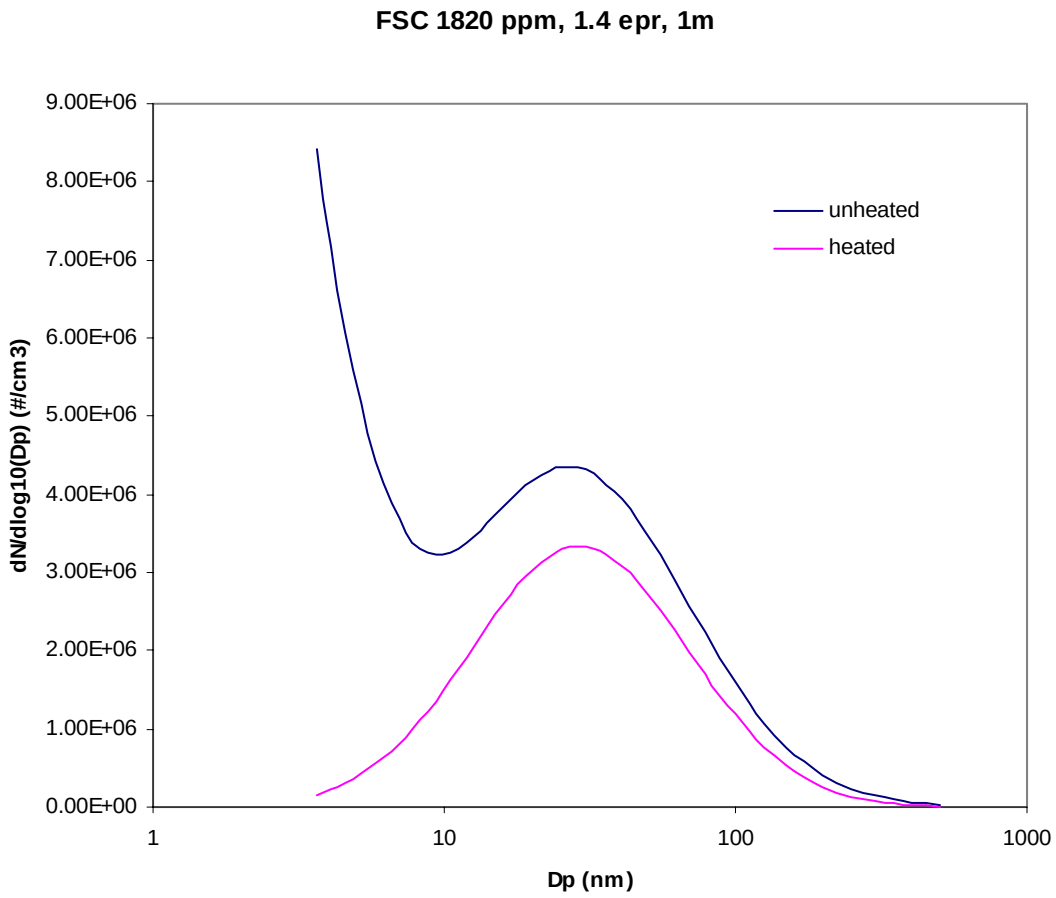

Figure 7.12 Aerosol size distribution when FSC is 1820 ppm, EPR is 1.4 and probe distance is 1 m.

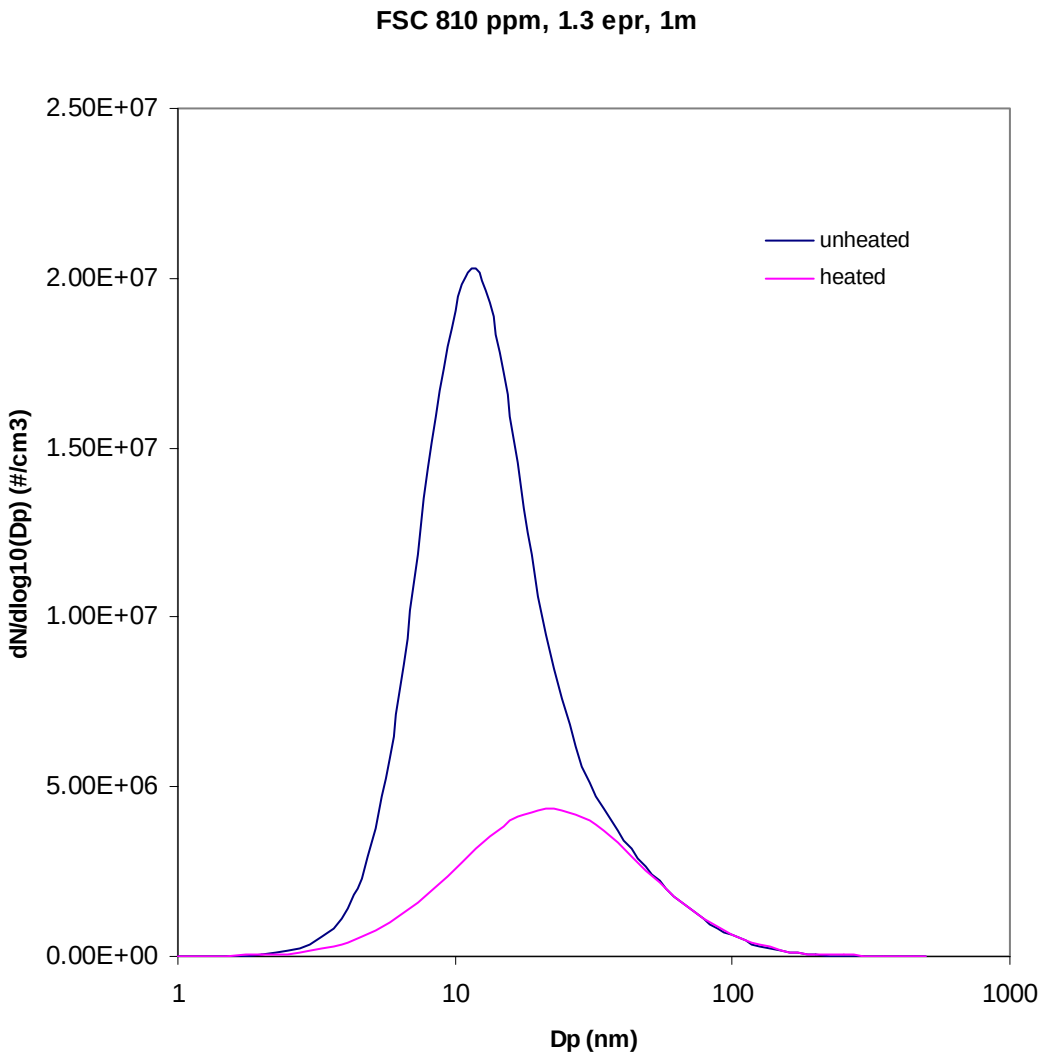

Figure 7.13 Aerosol size distribution when FSC is 810 ppm, EPR is 1.3 and probe distance is 1 m.

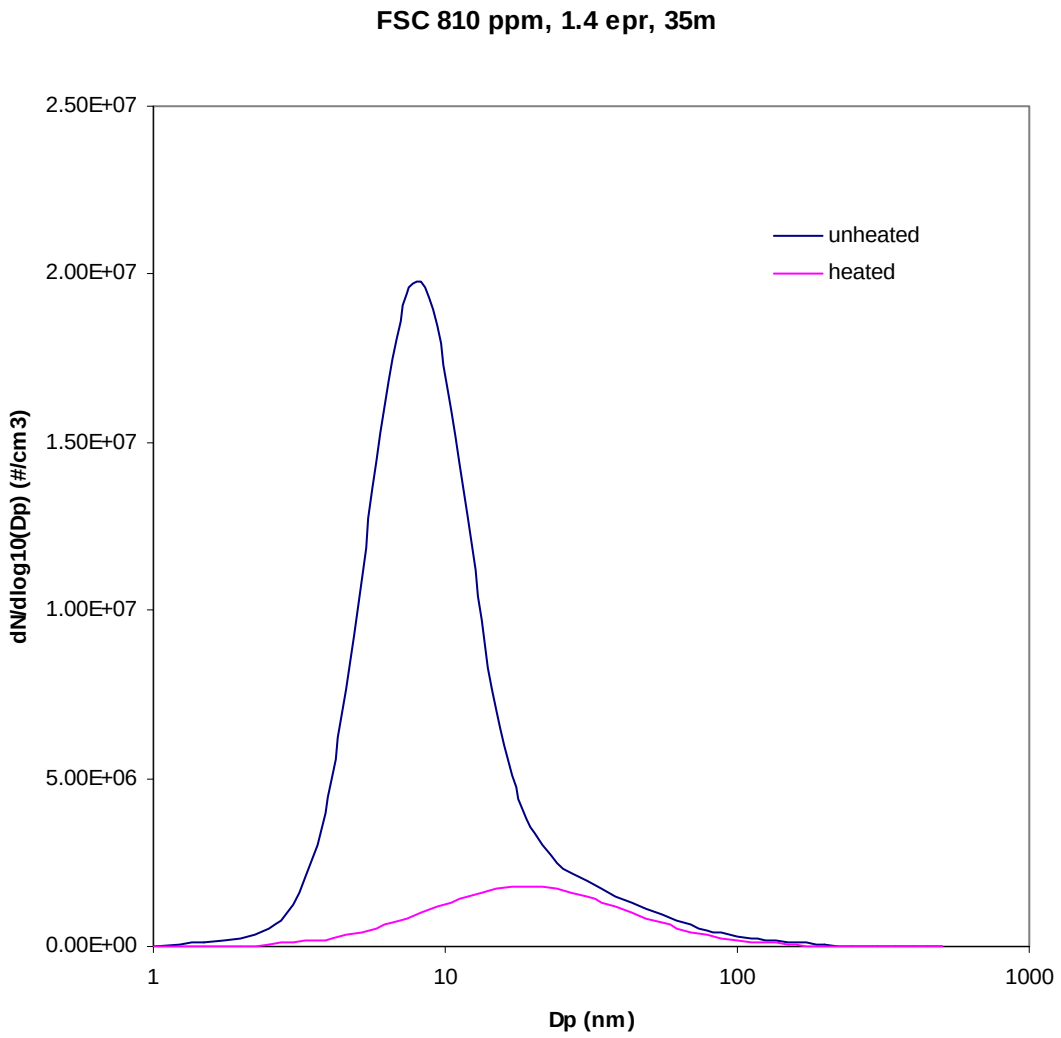

Figure 7.14 Aerosol size distribution when FSC is 810 ppm, EPR is 1.4 and probe distance is 35 m.

By comparing these three cases, it seems like the modes of non-volatile particles are quite consistent. All the non-volatile modes have peaks around 20 to 24 nm and concentrations are in the range of $4x10^6$ to $5x10^6$ #/cm^3. This indicates that non-volatile particle mode of aircraft generated aerosol size distribution is not effected by FSC of the fuel. However, the amount of sulfur content do influence the amount of volatile particles

emitted. This mode has the peak around 7 to 14 nm, and has higher particle concentration with higher FSC. The influence of FSC to the amount of particle emitted can be more easily observed by looking at the Number Emission Indices (nEI). Figure 7.15 shows the nEI for probe distance of 1 m. The data are the grand average of all the data measured. For idle, EPR of 1.03, the measurement is strongly influenced by the amount of unburned fuel and temperature of the surrounding area. Since the surrounding temperature increases with increasing of engine operation time, the results show wide range of fluctuation. This can be seen in Figure 7.15. In general, it seems that increases FSC will increase the amount of particle produced. Similar observations are seen in Figure 7.16 and 7.17, which show the nEI for probe distance of 10 and 35 m respectively.

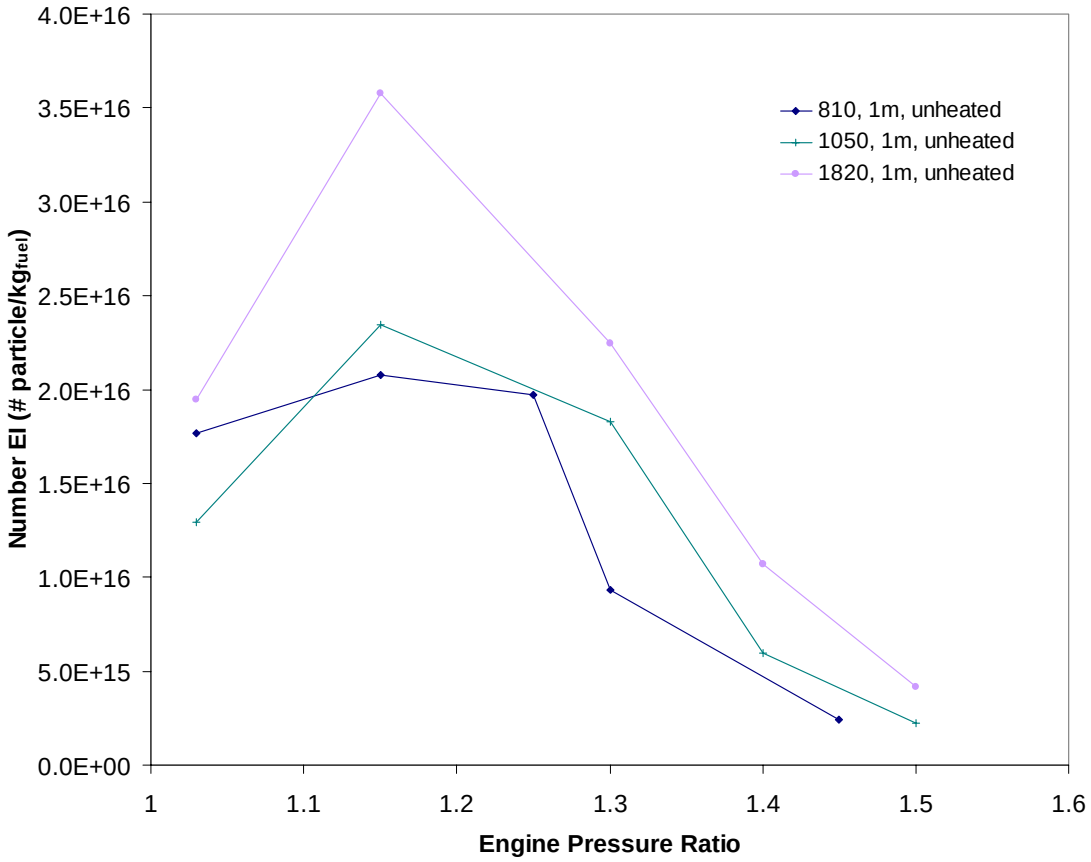

Figure 7.15 Number emission index for probe distance of 1 m.

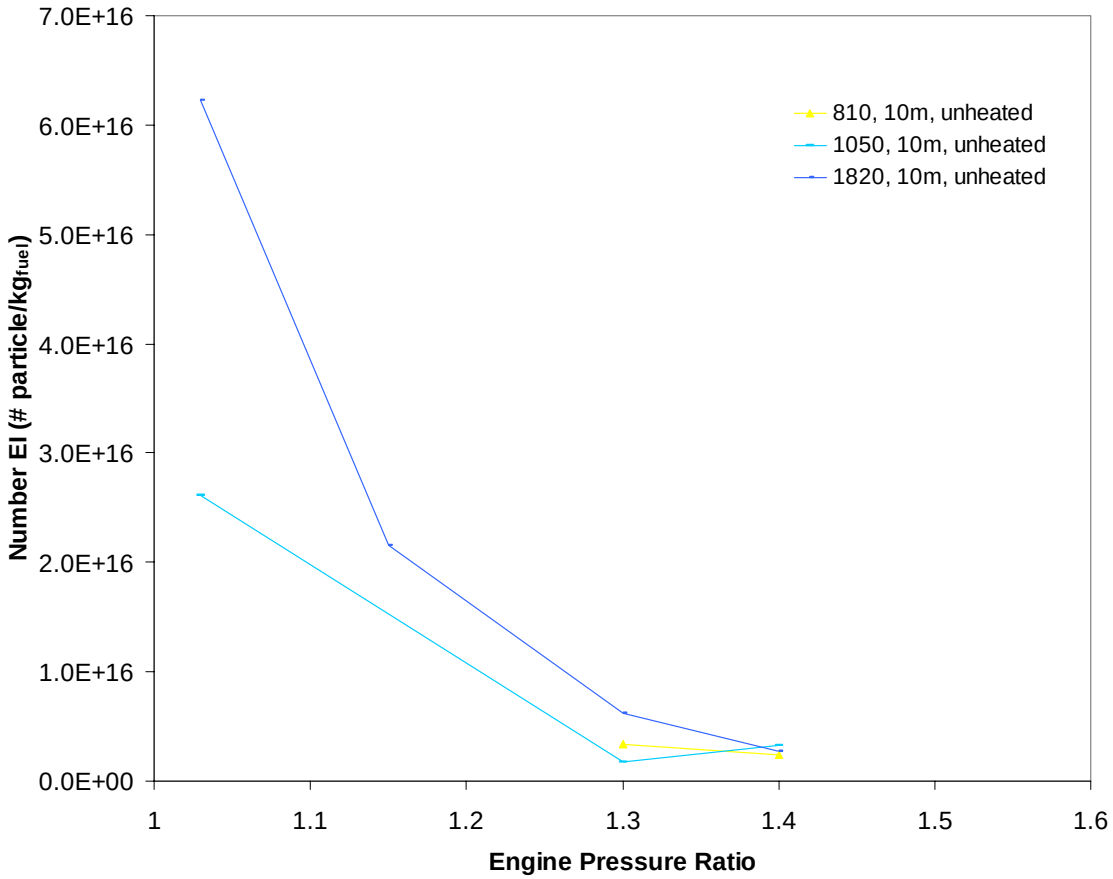

Figure 7.16 Number emission index for probe distance of 10 m.

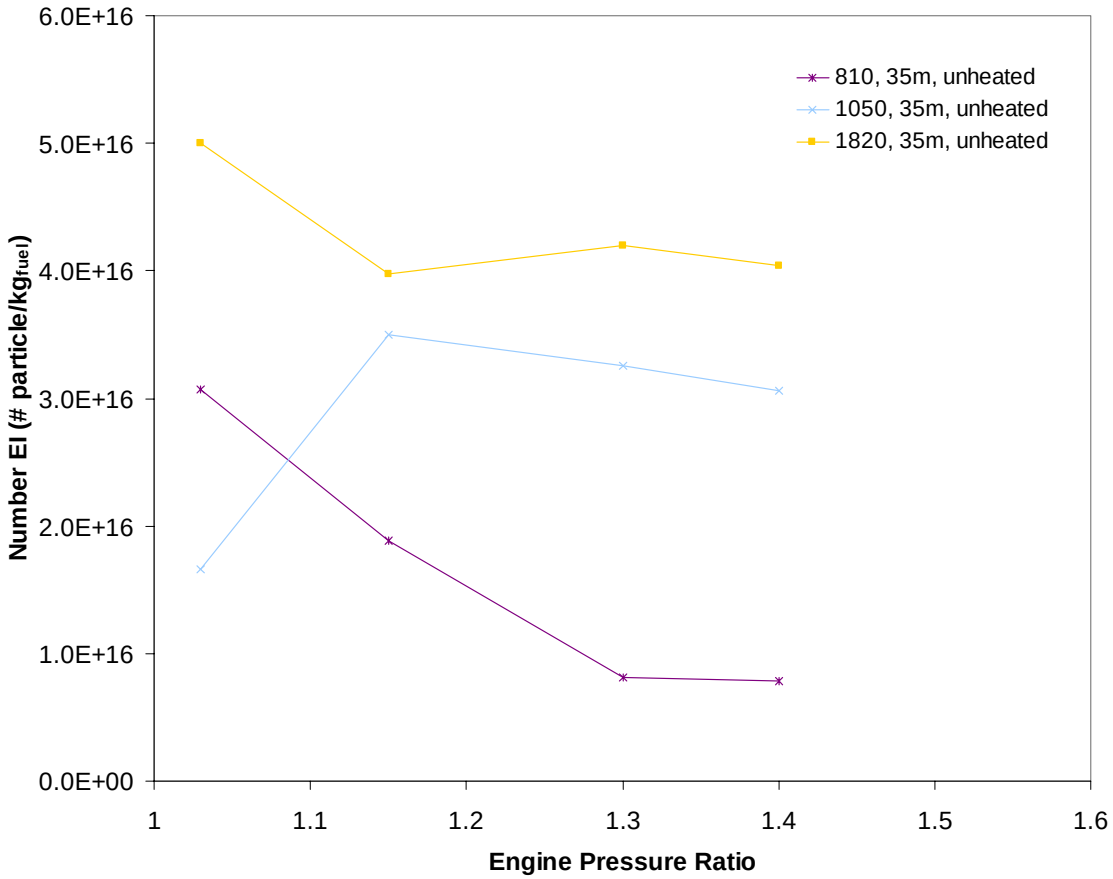

Figure 7.17 Number emission index for probe distance of 35 m.

Figure 7.18 to 7.20 show the Mass Emission Indices (mEI) for probe distance of 1, 10 and 35 m respectively. The results show that mEI are quite constant for high EPR and are in the range of 0.1 to 0.2 $g_{particle}/kg_{fuel}$. For low engine power, it seems like increasing the sampling distance decreases the mEIs. The possible reason is that the amount of unburned fuel sampled in closer distance is much higher than that in further away distance. Complete results for nEI and mEI are shown in Figure 7.21 and 7.22.

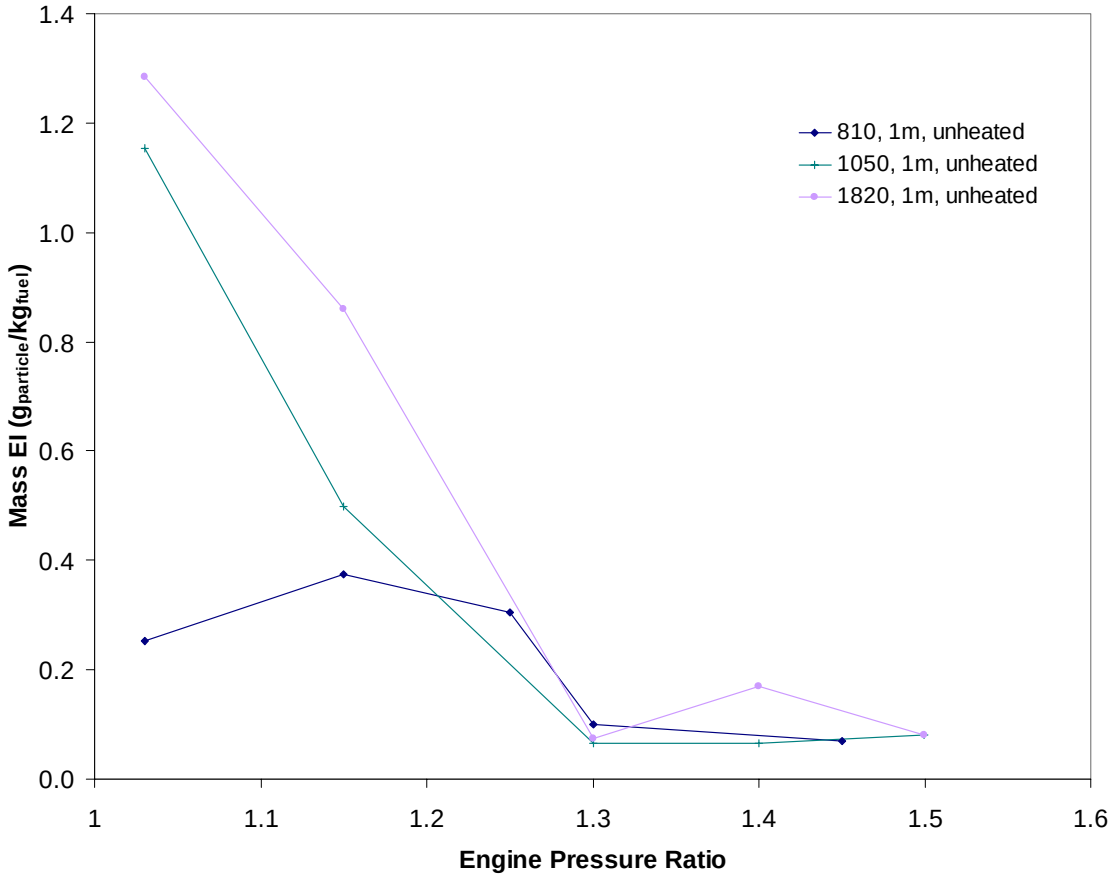

Figure 7.18 Mass emission index for probe distance of 1 m.

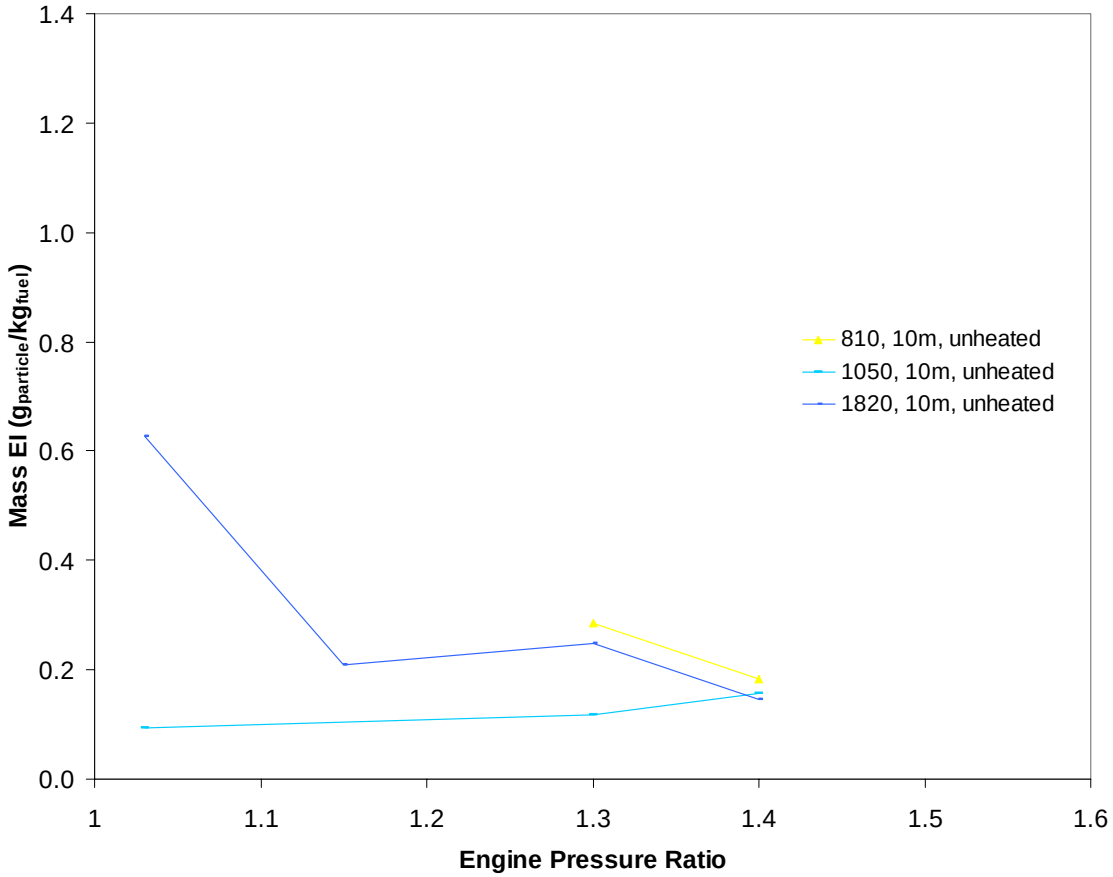

Figure 7.19 Mass emission index for probe distance of 10 m.

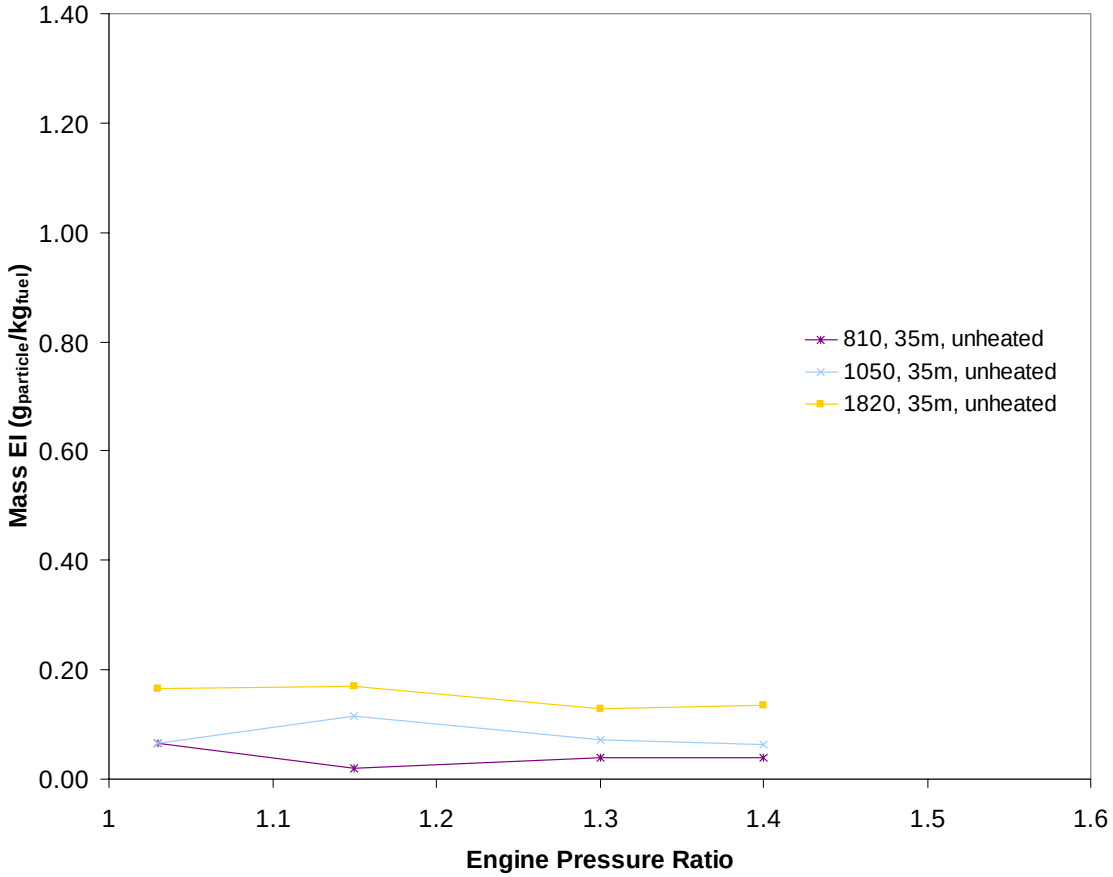

Figure 7.20 Mass emission index for probe distance of 35 m.

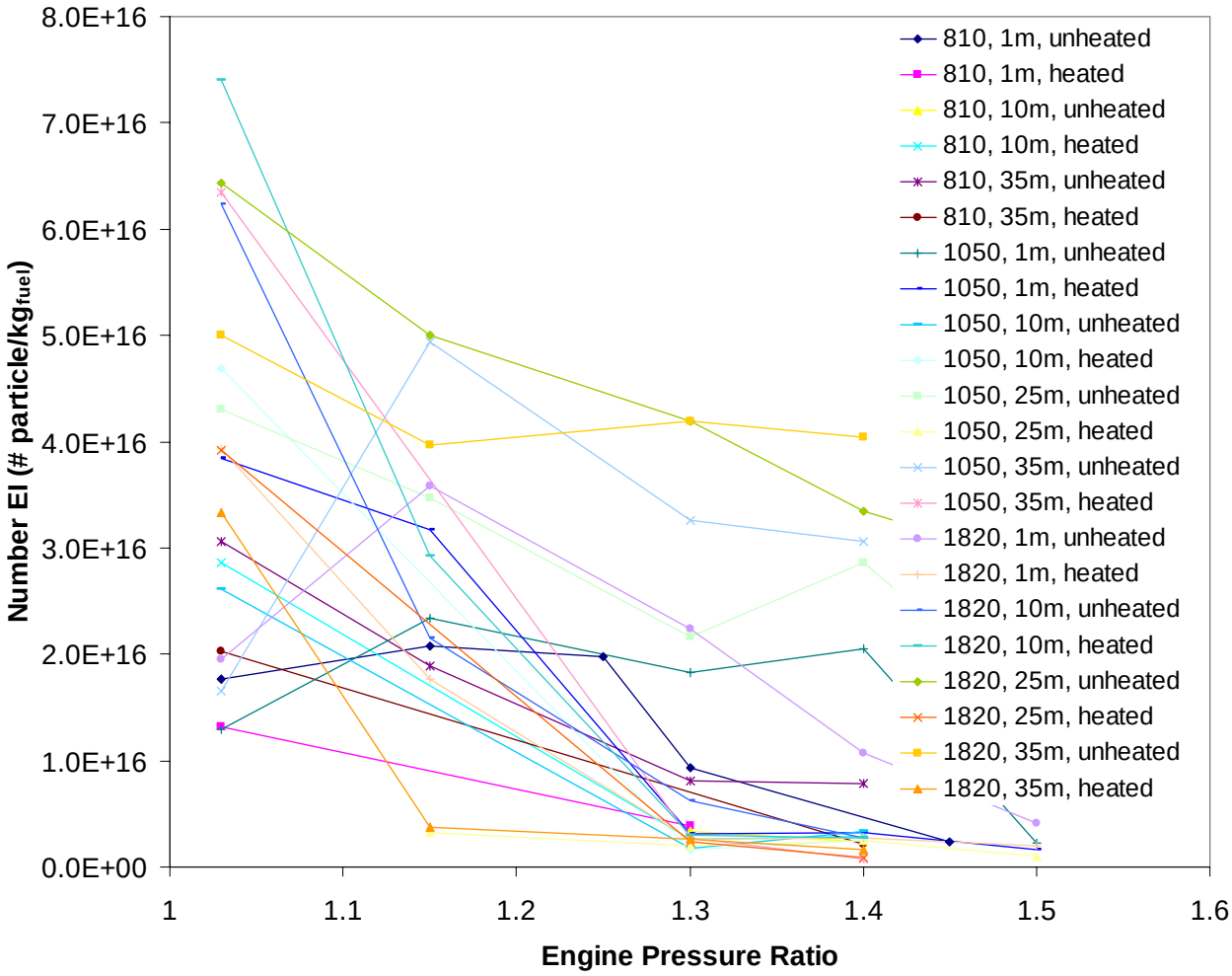

Figure 7.21 Number emission index for Boeing 757 engine.

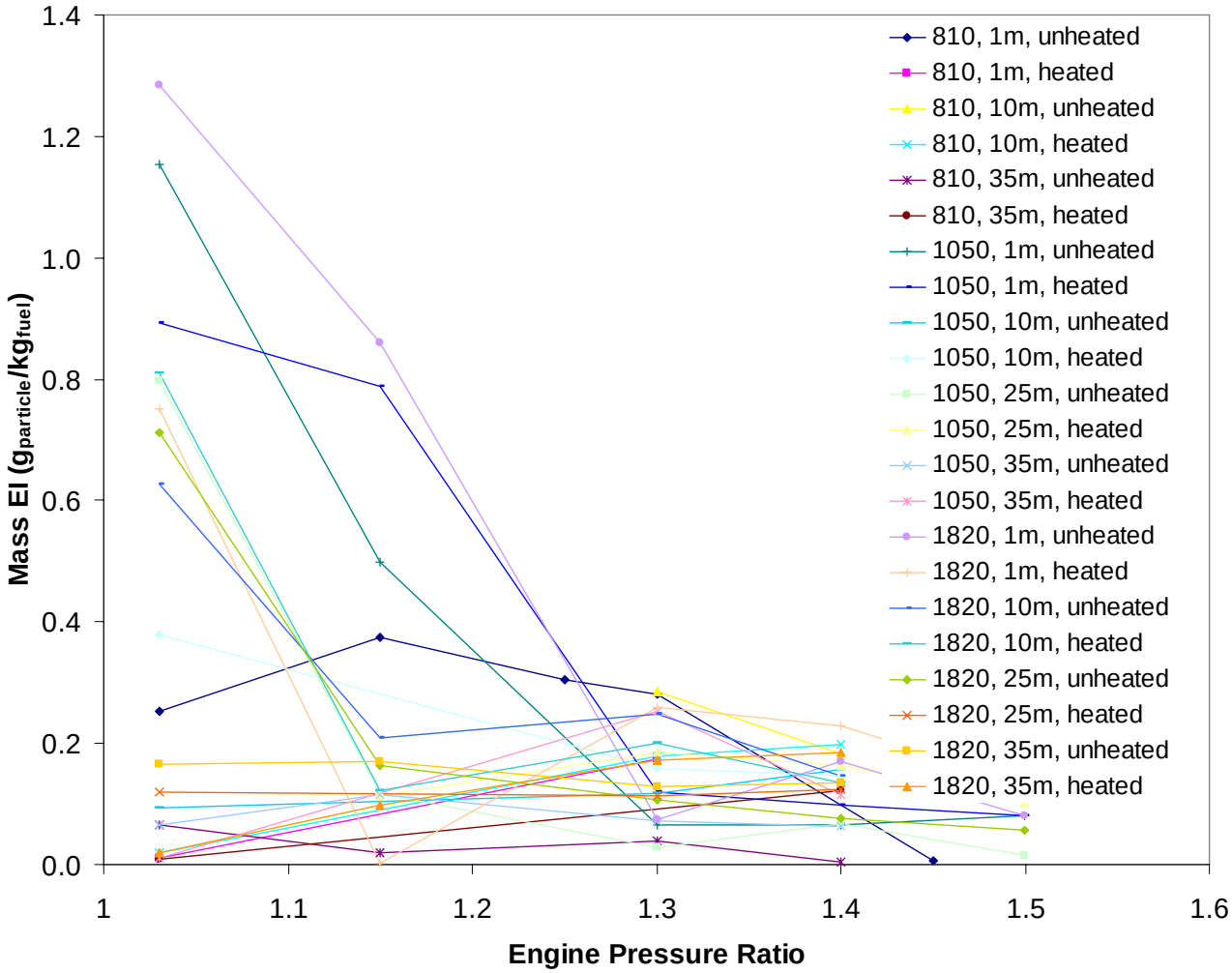

Figure 7.22 Mass emission index for Boeing 757 engine.

7.4 References

1. Anderson, B. E., Cofer, W. R., Bagwell, D. R., Barrick, J. W., Hudgins, C. H., and Brunke, K. E. (1998). Airborne Observations of Aircraft Aerosol Emissions, 1: Total and Nonvolatile Particle Emission Indices. *Geophysical Research Letter.* 25:1689-1692.

2. Anderson, B. E., Cofer, W. R., Barrick, J. W., Bagwell, D. R., and Hudgins, C. H. (1998). Airborne Observation of Aircraft Aerosol Emissions, 2: Factors Controlling Volatile Particle Production. *Geophysical Research Letter.* 25:1693-1696.

3. Chen, D., and Pui, D. Y. H. (1997). Numerical Modeling of the Performance of Differential Mobility Analyzers for Nanometer Aerosol Measurements. *Journal of Aerosol Science.* 28:985-1004.

4. Chen, D., and Pui, D. Y. H. (1999). A High Efficiency, High Throughput Unipolar Aerosol Charger for Nanoparticles. *Journal of Nanoparticle Research.* 1:115-126.

5. Chen, D., Pui, D. Y. H., Hummes, D., Fissan, H., Quant, F. R., and Sem, G. J. (1998). Design and Evaluation of A Nanometer Aerosol Differential Mobility Analyzer (Nano-DMA). *Journal of Aerosol Science.* 29:497-509.

6. Crump, J. G., and Seinfeld, J. H. (1982). Further Results on Inversion of Aerosol Size Distribution Data: Higher-Order Sobolev Spaces and Constraints. *Aerosol Science and Technology.* 1:363-369.

7. Crump, J. G., and Seinfeld, J. H. (1982). A New Algorithm for Inversion of Aerosol Size Distribution Data. *Aerosol Science and Technology.* 1:15-34.

8. Han, H.-S., Chen, D.-R., and Pui, D. Y. H. (2002). Numerical Evaluation of Stability and Accuracy of Data Inversion Algorithms. *In preparation*.

9. Han, H.-S., Chen, D.-R., Pui, D. Y. H., and Anderson, B. E. (2000). A Nanometer Aerosol Size Analyzer (nASA) for Rapid Measurement of High-Concentration Size Distributions. *Journal of Nanoparticle Research.* 2:43-52.

10. Miake-Lye, R. C., Anderson, B. E., Cofer, W. R., Wallio, H. A., Nowicki, G. D., Ballenthin, J. O., Hunton, D. E., Knighton, W. B., Miller, T. M., Seeley, J. V., and Viggiano, A. A. (1998). SOx Oxidation and Volatile Aerosol in Aircraft Exhaust Plumes Depend on Fuel Sulfur Content. *Giophysical Research Letters.* 25:1677-1680.

11. Schroder, F. P., Karcher, B., Petzold, A., Baumann, R., Busen, R., Hoell, C., and Schumann, U. (1998). Ultrafine Aerosol Particles in Aircraft Plumes: In Situ Observations. *Geophysical Research Letter.* 25:2789-2792.

12. Stolzenburg, M. R. 1988. An Ultrafine Aerosol Size Distribution Measuring System. *In* Mechanical Engineering. University of Minnesota, Minneapolis.

13. Wolfenbarger, J. K., and Seinfeld, J. H. (1990). Inversion of Aerosol Size Distribution Data. *Journal of Aerosol Science.* 21:227-247.

14. Wolfenbarger, J. K., and Seinfeld, J. H. (1991). Estimating the Variance in Solution to the Aerosol Data Inversion Problem. *Aerosol Science and Technology.* 14:348-357.

APPENDIX F: Real Time Characterization of Aircraft Particulate Emission by an Aerosol Mass Spectrometer During EXCAVATE 2002

[1]H. Boudries, [1]M. Canagaratna, [1]T. Onasch, [1]D. Worsnop, , [1]J. Wormhoudt,

[1]R. Miake-Lye [2]B. Anderson

[1]Aerodyne Research Inc., 45 Manning Road, Billerica, MA, USA

[2]NASA, Hampton, VA.

1. Introduction

In this report, preliminary results from ground-based measurements carried out as part of EXCAVATE (EXperiment to Characterize Aircraft Volatile Aerosol and Trace species Emissions) field campaign at NASA Langley Research Center (Hampton, Virginia, USA), of exhaust aerosols emitted by a Boeing 757 Rolls-Royce turbo engine are presented. During these measurements the aerosol chemical composition and size distribution for different engine thrust levels, sulfur fuel content, and different sampling distances behind the engine were characterized in real time by an aerosol mass spectrometer.

2. Sampling and Analysis

A series of experimental tests were conducted during EXCAVATE experiment to characterize the particle chemical composition and size distribution of major chemical components present in the exhaust of a Boeing 757. Figure 1 summarizes the condition of engine thrust, sulphate fuel composition and sampling distance behind the jet engine. Exhausts from three different fuels were tested (low sulfate fuel 810 PPM, intermediate 1050 ppm, and high 1820 ppm) at 5-engine thrust levels measured in engine pressure ratio (EPR), 1.03 (Idle), 1.15, 1.3, 1.4 and 1.5 EPR. Four different sampling distances (1, 10, 25 and 35 meters) behind the jet engine were used during this experiment. The exhaust aerosols PM2.5 emitted by the Rolls-Royce engine were

sampled and analyzed in real time by an Aerodyne aerosol mass apectrometer (AMS) with a resolution of 30 seconds.

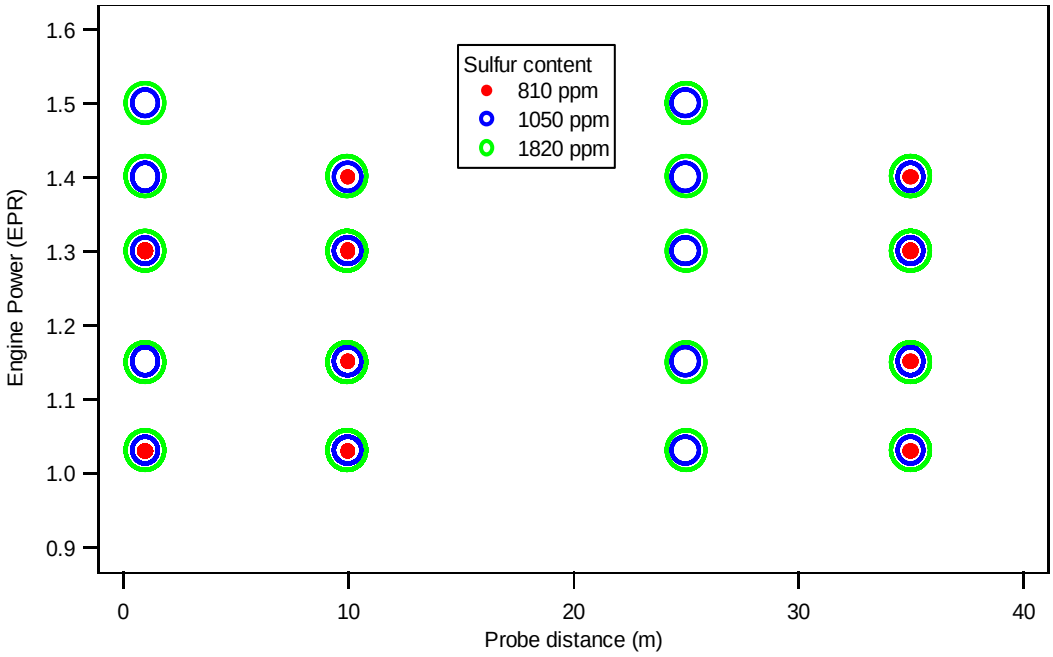

Figure 1: Aerosol sampling conducted during EXCAVATE experiment for several engine power, probe distance, and sulfur fuel content levels.

2.1. Aerosol Mass Spectrometer

Chemical and physical composition of nonrefractory volatile and semivolatile particles were measured in-situ and in real time using an aerosol mass spectrometer (AMS) developed at Aerodyne Research Inc, (Billerica, MA, USA). As presented in Figure 2, ambient aerosols below 2.5 μm are sampled into a vacuum and focused in an aerodynamic lens. The focused particle beam exiting the lens is directed into the particle-sizing chamber maintained at a pressure of 10^{-5} Torr. By modulating the particle beam with a chopper and using the time of flight of particles between the chopper and the detector, the particle velocity and the aerodynamic diameter can be obtained. The particle detection scheme consists of an oven that is coupled to a quadrupole mass spectrometer. When the particles hit the oven surface, the volatile and semivolatile components of particles are flash vaporized. The vaporization plume is ionized by an electron impact ionizer mounted at the entrance of a quadrupole mass spectrometer, operated at 70eV electron energy

and scanned in a range of 1-300 atomic mass units. Detailed information about the AMS is well documented in Jayne et al. (2000) and the data analysis (Jimenez et al., 2003).

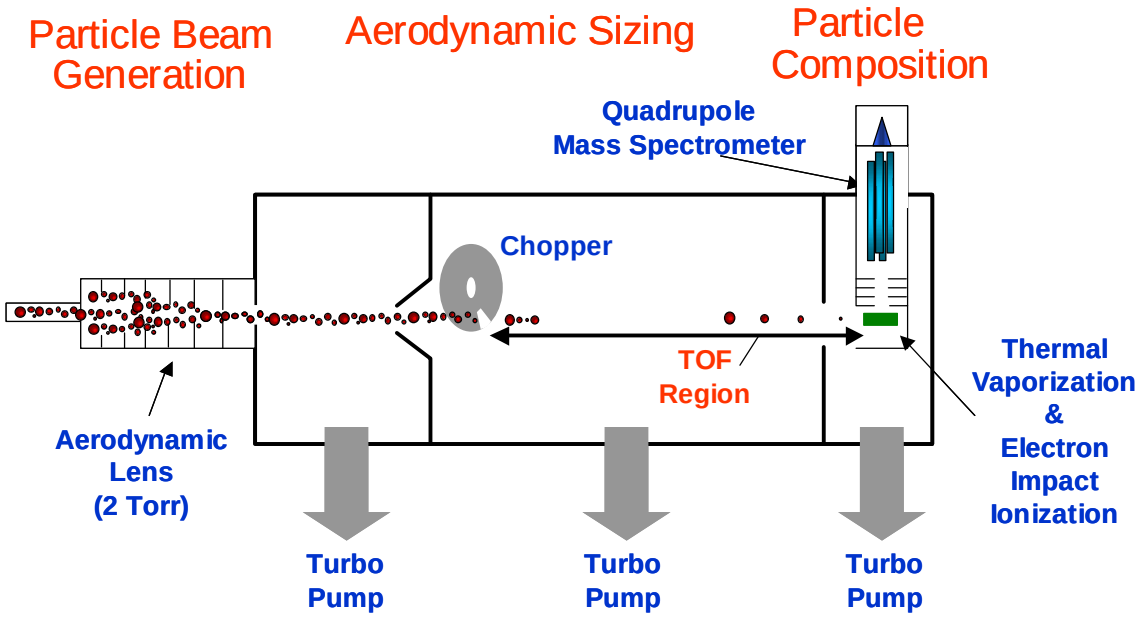

Figure 2: Aerosol nass spectrometer (AMS) used for chemical and physical composition of submicron aerosol.

Quantitative mass calibration of the instrument was performed by using a pure ammonium nitrate aerosol source. Particles were generated with an atomizer (TSI, Model 3076, USA) and then dried by passing the airflow through a silica gel. The monodisperse aerosol was generated by passing the polydisperse flow exiting the dryer into a differential mobility analyzer (TSI, Model DMA 3071). Detailed information about quantitative mass loading and size-distribution calibration is presented in Jayne et al. (2000).

3. Results and discussion

3.1 Chemical composition and size distribution of a Boeing 757 exhaust aerosols

Figures 3a and 3b show the time-series profiles of total organics measured during the entire experiment. The highest concentrations were observed during transient periods and gradually declined to reach a steady level until the next transient period. The transient period occurs during times when the engine power thrust is switched from one thrust level to the next, and last until the

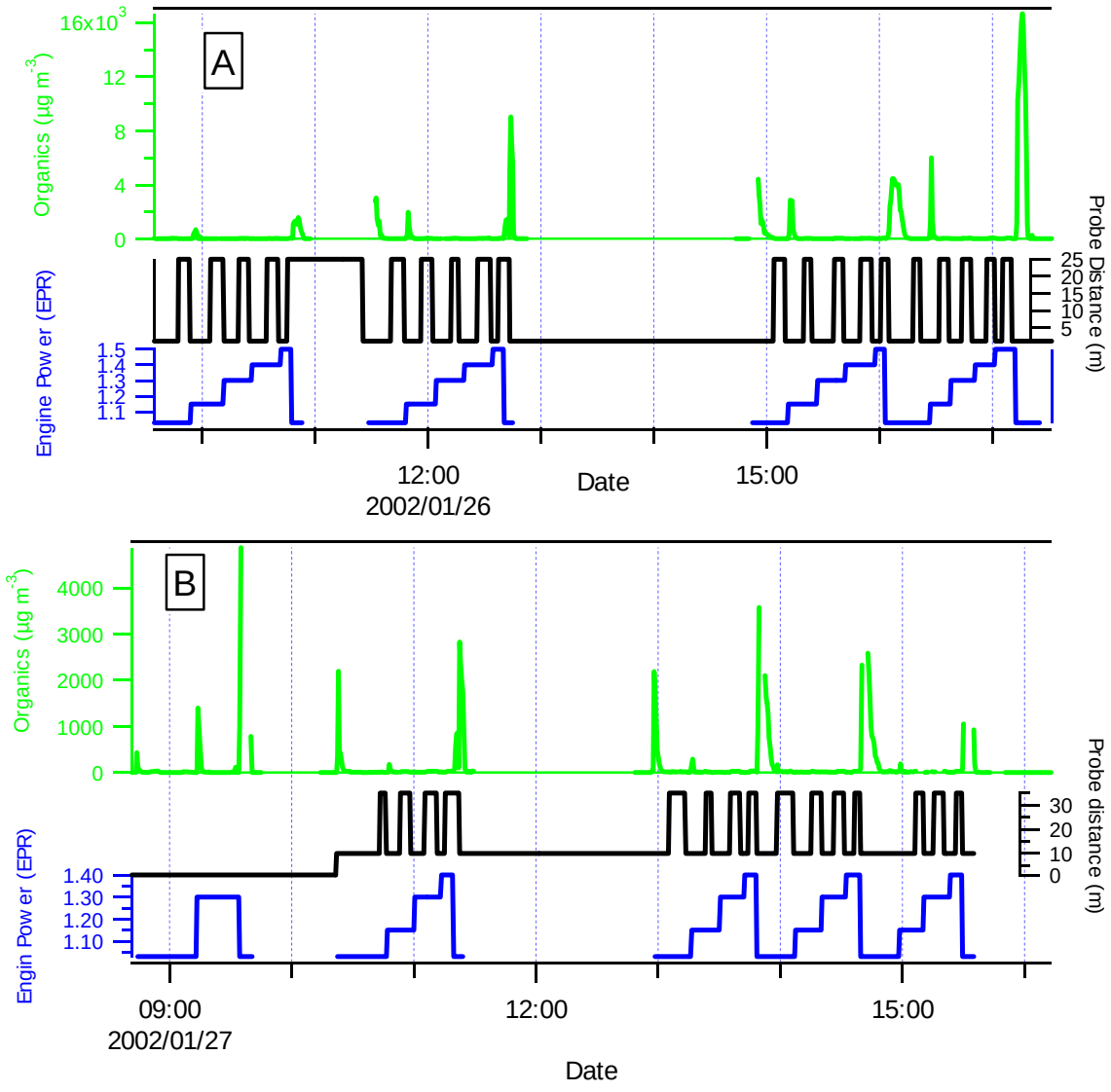

Figure 3: Time-series profiles of total organics measured during EXCAVATE experiment. A: experiment conducted on January 26, 2002. B: experiment conducted on January 27, 2002.

measured particle concentrations reach a steady-state condition. Figure 3 also shows that the most significant increases in concentration **(transient periods)** appear to happen especially during the startup (Idle to 1.15 EPR) and shut down procedures of the engine (high power to Idle).

3.1.1 Transient period

As already presented in Figures 3a and 3b, the transient periods are associated with a significant increase in total organics present in exhaust aerosols before declining to the steady levels. These experiments also show that the transient time varies from 5 to 8 minutes. For instance, a transient time during the start-up (from Idle to 1.15 EPR) takes about 10 minutes, and from 1.15 to 1.3 EPR takes about 6 minutes, and finally, from 1.5 EPR to Idle takes 7 to 8 minutes. It is also interesting to note that no increase in concentration was observed when the thrust engine was varied between 1.15 and 1.5 EPR.

The significant increase in concentration during transient periods could be explained by low efficiency combustion happening during the period of time when the engine adjusts to maximum efficiency combustion, and/or when additional oil is injected in the combustion chamber. Further information about the exact functioning of the engine (oil and fuel injection) during transient periods will be presented and discussed in another paper. In order to identify the source of organics present on aerosols, we have generated in our laboratory particles from pure JP-5 fuel and synthetic lubricating oil used during EXCAVATE and analyzed by the AMS. Figure 4 shows typical mass spectra of JP-5 fuel and synthetic lubricating oil. Analysis of these spectra mass spectra shows distinct mass spectra for fuel (JP-5) and lubricating oil. The turbine oil spectrum exhibits a strong signal at amu 55, 85, 99, 113, 127,155, 213, 227 and 241, that is not observed in the JP-5 fuel spectrum.

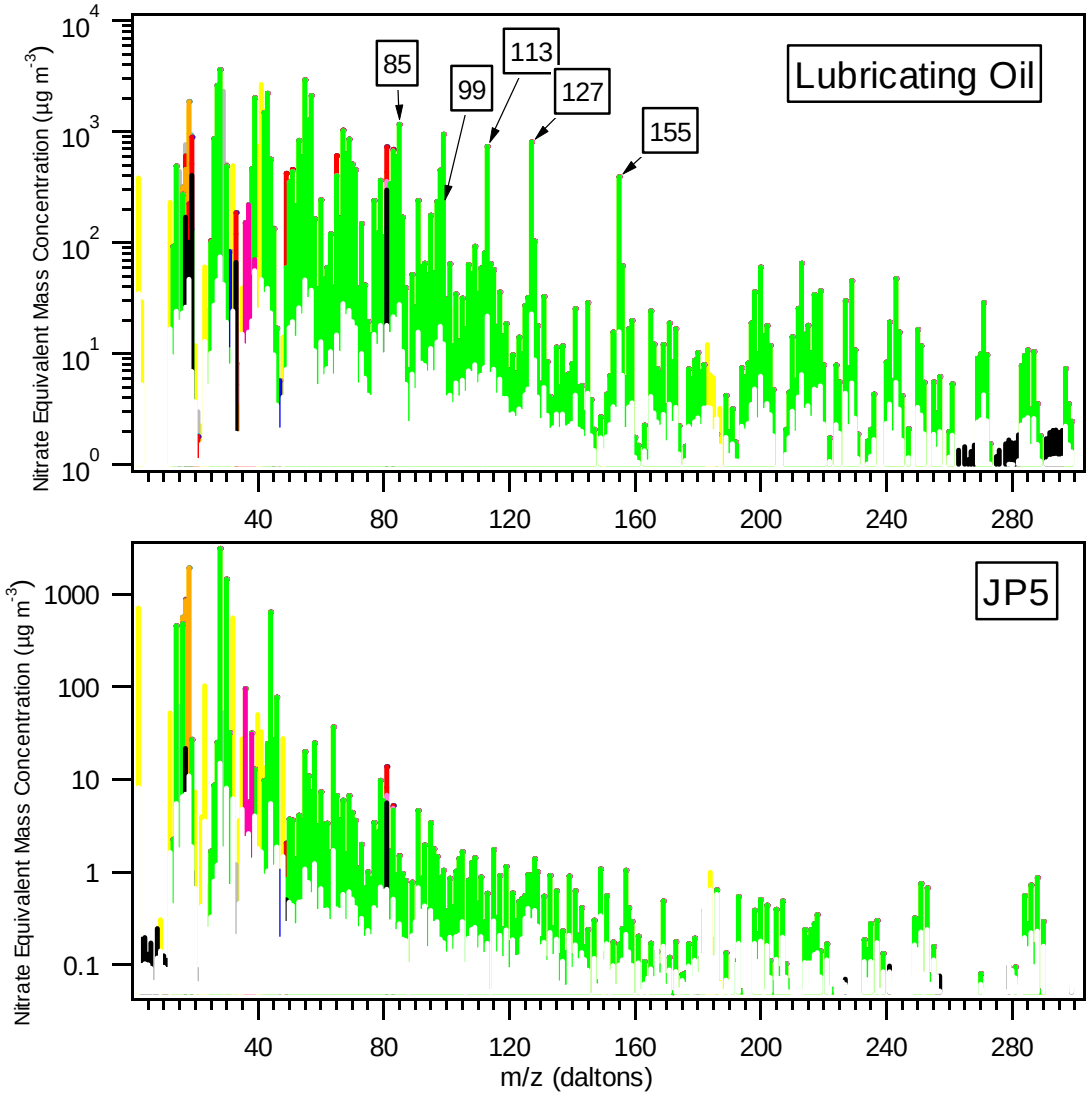

Figure 4: Typical mass spectra of JP5 and lubricating oil used during EXCAVATE field experiment.

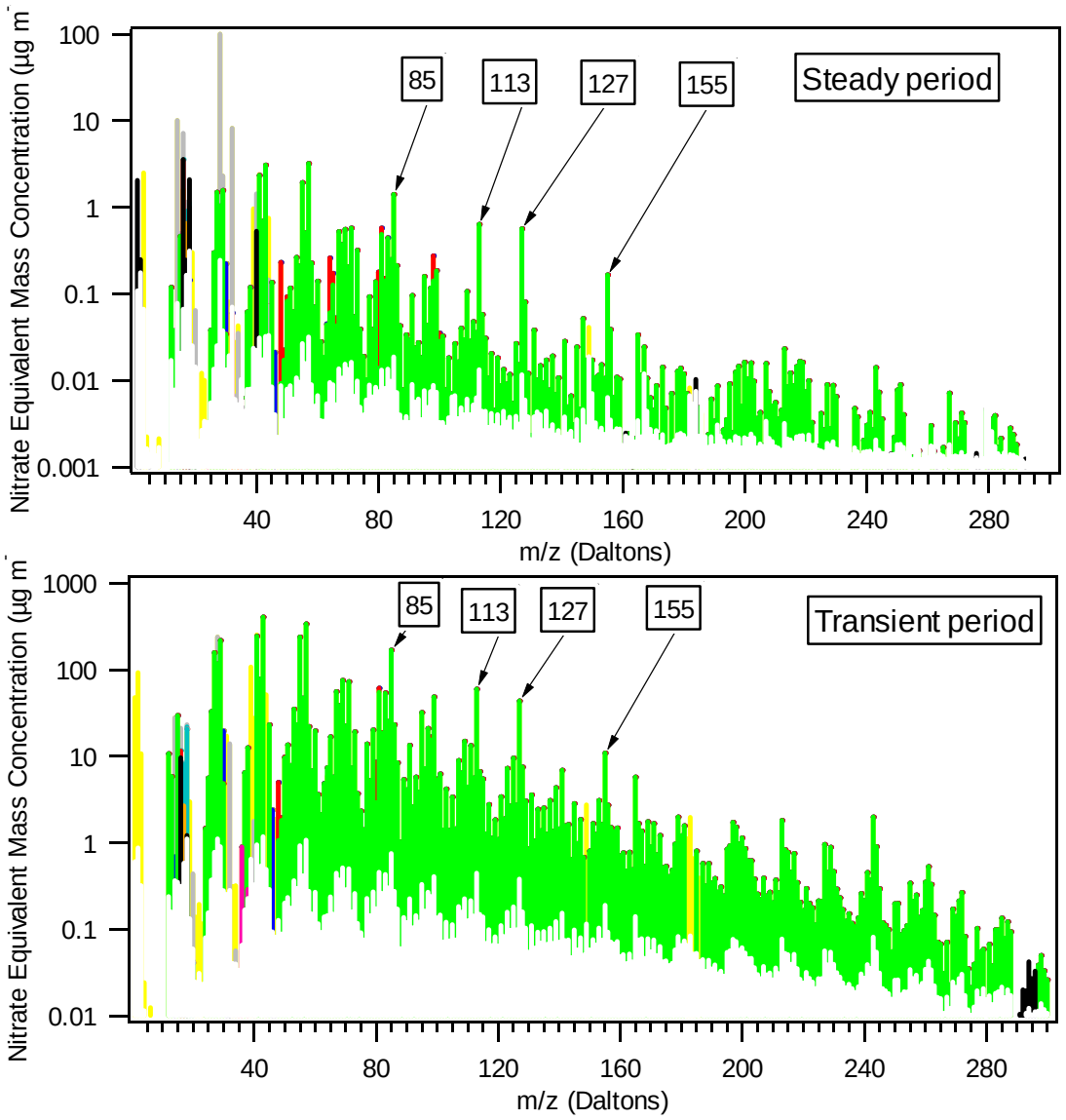

Figure 5: Typical mass spectrum measured during EXCAVATE.

The analysis of the mass spectra measured during EXCAVATE shows the presence of clear signals at amu 85, 99, 113, 127,155, 213, 227 and 241, during transient and steady conditions. An average mass spectra for transient and steady conditions is presented in Figure 5. These results suggest that the lubricating oil signature was always present in the particles emitted by the Rolls-Royce engine.

If we assume that the Rolls-Royce engine operates at different conditions (combustion efficiency, fuel and oil injection, etc.) we would expect to see a difference in aerosol composition between transient and steady conditions. In order to evaluate the variation in aerosol composition between transient and nontransient periods, variation of oil signature, plotted as function of total organics measured during the entire experiment (January 27, 2002), will be used. In this case, the oil signature is estimated as a total signal from amu 85, 99, 113, 127, 155, 213, 227, and 241. As shown in Figure 6, the oil-to-organic ratios show quite identical experimental slopes measured during transient and steady conditions equal to 0.438 (R^2= 0.86) and 0.451 (R^2=0.98), respectively. Only a slight difference of 2.8 percent in the experimental slope is observed, suggesting no significant variation in aerosol composition between transient and steady condition

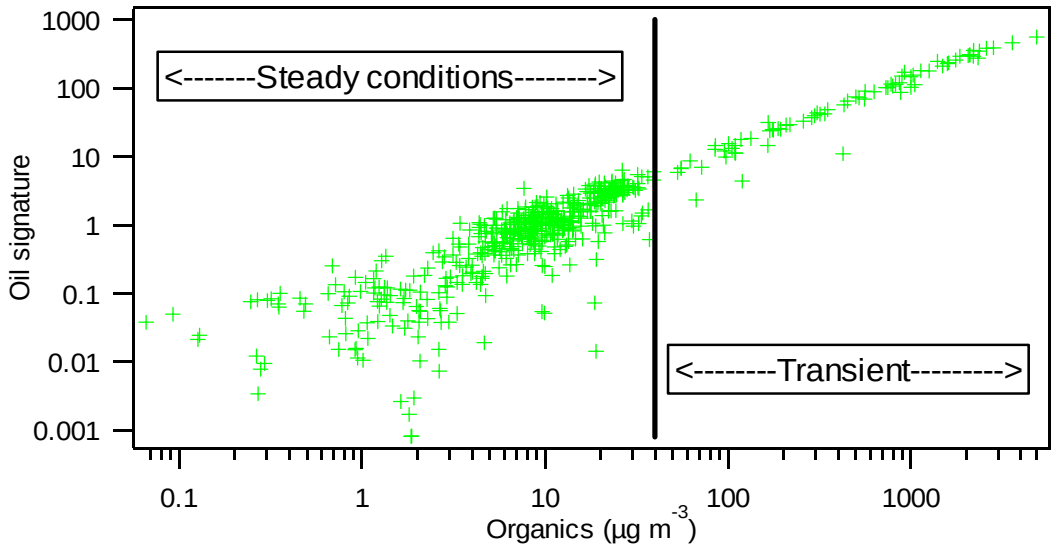

Figure 6: Variation of oil signature versus total organic during transient and steady conditions.

3.1.2 Non-transient period (steady conditions)

The nontransient period is characterized by a lapse of time where the concentrations are more or less steady during one particular setting of engine power and probe distance. Figure 7 illustrates the temporal trend of organics and sulfate mass loadings measured for four different engine power (Idle, 1.15, 1.3, 1.4 EPR) settings and two sampling probe distances (10 and 35 meters). During steady conditions, the organics and sulfate mass loadings were found in a range 1-35 μg m^{-3}, and 0.1–7 μg m^{-3} respectively. As presented in Figure 7, a significant increase in organics

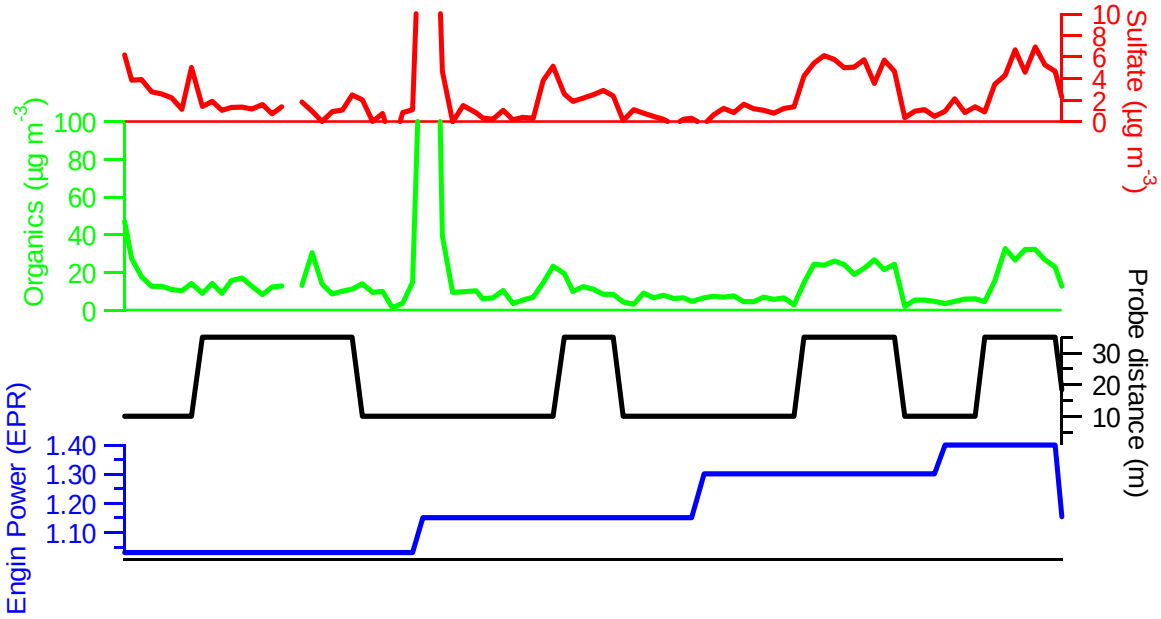

Figure 7: Variation of total organics and sulfate during steady condition as a function of engine power and probe distance.

and sulfate mass loading was observed when sampled between 10 and 35 meters. For instance, at engine power of 1.3 EPR, the organics concentrations increased from 5 to 25 μg m^{-3}. During the same period, sulfate also exhibits the same behavior. Their concentrations increased from 1 to 6 μg m^{-3}. The increase in concentration between 10 and 35 meters could be explained by condensation of gas-phase pollutants on preexisting aerosols occurring downstream of the exhaust plume. If this hypothesis is true, we would expect to see an increase in aerosol size distribution further downstream of the engine exhaust. Figure 8 shows the size distribution of

organics and sulfate as a function of probe distance (measured at 1, 10, 25, and 35 M) and at engine power of 1.4 EPR. This figure shows that the size distribution shift to larger sizes when sampled further downstream of the engine exhaust. This shift in size distribution confirms the presence of particle growth. Organics and sulfate seem to have similar aerodynamic diameters of about 30 nm when measured at 1 m behind the engine and increase when measured further downstream of the engine exhaust. The increase in the aerodynamic diameter of organic aerosols is found to be more pronounced than that of sulfate particles. For organics, the aerodynamic diameters increase from 30 to 300 nm, and from 30 to 70 nm for sulfate. The different growth behavior at the sulfate and organic containing particles suggests that they are externally mixed.

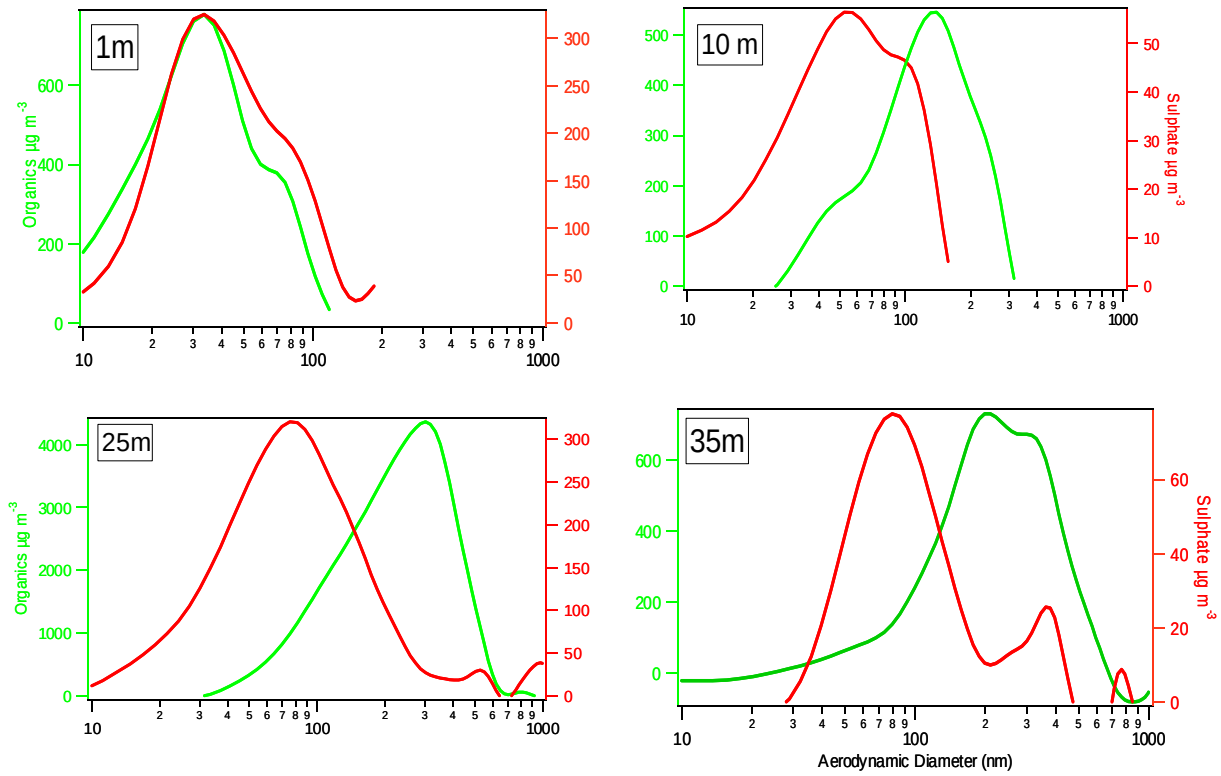

Figure 8: Variation of aerodynamic diameter of sulfate (red) and organics (green) as a function of probe distance and measured for engine power of 1.4 EPR.

3.2. Particle emission indices

The emission indices of sulfate and organics have been calculated for all engine power settings, sulfur fuel content and sampling distances behind the engine exhaust.

3.2.1. Influence of engine power settings

Figure 9 shows the variation if emission indices (EI) for sulfate and organics as a function of engine power. Here the data represent all samplings made at 1, 10, 25 and 35 M. The results

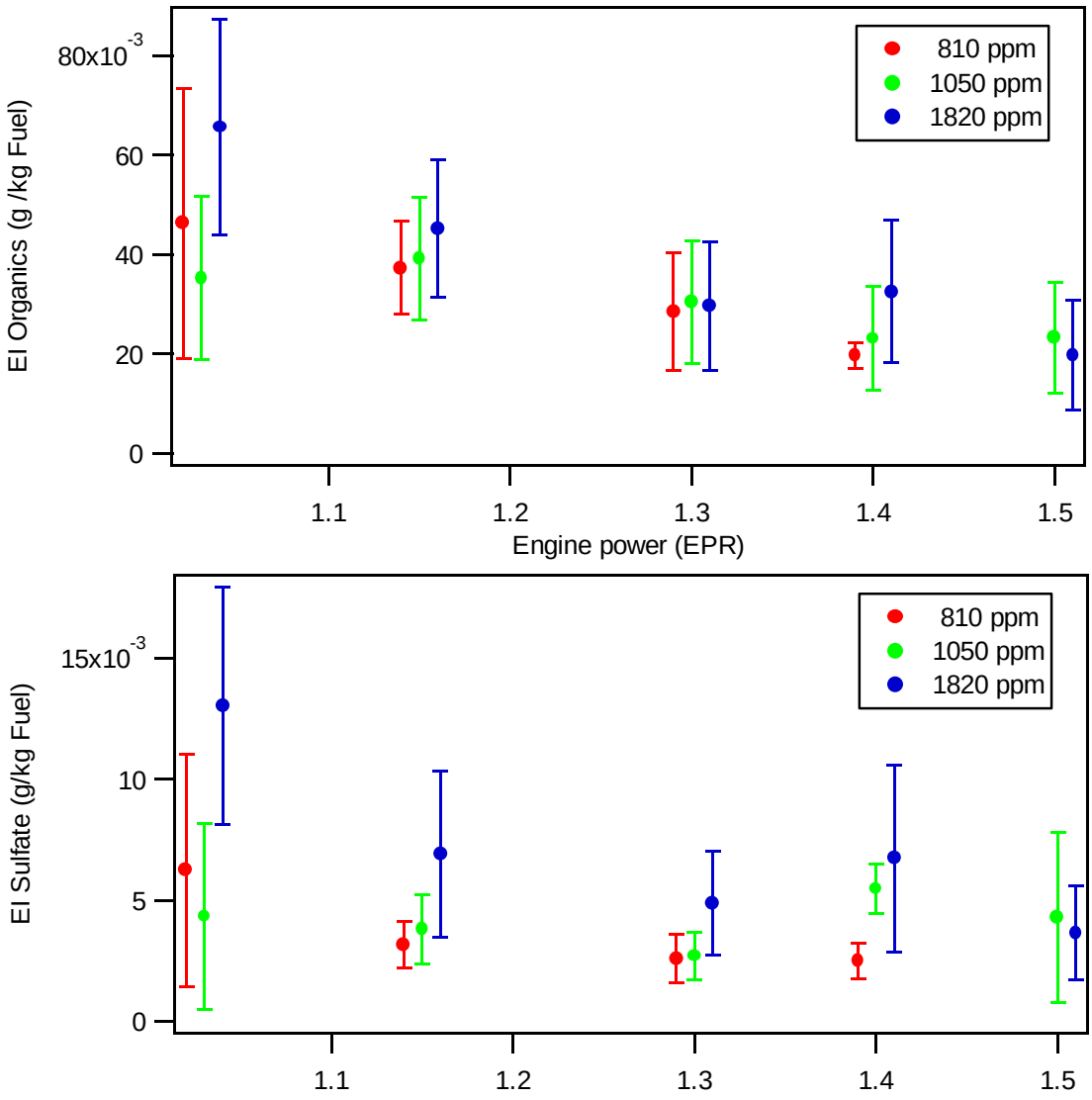

Figure 9: Emission indices versus engine power.
Error bars indicated experimental variability

show that the EI of organics decrease with engine power. At high engine power (1.5 EPR), the organic EI is estimated to 20-25 μg kg^{-1} of fuel, while at idle (1.03 EPR) the average EI is about 50 μg kg^{-1} of fuel. The decrease in EI as a function of engine power could be explained by better efficiency combustion at high engine power, and consequently, a reduction in the emissions of unburned fuel and oil. It is also important to note that the EI of organics as a function of engine power is found to be independent of fuel sulfur content.

Except for measurements made at idle (1.03 EPR), emission indices of sulfate appear to be independent of engine power settings and proportional to the fuel sulfur content. The highest EI correspond to the highest sulfur fuel content. For fuel sulfur content of 810 ppm, 1050 ppm and 1820 ppm, the average EI of sulfate are found equal to 2.5, 4 and 6 g kg^{-1} of fuel, respectively. The highest EI measured at idle could be due to quantification errors for sulfate from interference from organics. It is also possible that the steady-state was not really reached, and the high level reflects data measured from transient period.

3.2.2. Influence of sampling distance

Figure 10 shows the variation of EI as a function of sampling probe distance measured for all sulfur fuel content. Here the EI are found positively correlated with probe distance. The lowest EI are measured at 1 M behind the engine and the highest EI are measured at 35 M behind the engine. For all fuel used, the sulfate EIs increase with distance suggesting aerosol sulfate growth through gas to particle conversion downstream of the exhaust plumes. This conversion is occurring as the exhaust cool down as a consequence of dilution with ambient air. This is confirmed in Figure 8, where the size distribution of sulfate shift to bigger sizes when sampled downstream of the engine exhaust.

For sulfate, the EI are also found to be a function of sulfur fuel content. The lowest EI are measured for the lowest fuel sulfur content and vice-versa. At 35 M behind the engine, the sulfate EI increase by a factor of 2.89, while the fuel sulfur content increased by 2.14. Figure 11 shows the normalized Eis to 810 ppm of FSC as a function of probe distance. As presented in Figure 11,

good correlation between normalized EIs and sampling distance is observed, with an experimental slope of 1.348 $\times 10^{-4}$ (g kg^{-1} m^{-1}) and regression coefficient of R = 0.97. Within the uncertainty of our measurement, we can conclude that the EI is linearly proportional to fuel sulfur content.

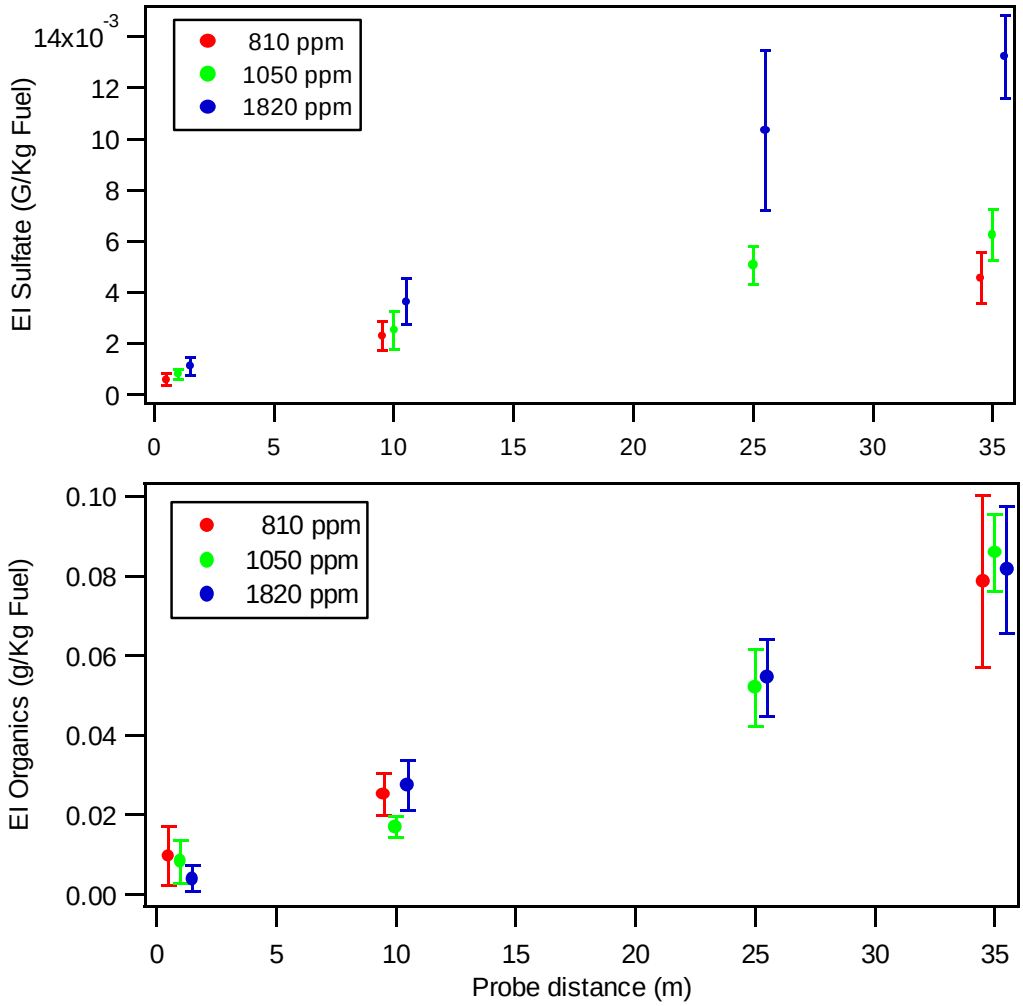

Figure 10: Emission indices versus probe distance.
Error bars indicated experiment variability.

While sulfate, organic emission indices are found to be independent of fuel sulfur content. Organic emission indices are positively correlated with sampling distance behind the engine. For instance, measurement made at 35 M behind the engine, the organics EI increase by a factor of 1.5 orders of magnitude to those measured at 1 M.

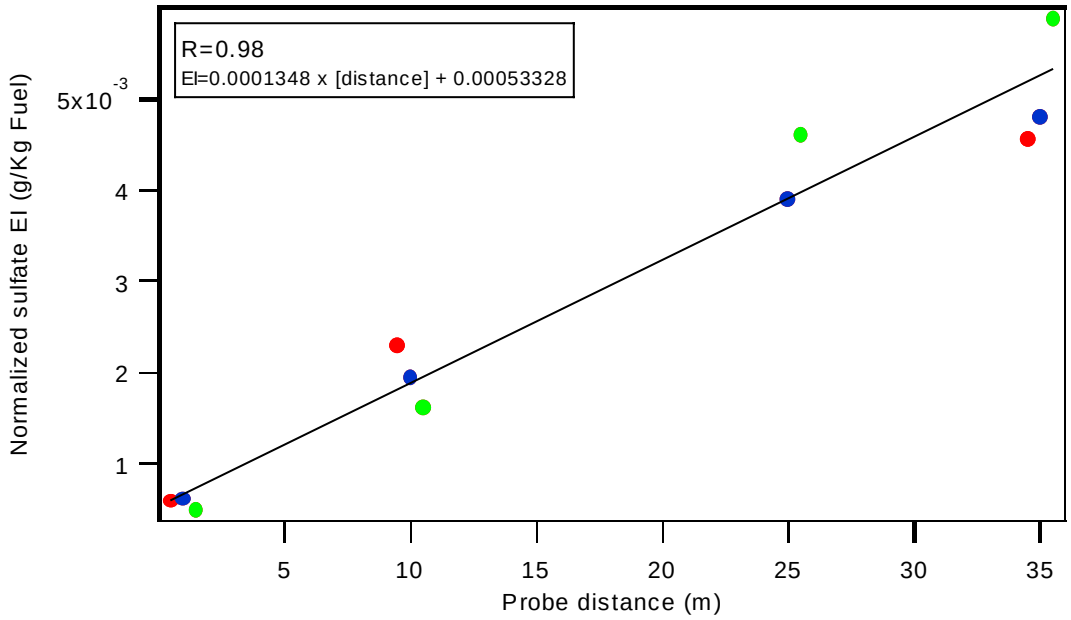

Figure 11: Emission indices normalized to 810 ppm of sulfur fuel content versus probe distance.

Conclusion

During EXCAVATE experiment, particulate emissions from a Boeing 757 equipped with a Rolls Royce engine were studied. Chemical and physical composition of PM2.5 was measured in real time with a resolution of 30 seconds. Time series profile of total organics and sulfate shows a presence of a transient period associated with extremely high mass loadings of pollutants. Thus, the transient period appears to happen during the start-up of the engine, from idle (1.03 EPR) to 1.15 EPR, and during engine shut down (1.5 to idle). Up to 5000 µg m^{-3} of organic was measured during transient period, whereas concentration during steady conditions was in a range of 1 to 30 µg m^{-3}. The presence of lubricating oil was found during steady and transient periods. Sulfate emission indices were found dependent on sulfur fuel content and positively correlated to the sampling probe distance. Organics emissions are also found positively correlated with sampling

distance but independent of sulfur fuel content. For EPR higher than 1.15, the EI are found more or less independent of the Engine power.

References

Brown R.C., Miake-Lye, R.C., Anderson, M.R. and Kolb, C.E, 1997: Aircraft sulfur emissions and the formation of visible contrails. Geophysical Research Letters, 24, pp. 385-388.

Curtius J., Arnold, F., Schulte, P, 2002: Sulfuric acid measurements in the exhaust plume of a jet aircraft in flight: Implication for the sulfuric acid formation efficiency. Geophysical Research Letters, 29, No.7, p. 10129.

Hagen D.E., Whitefield, P.D., 1996: . Particulate emissions in the exhaust plume from commercial jet aircraft under cruise conditions. Journal of Geophysical Research, 101, D14, pp. 19551-19557.

Jayne

Jensen E.J.,Toon, O.B., 1997: The potential impact of soot particles from aircraft exhaust on cirrus clouds. Geophysical Research Letters, 24, pp. 249-252.

Jimenez J. L., Jayne, J.T., Shi, Q., Kolb, C.E., Worsnop, D.R., Yourshaw, I., Seinfeld, J.H., Flagan, R.C., Zhang, X., Smith, K.A., Morris, J.W., Davidovits, P., 2003 : Ambient aerosol sampling using the Aerodyne Aerosol Mass Spectrometer. Journal of Geophysical Research 108, D7.

Miake-Lye R.C., Anderson, B.E., Cofer, W.R., Wallio, H.A., Norwicki, G.D., Ballenthin, J.O., Hunton, D.E., Knighton, W.B., Miller, T.M., Seeley, J.V., Viggiano, A.A., 1998: SOx oxidation and volatile aerosol in aircraft exhaust plumes depend on fuel sulfur content. Geophysical Research Letters, 25, No.10, pp.1677-1680.

APPENDIX G: AFRL Report on the NASA EXCAVATE Project

Thomas M. Miller, John O. Ballenthin, and Albert A. Viggiano

Air Force Research Laboratory, Space Vehicles Directorate,
29 Randolph Road, Hanscom AFB, MA 01731-3010

Introduction

The NASA EXCAVATE Project (Experiment to Characterize Aircraft Volatile Aerosol and Trace Species Emissions) took place in January of 2002 at NASA-Langley Research Center. The purpose was to analyze aerosol, gas and ion emissions from the jet engines of NASA Boeing-757 and T-38 aircraft operating with fuels of different sulfur levels, and with the Boeing 757 engine at distances of 1 and 10 m from the tip of the sampling pipe. This report concerns a subset of the measurements, those made by the Air Force Research Laboratory (AFRL) for emission indices of SO_2 and the concentration and mass speciation of chemiions, under various engine conditions (power setting and fuel type). [Radical-radical reactions (including excited-state reactions) in the combustion process can result in ionization (so-called chemiions).] The AFRL Chemical Ionization Mass Spectrometer (CIMS) was used to determine the mixing ratio of SO_2 in the engine exhaust. An AFRL Ion Mass Spectrometer (IMS) was used to determine the concentration and mass distribution of chemiions in the exhaust. A Gerdien condenser was used in an unsuccessful attempt to determine the chemiion concentration directly. The results of these measurements were expressed as emission indices by normalizing to NASA-Langley Research Center (LaRC) measurements of the mixing ratio of CO_2 in the exhaust, above ambient levels. Figure 1 shows the experimental setup used by all instruments.

Fig. 1. The test rig bolted to the tarmac behind a Boeing-757 engine. The IMS and CIMS instruments were mounted inside the test rig shown at the base of the sampling pipe. The Gerdien condenser was welded to the side of the sampling pipe. The tip of the sampling pipe was here 1 m behind the engine exhaust plane, and ran an additional distance of 2.29 m to the IMS inlet, or 2.51 m to the CIMS inlet. The sampling pipe had a different configuration for the T-38 aircraft, for which the engine was closer to the tarmac, and the pipe lengths were 2.22 m to the IMS inlet and 2.43 m to the CIMS inlet.

Instrumentation

The AFRL CIMS and IMS are identical except that the CIMS includes an ion source, producing ions which interact selectively with the sampled gas, while the IMS mass analyzes ions in the exhaust effluent stream that are produced in the combustion process. A sketch of the CIMS apparatus is shown in Fig. 2.

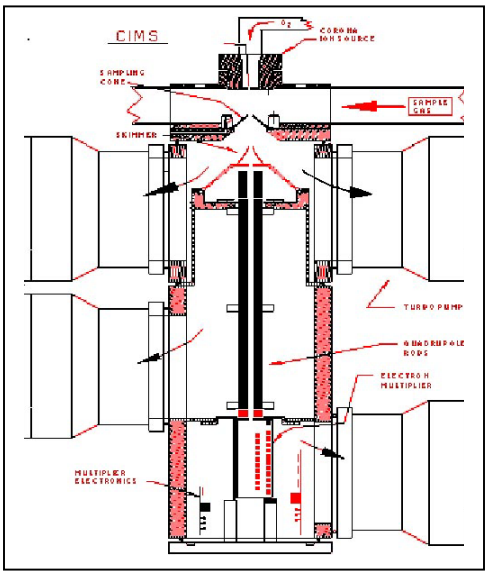

Fig. 2. The AFRL CIMS apparatus. The engine exhaust effluent entered from the right after being diluted with N_2. O_3^- ions were introduced into the effluent stream from the top. Within nano-seconds, the O_3^- ions reacted with CO_2 to yield CO_3^- ions. These ions, and their hydrates, then react with trace species in the engine effluent, notably SO_2 molecules. Ultimately, the SO_2 appears in the mass spectrum as SO_5^- and its hydrates. There is no background signal at those masses. Other trace species can be similarly detected: CO_3^- reacts with H_2SO_4 to give HSO_4^- and $CO_3^-(H_2SO_4)$; HNO_3 molecules yield $CO_3^-(HNO_3)$; and HCN ends up as $CO_3^-(HCN)$. Other gases such as NO, NO_2, and H_2S may be detected, but with much reduced efficiency.

The IMS does not require the dilution stage or the ion source, as it is being used to sample ions already existing in the engine exhaust effluent. The IMS electric quadrupole mass spectrometer was operated at a lower rf frequency than used with the CIMS because of previous reports of quite large ion clusters in aircraft exhaust. Because of this, the mass resolution and transmission efficiency of the IMS were both lower than with the CIMS instrument. As it turns out, however, the EXCAVATE sampling system placed the IMS much closer to the engine exhaust plane than in earlier work, and the ion clustering was minimal. That is, the core ions were observable, e.g., HSO_4^-.

The CIMS and IMS setup was complicated by having to deal with predicted temperatures which could result in melting of some of the materials used in the CIMS and IMS construction (e.g., solder and Teflon). In addition, the severe vibrations experienced in the test rig were unanticipated; two vacuum pump control circuit boards failed, and two calibration-gas flowmeters failed. The IMS lost its sampling orifice after the T-38 experiments were completed, due either to heating or vibration or both. On the final day of the experiment, a rotary vacuum pump failed, probably because the line voltage was rather low due to the long distances over which wiring was run at the remote test site. As a result of these problems, only the IMS was operating throughout the T-38 measurement period, and only the CIMS was operating during the Boeing-757 measurement period. The Gerdien condenser will be discussed in a later section.

IMS Results

Negative ion mass spectra were obtained for chemiions in the T-38 exhaust plume for engine rpm values of 49.5, 60, 70, 80, 90, and 100% of maximum. The results are significant because they were obtained much closer to the engine exhaust plane than in any previous work. Two examples of the IMS mass spectra are shown in Figs. 3 and 4. The results show that the total number of ions increases with engine rpm (with one exception discussed below) and that the mass spectrum moves to lower ion mass. Both observations are a result of the increased temperature and higher exhaust velocity (faster sampling) at higher rpm. At 100% rpm the major ion peak is HSO_4^-, which results from ion-molecule reactions taking place between the combustor and the sampling orifice of the IMS. An obvious reaction would involve NO_3^- and H_2SO_4, but the engine exhaust is too hot for H_2SO_4 to exist, so a more complete modeling of the ion chemistry in the sampling system will be suggested when these data are published. H_2SO_4 is clearly seen in the CIMS results as discussed in the following section.

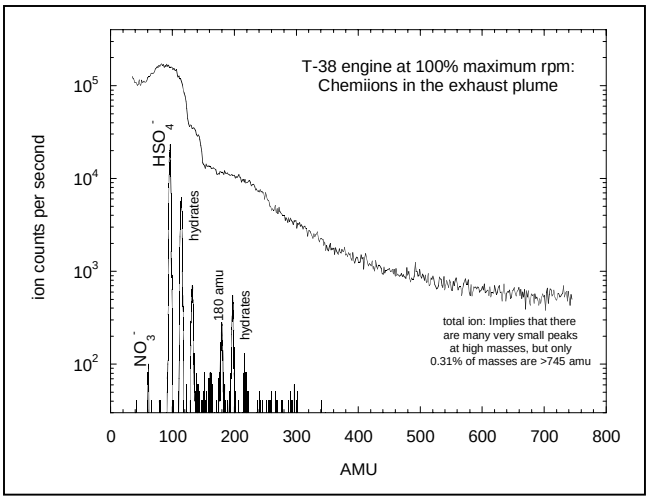

Fig. 3. Mass analysis of chemiions in the exhaust of the T-38 jet engine at a point 3.22 m following the engine exhaust plane, at 100% of maximum compressor rpm. The upper line is the total transmitted ion current through the mass spectrometer at zero resolving power. It shows that 90% of the ion masses are below 140 amu.

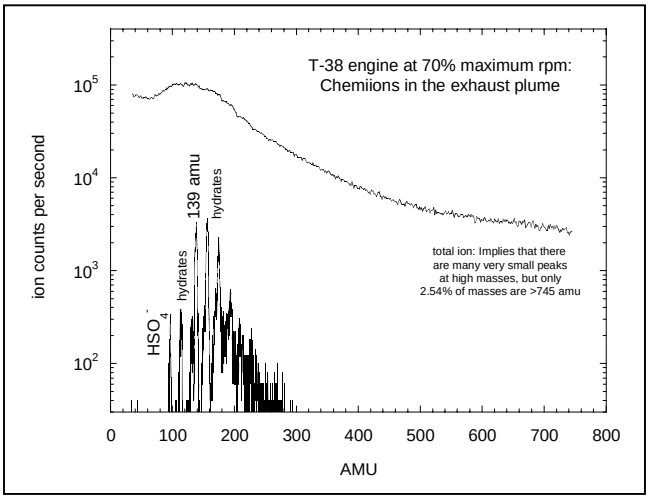

Fig. 4. Mass analysis of chemiions in the exhaust of the T-38 jet engine at a point 3.22 m following the engine exhaust plane, at 70% of maximum compressor rpm. The upper line is the total transmitted ion current through the mass spectrometer at zero resolving power. It shows that 90% of the ion masses are below 330 amu.

Some of the ion masses are as yet unassigned to a particular molecular species and may remain unassigned. In earlier work the unidentified masses were declared to be "oxyhydrocarbons," and this may be the best one can do at the present time.

The "total ion" data, as illustrated in Figs. 3 and 4, may be used to estimate the ion concentration (plasma density) at the engine exhaust plane. The ion concentration at the IMS sampling orifice is much lower than at the engine plane because of ion-ion mutual neutralization reactions that take place in the exhaust stream. The ion-ion mutual neutralization reaction rate constant is known to be about 10^{-26} cm^6 s^{-1} at atmospheric pressure and is approximately independent of the ion type because the neutralization is mobility-limited at this pressure. A temperature correction must be estimated. To determine the ion concentration at the engine exhaust plane from the total ion data, one needs (a) the detection efficiency of the IMS, (b) the gas temperature, and (c) the sampling time or velocity of the exhaust gas. Item (a) decreases with temperature because ions are swept into the IMS sampling orifice by the gas in the sampling pipe, and the throughput of gas is temperature dependent. The detection efficiency of the IMS was measured at room temperature in the laboratory at 1 atm pressure and found to be 980 cm^{-3} per ion count per second. The result of the calculations, effectively working backwards from the total ion signal to the engine exhaust plane, is shown in Fig. 5. An additional upward correction of the exhaust ion concentration may be made at a later date due to the problem of sampling from a high-velocity stream. This effect is discussed in the next section in regard to CIMS sampling of the Boeing-757 exhaust, but will not be as large an issue for the lower-velocity exhaust stream of the T-38.

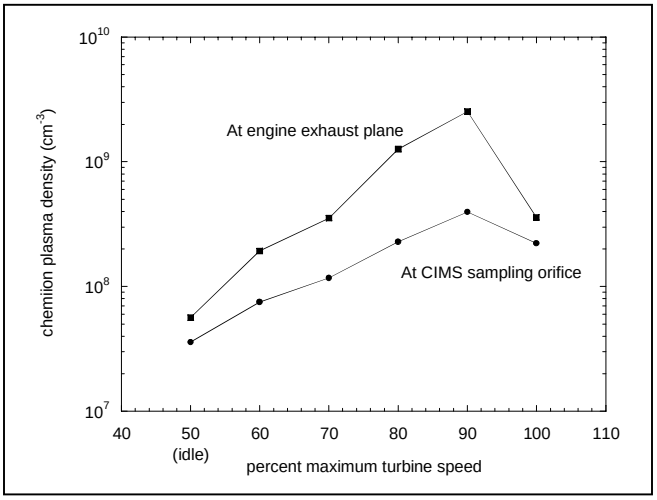

Fig. 5. The result of modeling backwards from the total IMS ion signal to obtain the ion concentration at the exhaust plane of the T-38 jet engine. Ion loss in the sampling path is due to ion-ion mutual neutralization.

The result that the ion concentration at 100% maximum rpm is lower than that at 90% is counterintuitive, but (a) the measurements were quite clear, and (b) both AFRL and NASA-LaRC measured a lower temperature at 100% maximum rpm than at 90%. Below, Fig. 6 shows the ion mass spectrum at 90% maximum rpm. The total ion signal is greater than that at 100% maximum rpm (Fig. 3), and even the HSO_4^- intensity is greater in this case. But the mass range of the ion spectrum is greater than in the 100% case, consistent with a longer reaction time in the sampling process.

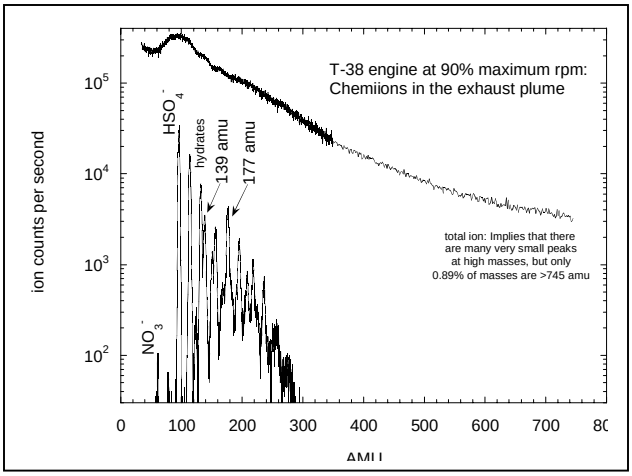

Fig. 6. Mass analysis of chemiions in the exhaust of the T-38 jet engine at a point 3.22 m following the engine exhaust plane, at 90% of maximum compressor rpm. The upper line is the total transmitted ion current through the mass spectrometer at zero resolving power. It shows that 90% of the ion masses are below 290 amu.

The IMS sampling orifice fell off at the completion of the T-38 test series. It was not possible to replace it in the field because the IMS sampling orifice plate was welded to the sampling pipe inside the test rig and not accessible in the time available. It would have been useful to examine the positive ion mass spectrum, even briefly. Earlier work at 29 m behind a jet engine showed ions at almost every mass, up to hundreds of amu, all of low intensity. The EXCAVATE test rig was so close to the engine that we could probably identify the core positive ions in a second EXCAVATE project. Furthermore, knowing now that a large mass range is not needed for the close sampling distances possible with EXCAVATE, the IMS could be set up for greater mass resolution and transmission efficiency.

CIMS Results

A typical CIMS spectrum is shown in Fig. 7. CO_3^- ions are converted mostly to CO_3^- hydrates by H_2O in the exhaust stream. The hydrated ions may react more efficiently with trace gases than CO_3^- itself. The appearance of SO_5^- and its hydrates indicates the concentration of SO_2 in the diluted effluent in the CIMS flow tube. Other species detected (NO, HCN, HNO_3, and H_2SO_4) are indicated by labels on the respective characteristic mass peaks in Fig. 7. For the EXCAVATE data analysis, the reactant ion intensity was taken to be the sum of the CO_3^- intensity and of its hydrates. Likewise, the product ion intensity was taken to be that of SO_5^- and its hydrates. The background signal for the product ions was ignored, as it was only a few counts per second with the engine off.

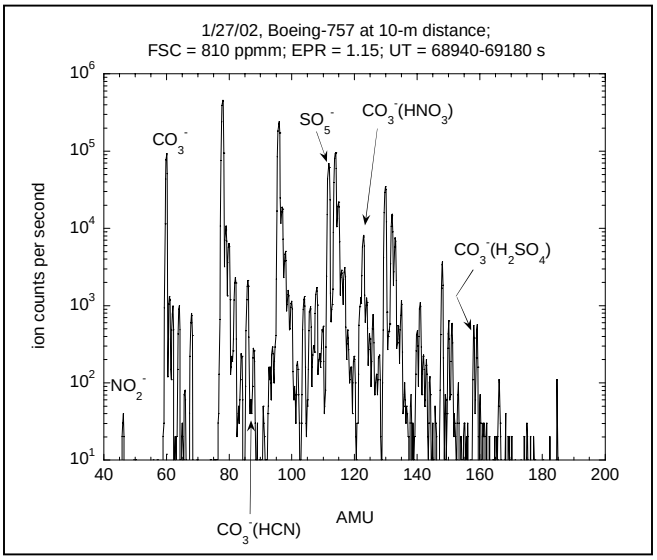

Fig. 7. A typical CIMS spectrum of the Boeing-757 exhaust from a distance of 10-m. Major mass peaks not labeled are hydrates of those that are marked; in particular, the mass peak beside the SO_5^- peak is the 3rd hydrate of CO_3^-. In a case such as this, the engine effluent is attenuating the reactant ions (including hydrates) by about 11%.

The CIMS measurements of SO_2 in the exhaust of the Boeing-757 suffered from three problems: (a) there was insufficient dilution of the engine effluent with N_2 gas; (b) the *in situ* SO_2 calibration system failed due to mechanical vibration; and (c) sampling from a high-velocity effluent stream left us with a difficult-to-quantify flow into the CIMS system. Dilution of the effluent is needed because the CIMS is too sensitive for sampling close to an engine; the system was designed for sampling plumes at a distance of miles. The CIMS effluent sampling orifice was made—in hindsight—much too large, and the liquid nitrogen tank would not supply enough N_2 to make up the dilution factor needed. The large concentration of SO_2 entering the CIMS flow tube taxed the CO_3^- detection scheme. The ideal situation is to have so little gas reacting with the CO_3^- (and hydrates) that only a few percent of the precursor ions were lost to reaction. In such a case, the response of the system is linear and easily calibrated. It was felt at the time that post-mission laboratory calibrations with known concentrations of H_2O and SO_2 would allow us to give SO_2 mixing ratios, even if somewhat less accurate than normal. However, when the reactant gas concentration is high enough to put us in the nonlinear region of trace gas detection, one must not only simulate the H_2O and SO_2 concentrations, but those of all the other (unknown) trace gas species as well, since all contribute to the nonlinear behavior. The bottom line is that while the results come out quite reasonable, on average, the precision and accuracy leave the results unsatisfying.

The final problem listed above, of sampling from a high-velocity stream, became evident when data from any of the test series were plotted versus increasing engine pressure ratio (EPR). The worst possible case is shown in Fig. 7, for the highest fuel sulfur content (FSC) and the closest engine sampling distance. At higher EPR, more fuel is burned, hence more SO_2 is produced; but the raw CIMS ion signal showed a roughly unchanging SO_2 intensity, once the engine was started. Furthermore, in this worst case, the product ion intensity is greater than the intensity of the unreacted precursor ions—that is, we are very much into the nonlinear detection regime because of insufficient dilution of the engine effluent. (For all of the data from the 10-m sampling distance, for which

the engine effluent was cooler and of lower velocity, the unreacted precursor ion intensity is always greater than the product ion intensity.)

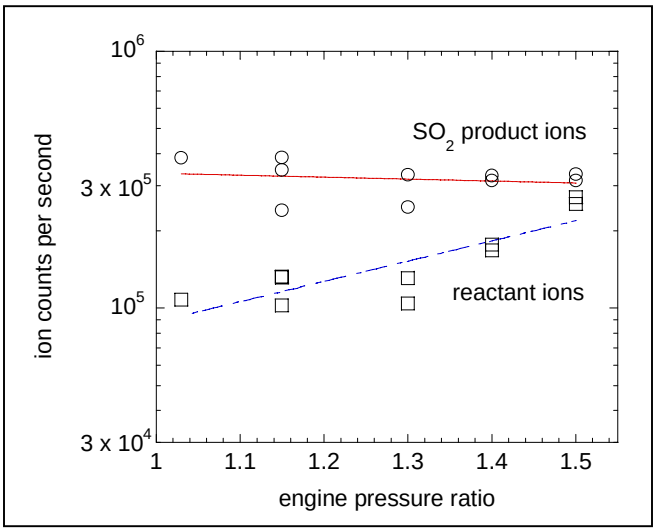

Fig. 8. Raw CIMS data from one of the Boeing-757 experiments with the engine exhaust plane 1-m from the tip of the sampling pipe, and a fuel sulfur content of 1820 ppmm. For simplicity, the "reactant ions" points are the sum of CO_3^- and its hydrates, and the "SO_2 product ions" is the sum of SO_5^- and its hydrates.

The fact that the intensity of unreacted precursor ions is *increasing* with EPR means that there is less engine effluent (and hence less SO_2) entering the CIMS flow tube as the engine is spooled up. It is apparent that the CIMS sampling orifice is passing much less engine effluent as the velocity of the exhaust in the engine sampling tube increases. A part of this is the known decrease in throughput of effluent as the temperature of the gas is increased with EPR. Another part is due to the nominal Bernoulli effect, calculated from the velocity of the engine exhaust, measured as it entered the sampling pipe. A third part seems to be due to an enhanced velocity effect as the gas in the sampling pipe passes over the conical sampling plate of the CIMS, in the same manner that early wind tunnels could produce a supersonic flow by placing a small bump before a model. Correcting for this effect would be nearly impossible except that data were obtained for two different engine sampling distances (1 and 10 m). The analysis procedure was to (a) simulate each of the 10-m data sets (for which the precursor ion attenuation is not excessive) in the laboratory to obtain sensitivity factors and SO_2 mixing ratios, (b) use the NASA-LaRC exhaust velocity and CO_2 measurements to deduce the effect that the velocity of the exhaust has on the effluent flow into the CIMS flow tube, (c) use laboratory simulations of the 1-m data sets to obtain sensitivity factors (for the case of large attenuation of the precursor ion intensity), and (d) apply the effluent flow correction obtained in part (b) to adjust the sensitivity factors for the 1-m data, and obtain SO_2 mixing ratios. Finally, the NASA-LaRC CO_2 measurements were used to place the results on an emission index scale of grams of SO_2 per kilogram of fuel. The NASA-LaRC FSC analysis was used to express the results in terms of fraction of FSC appearing as SO_2.

The table below gives a comparison of the difference in sampling the Boeing-757 exhaust at the two different distances. The exhaust gas is much hotter in the 1-m case, and moving much faster.

Table 1. NASA-LaRC data for the average Boeing-757 exhaust velocities and temperatures (T) during EXCAVATE, for the engine exhaust plane 1 or 10 m from the tip of the sampling pipe. Engine idle is EPR = 1.03; takeoff power is EPR = 1.7.

EPR	T at 1 m	T at 10 m	velocity at 1 m	velocity at 10 m
1.03	580 K	329 K	73 m/s	45 m/s
1.15	615	350	187	131
1.30	640	378	275	192
1.40	660	397	319	221
1.50	686	-	351	-

The formulas used in the SO_2 data presentation are the same ones used in analyzing the NASA-Glenn engine test results:

(a) If all the fuel sulfur were to be converted into SO_2, a fuel sulfur content (FSC) of 810 ppmm (0.081% S by mass) would give 0.00081 kg of S per kg of fuel or 0.00162 kg (1.62 g) of SO_2 per kg of fuel. Thus EI(SO_2) = 1.62 g/kg. The units may at times be expressed explicitly as g(SO_2)/kg(fuel), or abbreviated as g/kg. A FSC of 1050 would yield EI(SO_2) = 2.10 g/kg; and a FSC of 1820 would yield EI(SO_2) = 3.64 g/kg.

(b) EI(SO_2) = (64/12) (0.87) (SO_2 ppbv/CO_2 ppmv); the 0.87 is the fraction of carbon by mass, in the fuel. Dividing ppbv by ppmv puts the units of EI as g/kg, or more precisely as g(SO_2)/kg(fuel). Thus, EI(SO_2) = 4.64 (SO_2 ppbv/CO_2 ppmv).

The results are shown in Figs. 9 and 10 for the Boeing-757 at 1 and 10 m distances and are tabulated in Table 2. Points obtained on one data run in Fig. 9 (for a FSC of 1050) lie above 1, which is clearly not possible if the relevant parameters are accurate. We note that the amount of SO_2 measured was similar for the two data runs for FSC = 1050, but the CO_2 measurements were lower for the second set of data, leading to higher EI(SO_2) and higher fraction of FSC (above 1).

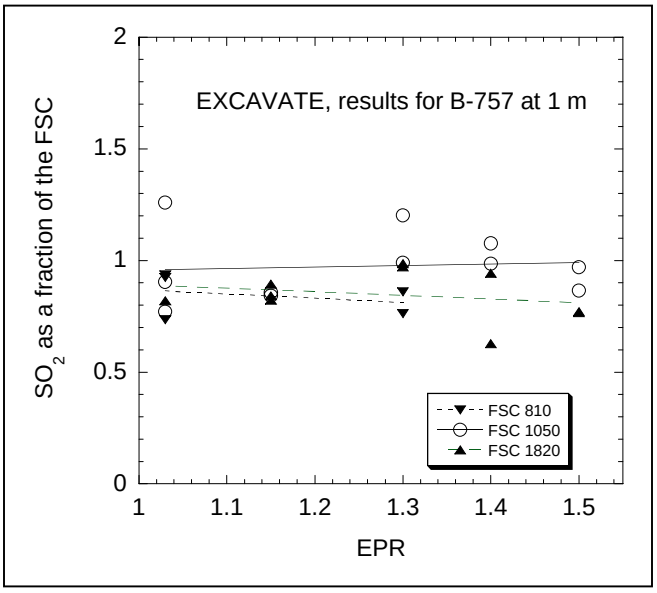

Fig. 9. SO_2 in the exhaust of the Boeing-757 at a distance of 1 m from the tip of the sampling pipe, as a fraction of the fuel sulfur content (FSC), as a function of the engine pressure ratio (EPR). Engine idle is EPR = 1.03; takeoff power is EPR = 1.7.

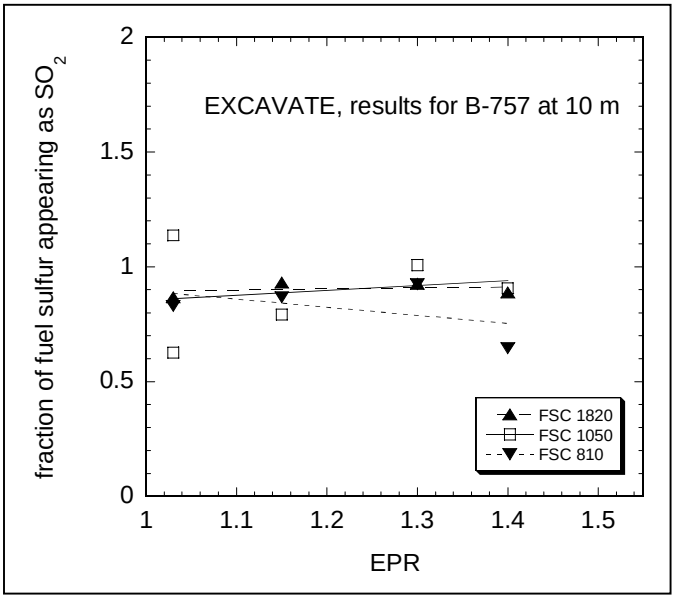

Fig. 10. SO_2 in the exhaust of the Boeing-757 at a distance of 10 m from the tip of the sampling pipe, as a fraction of the fuel sulfur content (FSC), as a function of the engine pressure ratio (EPR).

Table 2. Results of the Boeing-757 test series in January 2002. The temperature (T) and CO_2 measurements are those of NASA-LaRC. NASA-LaRC was also responsible for the

fuel sulfur analysis. The final column gives the SO_2 as a fraction of the FSC. The number of decimal places in the table exceeds the number of significant figures to avoid roundoff errors in further calculations.

Jul'n Day	start UT s	end UT s	D m	EPR	fuel S ppmm	T K	CO_2 ppmv	SO_2 ppbv	EI g/kg	fraction fuel S
26	53880	54180	1	1.15	1050	602	17938	6832	1.767	0.842
26	54720	55080	1	1.30	1050	623	21723	11819	2.525	1.202
26	55620	55980	1	1.40	1050	633	25512	12422	2.259	1.076
26	56520	56820	1	1.50	1050	633	28167	12366	2.037	0.970
26	57000	57180	1	1.03	1050	607	15544	8866	2.647	1.260
26	60510	60570	1	1.15	1820	611	21347	13764	2.992	0.822
26	60877	60985	1	1.15	1820	611	21347	14106	3.066	0.842
26	61540	61822	1	1.30	1820	634	25463	19710	3.592	0.987
26	62340	62710	1	1.40	1820	653	28360	20977	3.432	0.943
26	63268	63345	1	1.50	1820	680	30698	18571	2.807	0.771
26	71910	72210	1	1.03	1820	597	16722	10749	2.983	0.819
26	72810	73110	1	1.15	1820	621	20902	14651	3.252	0.894
26	73680	73980	1	1.30	1820	662	26689	20351	3.538	0.972
26	74640	74940	1	1.40	1820	692	30721	15161	2.290	0.629
26	75480	75590	1	1.50	1820	718	33429	20091	2.789	0.766
26	76320	76740	1	1.03	1050	628	13764	5638	1.901	0.905
26	77280	77400	1	1.15	1050	631	21973	8520	1.799	0.857
26	78420	78600	1	1.30	1050	668	26368	11809	2.078	0.990
26	78780	78900	1	1.40	1050	696	30360	13542	2.070	0.986
26	79650	79740	1	1.50	1050	712	33499	13141	1.820	0.867
26	80310	80640	1	1.03	1050	576	14390	5015	1.617	0.770
27	49740	50040	1	1.03	810	567	15714	5134	1.516	0.936
27	50760	51060	1	1.03	810	574	16040	5170	1.496	0.923
27	51240	51420	1	1.30	810	634	24348	7314	1.394	0.860
27	52020	52350	1	1.30	810	623	24632	6561	1.236	0.763
27	52440	52500	1	1.03	810	599	15527	3986	1.191	0.735
27	56280	56700	10	1.03	1050	322	1621	644	1.842	1.137
27	56910	57060	10	1.15	1050	344	2439	732	1.393	0.793
27	57660	57900	10	1.30	1050	372	3722	1310	1.633	1.008
27	58380	58560	10	1.40	1050	394	5004	1584	1.468	0.906
27	58680	58920	10	1.03	1050	330	1726	378	1.016	0.628
27	64860	65210	10	1.03	1820	335	1648	1074	3.021	0.830
27	65932	66070	10	1.15	1820	351	2432	1656	3.159	0.868
27	66693	66880	10	1.30	1820	378	3907	2833	3.364	0.924
27	67380	67640	10	1.40	1820	400	5220	3566	3.169	0.647

27	68020	68340	10	1.03	810	327	1599	485	1.405	0.867
27	68940	69180	10	1.15	810	359	2428	790	1.509	0.932
27	69700	69890	10	1.30	810	382	3799	1230	1.501	0.926
27	70410	70670	10	1.40	810	401	5085	1577	1.440	0.889

Gerdien Condenser

The Gerdien condenser was intended to provide a direct measurement of the charge density in the engine exhaust. The Gerdien condenser had a 12-inch current collector length and 1-inch I.D. The principle of operation is to apply a voltage sufficient to sweep all ions to the central collector or to the tube walls. The ion density (assuming singly-charged ions) could then be deduced if the exhaust velocity was known (a parameter provided by NASA-LaRC). Furthermore, if the signal-to-noise ratio is high enough, one can infer information about the relative mobilities (and hence masses) of the charge carriers from changes in the collected current with applied voltage. The Gerdien condenser worked well in a laboratory setting with ions in a clean gas flow, but failed in the field. Within a few minutes of engine startup, only small currents that appeared to be leakage currents were obtained. Examination of the Gerdien condenser after the test showed it to be coated with what appeared to be baked-on oil. This observation is consistent with the diesel-oil smell of the exhaust at startup or upon any increase in power, and with measurements of unburned oil or fuel, made by the aerosol groups. Thus, we were unable to provide an independent (and potentially more accurate) measurement of the concentration of chemiions in the jet exhaust for comparison to that deduced from the IMS data, but we learned valuable lessons from this first attempt: (1) the Gerdien condenser must be protected during engine startup, and indeed should only be exposed to the exhaust during a brief measurement period—there are various ways of doing this; and (2) the wiring must be protected from the coastal Virginia dew and rain. It should also be mentioned for future reference that the Gerdien condenser must be firmly mounted because of the severe vibrations experienced during the tests; the unit became airborne during one measurement period due to an error in welding the unit to the sampling pipe.

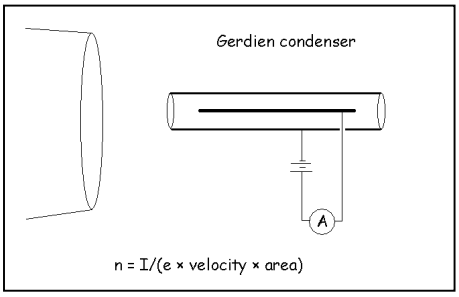

Fig. 11. A sketch of the Gerdien condenser mounted behind the engine exhaust plane. The electric potential between the inner and outer conductors is normally swept positively and negatively in order to deter-mine the positive and negative ion concentrations separately (assuming predominantly singly-charged ions).

Conclusions

The measurement of the concentration of negative chemiions and their mass distribution in the T-38 exhaust was the most successful portion of the AFRL work in EXCAVATE. The EXCAVATE setup allowed us to get closer to the engine exhaust plane than in any previous work of this type, enabling us to see the core ions, which show up as ion clusters at greater distances. These measurements are important because of the speculations and theoretical work on ion-induced nucleation of aerosols.

The CIMS measurements of SO_2 mixing ratios were unsatisfying; the results are in the right ballpark, but are not accurate enough to allow one to make definite statements about the speciation of fuel sulfur into gas phase and aerosol sulfur. The Gerdien condenser measurements failed due to coating of the instrument with engine oil, but the experience was valuable in showing how such measurements could be carried out in the future. In any case, the IMS measurements provided a good estimate of the plasma density at the T-38 engine exhaust plane.

Appendix H: Particle Size Distributions Measured in B757 Engine Plume During EXCAVATE

Terry Sanders, Paul Penko, Steve Culler, Monica Rivera*

NASA Glenn Research Center
*University of Toledo/NASA Glenn Research Center

I. Test Description

A ground-based test, the Experiment to Characterize Aircraft Volatile Aerosols and Trace Species Emissions (EXCAVATE), was conducted at NASA Langley Research Center, January 26 – 27, 2002, with a Boeing 757 aircraft. The aircraft was anchored on a tarmac and two probes were positioned downstream of the right-side engine, a Rolls Royce RB211-585. One probe was designed and fabricated by Arnold Engineering Development Center (AEDC) and had a 45.6 mm (1.794 in.) ID, Fig. 1. A second probe, constructed of 6.4 mm (0.25 in.) stainless-steel tubing at NASA Langley Research Center, had a 6 mm (0.22 in.) ID. The engine was run on JP-5 with three different sulfur concentrations, 810 ppm, 1050 ppm, 1820 ppm; and was operated over a range of power settings from idle to near-full power. Particulate size-distributions and concentrations were measured at four downstream axial locations: 1 m and 10 m with the AEDC particulate probe, and 25 m and 35 m with the Langley probe. Fuel with various sulfur contents was tested to address the long-standing question of the role of sulfur in the formation of volatile species. Several experimental and modeling studies have shown a correlation between fuel sulfur-content and particulate-emissions.[1-5] The object of EXCAVATE was to further study the effect of sulfur content on particulate number-concentration and size-distribution as a function of location in the engine plume and engine operating conditions.

II. Test Matrix

The test parameters are listed in Table 1. EPR is engine pressure-ratio which was varied from 1.03 (idle) to 1.5 (slightly less than take-off power). Dilution-ratio is the amount of dry, clean diluent added to the drawn exhaust-sample at the probe tip, and was calculated from the difference in carbon dioxide concentration between the exhaust-sample and diluted-sample. The JP-5 had an as-delivered sulfur-content of 810 ppm. Tetrahydrothiophene was blended with the JP-5 to obtain sulfur-concentrations of 1050 and 1820 ppm.

III. System Description and Experimental Approach

A mobile lab, the Particulate and Gaseous Emissions Measurement System (PAGEMS), was used during EXCAVATE to measure particulate-emissions in the Boeing 757 engine-plume. Distributions of particulate number-concentrations from 10 nm to 450 nm

were obtained using the equipment and hardware shown in Fig. 2. The measurement system included two Zalabsky differential-mobility analyzers (DMAs)[4], two Met One condensation-nuclei counters (CNCs), a TSI 3022 condensation-particle counter (CPC) (*CNC and CPC are trade names for the same type of instrument*), two stainless-steel 30-liter sample-storage tanks, a dew-point hygrometer, two filter-needle diluters, forty valves, and three vacuum pumps, one diaphragm and two vane pumps. Other components were an industrially-hardened computer, five ^{210}Po bi-polar chargers, several electrically-heated sample-transport lines, and thermocouples and pressure transducers. PAGEMS also has a suite of gaseous-emission analyzers that were not used in EXCAVATE and are not discussed here.

A custom-written LabVIEW program controlled the hardware and instrumentation for particle sampling and data acquisition via an Omega OM-1050 Remote Measurement and Control System. Temperatures, voltages, valve positions, pressures, relative humidity and flow rates were monitored by the OM-1050 and the data recorded every second.

Sample was extracted from the exhaust of the engine with the two probes previously described. The sample was diluted at the probe tip with dry nitrogen to reduce humidity, particle concentration and inhibit particle coagulation. The dilution-ratio, defined as

DR = TFR/SFR

where

TFR = undiluted sample flow rate + diluent flow rate, lpm
SFR = undiluted sample flow rate, lpm

varied from ~ 2:1 to 28:1 depending on engine condition and test parameter (see Table I). A common manifold with several tee-off points supplied sample to various research groups with a variety of measurement instruments. From this tee-off point a 30 m long electrically-heated line (6.25 mm OD) transported sample to PAGEMS. The line temperature was held to 180 C to prevent water-vapor condensation. On entering PAGEMS, the sample passed through a ^{210}Po bipolar charger exposing the particles to ions of plus and minus polarities to give them a known Boltzmann's charge distribution.

A fraction of the incoming sample, 1.5 liters per minute (lpm), was pulled into the TSI 3022 CPC. The CPC measured the total number-concentration of particulates in the diluted sample. This counter has an upper measurement limit of 10^7 particles/cc. To avoid exceeding this limit, a set of filter-needle diluters (FND) upstream of the TSI 3022 (see Fig. 2) further diluted the particle-concentrations by either 17:1 or 29:1. The design and construction of the FNDs are described in [6], and are essentially Whatman paper filters with hypodermic needles at the center of the filter. The diluters were calibrated to have a mean dilution-ratio over a range of particle sizes, in this case 10 nm – 450 nm.

The incoming sample was first stored in one of the 30-liter tanks. During a tank fill, the data acquisition system monitored the total number-concentration. Before filling with sample, the tank was purged for 3 minutes with dry particle-free air. For the range of plume particle-concentrations (10^5 to 10^7 particles/cc) encountered in EXCAVATE, a fill time of 3 – 5 minutes was required.

Following tank-fill, approximately 1.5 lpm of sample was drawn through another ^{210}Po bipolar charger then into a DMA. In the DMA, particles pass through a high-voltage electric field and the positively-charged particles are attracted to a negatively-charged center electrode. The electrode is surrounded by an annular-sheath of filtered air, at a rate of approximately 20 lpm, and has a small slit opening at the base. Depending on the voltage, particles with a certain electrical-mobility, and therefore size, migrate through the sheath air and exit through the slit. A Met One CNC downstream of the DMA measures the number-concentration of the mono-disperse aerosol from the DMA. Voltages were set on the center electrode to classify particles in the range of 10 nm to 450 nm. This process of classifying a particle sample with the DMA and counting the particles in the sample was termed a "sweep". The sweep data was then analyzed post-test to obtain the size distribution using an inversion algorithm provided by the University of Missouri-Rolla.[7] The total number-concentration was used in the inversion algorithm to normalize the measured size-distributions. More detailed information on the operating principles of the condensation-particle counters and differential-mobility analyzer, and their application in measuring particle-concentrations and size-distributions can be found in several texts.[8-9]

In the first phase of measurements, the AEDC particulate-probe was located at 1 m and the Langley probe at 25 m from the engine exit-plane. The aircraft was then moved forward about 9 m whereby the AEDC and Langley probes were at 10 m and 35 m, respectively, from the engine exit-plane. At both positions of the aircraft, the engine was operated over a range of pressure-ratios from idle (1.03 EPR) to near-full power (1.5 EPR) on fuel with each of three sulfur-concentrations: 810 ppm, 1050 ppm, and 1820 ppm. In all, particle measurements were made at 1 m, 10 m, 25 m, and 35 m downstream of the engine exit-plane. Dilution-ratios were varied, along with the other test parameters (see Table 1), and on average were about 9:1.

IV. Discussion of Results

Because of computer malfunctions, a number of measurements for certain engine operating points and probe locations were missed. In the context of the total test matrix, the data set is incomplete. Furthermore, the measurement system does not distinguish volatile and non-volatile particles. Consequentially, all particles present in the sample that reached the measurement equipment were counted.

In regard to exhaust-sample dilution, a test for the effect of sample-dilution on particle-distributions and concentration (corrected for dilution) was conducted at the University of Minnesota in July of 2003. An important result from that exercise was that probe and line losses reach a minimum at a dilution-ratio of ~8:1. For a dilution-ratio of 6:1, there was 2-5% greater loss, depending on particle size, than for the 8:1 dilution-ratio. Based on these findings, the EXCAVATE data for dilution-ratios less than about 6:1 were not considered.

The EXCAVATE test points are listed in Table 1. Each point has a run number and is described in terms of engine pressure-ratio (EPR), probe-location, fuel sulfur-content and dilution-ratio. Each point has an associated sweep-number specific to PAGEMS. Table 2 contains statistical information on the particle size-distributions for all the test points. The statistics were calculated using the Hatch-Choate equations from Hinds.[8] The data from the 1-m probe-location are the most complete and results are drawn primarily from this set. Particle-distributions for the 1-m probe-location are plotted in Figs. 3, 4, 5, and 8 for various EPRs and fuel sulfur-concentrations. Fig. 6 is for a probe location of 25 m and Fig. 7, for probe-locations of 1 m and 25 m. Count mean-diameter (CMD) as a function of fuel sulfur-concentration and EPR are plotted in Figs. 9 and10.

For the data at the 1-m probe-location:

1. In Fig. 3, fuel sulfur-content is 810 ppm. For an EPR of 1.03 the mode is ~15 nm. At an EPR of 1.3, the mode is shifted by a factor-of-two to 31 nm.
2. In Fig. 4 a shift in mode occurs as a function of EPR. For an EPR of 1.15, the mode is ~21 nm and, for 1.3, is ~ 28 nm.
3. In Fig. 5, sulfur content is 1820 ppm and the parameter is EPR. The mode shifts from ~25 nm at an EPR of 1.15 to ~35 nm for an EPR of 1.4.
4. For the size distributions plotted in Fig. 8, the mode remains about constant at ~30 nm for varying sulfur-content from 810 ppm to 1820 ppm at a constant EPR of 1.3.
5. In Fig. 9, the CMD increases from ~35 nm to ~55 nm over a range of EPR from 1.15 to 1.5 for a constant fuel sulfur-content of 1820 ppm.
6. In Fig. 10, the CMD remains about constant for a fuel sulfur-concentration ranging from 810 ppm to 1820 ppm and a fixed EPR of 1.3.

For the 25-m probe-location:

1. In Fig. 6, the CMD of the distributions is ~53 nm, indicating an increase in particle-size with distance in the plume from 1 m to 25 m.
2. In Fig. 7, there is a shift in mode with probe-location from ~28 nm at 1 m to ~40 nm at 25 m.

Results for the integrated values of the distributions, i.e. total number-count, number-based emission-index (EI_{number}) and mass-based emission-index (EI_{mass}) are given in Figs. 9 -14. The number- and mass-based emission-indices normalize the total particle-count and particle-mass for fuel burn-rate. The equation for number- and mass-based emission-indices is:

$$EI(X) = (\Delta X/\Delta CO_2) \times EI(CO_2) \times (M_{air}/\rho_{air}\, M_{co2}) \text{ [g/kg fuel]} \qquad (1)$$

ΔX = mass or number of particulate matter/unit volume of exhaust, above ambient, g/cc or #/cc
ΔCO_2 = concentration of CO_2 in exhaust above ambient, volume fraction
$EI(CO_2)$ = emission index of CO_2, ~ 3160 g/kg fuel burned
M_{air} = molecular mass of air, 29 kg/kmol

M_{co2} = molecular mass of CO_2, 44 kg/kmol
ρ_{air} = density of air, 1.295 g/cc for P_{std} = 101.326 kPa, T_{std} = 273 K

Particle-mass is calculated from the number distributions assuming that the particles are spherical and their density is 1 g/cc.

For the integrated values of the distributions:

1. Fig. 11 shows the change in total number-count as a function of EPR for a probe-position of 1 m and sulfur-content of 1820 ppm. There is a trend of increasing number count with EPR, ranging from about 1.86 $x10^7$ #/cc at an EPR of 1.15 to 2.09 $x10^7$ #/cc at an EPR of 1.4.
2. Fig. 12 is a plot of total number-count as a function of fuel sulfur-content for a probe-position of 1 m and EPR of 1.3. The number-count changes about an order-of-magnitude for a doubling of sulfur-content, ranging from 2.79 $x10^6$ #/cc at a sulfur-concentration of 810 ppm, to 1.84 $x10^7$ #/cc for a sulfur-concentration of 1820 ppm.
3. In Fig. 13, the results for EI_{number} show a different trend than total number count with EPR, with the highest value occurring at an EPR of 1.15.
4. In Fig. 14, the EI_{number} shows a trend similar to the total-number count as a function of fuel sulfur-content.
5. The EI_{mass}, plotted as a function of EPR in Fig. 15, has a minimum at an EPR of 1.15. This occurs because the count mean-diameter is smaller for an EPR of 1.15 than it is for higher EPRs.
6. The EI_{mass} as a function of sulfur-content, Fig. 16, shows a similar trend as the EI_{number} in Fig. 14.

VI. Experimental Uncertainty

Two components of experimental uncertainty are addressed. The first type, commonly known as systemic error, entails diffusional particle loss in the sample transport line and DMA. Diffusional loss in the transport line is termed line-transmission efficiency and diffusional loss in the DMA, DMA efficiency. Particle loss in the transport line is a function of flow rate, line diameter, and density of the aerosol medium, expressed as Reynolds Number; and line length and particle size. For this test, Reynolds Numbers were < 2 x 10^3, with the flow largely laminar. Calculated transmission efficiencies, for 30.5 m (100 ft.) of 6.4 mm (0.25 in.) tube heated to 180 C (350 F), vary from about 60% for a particle size of 10 nm to nearly 98% for particles > 100 nm. DMA efficiency is from ref. [3] and is 3%. The data presented in this report are not corrected for transmission-line or DMA losses.

Uncertainty in the data, i.e. precision error, is given as the upper and lower values of quantities calculated from the size distributions such as total number-count or EI. In most cases, a sufficient number of data points at a given condition are not available for standard statistical analysis, e.g. standard deviation. Plotted values are the mean of the

calculated quantities for test conditions where there is more than one data point. In some cases, only one data point is available and is presented with no uncertainty bar.

VII. Summary

In general, total number-count, number-based EI and mass-based EI increase with fuel sulfur-content and EPR. CMD increases with EPR but is about constant with fuel sulfur-content for a fixed location in the exhaust plume. The limited comparison of the particle-distributions at the 1-m and 25-m probe-locations indicates that the mode and CMD both increase with distance in the plume.

Unfortunately, problems encountered with the equipment did not allow measurement of particle-distributions at all test points. In particular, data at various probe-locations in the engine-plume, other than 1 m, are sparse. Furthermore, there is no distinction in the data between volatile and nonvolatile particle number-concentrations.

Acknowledgments

The contribution of Alexia Finotello, Summer Intern, is greatly appreciated in the analysis and archiving of the data. The EXCAVATE Project was organized and funded by the UEET Project Office, Dr. Chowen Wey, Project Manager. Her encouragement and support are most appreciated.

VIII. References

1. Brown, R.C., Anderson, M.R., Miake-Lye, R.C., and Kolb, C.E., "Aircraft Exhaust Sulfur Emissions", Geophys. Res. Lett. Vol. 23, pp. 3603-3606, 1996.
2. Fahey, D.W. *et al.,* "Emission Measurements of the Concorde Supersonic Aircraft in the Lower Stratosphere", Science Vol. 270, pp. 70-74, 1995.
3. Karcher, B., Peter, Th., Biermann, U.M., and Schumann, U., "The Initial Composition of Jet Condensation Trails", J. Atmos. Sci., Vol. 53, pp. 3066-3083, 1996.
4. Schmid, O. Tandem Differential Mobility Analyzer Studies and Aerosol Volatility, Ph.D. Thesis, University of Missouri, Rolla, Missouri, 2000.
5. Schumann, U., Strom, J., Busen, R., Baumann, R., Gierens, K., Krautstrunk, M., Schroder, F.P., and Stingl, J., "In situ observations of particles in jet aircraft exhaust and contrails for different sulfur-containing fuels", J. Geophys. Res., 101, pp. 6853-6869, 1996.
6. Olson, D.D., Trueblood, M.B., and Whitefield, P.D., "The Development of a Novel Dilution Technique for Sub-micron Particulate Characterization", OURE Program Report, University of Missouri-Rolla, 1996.
7. Hagen, D. E., and Alofs, D. J., "A Linear Inversion Method to Obtain Aerosol Size distributions from Measurements with a Differential Mobility Analyzer", Aerosol Science and Technology, Vol. 2, pp. 465-475, 1983.

8. Hinds, W. C. *Aerosol Technology;* Wiley: New York, 1999.
9. Willeke, K., and Baron, P.A., *Aerosol Measurement*;Van Nostrand Reinhold: NewYork, 1993.

IX Appendix A: Hardware dimensions and system parameters.

Dimensions of the Zalabsky Differential Mobility analyzers used for the EXCAVATE tests.

Rod O.D., cm	Cylinder I.D., cm	Length, cm
r =4.445	r =2.540	72.77

Flow rates through the DMA and the high voltage range used in the measurements.

DMA aerosol flow rate, lpm	DMA sheath flow rate, lpm	Initial DMA sweep Voltage, V	Final DMA sweep Voltage, V
1.5	20	17.5	14, 532

Table 1. EXCAVATE Test Parameters

Run Number	EPR	Probe Location, m	Fuel Sulfur, ppm	Dilution Ratio	Sweep Number
31	1.15	1	1050	6.14	13
33	1.3	1	1050	7.15	14
33	1.3	1	1050	7.15	15
31	1.15	1	1050	6.14	16
37	1.4	25	1050	17.24	17
40	1.5	25	1050	18.1	18
40	1.5	25	1050	18.1	19
43	1.03	1	1820	4.52	20
46	1.15	1	1820	7.97	21
46	1.15	1	1820	7.97	22
49	1.3	1	1820	7.96	23
49	1.3	1	1820	7.96	24
52	1.4	1	1820	8.09	25
53	1.4	25	1820	20.23	26
56	1.03	25	1820	28.74	27
60	1.03	1	1820	4.55	01
63	1.15	1	1820	9.44	02
63	1.15	1	1820	9.44	03
66	1.3	1	1820	8.95	04
68	1.4	1	1820	9.29	05
69	1.4	1	1820	11.46	06
71	1.5	1	1820	10.67	07
78	1.15	1	1050	8.68	08
78	1.15	1	1050	8.68	09
82	1.3	25	1050	22.67	10
84	1.4	1	1050	9.29	11
88	1.5	25	1050	21.01	12
93	1.03	1	810	5.04	28
97	1.03	1	810	11.28	29
98	1.3	1	810	7.44	30
99	1.3	1	810	15.84	31
102	1.03	10	1050	1.6	32
103	1.03	10	1050	1.98	33
105	1.15	35	1050	2.99	34
108	1.3	10	1050	3.39	35
109	1.3	35	1050	3.88	36
109	1.3	35	1050	3.88	37
115	1.03	10	1820	2.38	38
115	1.03	10	1820	2.38	39
118	1.15	10	1820	3.52	40
121	1.3	10	1820	4.36	41
124	1.4	35	1820	6.15	42
124	1.4	35	1820	6.15	43
127	1.03	10	810	2.08	44
130	1.15	10	810	2.34	45
133	1.3	10	810	3.47	46
137	1.4	35	810	4.5	47
139	1.03	35	1820	2.89	48
141	1.15	10	1820	2.51	49
145	1.3	35	1820	3.87	50

Table 2. EXCAVATE Statistical Data

Run Number	Sweep Number	Standard Deviation	Geometric Standard Deviation	Count Median Dia., nm	Mode nm	Count Mean Dia., nm	Average Mass Dia., nm	Mass Median Dia., nm	Mass Mean Dia., nm	Mass EI g/kg fuel	Number EI #/kg fuel
31	13	23.8	1.1	30	23	33	42	61	68	6.02E-06	1.51E+16
33	14	32.4	1.2	37	28	42	55	83	95	2.66E-06	3.09E+15
33	15	36.1	1.2	40	30	46	60	92	106	3.46E-06	3.09E+15
31	16	43.4	1.1	47	36	53	69	102	116	5.03E-06	2.91E+15
37	17	21.7	1.4	22	12	30	58	151	208	2.12E-05	1.92E+16
40	18	42.3	1.2	44	30	53	77	134	162	2.90E-05	1.65E+16
40	19	42.3	1.2	43	28	53	81	153	188	2.95E-05	1.65E+16
43	20	48.5	1.2	49	34	58	84	143	171	1.31E-05	4.57E+15
46	21	14.8	1.3	19	12	23	37	76	96	7.89E-06	1.55E+16
46	22	13.5	1.2	18	12	23	34	62	77	3.88E-06	1.55E+16
49	23	34.7	1.1	39	30	44	58	87	99	1.18E-05	1.18E+16
49	24	36.8	1.2	40	30	46	62	96	111	1.45E-05	1.18E+16
52	25	44.0	1.2	46	35	54	72	112	129	2.16E-05	1.15E+16
53	26	46.4	1.2	48	35	56	76	122	142	1.53E-04	7.23E+16
56	27	48.5	1.2	50	38	58	78	121	140	3.25E-04	1.39E+17
60	1	36.8	1.4	33	17	46	90	248	347	4.66E-05	1.31E+16
63	2	29.2	1.2	33	25	39	52	82	95	6.11E-06	8.82E+15
63	3	30.4	1.2	35	26	40	54	83	96	6.40E-06	8.82E+15
66	4	38.1	1.2	41	30	48	65	101	118	9.49E-06	7.22E+15
68	5	41.7	1.2	44	31	51	71	116	137	1.59E-05	9.27E+15
69	6	41.9	1.2	44	33	51	70	110	128	1.98E-05	1.20E+16
71	7	45.5	1.2	47	35	55	75	119	138	2.91E-06	1.41E+16
78	8	25.4	1.3	27	16	35	58	126	162	1.96E-06	2.64E+15
78	9	27.7	1.3	30	19	37	58	114	142	2.13E-06	2.64E+15
82	10	49.2	1.1	52	40	59	76	111	126	2.94E-05	1.35E+16
84	11	42.0	1.2	44	32	52	71	112	131	5.48E-06	3.26E+15
88	12	45.6	1.2	48	36	55	74	113	130	6.96E-05	3.60E+16
93	28	20.7	1.2	26	20	30	40	61	70	3.07E-07	5.82E+14
97	29	20.9	1.3	24	15	30	48	95	120	1.25E-06	2.34E+15
98	30	37.3	1.2	41	31	47	62	93	107	1.05E-06	8.70E+14
99	31	38.1	1.2	41	30	48	65	103	119	4.88E-06	3.93E+15
102	32	14.4	1.3	18	12	23	36	69	85	3.25E-07	8.30E+14
103	33	3.4	1.1	12	11	13	14	16	17	1.43E-07	1.46E+15
105	34	4.8	1.0	14	12	14	15	17	18	1.17E-07	2.07E+15
108	35	36.4	1.2	39	27	46	67	116	139	1.91E-06	1.48E+15
109	36	32.6	1.3	33	21	42	69	141	180	2.54E-06	1.90E+15
109	37	33.6	1.3	34	22	43	68	135	170	2.67E-06	1.90E+15
115	38	49.9	1.5	39	17	60	140	500	763	9.87E-06	1.66E+15
115	39	25.1	1.5	21	9	32	74	260	395	5.36E-06	1.66E+15
118	40	31.9	1.2	35	24	41	59	100	120	3.04E-06	2.58E+15
121	41	41.1	1.2	44	33	51	68	105	122	3.61E-06	2.36E+15
124	42	42.8	1.2	45	33	52	71	112	130	6.48E-06	3.49E+15
124	43	26.0	1.5	24	11	36	77	245	360	4.35E-06	3.49E+15
127	44	45.0	1.2	47	35	55	73	114	132	2.58E-06	1.30E+15
130	45	36.6	1.1	41	32	46	59	85	96	1.28E-06	1.10E+15
133	46	38.6	1.2	41	30	48	67	109	128	2.18E-06	1.50E+15
137	47	49.1	1.2	50	37	58	79	123	143	5.61E-06	1.90E+15
139	48	7.6	1.1	14	11	16	21	30	33	8.38E-07	3.18E+15
141	49	34.2	1.1	39	30	44	56	81	92	1.30E-06	1.29E+15
145	50	42.9	1.2	46	34	52	70	106	123	3.11E-06	1.82E+15

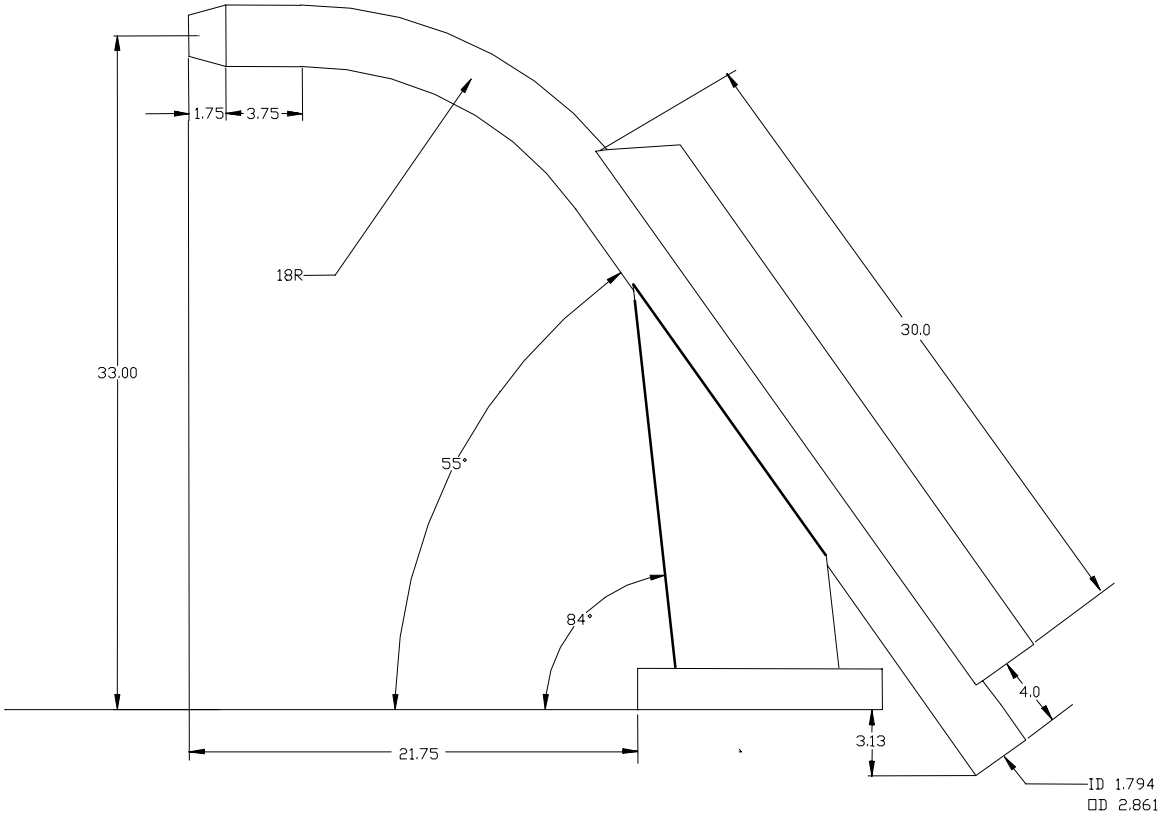

Fig. 1. AEDC particulate probe (dimensions are in inches).

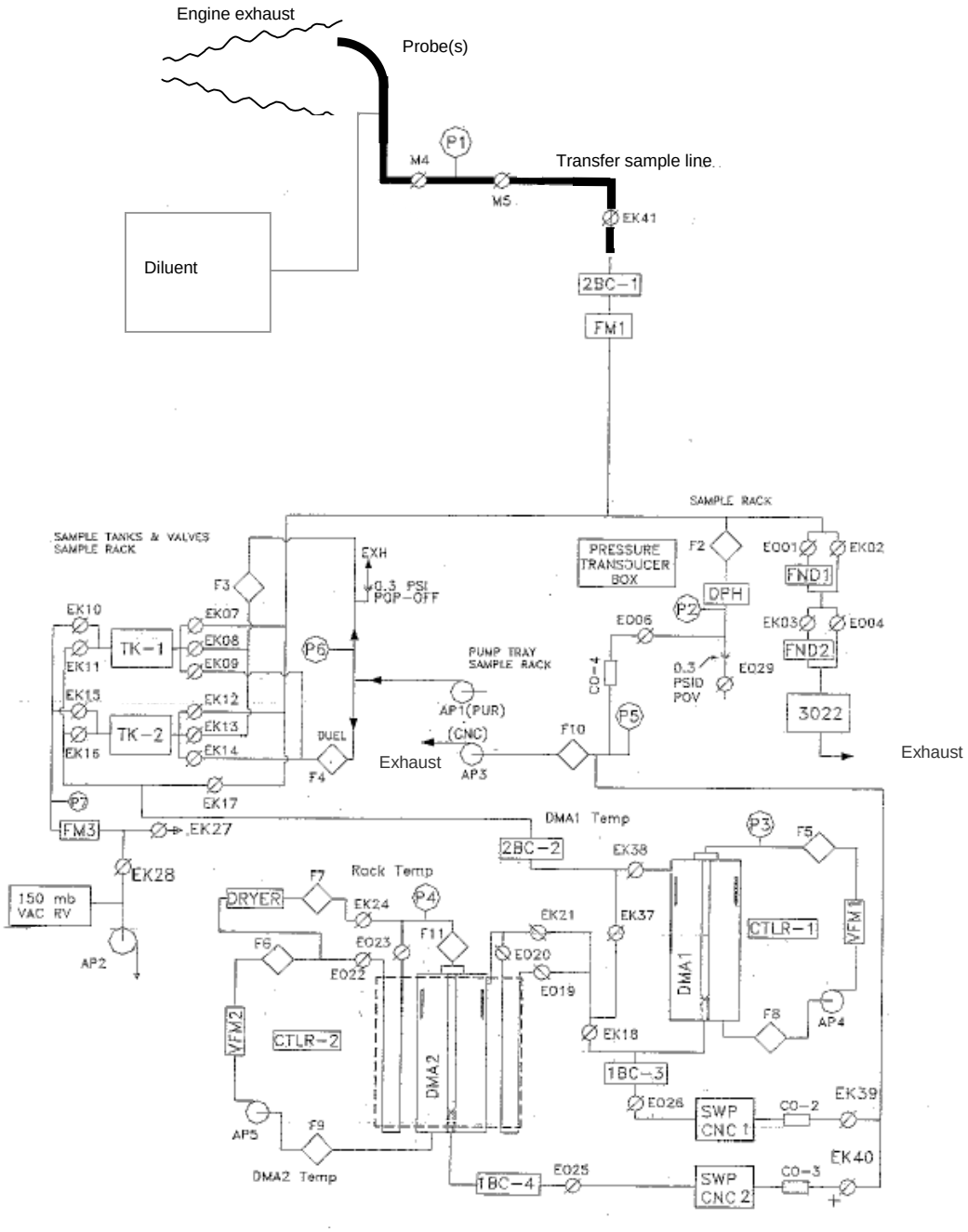

Fig. 2. Layout of Particulate and Gaseous Emissions Measurement System.
BC – bipolar charger, FM# - mass flow meter, FND# - filter needle diluter, DPH – dew point hygrometer, TK# - sample storage tank, AP# - vacuum pump, DMA# - differential mobility analyzer, SWP CNC# - sweep condensation nuclei counter, 3022 – TSI 3022 condensation particle counter, F# - filter, P# - pressure transducer, EK – normally closed solenoid valve, EO – normally opened solenoid valve, MV# - manual valve, CO# - critical orifice, CTRL# - controller, VFM# - volumetric flow meter

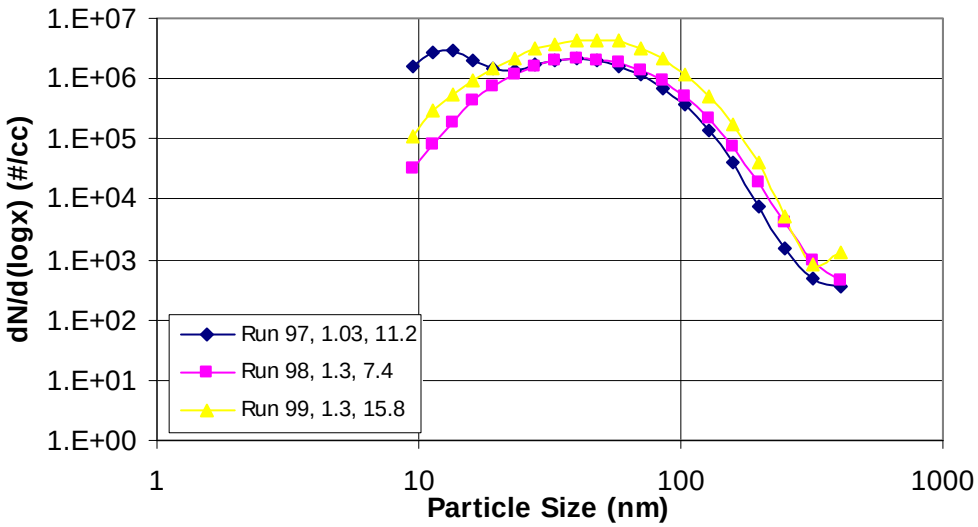

Fig. 3. Particle size distributions, probe distance 1 m, fuel sulfur content 810 ppm; parameters are engine pressure ratio and dilution ratio.

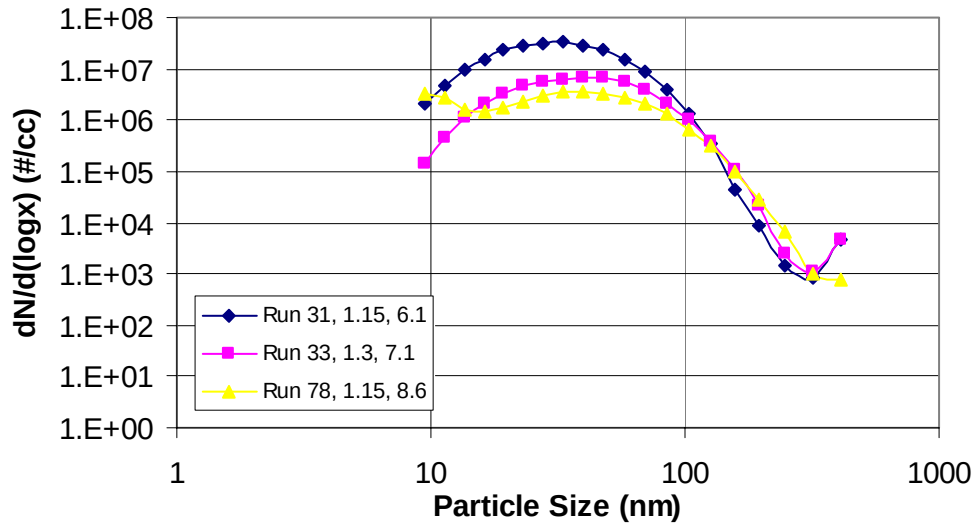

Fig. 4. Particle size distributions, probe distance 1 m, fuel sulfur content 1050 ppm; parameters are engine pressure ratio and dilution ratio.

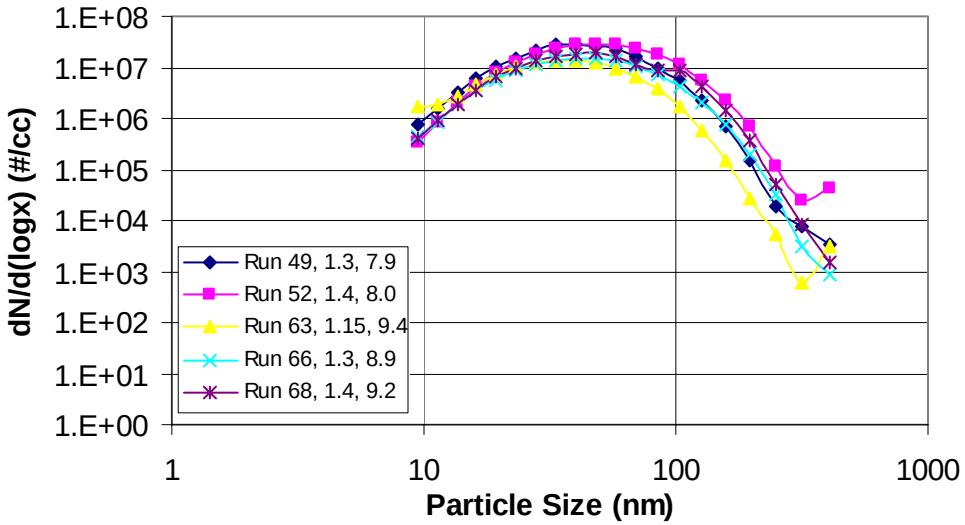

Fig. 5. Particle size distributions, probe distance 1 m, fuel sulfur content 1820 ppm; parameters are engine pressure ratio and dilution ratio.

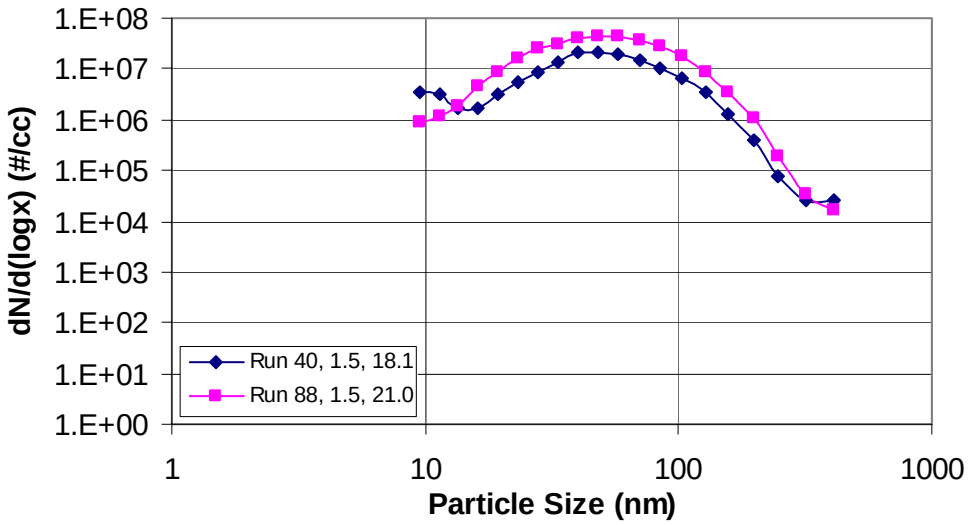

Fig. 6. Particle size distributions, probe distance 25 m, fuel sulfur content 1050 ppm; parameters are engine pressure ratio and dilution ratio.

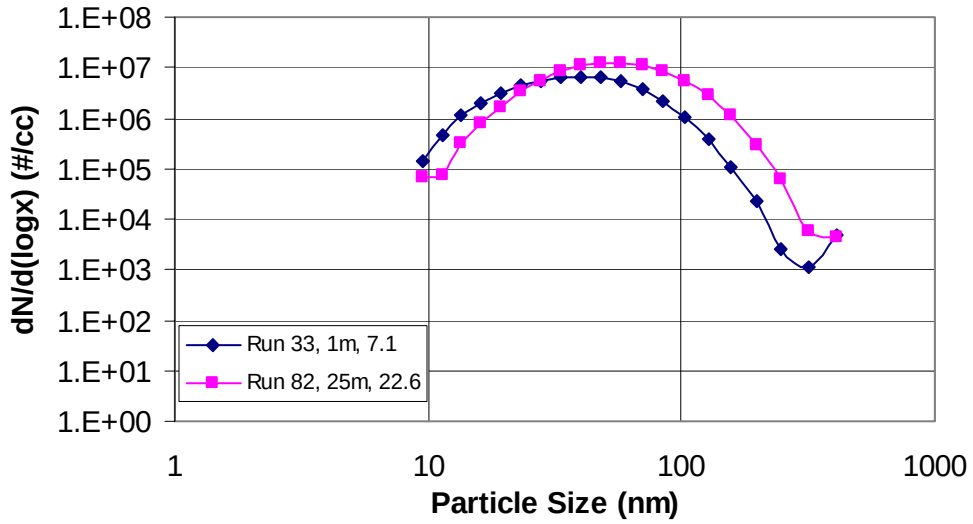

Fig. 7. Particle size distributions, engine pressure ratio 1.3, fuel sulfur content 1050 ppm, parameters are probe distance and dilution ratio.

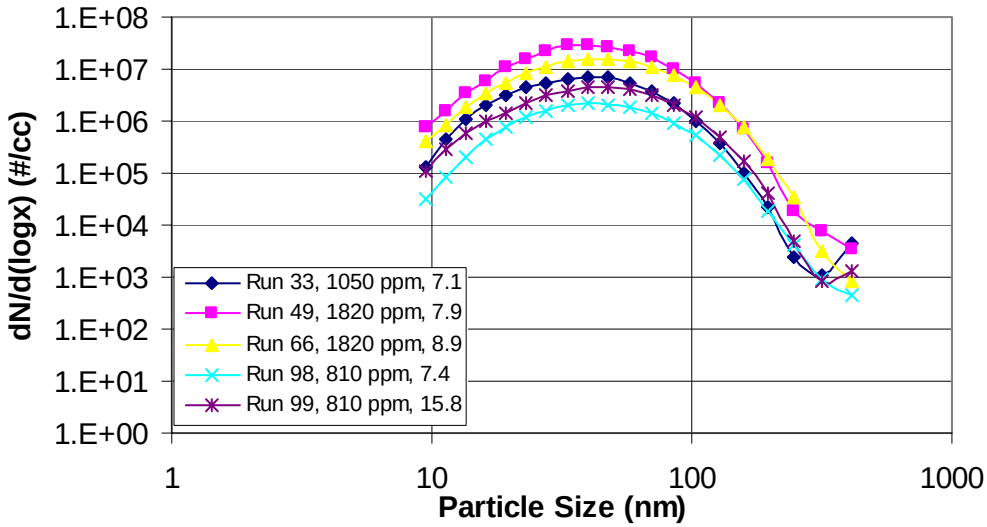

Fig. 8. Particle size distributions, engine pressure ratio 1.3, probe distance 1 m, parameters are fuel sulfur content, and dilution ratio.

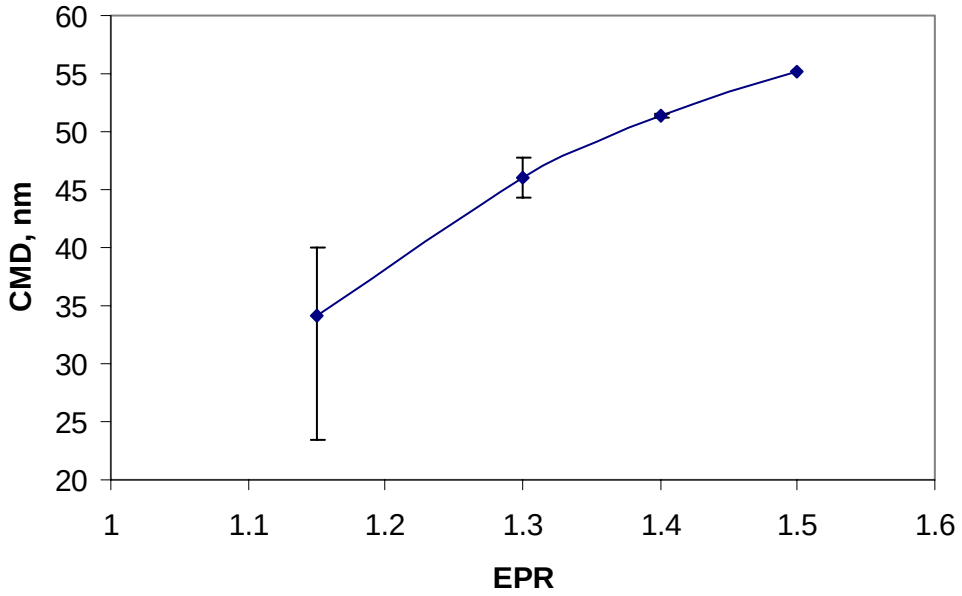

Fig. 9. Change in count mean diameter with engine pressure ratio. Probe distance is 1 m and fuel sulfur content is 1820 ppm. Data are for runs 46, 63, 49, 66,68, 69, and 71.

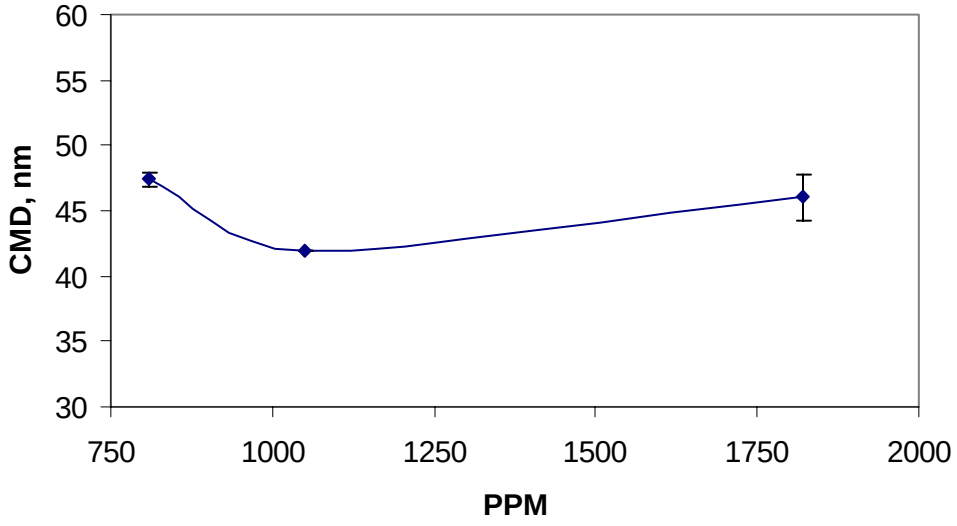

Fig. 10. Change in count mean diameter with fuel sulfur content. Probe distance is 1 m and engine pressure ratio is 1.3. Data are for runs 98, 99, 33, 66, and 49.

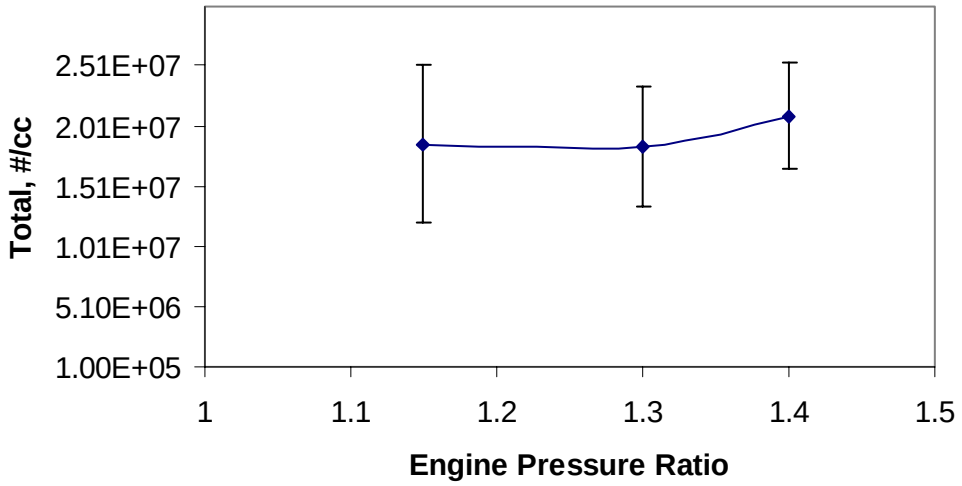

Fig. 11. Change in total particle number density with engine pressure ratio. Total number densities are averages of run 63, 46, 66, 49, 68 and 52.

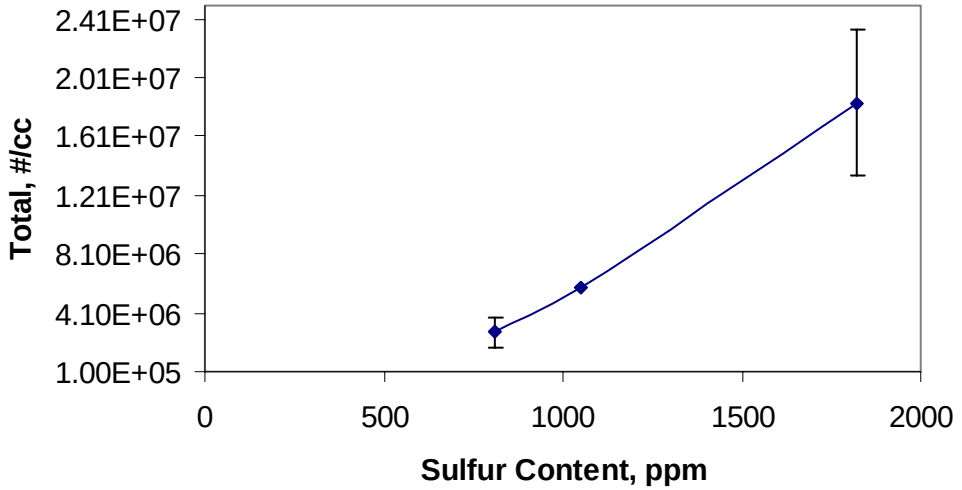

Fig. 12. Change in total particle number density with fuel sulfur content. Total number densities are averages of run 98, 99, 33, 66, and 49.

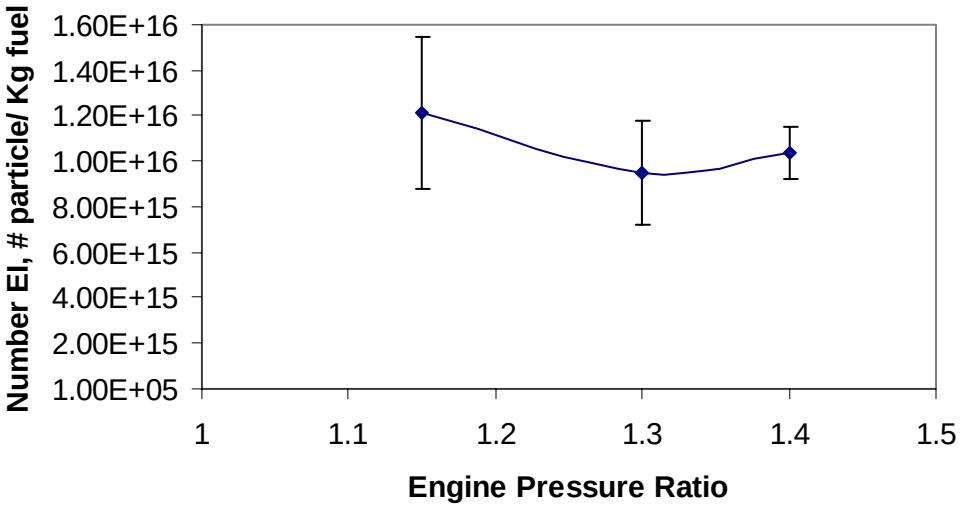

Fig. 13. Change in number based Emissions Index with engine pressure ratio. Probe distance is 1 m and fuel sulfur content is 1820 ppm. Emissions Indices are averages of run 63, 46, 66, 49, 68 and 52.

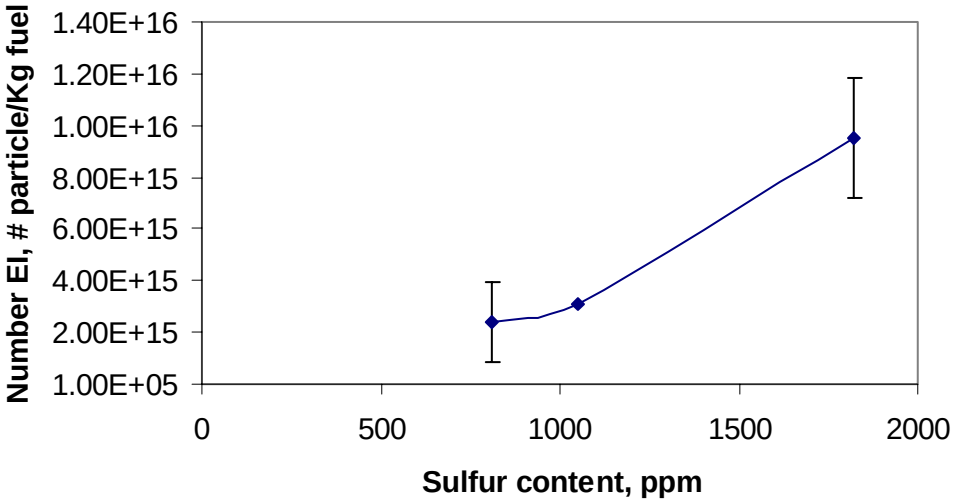

Fig. 14. Change in number based Emissions Index with fuel sulfur content. Probe distance is 1 m and engine pressure ratio is 1.3. Emissions Indices are averages of run 98, 99, 33, 66, and 49.

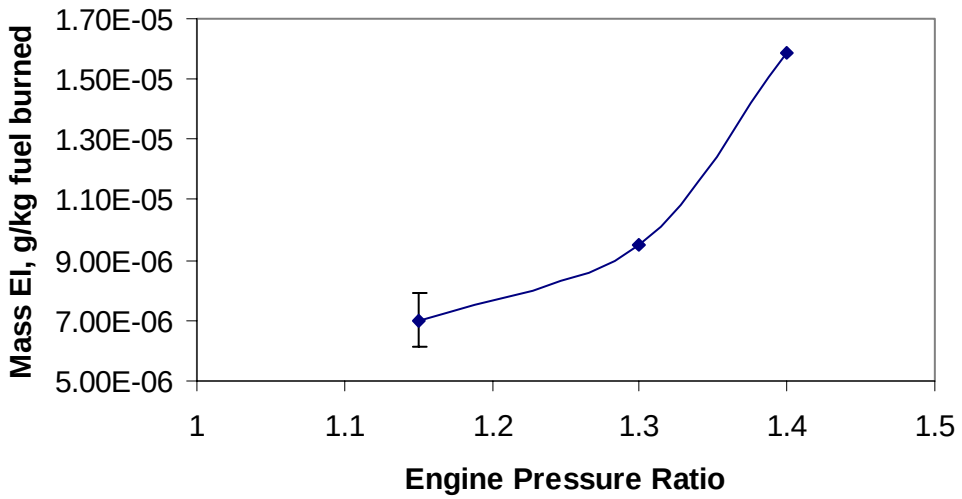

Fig. 15. Change in mass based Emissions Index with engine pressure ratio. Probe distance is 1 m and fuel sulfur content is 1820 ppm. Emissions Indices are averages of run 63, 46, 66, 49, 68 and 52.

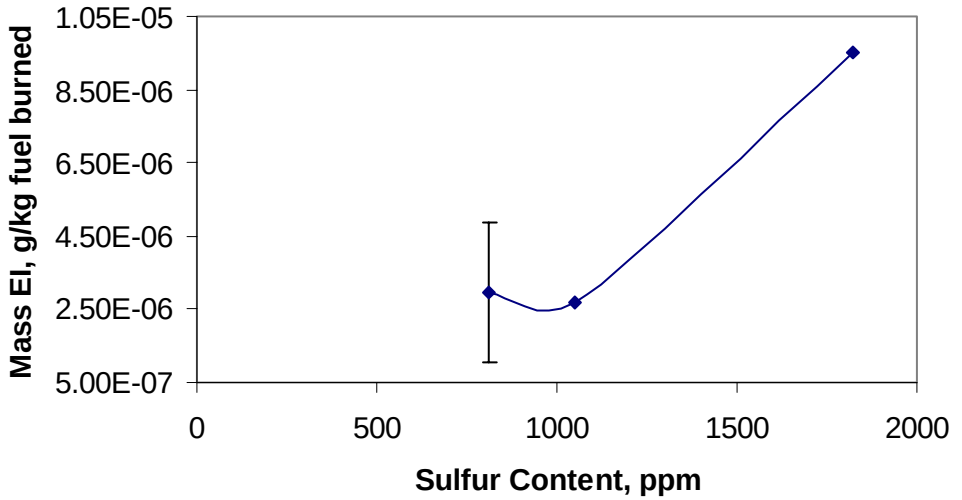

Fig. 16. Change in mass based Emissions Index with fuel sulfur content. Probe distance is 1 m and engine pressure ratio is 1.3. Emissions Indices are averages of run 98, 99, 33, 66, and 49.

REPORT DOCUMENTATION PAGE

Form Approved
OMB No. 0704-0188

The public reporting burden for this collection of information is estimated to average 1 hour per response, including the time for reviewing instructions, searching existing data sources, gathering and maintaining the data needed, and completing and reviewing the collection of information. Send comments regarding this burden estimate or any other aspect of this collection of information, including suggestions for reducing this burden, to Department of Defense, Washington Headquarters Services, Directorate for Information Operations and Reports (0704-0188), 1215 Jefferson Davis Highway, Suite 1204, Arlington, VA 22202-4302. Respondents should be aware that notwithstanding any other provision of law, no person shall be subject to any penalty for failing to comply with a collection of information if it does not display a currently valid OMB control number.
PLEASE DO NOT RETURN YOUR FORM TO THE ABOVE ADDRESS.

1. REPORT DATE *(DD-MM-YYYY)*	2. REPORT TYPE	3. DATES COVERED *(From - To)*
01- 08 - 2005	Technical Memorandum	

4. TITLE AND SUBTITLE

Experiment to Characterize Aircraft Volatile Aerosol and Trace-Species Emissions (EXCAVATE)

5a. CONTRACT NUMBER

5b. GRANT NUMBER

5c. PROGRAM ELEMENT NUMBER

6. AUTHOR(S)

Anderson, B. E.; Branham, H.-S.; Hudgins, C. H.; Plant, J. V.; Ballenthin, J. O.; Miller, T. M.; Viggiano, A. A.; Blake, D. R.; Boudries, H.; Canagaratna, M.; Miake-Lye, R. C.; Onasch, T.; Wormhoudt, J. Worsnop, D.; Brunke, K. E.; Culler, S.; Penko, P.; Sanders, T.; Han, H.-S.; Lee, P.; Pui, D. Y. H.; Thornhill, K. L.; and Winstead, E. L.

5d. PROJECT NUMBER

5e. TASK NUMBER

5f. WORK UNIT NUMBER

23-622-45-02

7. PERFORMING ORGANIZATION NAME(S) AND ADDRESS(ES)

NASA Langley Research Center
Hampton, VA 23681-2199

8. PERFORMING ORGANIZATION REPORT NUMBER

L-19019

9. SPONSORING/MONITORING AGENCY NAME(S) AND ADDRESS(ES)

National Aeronautics and Space Administration
Washington, DC 20546-0001

10. SPONSOR/MONITOR'S ACRONYM(S)

NASA

11. SPONSOR/MONITOR'S REPORT NUMBER(S)

NASA/TM-2005-213783

12. DISTRIBUTION/AVAILABILITY STATEMENT

Unclassified - Unlimited
Subject Category 45
Availability: NASA CASI (301) 621-0390

13. SUPPLEMENTARY NOTES

An electronic version can be found at http://ntrs.nasa.gov

14. ABSTRACT

The Experiment to Characterize Aircraft Volatile and Trace Species Emissions (EXCAVATE) was conducted at LaRC in January 2002 to assay the production of aerosols and aerosol precursors by a modern commercial aircraft, the Langley B757. Participants included the Aerodyne tunable diode laser and aerosol mass spectrometers teams; the NASA GRC Particle and Gaseous Emissions Measurement System group; the Air Force Research Laboratory mass spectrometer group; the University of Minnesota Aerosol Research particle characterization group; the University of California Irvine whole air sampling group; and the LaRC in situ measurements group. Measured parameters included exhaust gas velocity, temperature, and CO2 concentration; engine pressure ratios/power settings, fan speeds, combustor temperatures, and fuel-flow rates; sample stream CO2, SO2, SO3, H2SO4, HONO, HNO3, nonmethane hydrocarbons, and halocarbons; aerosol number densities and size distributions as a function of sample temperature; and aerosol mass and composition. Data were collected behind both the Langley T-38A (J85-GE engine) and B-757 (RB211) at sampling distances ranging from 1 to 35 m as the aircraft burned fuels with a variety of fuel sulfur concentrations. A detailed experiment description along with measurement results are presented within this report.

15. SUBJECT TERMS

Emission indices; Black carbon; Size distributions; Number densities; Nonvolatile particles; Volatile particles; Hydrocarbons

16. SECURITY CLASSIFICATION OF:			17. LIMITATION OF ABSTRACT	18. NUMBER OF PAGES	19a. NAME OF RESPONSIBLE PERSON
a. REPORT	b. ABSTRACT	c. THIS PAGE			STI Help Desk (email: help@sti.nasa.gov)
					19b. TELEPHONE NUMBER *(Include area code)*
U	U	U	UU	175	(301) 621-0390